BIOFABRICATION OF FUNCTIONAL LIVER TISSUE CONSTRUCT BY THREE-DIMENSIONAL ORGANOID BIOPRINTING

ROOPESH R. PAI

Ph.D. THESIS

2022

SREE CHITRA TIRUNAL INSTITUTE FOR
MEDICAL SCIENCES AND TECHNOLOGY, TRIVANDRUM
Thiruvananthapuram

An Institution of National Importance established by an Act of the Indian Parliament
(Act No.52 of 1980)

Dept. of Science and Technology, Govt. of India
www.sctimst.ac.in

BIOFABRICATION OF FUNCTIONAL LIVER TISSUE CONSTRUCT BY THREE-DIMENSIONAL ORGANOID BIOPRINTING

A THESIS PRESENTED BY
ROOPESH R. PAI

TO

THE SREE CHITRA TIRUNAL INSTITUTE FOR
MEDICAL SCIENCES AND TECHNOLOGY, TRIVANDRUM
Thiruvananthapuram

IN PARTIAL FULFILMENT OF THE REQUIREMENTS
FOR THE AWARD OF

DOCTOR OF PHILOSOPHY

2022

DECLARATION BY THE STUDENT

CERTIFICATE

I Roopesh R. Pai hereby certify that I have personally carried out the work depicted in the thesis entitled, “Biofabrication of Functional Liver Tissue Construct by Three-Dimensional Organoid Bioprinting”. No part of the thesis has been submitted for the award of any other degree or diploma prior to this study.

Signature Roopesh

Name of the Candidate: Roopesh R. Pai

Date: 22.11.2022

Reg. no: 2016/PHD/09

श्री चित्रा तिरुनाल आयुर्विज्ञान एवं प्रौद्योगिकी संस्थान, त्रिवेंद्रम, जैवचिकित्सकीय प्रौद्योगिकी स्कंध
पूजप्पुरा, तिरुवनन्तपुरम - 695 012, केरल, भारत
SREE CHITRA TIRUNAL INSTITUTE FOR MEDICAL SCIENCES AND TECHNOLOGY, TRIVANDRUM
BIO MEDICAL TECHNOLOGY WING
POOJAPPURA, THIRUVANANTHAPURAM - 695 012, KERALA, INDIA
(एक राष्ट्रीय महत्व का संस्थान, विज्ञान एवं प्रौद्योगिकी विभाग, भारत सरकार)
An Institution of National Importance, Department of Science & Technology, Government of India)
टेलीफॉन नं./Telephone No: 0471-2340801/2520450, फैक्स/Fax: 0471-2341814
ई-मेल/E-mail:sct@sctimst.ac.in वेबसाइट/Website : www.sctimst.ac.in

CERTIFICATE BY THE RESEARCH GUIDE

Dr. Anil Kumar PR
Scientist G, Division of Tissue Culture
Department of Applied Biology,
BMT wing, SCTIMST, Trivandrum

This is to certify that **Mr. Roopesh R. Pai**, in the Division of Tissue Culture, Department of Applied Biology of this Institute has fulfilled the requirements prescribed for the Ph.D. degree of the Sree Chitra Tirunal Institute for Medical Sciences and Technology, Trivandrum.

The thesis entitled, "*Biofabrication of Functional Liver Tissue Construct by Three-Dimensional Organoid Bioprinting*" was carried out under my direct supervision. No part of the thesis was submitted for the award of any degree or diploma prior to this date.

Clearance was obtained for this study from the Institutional Animal Ethics Committee for liver cell isolation and from Institutional Committee for Stem Cell Research for Mesenchymal Stem Cell isolation and culture.

Signature

Date 22.11.2022

The thesis entitled

Biofabrication of Functional Liver Tissue Construct by Three-Dimensional Organoid Bioprinting

Submitted by

ROOPESH R. PAI

for the degree of

Doctor of Philosophy

of

SREE CHITRA TIRUNAL INSTITUTE FOR
MEDICAL SCIENCES AND TECHNOLOGY, TRIVANDRUM

Thiruvananthapuram

is evaluated and approved by

Dr. Anil Kumar P.R
(Research guide)

(Name & Signature of thesis examiner)
Prof. Dr. Geetha Manivasagam

DEDICATED TO MY FAMILY AND

TEACHERS

ACKNOWLEDGEMENTS

I present this dissertation with a true sense of gratitude, satisfaction, and the divine favour of God. The work presented in this thesis would not have been accomplished without the close cooperation of numerous people who offered assistance when it was needed. I take this opportunity to thank them all for their significant contributions.

I express my deep gratitude and sincere thanks to my mentor Dr. Anil Kumar P.R, for providing this opportunity to pursue and complete this study. His enthusiasm about science and the scientific approach he practised towards solving a research problem, has always inspired me to develop my scientific temperament and independent thinking capability. I express my sincere gratitude for his constant support, contributions of ideas and feedback without which this dissertation would not have been completed successfully.

I thank my Doctoral Advisory Committee Members Dr. V Kalliyana Krishnan, Retd. Scientist G, Division of Dental Products, SCTIMST, Trivandrum, Dr. T.V Kumary, Retd. Scientist G, Division of Tissue Culture, SCTIMST, Trivandrum, Dr. Roy Joseph, Scientist G, Division of Polymeric Medical Devices, SCTIMST, Trivandrum, Dr. Ramesh P., Scientist G, Division of Polymeric Medical Devices, SCTIMST, Trivandrum and late Dr. Meenu Hariharan, Gastroenterologist, PRS Hospital, Trivandrum for their valuable time, suggestions, and encouragement right from the beginning of my work.

I extend my sincere thanks to all members of the Division of Tissue Culture, for their direct or indirect help during my work. Specifically, to mention are: Mrs. Deepa Raj for her assistance during primary cell isolation, polymer synthesis and characterization. Technical support given by Mrs. Usha Vasudev and Mr. Vinod D. is highly appreciated. I acknowledge the timely support and valuable suggestions from Dr. Senthilkumar Muthusamy and Dr. Naresh Kasoju. I thank all my colleagues Dr. Balu Venugopal, Ms. Sneha, Mrs. Shilpa, Mrs. Anupama, Ms. Kripamol, Mrs.

Aswathy, Mrs. Jimna, Mr. Subash and Mr. Seenuvasan for their compassion and friendship.

I express my deep gratitude to Dr. Shiny Velayudhan, Scientist E, Division of Dental Products for her unmatched intellectual and moral support in the synthesis and characterization of bioink for my work. I also thank Dr. Harikrishnan V.S, Dr. Sachin J. Shenoy, Mr. Manoj, Mr. Sunil Kumar and Mr. Sharath for their support and help in animal handling during my experiments. I also express my sincere thanks to Dr. Sabareeswaran, Mrs Sulekha Baby, Mr. Joseph and Ms Sandhya for histopathology analysis, to Dr. Lissymol P.P, and Dr. Deepu for providing access to the lyophilization facility and Micro CT analysis, to Dr. Anugya and her team for helping me with the rheological analysis.

I gratefully acknowledge SCTIMST for the Institute Fellowship provided during my doctoral program. I thank the Director, SCTIMST, and Head, BMT wing for providing the facilities to carry out this research work. I will be always obliged to Prof. Ajith Kumar, Dean and Dr. P.V Mohanan, the Associate Dean, PhD, SCTIMST, for their support both in academic and administrative level. I am thankful to Dr. Santhosh Kumar Registrar, SCTIMST, Mrs. Radha M., Deputy Registrar, SCTIMST and staff of the academic division for all the academic assistance in this journey.

I have no words to express my gratitude and heartfelt thanks to my family members who always stood with me throughout all the difficult times and directed me to things that really matter in life. I am always indebted to my parents for their encouragement, love and prayers. I thank my wife Mrs. Anupama and my son Madhav for their compassionate love, understanding and for being my strength during hardships.

Finally, above all I thank God Almighty for showering his blessings on me.

TABLE OF CONTENTS

LIST OF FIGURES

LIST OF TABLES

LIST OF ABBREVIATIONS

3D : Three-dimensional
ATP : Adenosine triphosphate
CAD : Computer-aided designing
CD : Cluster of differentiation
CPr : Cartridge pressure
CYP450 : Cytochrome P450
DMEM : Dulbecco's modified Eagle's medium
EGF : Epidermal growth factor
FBS : Feal bovine serum
GelMA : Gelatin methacrylamide
GMA : Glycidyl methacrylate
HdCC : Hanging drop culture chamber
HGF : Hepatocyte growth factor
IMDM : Iscove's modified Dulbecco's medium
LCST : Lower critical solution temperature
LPMT : Liver parenchymal microtissue
MEM : Minimum essential medium
MSC : Mesenchymal stem cell
NGMA : N-isopropyl-co-glycidyl methacrylamide
NIPAAm : N-isopropyl acrylamide
NPC : Non-Parenchymal cells
PET : Polyethylene terephthalate
PSTC : Polystyrene tissue culture grade
PVC : Polyvinyl chloride
UHMWPE : Ultra-high molecular weight polyethylene
UV : Ultra violet
VCT : Valve closing time
VOT : Valve opening time

SYNOPSIS

Liver is the largest visceral organ in the human body that performs many vital functions. According to the Global Disease Burden Study 2019, the global incidence of liver disease in the year 2019 was 266.5 million and among which 1.34 million people died worldwide. Currently, liver transplantation is the only viable cure for patients progressing to end-stage liver diseases. Meanwhile, lack of available liver donors for transplantation has become the primary impetus for using alternative methods such as tissue engineering. Tissue engineering is an advanced field in biomedical science that aims to develop biological substitutes capable of restoring damaged tissue. Biomedical technologies have advanced to such a level that engineered tissues can be clinically used. Tissue-engineered functional liver tissue constructs have immense potential in two domains of human health care. Firstly, it can be a promising substitute for liver transplantation. Secondly, it can be a model for predicting drug-induced liver injury. Conventional tissue engineering follows a top-down approach where cells are seeded over a biocompatible prefabricated scaffold to mature into a functional tissue equivalent. The limitation of this approach is the non-uniform distribution of cells within the scaffold and the lack of tissue organization. Recently, three-dimensional (3D) bioprinting has emerged as a bottom-up assembly approach to fabricate customized tissue constructs by layer-by-layer deposition of cells and biomaterials with precise control over the spatial distribution of cells. However, the current know-how on 3D bioprinting does not address the lack of tissue organization within bioprinted tissue constructs. *In vivo*, the major functional liver cell hepatocytes are organized into plates with intact cell-cell contact that gives rise to

hepatocyte polarization. Hepatocyte polarization is important to maintain the mature hepatic functions and therefore, attaining tissue-like organization within the bioprinted liver construct is essential. In this scenario, self-organized cellular aggregates known as organoids can be used for bioprinting to achieve the histoarchitecture of the liver partially or completely. Meanwhile, a scalable method to generate intact organoids is required for bioprinting applications. The current organoid culture method uses matrigel and it requires mechanical or enzymatic treatments to harvest the organoids that affect cellular integrity and scalability. In this context, the thermoresponsive culture dishes which allow enzyme-free cell retrieval with intact cell–cell contacts, will be a scalable platform for organoid culture and non-invasive retrieval.

On this backdrop, it is hypothesized that "Three-dimensional bioprinting of hepatic tissue organoids formed on the thermoresponsive substrate can be used to develop a structurally organized functional liver tissue construct." To test the hypothesis, following objectives were put forward.

1. Development of suitable bioink for organoid bioprinting.
2. Generation of hepatic organoids using thermo-responsive culture substrate.
3. Designing and 3D Bioprinting of *in vitro* liver construct.
4. Functional evaluation of 3D Bioprinted liver tissue construct.

The thesis comprises a proof-of-concept study highlighting two key aspects, (1) the generation of hepatic organoids using a thermoresponsive substrate and (2) 3D bioprinting of hepatic organoids to achieve a structurally organized functional liver tissue construct.

The thesis is divided into five chapters - Chapter 1-Introduction, Chapter 2-Literature review, Chapter 3-Materials and Methods, Chapter 4-Results and Discussion and Chapter 5-Summary and Conclusion.

Chapter 1 introduces the area of research beginning with a description of the organ liver, its anatomy and physiology followed by liver diseases, their complications and their impact on society. The current treatment strategies using liver-assist devices, hepatocyte infusion, and liver transplantation are discussed with their advantages and limitations. The chapter then details the relevance of tissue engineering in liver regenerative therapy. The current approaches in liver tissue engineering and their limitations are highlighted. The chapter then defines the research problem. To address the research problem a research hypothesis is formulated and the objectives through which the hypothesis can be proved are enumerated in this chapter. The chapter ends with a mention on the scope of the thesis.

Chapter 2 reviews the relevant literature on recent advances in liver tissue engineering, with a focus on approaches aimed at *in vitro* reconstruction of liver tissue architecture. The chapter begins with a brief note on the relevance of liver tissue engineering in the past decade and later dives into the literature on the basic elements of liver tissue engineering, i.e., the cell sources and biomaterials. Thereafter, a review of the various approaches in liver tissue engineering is presented, highlighting their advantages and major limitations. Finally, a detailed review is presented focusing on the current progress in process methodologies attempted in 3D cell culture and 3D bioprinting field with an emphasis on reconstruction of liver tissue architecture in bioengineered tissues.

Chapter 3 contains a structured experimental design elaborating the materials, equipment and protocols involved in the study. The chapter begins with the synthesis, physicochemical characterization, and biological evaluation of Gelatin Methacrylamide (GelMA). The methacrylation of gelatin was confirmed by ^{1}H-NMR spectroscopy and quantified by ninhydrin assay. Different concentrations of GelMA polymer solution containing photoinitiator were cross-linked by UV light of 365 nm. The properties of hydrogels like swelling, weight loss, compressive strength and cytotoxicity were analyzed. The suitability of GelMA for organoid bioprinting was initially evaluated using the HepG2 microtissue or spheroid model. A high-throughput methodology for liver parenchymal microtissue (LPMT) production was devised by combining a microvalve-based cell printing technique with a novel hanging-drop culture chamber. The LPMTs were cultured within a GelMA hydrogel sandwich and their liver-specific functions were evaluated. A GelMA bioink formulation without cells was analyzed for its rheological characteristics and printability.

To prepare the thermoresponsive substrate, a copolymer poly (N-isopropyl acrylamide-co-glycidyl methacrylate) (NGMA) was synthesized and characterized. The copolymer was characterized by ^{1}H-NMR spectroscopy, differential scanning calorimetry and gel permeation chromatography. NGMA was coated on a cell culture dish, its cytocompatibility and thermoresponsive property were tested. Two different strategies were tested to generate hepatic organoids using NGMA dishes. Finally, an optimal strategy was implemented to generate organoids as described hereafter. The rat bone marrow-derived mesenchymal stem cells (MSCs) and rat liver cells were isolated and characterized by immunostaining. The MSCs were then seeded in NGMA coated dish to form a feeder layer and rat liver cells were cocultured on the feeder layer for 72 h to form organoids. The organoids were then easily retrieved from the dish by keeping them at 4°C for 10 min. The cell viability, liver-specific functions, histomorphology and expression of tissue-specific markers were analyzed. A three-dimensional construct of size 14x14x2 mm was designed using a freehand computer-aided designing software. The design and printing parameters were optimized for bioprinting organoids. Retrieved hepatic organoids were suspended in GelMA bioink and were bioprinted. Constructs bioprinted using cell-suspended bioink was considered as a control. The cell construct comprised of all cell types present in organoids. The constructs were cultured for two weeks in Iscove's Modified Dulbecco's medium supplemented with growth factors. Finally, the liver-specific functions mainly albumin synthesis, ammonia detoxification, drug-induced cytochrome P450 activity and glycogen storage were evaluated for both the constructs. The expression of mature hepatic genes was quantified by qRT-PCR. The histomorphology of the bioprinted construct was analyzed by H&E staining. Laterally, the expression of tissue-specific markers was confirmed by immunofluorescence staining.

Chapter 4, presents the results obtained and discusses the results in comparison to previous findings. The ^{1}H-NMR spectrum of GelMA showed proton peaks corresponding to the methacrylamide group and the mean degree of methacrylation was 77%. The GelMA hydrogel showed optimal physical properties and was non-cytotoxic. The LPMTs cultured in GelMA hydrogel sandwich showed enhanced liver functionality. The GelMA bioink formulation exhibited shear-thinning property and excellent printability. The ^{1}H-NMR spectrum of NGMA showed proton peaks corresponding to the individual monomers. The lower critical solution temperature of

NGMA was determined to be 29.02 °C and the molecular weight average (Mw) was 97,115. NGMA coated dish was non-cytotoxic and exhibited thermoresponsive property. The rat liver cells and MSCs organized to form hepatic organoids in NGMA coated dishes. The retrieved organoids were viable, functional, and exhibited tissue-like histomorphology with the expression of tissue-specific markers. The bioprinted hepatic organoid constructs outperformed the cellular construct. The expression of liver-specific genes and the functions like albumin synthesis, ammonia detoxification and drug-induced cytochrome P450 enzyme activity was significantly higher in the organoid construct. Histomorphological analysis revealed hepatic plate-like tissue organization in the organoid construct whereas in the cellular construct there was no sign of tissue organization. The results substantiate that achieving tissue organization within the bioprinted construct will enhance the functional capability of liver cells *in vitro*.

Chapter 5 summarizes the results and conclusions are drawn. An optimal bioink formulation containing GelMA was developed for organoid bioprinting. Viable and functional hepatic organoids were generated from NGMA-coated culture dishes. Three-dimensional bioprinting of hepatic organoids using GelMA bioink allowed biofabrication of tissue-mimetic functional liver constructs. In conclusion, the study emphasizes the fact that hepatic organoids derived from the thermoresponsive substrate are ideal building blocks for 3D bioprinting to achieve histomimetic functional liver tissue construct. The methodology presented in this study can be applied to develop human liver organoid constructs for drug testing and regenerative therapy.

Chapter 1

INTRODUCTION

1.1 Liver

The liver is the largest solid organ and the largest gland of the human body, situated in the right hypochondrium, below the diaphragm in the abdomen. An adult human liver weighs between 1.3 and 1.5 kg. It is the only visceral organ that can regenerate completely without any loss of function and performs a wide range of vital functions (Kalra *et al.*, 2022).

1.1.1 Liver anatomy

The gross structure of the human liver can be divided into four parts or lobes: the right lobe, the left lobe, the caudate lobe, and the quadrate lobe (Abdel-Misih and Bloomston, 2010). The falciform ligament separates the lobes. This ligament is a band of tissue that keeps the liver anchored to the diaphragm. Each lobe comprises thousands of lobules, which are the structural units of the liver. The functional unit of liver is explained in two different ways as, 1) classic liver lobule and 2) hepatic acinus. A classic liver lobule structure consists of a hexagonal compartment made up of hepatic plates separated by sinusoidal capillaries that converge toward a central efferent vein (Figure 1) (Vernon, Wehrle and Kasi, 2021). The hepatic plate comprises columns of hepatocytes, often one cell thick in mammals. A portal triad at each vertex of the hexagonal unit consists of a portal vein, hepatic artery, and hepatic bile duct.

The oxygenated blood from the hepatic artery and the portal vein opens into the sinusoidal capillaries to pass through the hepatocytes before draining out through the central vein. The lobule constitutes all liver cell types assembled in a distinct pattern to perform specific liver functions. The hepatic acinus is an ellipsoidal structure that covers a mass of hepatocytes with terminal hepatic venules on the periphery and a tiny portal tract in the middle (Krishna, 2013). It is partitioned into zones 1, 2, and 3, with zone 1 enclosing the hepatocytes adjacent to the portal tract and zone 3 enclosing the hepatocytes adjacent to central vein. Blood from the portal tract flows from the zone 1 to zone 3 through these zones to the central vein with a decreasing oxygen and nutrient gradient.

The cells in the liver can be categorized as parenchymal and non-parenchymal cells. The hepatocytes are the primary parenchymal cell type in the liver that accounts for approximately 80 % of the total liver volume and 70 % of liver cell mass (Blouin, Bolender and Weibel, 1977a). They are highly polarized epithelial cells with a distinct apico-basal polarity that accounts for liver functionality. The apical surface of the neighboring hepatocytes enclosed by the tight junction forms a canaliculus through which the bile acids and salts are transported to the bile duct. The basolateral surface of the hepatocyte confronts the perisinusoidal space, also known as the space of Disse (Krishna, 2013). The cholangiocytes (biliary epithelial cells) are the second parenchymal cell type that form 3-5 % of total liver cell mass (Hall *et al.*, 2017). These cells line the bile duct and regulate the flow, composition and pH of bile secreted by hepatocytes. The non-parenchymal cell fraction consists of sinusoidal endothelial cells (16%), Kupffer cells (tissue-resident macrophages) (12%), hepatic stellate cells (8%) and pit cells (natural killer cells) (Damania, Jain and Kumar, 2014). The sinusoidal endothelial cells are specialized cells that are in direct contact with the blood. They are fenestrated and line the sinusoidal capillaries permitting free exchange of macromolecules between hepatocytes and blood. The Kupffer cells and pit cells reside within sinusoidal side helping in scavenging blood-borne pathogens. The hepatic stellate cells are found in the space of Disse, and they serve as a reservoir for vitamin A and lipid molecules. The hepatocytes perform all primary functions of the liver in concert with the non-parenchymal cells.

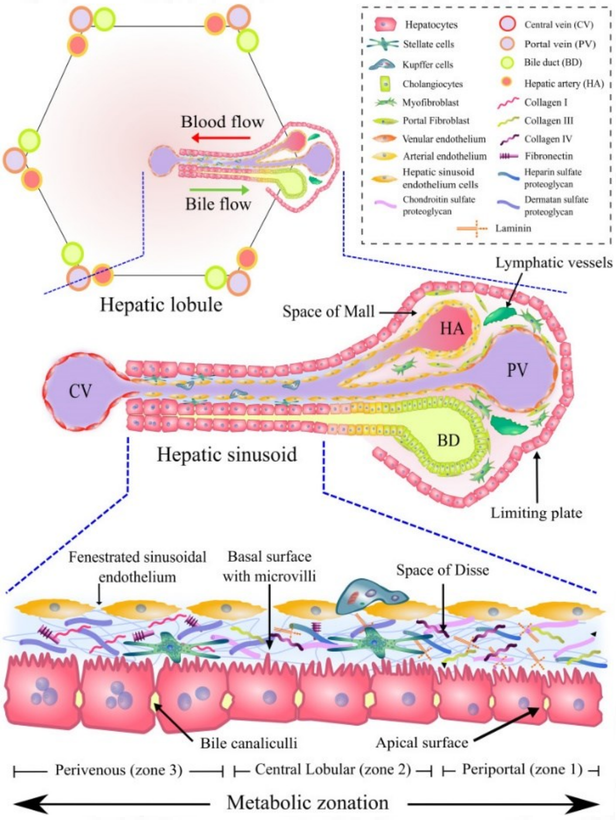

Figure 1. Diagrammatic representation of the microarchitecture of liver lobule and sinusoid. Reproduced with permission from Agarwal, *et al;*2021.(Agarwal, Banerjee, Konwarh, Esworthy, Kumari, Onesto, Das, Lee, Wagener, Makvandi, Mattoli, Ghosh, Maiti, Zhang and Ibrahim T Ozbolat, 2021)

1.1.2 Liver physiology

The primary functions of the liver consist of the metabolism of proteins, carbohydrates and lipids, detoxification of xenobiotics, and they serve as a reservoir for blood and several other micronutrients (Khonsary, 2017). The protein metabolism function includes deamination of amino acids, converting ammonia to urea, and synthesis of serum proteins. Simultaneously, the liver regulates blood glucose levels through gluconeogenesis and glycogen storage. In the liver, the oxidation of fatty acids can liberate a tremendous amount of energy. Meanwhile, the synthesis of cholesterol and lipoproteins helps to form bile acids and transport lipid molecules to other tissues. As a gland, the liver also performs many endocrine and exocrine functions. The endocrine secretion of several plasma proteins including coagulation factors helps in regulating blood clotting. At the same time, the exocrine transport of bile acids into the intestine facilitates digestion and absorption of dietary fat. Detoxification of xenobiotics is an output of the biotransformation process in liver. Biotransformation is an enzyme-mediated biochemical modification of xenobiotics to hydrophilic form for easy elimination from the body (Phang-Lyn and Llerena, 2022). Enzyme isoforms belonging to the Cytochrome P-450 (CYP450) and UDP-glucuronosyltransferase families mediate the major biotransformation in hepatocyte (P Sharma, 2014). As a blood reservoir, liver holds about 13% of the body’s total blood supply at any given moment. Similarly, micronutrients such as vitamin A, D, E, K, and B12, metals like iron, copper and trace elements such as zinc, selenium, manganese, molybdenum and cobalt are stored in liver.

Another characteristic feature that adds to the complexity of the liver is the zonation of liver functions within a lobule (Agarwal, Banerjee, Konwarh, Esworthy, Kumari, Onesto, Das, Lee, Wagener, Makvandi, Mattoli, Ghosh, Maiti, Zhang and Ibrahim T. Ozbolat, 2021). The unidirectional flow of blood within liver lobule causes a progressive decrease in concentration of oxygen and nutrients towards the central vein due to their sequential consumption by cells along the radial axis of lobule. Such a variable microenvironment give rise to a graded expression of tissue morphogens and causes spatial compartmentalization of liver metabolic functions along the radial axis of lobule, a phenomenon known as metabolic zonation (Manco and Itzkovitz, 2021). The liver lobule consists of three metabolic zones namely, periportal (zone 1), centrilobular (zone 2) and perivenous (zone 3) (Figure 1). High-energy demanding processes such as gluconeogenesis, cholesterol biosynthesis, urea genesis and protein secretion occur in zone 1. While processes such as glycolysis, xenobiotic metabolism and lipogenesis occur in zone 3. The intermediate zone 2 is known as the transition zone and the hepatocytes present here are involved in synthesis of iron-regulating hormone hepcidin and are major contributors to liver regeneration (Wei *et al.*, 2021). Like hepatocytes, the NPCs also exhibit heterogeneity in their gene-expression and function at different zones (Cunningham and Porat-Shliom, 2021).

1.1.3 Liver diseases: types of liver diseases and their complications

Abnormal liver condition can impair many critical functions within the body and can be fatal. If unnoticed, the insult to liver can progress to non-functional stage of liver disease. Diseases of liver can be caused by various factors such as microbial infections, alcohol and drug abuse, immune disorder, tumor and inherited gene mutations. Liver diseases can be broadly classified as acute or chronic based on the duration for initiation of liver dysfunction. Acute liver failure (ALF) is a life-threatening condition in which liver function deteriorates rapidly within a few days or weeks due to extensive hepatocyte death. Being a key player in biotransformation of drugs and other xenobiotics, liver is highly susceptible to DILI. Cytochrome P-450 enzyme mediated reactions may produce toxic secondary metabolites that lead to liver injury through many different mechanisms (Lee, 2003). End stage of ALF often leads to jaundice, cerebral edema, bleeding disorders, kidney failure and infections.

In chronic liver disease (CLD) there is a progressive destruction of liver tissue over months, years or decades. It begins with an inflammation of liver, initiating fibrosis and then progresses to cirrhosis through end-stage liver diseases (ESLDs) ESLD cannot be reversed and only hope to save the patient is liver transplantation (Tajir and Shimizu, 2013). The potential causes of acute liver failure include drug overdose, intake of toxins, and autoimmune hepatitis, leading to complications such as cerebral edema, gastrointestinal bleeding, and kidney failure. The prevalent etiologies of CLD are hepatitis C virus (HCV), hepatitis B virus (HBV), alcohol-related liver diseases (ARLD) and non-alcoholic fatty liver diseases (NAFLD). Hepatitis C virus is a single-stranded RNA virus that promotes hepatic inflammation and fibrosis, leading to liver carcinoma and cirrhosis upon infection (Tagle, Lemon and Schiff, 2006). Hepatitis B virus is a double-stranded DNA virus recognized as the agent responsible for serum hepatitis. It is the most common parenterally transmitted hepatitis virus, which causes complications similar to the HCV infection (Tagle, Lemon and Schiff, 2006). ARLD is associated with excess alcohol intake, causing a build-up of fat in the liver, leading to cirrhosis, internal bleeding, encephalopathy, ascites and liver cancer (Osna, Donohue and Kharbanda, 2017). In contrast, NAFLD is metabolic dysfunction that also causes the accumulation of fat in the liver, the cause for which is unknown. However, obesity and type 2 diabetes are considered strong risk factors for NAFLD (Manne, Handa and Kowdley, 2018). NAFLD is classified into two types based on severity of inflammation. Simple fatty liver is a condition in which there is little or no inflammation. Non-alcoholic steatohepatitis (NASH) is a severe form of the fatty liver disease marked by severe inflammation and liver cell damage which may lead to liver cirrhosis or cancer (Manne, Handa and Kowdley, 2018).

1.1.4 Liver diseases – Global status

Liver diseases are steadily increasing around the globe, affecting individuals in all age groups. According to the 2017 Global Burden Disease (GBD) study, 2.14 million deaths per year have been attributed to liver cirrhosis and cancer, contributing 3.5% of total deaths worldwide (James *et al.*, 2018). Earlier, reports show that drug-induced liver injury (DILI) accounts for half of the total cases of ALF in western countries (Wei *et al.*, 2007; Reuben, Koch and Lee, 2010). Alcohol consumption and obesity is the principal cause of chronic liver diseases (CLD) in western and industrialized countries, while viral hepatitis is the primary cause in Asian countries. CLD is the 10th cause of death worldwide and have caused 1.32 million deaths in 2017, among which two-third are men and one-third are women (Cheemerla and Balakrishnan, 2021). CLD imposes huge financial burden on patients and impair their quality of life. According to a recent study on CLD patients in USA, the total inpatient hospitalization cost increased from $14.9 billion to $18.8 billion from 2012 to 2016

(Hirode, Saab and Wong, 2020). Meanwhile another cost-of-illness study was conducted in patients at different stages of CLD in Italy (Scalone *et al.*, 2015). The study results revealed that direct costs and loss of productivity increase with the disease progression from chronic hepatitis to cirrhosis, to hepatocellular carcinoma (HCC) and orthotopic liver transplantation (OLT). The costs increased from < €200/patient-month in HCV-infected patients with hepatitis to > €3000/patient-month in HBV infected patients with OLT.

1.1.5 Liver diseases – National status

According to the data published by World Health Organization in 2018, liver disease is the tenth most common cause of death in India accounting for 3% of total deaths (*Liver Disease in India*, 2016). The age adjusted death rate is 23 per 100,000 of population. In India, about 60%-90% of ALF is caused by hepatitis viruses and it mainly affect the young population with female predominance (Acharya, 2021). Alcohol related liver disease, non-alcoholic liver disease and hepatitis B and C, are the major contributors of liver cirrhosis and related mortality (Thuluvath, Saraya and Rela, 2021). According to a multicentric study in North India, the incidence of ARLD, NAFLD and Hepatitis B were 34.3 %, 9 % -32 % and 33.3 % (Mukherjee *et al.*, 2017). WHO reported that around 10 lakh patients with liver cirrhosis are newly diagnosed every year in India. The surge in liver diseases is attributed to the increased consumption of alcohol and high calorie diet accompanied by the unawareness of viral diseases and their mode of transmission. The factors that contribute to acute liver failure in India includes malnutrition, parasitic infections and the inappropriate use of unproven herbal supplements (Acharya, 2021). Treatment of chronic liver diseases poses a huge financial burden for patients in India with a cost of US$ 1500 for diagnosis and around US$ 5000 for intensive care treatment (Prinja *et al.*, 2018).

1.1.6 Current treatment strategies for liver failure

Despite having a tremendous capacity for regeneration, clinical conditions like ALF or ESLD can deteriorate the ability of liver to operate and regenerate. The current treatment strategies to combat such critical conditions mainly include liver transplantation, hepatocyte transplantation and use of extracorporeal liver-assist devices.

1.1.6.1 *Liver transplantation*

Liver transplantation is considered as the gold standard therapy for liver failure. In this treatment method a diseased or damaged liver is replaced with a healthy one. There are three main types of liver transplants, orthotopic transplant (deceased donor), living donor transplant and split type liver transplant. According to a previous report, 126,670 solid organ transplantations were recorded worldwide in the year 2015, out of which liver transplantation accounts for 22% and ranks second among the solid organ transplants worldwide (Asrani *et al.*, 2019). In addition, the Global Observatory on Donation and Transplantation revealed that 27,759 liver transplants were carried out in 2015, with living donors accounting for 21% of those transplants (Mahillo *et al.*, 2018). While in India, living donors contribute to 80 % and deceased donor to 20 % of the total liver transplants (Narasimhan, Kota and Rela, 2016). From 2011 to 2014, the rate of liver transplantation increased steadily, and from 2014 to 2015, it increased dramatically by 6.1 percent (Asrani *et al.*, 2019). These figures, however, do not even come close to covering 10% of the global demand for liver transplants and in India about 25-30 thousand transplants are needed annually. The main obstacles to liver transplantation are severe shortage of liver donors, the short window (12 to 15 h) for cryopreserving donor organs prior to transplantation (Tas *et al.*, 2021), the absence of a structured database, which slows down the process of assigning matched donors to patients in need of transplants, the risk of organ rejection and complications associated with long-term-immunosuppression.

1.1.6.2 *Hepatocyte transplantation*

Successful outcomes of auxiliary partial orthotopic liver transplantation, suggests that whole liver replacement is not necessary for the restoration of liver function (Rela, Kaliamoorthy and Reddy, 2016). This raises the option of using hepatocytes as a source of cells for the treatment of liver diseases. Cell-based therapy aims at engraftment of functional hepatocytes into the patient’s liver by infusing hepatocytes through the vascular network such as portal vein (Iansante *et al.*, 2017). The advantage of cell-based therapy is that it is minimally invasive and the procedure can be repeated as per the requirement of the patient. Hepatocyte transplantation has gone from the lab to the clinic during the past 20 years and have resulted in partial correction of several human liver diseases including phenylketonuria, factor VII deficiency, urea cycle disorders, glycogen storage disease type 1, and acute liver failure.

However, there are several limitations that needs to be addressed to obtain an outcome equivalent to liver transplantation. Primarily, an adequate number of high-quality donor hepatocytes are not available for clinical use (Forbes, Gupta and Dhawan, 2015). Secondly, there is a restriction in number of cells that can be infused through portal vein as it may obstruct the microcirculation leading to other complications (Dhawan, 2015). Thirdly, the percentage of engrafted hepatocyte in host liver is very less (Soltys *et al.*, 2017). Of late, to address these limitations several new strategies have been devised and proven successful in animal models (Ohashi *et al.*, 2007; Schwartz *et al.*, 2014; Shibuya *et al.*, 2021a). But their translation to human subjects requires further validation and process optimization to obtain a desired outcome.

1.1.6.3 *Extracorporeal liver-assist devices*

Extracorporeal liver-assist devices are temporary life-supporting devices that modulate the blood/plasma parameters to assist the liver function of the patients awaiting a liver transplantation. Liver assist devices are categorized into artificial liver assist (ALA) devices and bioartificial liver assist (BAL) devices. ALA devices use mechanical methods for removing toxic compounds and do not provide significant improvements in patient life span. While, BAL devices are more effective than ALA, as it contains a cellular component (hepatocytes) combined with a bioreactor which can perform a wide range of synthetic and biochemical functions of liver. There are four major configurations of BAL devices mainly hollow fiber devices, packed bed devices, flat plate systems and encapsulation-based suspension reactors (Chamuleau, 2009). The major challenges in implementing BAL devices for clinical use are, the procurement of large number of human hepatocytes, poor oxygen availability and chances of shear stress during perfusion and limited volume of the bioreactor. The use of alternative cell source like stem-cell derived hepatocytes and the improvisations in the bioreactor design using fluid dynamic modelling are promising steps towards clinical use.

1.2 Need for advanced biomedical research

In spite of advancements in surgical procedures, the organ shortage poses a great barrier to liver transplantation and the extracorporeal liver-assist devices may not provide long-term support for patients waiting for a liver transplant. In addition, the inefficiency of conventional *in vitro* liver models greatly contributes towards the incidence of DILI during clinical trials, leading to drug-withdrawal which poses a huge financial burden to the drug manufacturers. With due consideration to the above facts there is always a need for advanced biomedical research on alternative approaches to develop liver tissue substitute that mimics the architectural and physiological aspects of liver.

1.3 Liver tissue engineering

Tissue engineering is an interdisciplinary field of science that applies principles of engineering and life science towards the development of biological substitutes that restore, maintain, or improve tissue function.(Langer and Vacanti, 1993) To engineer a tissue construct three key elements are utilized, these are 1) cells - perform the functions of tissue of interest, 2) scaffolds - provide structural support for cell attachment, proliferation and migration, and 3) biomolecules - provide growth-stimulating signals for cells to organize into a tissue. The primary goal of liver tissue engineering is to restore liver functions fully or partially by developing an implantable liver tissue construct for *in vivo* liver regeneration. The secondary goals include development of efficient extracorporeal liver assist devices to bridge the gap between patients and liver transplantation, and to develop human-relevant *in vitro* models to predict DILI and study liver diseases.

1.4 Approaches in liver tissue engineering

To achieve the goals of liver tissue engineering two different approaches namely top-down approach and bottom-up approach have been practiced in liver tissue engineering.

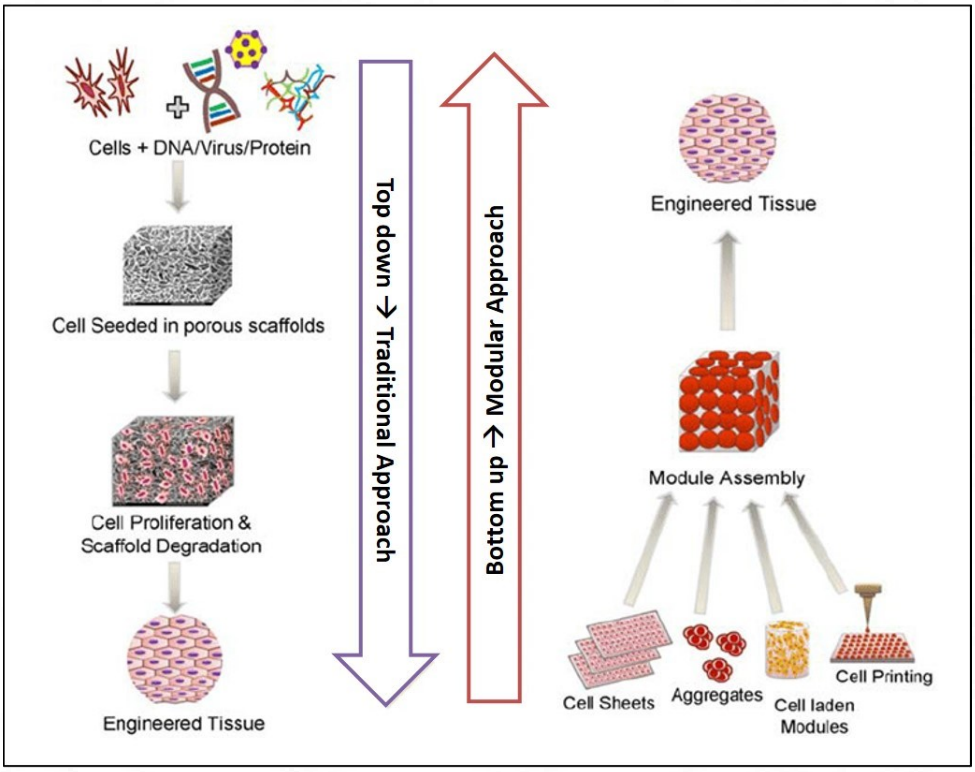

Figure 2. Tissue engineering approaches. (a) Traditional or top-down approach and (b) Modular or bottom-up approach. Adapted from Annamalai *et al*.,(Tiruvannamalai-Annamalai, Armant and Matthew, 2014)

1.4.1 Top-down approaches

Pioneer research in liver tissue engineering aimed at developing implantable cell-matrix constructs based on top-down approach. In the top-down or traditional approach cells are seeded over a prefabricated scaffold to develop into a functional tissue construct (Figure 2 a) (Schmidt *et al.*, 2021). A major progress was made in this approach with respect to the design and fabrication of biocompatible scaffolds. The composition and design of the scaffold can be fine-tuned to obtain adequate porosity for proper mass transfer and to provide relevant biochemical and biomechanical cues for long-term survival and functioning of hepatocytes. Both natural and synthetic polymers have been used for scaffold preparation. A wide variety of scaffolds in various forms like hydrogel, films, fibrous mats, etc. have been fabricated by different methods such as solvent casting, electrospinning, freeze-drying and gas foaming. Despite making a huge advancement in scaffold preparation, the top-down approach suffers from several limitations pertaining to the thickness of three-dimensional (3D) scaffolds affecting cell seeding, vascularization and mass transfer (Schmidt *et al.*, 2021). Incomplete cell penetration and non-uniform distribution of cells inside the scaffold, low cell density, lack of vascularization and tissue-level cell organization are posing great challenge.

1.4.2 Bottom-up approaches

To address the limitations of top-down approach, bottom-up or modular approach was introduced. The bottom-up approach, relies on self-assembly or directed assembly of microscale 3D cell aggregates or cell-laden modules to form macroscale functional tissue construct (Figure 2 b) (Schmidt *et al.*, 2021). In this approach, two different strategies are followed for producing cellular building units. The first strategy utilizes the inherent ability of cells to self-assemble and secrete ECM to form intact tissues. Cell sheet technology is one of the outputs of this strategy. It is a non-invasive technology that uses thermoresponsive culture substrate to harvest intact cell monolayer as a sheet without any enzyme treatment. Cell sheets comprising hepatocytes alone or in combination with endothelial cells have been stacked over one another to fabricate 3D liver constructs.

Three-dimensional (3D) culture of cells as aggregates is another approach to produce microscale liver tissue equivalents *in vitro*. They are considered excellent building blocks for modular assembly approach, because they facilitate *in vivo*-like cell-cell and cell-matrix interactions and mimic physiological gradients of nutrients and gases. Spheroids and organoids are the two main types of 3D cellular aggregates and they have been shown to enhance and maintain liver cell functions for long-term *in vitro*. Spheroids are simple 3D cellular aggregates formed primarily due to self-aggregation of cells when cultured on non-adherent surfaces. The intrinsic ability of hepatocytes to self-aggregate via E-cadherin molecules has been very well exploited to develop homotypic and heterotypic liver spheroids, the latter containing NPCs or non-liver-derived cells.

Organoids are complex 3D cellular clusters formed by aggregation and self-organization of either differentiated stem cells or progenitor cells, or cells derived exclusively from primary tissue (Fatehullah, Tan and Barker, 2016). They are considered as organ buds as they often exhibit organ-specific functionality and microanatomy. The presence of stem cell population in organoids allows self-renewal and makes them amenable to *in vitro* expansion. Simple and complex liver organoids containing hepatocytes, cholangiocytes and non-liver derived cells have been generated by culturing cells inside hydrogel scaffolds like Matrigel^{TM} supplemented with adequate growth factors.

The second strategy in bottom-up approach utilizes matrix embedded cells as building units for modular assembly. Here, the cell-laden modules are generated either by manual casting or by using automated additive manufacturing technology known as 3D bioprinting. 3D bioprinting allows fabrication of customized tissue constructs by precise controlled deposition of bioink (formulation of cells, biomaterials and biomolecules) in a layer-by-layer fashion according to a computer design. It facilitates macroscale tissue fabrication with better control over the distribution of cells and scaffolding material within the bioengineered tissue. Various bioink formulations and bioprinting modalities have been reported for liver tissue bioprinting with the aim of biofabrication of 3D liver construct *in vitro* (Agarwal, Banerjee, Konwarh, Esworthy, Kumari, Onesto, Das, Lee, Wagener, Makvandi, Mattoli, Ghosh, Maiti, Zhang and Ibrahim T. Ozbolat, 2021).

1.4.3 Other approaches

Other approaches in liver tissue engineering includes liver decellularization-recellularization and microfluidic-based culture techniques. Liver decellularization and recellularization has emerged as a promising approach to engineer whole organ *ex vivo*. The decellularization process eliminates resident cells from the liver while retaining the ECM components and architecture. Followed by the recellularization process enables seeding of allogenic liver cells via portal vein or bile duct under control conditions. An advantage of this approach is that the presence of intact vascular network allows easy integration of the engineered tissue with the host circulatory system.

The microfluidics-based culture system utilizes microfabrication technologies to pattern cells in a microfluidic chamber to stimulate *in vivo* cell assembly and fluid flow. Microfluidic devices like liver-on-chip have enabled generation of various aspects of liver lobules such as hepatic cord structures, liver sinusoid and metabolic zonation. These culture systems have immense application as *in vitro* models for drug testing and disease modelling.

1.5 Challenges in liver tissue engineering

The major challenges in liver tissue engineering are 1) identification of an adequate cell source, 2) preservation of hepatocyte function *in vitro*, 3) integration with vascular channels and biliary tree (Agarwal, Subramanian and Maiti, 2019). Identifying an adequate cell source for hepatocytes and non-parenchymal cells is an incredibly challenging task. Obtaining primary cells from patients is difficult and therefore alternate cell sources like progenitor cells and stem cells have been explored for liver tissue engineering. However, complex differentiation protocols, low differentiation efficiencies and underlying risk of tumorigenesis hinders their clinical application.

Maintenance of hepatocyte function *in vitro* is really challenging. The primary hepatocytes or hepatocyte-like cells undergo rapid dedifferentiation and functional deterioration in monolayer culture. This is due to lack of appropriate 3D microenvironment essential to preserving hepatocyte morphology and function (Gijbels, Vanhaecke and Vinken, 2019). Recent advances in 3D culture of liver cells have shown improvement in maintaining hepatocyte polarized cuboidal cell morphology and liver-specific functions. However, the complex liver microarchitecture and physiology could not be recapitulated completely till now. The major determinants in achieving complex liver microstructure during liver tissue engineering includes the scaffolding matrix, spatial distribution of liver cells and their interaction, cellular density and supply of adequate growth factors and oxygen. The matrix composition, stiffness, pore size and pore geometry are critical for providing hepato-specific biochemical and biomechanical cues, and for ensuring proper mass transfer within the engineered tissue. The heterotypic interaction between hepatocytes and NPCs has important role in regulating hepatocyte gene expression and functions like bile secretion and biotransformation (Natarajan, Moeun and Kidambi, 2021). Achieving a cell density similar to native liver tissue is essential for efficient cell-cell interaction and to mediate intracellular signal transduction. Supplementation of growth factor in adequate amounts and at proper duration while maintaining appropriate oxygen tension *in vitro* is detrimental for hepatocyte survival and function.

Finally, to achieve a fully functional implantable liver tissue construct it is essential to integrate biliary and vascular network. Bile canaliculi formation has been demonstrated *in vitro* but a complete biliary duct and its associated channels have not been engineered (Palakkan, P.R. and V, 2013). It is important to prevent bile accumulation within engineered construct as it may negatively affect the functions of hepatocytes. Complete vascularization of engineered liver tissue construct has been challenging task for decades. Vascularization is important to overcome diffusion limitations and adequate supply of nutrients to ensure long-term viability of cells inside the 3D construct. Although liver decellularization-recellularization approach has enabled to preserve the vascular and biliary network, exact cellular distribution within this network has not been achieved post-recellularization.

1.6 Problem statement

Liver tissue function can be greatly attributed to the spatial organization of the chief functional cell hepatocyte and their interaction with non-parenchymal cells (Bale *et al.*, 2016). In vivo, the major functional liver cell hepatocytes are organized into plates with intact cell-cell contact that gives rise to hepatocyte polarization. Hepatocyte polarization is important to maintain the mature hepatic functions and therefore, to realize a functional liver tissue substitute it is essential to achieve tissue-like cellular organization within the engineered tissue. Three-dimensional (3D) bioprinting has enabled the biofabrication of liver tissue constructs with complex geometries carrying unique biomaterials and multiple cell types. However, the current methodologies for liver tissue bioprinting fail to mimic tissue-specific cellular organization within the construct as they utilize bioinks carrying individual dispersed cells.

1.7 Conceptualization and formulation of hypothesis

Conventional 3D bioprinting method using dispersed cell-laden bioink fail to mimic tissue-like cellular organization within bioprinted liver construct. This can be to lack of adequate cell-cell interaction and cellular organization. In this scenario, self-organized hepatic organoids can be a better cell component in the bioink for liver tissue bioprinting. However, the method of hepatic organoid culture method greatly relies on encapsulation of hepatocytes within hydrogel matrices, that makes their retrieval strenuous and affects its integrity. To overcome this limitation, it is sensible to apply the principles of spontaneous cell organization and cell sheet technology for organoid culture and retrieval. By applying these principles, it is possible to establish a scalable, non-invasive method to generate intact hepatic organoids for liver 3D bioprinting.

Hence, we propose that a combinatorial approach utilizing the merits of all the three technologies- organoid, cell sheet and 3D bioprinting, will allow multiscale tissue fabrication and we hypothesize that *"Three-dimensional bioprinting of hepatic organoids formed on a thermoresponsive substrate can be used to develop a structurally organized functional liver tissue construct."*

1.8 Aims and objectives

The aim of this study is to biofabricate a functional liver tissue construct mimicking tissue-like cellular organization by means of three-dimensional organoid bioprinting.

To accomplish this aim four major objectives are formulated as given below.

1. Development of suitable bioink for organoid bioprinting.
2. Generation of hepatic organoids using thermo-responsive culture substrate.
3. Designing and 3D Bioprinting of in vitro liver construct.
4. Functional evaluation of 3D Bioprinted liver tissue construct.

1.9 Scope of the study

The study as a whole will explore the possibilities of 3D bioprinting using hepatic organoids as a cell source for achieving tissue-like organization in an *in vitro* liver construct. The study covers the areas of bioink development, hepatic organoid generation using thermoresponsive substrate, computer-aided designing of liver construct, development of process methodology for organoid bioprinting and the functional characterization of the bioprinted liver construct.

1.10 Structure of the thesis

The thesis is divided into five chapters. Chapter 1-Introduction, Chapter 2-Literature review, Chapter 3-Materials and Methods, Chapter 4-Results and Discussion and Chapter 5-Summary and Conclusion. Chapter 1 introduces the area of research and defines the research problem. To address the research problem a research hypothesis is formulated and the objectives through which the hypothesis can be proved are enumerated in this chapter. The chapter ends with a mention on the design and scope of the thesis. Chapter 2 reviews the relevant literature on the various elements and approaches in liver tissue engineering with a focus on reconstruction of liver architecture using these approaches. The chapter describes the advancements in each approach and highlights their advantages and major limitations. Chapter 3 contains a structured experimental design elaborating the materials, equipment and protocols involved in the study. Chapter 4 presents the obtained results related to each objective of the thesis and discusses the results in comparison to previous findings. Chapter 5 summarizes the results and draws a conclusion based on the major achievements and limitations of the study. The chapter ends with a remark on future direction of research related to this study.

Chapter 2

REVIEW OF LITERATURE

2.1 Relevance of liver tissue engineering

Liver is a classic example of structure-function analogy in which complex architecture is essential to tissue function. Liver tissue engineering is considered to be the most promising approach for creating histo-mimetic liver tissue substitutes, as it provides numerous opportunities to manipulate individual components needed for tissue fabrication (Mazza *et al.*, 2018). The advancements in 3D culture methods and biofabrication techniques have facilitated partial reconstruction of liver microstructures in bioengineered tissues. There are many clinical and commercial applications awaiting a reliable way of regenerating or reconstructing a long-term working liver system, which is a major drive to engineer liver tissue. A literature search on web of science database, with the search topic “liver tissue engineering” showed that there has been a four-fold increase in the number of published research articles related to liver tissue engineering in the last decade (Figure 3). This shows the growing relevance of liver tissue engineering in the current research domain.

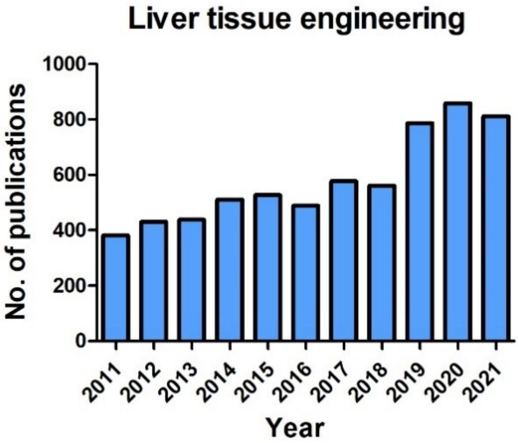

Figure 3 Relevance of liver tissue engineering. Graph depicting the trend in the number of publications related to liver tissue engineering in the last decade. (Data obtained from Web of Science database, https://www.webofscience.com/)

2.2 Cell sources for liver tissue engineering

Liver is the largest visceral organ having approximately 140 million cells per gram of liver (Sohlenius-Sternbeck, 2006). Hence, a huge number of functional cells are required to engineer liver tissue substitutes. The liver functions are expressed by the hepatocytes and therefore several sources of hepatocytes including the primary hepatocyte, hepatic cell lines and stem cell-derived hepatocyte-like cells have been used for liver tissue engineering. Increasing evidence suggest that non-parenchymal cells (NPCs) are essential for maintenance of hepatocyte function *in vitro* and in this regard, efforts have been directed towards development of NPC lines for liver tissue engineering.

2.2.1 Primary liver cells

Primary human hepatocytes are considered the gold standard for liver tissue engineering as they provide the complete spectrum of differentiated functions. However, the cells tend to dedifferentiate in conventional monolayer culture and the availability of fresh human hepatocyte is limited as they are mostly isolated from cadaveric liver (Hu and Li, 2015). The hepatocytes isolated from cadaveric liver are mostly cryopreserved and have been used in bioartificial liver devices (Baccarani *et al.*, 2004). Meanwhile, a recent study has shown that by redefining the composition of culture medium, human hepatocyte could be expanded 10,000-fold *in vitro* and the expanded cells in 3D culture condition could express mature hepatocyte phenotype (Zhang *et al.*, 2018). Similar to hepatocytes, primary non-parenchymal cells (NPCs) have also been isolated and used in co-culture systems. Evidence suggests that NPCs and extrahepatic NPCs (HUVEC) are capable of augmenting hepatocyte function *in vitro* (Bhatia *et al.*, 1999a).

2.2.2 Hepatic cell lines

Human hepatocyte cell lines are used as an alternative to primary hepatocyte as they can be easily propagated and maintained *in vitro.* Tumor-derived hepatocyte cell lines such as HepaRG, C3A and HepG2 are widely used as a cell source for BALs like Extracorporeal Liver Assist Device (Hoekstra and Chamuleau, 2002). However, incomplete expression of drug metabolizing enzymes and the possibility to transmit tumorigenic factors limits their usage. Immortalized human hepatocyte cell lines were developed by retrovirus-mediated transfer of oncogenes. To attain a better control over tumorigenicity, hepatocyte cell lines (NKNT-3) with reversible immortalization ability were developed by inserting Cre/loxP recombination sites and anti-viral drug sensitive suicide gene (Kobayashi *et al.*, 2000). Non-parenchymal cell lines such as endothelial cells (HNNT-2) and stellate cells (TWNT-1) were also developed using this technology (Noguchi *et al.*, 2002; Watanabe *et al.*, 2003). However, long-term stability and differentiated functionality have not been studied in detail.

2.2.3 Stem cells

Stem cells are a promising alternative cell source for liver tissue engineering due to their proliferation capacity and differentiation ability to form hepatic cell types. However, an efficient protocol for complete differentiation of stem cells into mature hepatocyte is still under development. Despite having several advantages, the embryonic stem cells (ESC) have not been extensively used in clinics due to ethical issues and possible teratoma formation from undifferentiated cells (Payne *et al.*, 2011). In this scenario, the adult stem cells like mesenchymal stem cells (MSC) from adult tissues such as bone marrow and adipose tissue is considered as the best viable cell source due to their immunomodulatory capabilities and pluripotency (Gao *et al.*, 2016). Interestingly, co-culture of MSCs with primary hepatocytes have shown to augment growth and long-term maintenance of liver functions due to the secretion of mitogenic growth factors like hepatocyte growth factor (HGF) by MSCs (Gu *et al.*, 2009). Hence, this coculture system has been widely exploited for liver tissue engineering. Furthermore, MSCs have no risk of teratoma formation and autologous cells can be isolated from various tissues of the patient. MSCs harvested from different tissues (bone marrow, adipose tissue and amniotic fluid) have also been transdifferentiated into hepatocyte which makes them suitable for liver tissue engineering (Stock *et al.*, 2008; Zheng *et al.*, 2008).

The development of induced pluripotent stem cells (iPSC) has also helped to address the limitations of ESCs. Human iPSC lines have been successfully differentiated into hepatocytes and non-parenchymal cells (Koui *et al.*, 2017). In spite of these advancements, the concerns over very low efficiency of reprogramming and teratoma formation due to changes in cell cycle regulators limits their clinical application. To bypass the complex reprogramming process involved in iPSC development, induced hepatocyte-like cells (iHep) were generated from adult cells by overexpressing hepatocyte lineage specific transcription factors. However, recent studies have reported phenotypic instability of iHep cells produced by forced expression of Foxa2/Hnf4a in mesenchymal stromal cells (Orge *et al.*, 2020).

Of late, leucine-rich repeat-containing G protein-coupled receptor 5 (LGR5)–positive adult stem cells have emerged as new cell source for liver regeneration. According to a recent study, the LGR5 cells were expanded 40-fold when cultured in a spinner flask and the cells formed organoids which when differentiated showed mature hepatocyte function (Schneeberger *et al.*, 2020). However, LGR5 positive hepatocytes were found to be the main cellular origin of diethylnitrosamine (DEN)-induced hepatocellular carcinoma in mouse model and high expression of LGR5 receptor in gastrointestinal cancer tissues indicate their potential tumorigenicity which is not desirable for clinical use (Hirsch *et al.*, 2014; Wang and Liu, 2015; Ang *et al.*, 2019). The availability of suitable cell types remains to be a major issue in liver support and regeneration therapy. A better understanding of the cellular signaling pathways involved in differentiation of stem cells into functionally mature hepatocyte would be beneficial for liver tissue engineering.

2.3 Biomaterials for liver tissue engineering

In tissue engineering, scaffolds play the role of extracellular matrix (ECM) present in a tissue. Hence, it is essential to recapitulate ECM properties in a scaffold intended for tissue engineering application. *In vivo,* the ECM provides a three-dimensional (3D) microenvironment for cells to adhere, proliferate, migrate, differentiate and interact with other cells. The ECM composition, topography, porosity and biomechanical properties influence cell physiology. The liver ECM consists of collagen (type I-IV), laminin, fibronectin, elastin and glycosaminoglycans (GAGs) all of which are distributed in a gradient manner within a liver lobule. Type I collagen forms the structural framework of the liver ECM over which other components are attached. The cell-matrix interactions help to maintain hepatocyte function and polarity, and guides liver regeneration after a physiological insult. In this regard, various biomaterials have been utilized for scaffold preparation. A biomaterial is defined as "a material designed to take a form that can direct, through interactions with living systems, the course of any therapeutic or diagnostic procedure" (Ghasemi-Mobarakeh *et al.*, 2019). Several polymers originating from natural and synthetic sources have been qualified as biomaterials and are used in different topographies (films, coatings, sponges, 3D hydrogels, microbeads and nanofibers) as scaffolds to reconstruct the liver ECM (Jain, Damania and Kumar, 2014). Scaffolds for tissue engineering should have some basic qualities such as high porosity with interconnected pores to ensure cellular penetration and adequate diffusion of nutrients to cells within the construct, biodegradability matching the rates of ECM production by cells and mechanical strength or stiffness matching the native tissue ECM. For liver tissue engineering scaffolds that mimic the native liver ECM composition and stiffness have been shown to augment liver cell organization and function (Pinkse *et al.*, 2005; Natarajan, Moeun and Kidambi, 2021).

2.3.1 Natural polymers

Natural polymers are a class of biomaterials isolated from natural sources. They harbor biological recognition sites essential for cell interaction and function. Polymers such as collagen, gelatin, hyaluronic acid, chitosan and alginate have been extensively used for scaffold preparation (Jain, Damania and Kumar, 2014). Being the most abundant component of liver ECM, type I collagen is considered the most appropriate biomaterial for liver tissue engineering (LTE). It has several cell binding motifs, low immunogenicity, and high biocompatibility and biodegradability (Dong and Lv, 2016). Monolayer culture of hepatocytes on collagen coatings and collagen sandwich hydrogel are well established culture systems. However, collagen like other natural polymers have low mechanical strength and high cost. Therefore, efforts were directed towards utilizing its derivate gelatin as a substitute.

Gelatin is a hydrolyzed form of collagen which retains the structural features of collagen. However, being soluble at physiological condition, gelatin must be crosslinked by chemical or enzymatic methods to prepare stable scaffolds. Hepatocyte encapsulated gelatin hydrogels have been used to fabricate three-dimensional structures using rapid prototyping technology (Wang *et al.*, 2006). Inclusion of gelatin in various composite scaffolds containing chitosan and silk-fibroin has been shown to improve cell adhesion, biodegradation and mechanical strength (Yang *et al.*, 2012; Harwate *et al.*, 2021).

Taking into consideration the low mechanical strength of gelatin scaffolds, functionalization of gelatin was caried out to improve the mechanical properties. Gelatin methacrylamide (GelMA) is a functionalized gelatin derivative formed by substitution reaction between methacrylic anhydride and reactive amines (lysine and hydroxylysine) of gelatin (Lee, Shirahama, N.-J. Cho, *et al.*, 2015). GelMA undergoes photoinitiated free radical polymerization to form covalently crosslinked hydrogel. The hydrogel has close resemblance to native ECM due to the presence of cell binding and enzyme responsive peptides motifs, and exhibits excellent biocompatibility, biodegradability and tunable mechanical properties (Nichol *et al.*, 2010; Lee *et al.*, 2016). The characteristics of the GelMA hydrogel can be fine-tuned by manipulating the parameters during synthesis (by varying degree of functionalization) or during crosslinking (by varying polymer concentration, photoinitiator concentration or crosslinking time). In addition, the photocurable and viscoelastic properties of GelMA hydrogel precursor solution makes it amenable to different microfabrication techniques including 3D bioprinting, photopatterning and micromolding (Yue *et al.*, 2015). This has enabled fabrication of geometrically complex 3D matrices for culturing liver cells, spheroids and organoids (Bhise *et al.*, 2016; Ma *et al.*, 2016; Bouwmeester *et al.*, 2021).

Fibronectin and laminin are two important ECM glycoproteins that have been utilized independently or in combination with other biomaterials for liver tissue engineering. *In vivo*, fibronectin has been shown to provide survival benefits to rat hepatocytes after liver injury by retaining the expression of anti-apoptotic protein Bcl-xL (Moriya *et al.*, 2012). While *in vitro* study showed that fibronectin could regulate rat fetal hepatocyte morphology and cell organization, facilitating formation of elongated cord-like structures similar to hepatic plate organization (Sánchez *et al.*, 2000). Interestingly, Wang *et al.*, (2016) reported that ECM proteins like fibronectin and collagen have distinctive roles in regulating Huh-7.5 cell genotype during 3D *in vitro* culture (Wang *et al.*, 2016). The expression of genes coding cell adhesion proteins such as cadherins, occludin, claudin-1 and integrin alpha-5 were higher in cells cultured on fibronectin-coated 3D microporous scaffolds compared to collagen-coated scaffolds after 14 days of culture. A similar trend was observed with genes representing liver functional markers like albumin, CYP3A4, hepatic nuclear factor 4-alpha and glucose-6 phosphatase. While cells cultured on collagen-coated scaffolds showed higher expression of genes coding proteins like integrin beta-1, alpha-1 antitrypsin and CYP3A7.

Of late, Das *et al.*, (2020) studied the synergistic effects of fibronectin and collagen in supporting Huh-7.5 cell viability and function (Das *et al.*, 2020). The authors reported that cells cultured on a 3D electrospun poly (lactide-co-glycolide) scaffold modified with collagen and fibronectin in the ratio 3:1 improved the expression of albumin gene by ~8 to 10-fold, CYP3A4 gene by ~5 to 7-fold and CYP3A7 gene by ~4 to 4.5-fold in comparison to single-protein modified scaffolds. On the same line, Li *et al.*, (2022) investigated the synergistic effects of glycoproteins fibrinogen and fibronectin on liver functions of hepatic spheroids (Li *et al.*, 2022). Fibrinogen was shown to improve hepatocyte aggregation and hepatic functions by facilitating fibronectin assembly on cell surface and thereby activating Integrin-Wnt/β-catenin pathway.

Laminin is an adhesion protein present abundantly in basal lamina of the epithelial tissue. The prominent role of laminin in promoting hepatic differentiation of stem cells as well as its involvement in the formation and maintenance of vascular structure makes it an ideal component of liver tissue scaffolds. An early study comparing the effects of laminin, fibronectin and collagen on liver cell culture showed that laminin-coated dishes promoted the attachment and proliferation of mouse fetal liver cells while other two proteins supported adult liver cells (Hirata *et al.*, 1983). Later, Kanninen *et al.*, (2016) reported the stage-specific role of laminin isoforms laminin-511 and laminin-521 during hepatic lineage differentiation (Kanninen *et al.*, 2016). Matrices containing laminin isoforms improved the hepatic fate specification efficiency of human iPSC derived definitive endoderm cells. The ability of laminin in promoting hepatogenic differentiation of human adipose-derived MSCs has also been reported (Mohammadpour *et al.*, 2018). Laminin containing gelatin cryogel scaffold enhanced MSC attachment and proliferation, and the differentiated hepatocyte-like cells expressed hepatocyte specific markers with striking similarity to HepG2 cells.

Another native component of liver ECM is hyaluronic acid (HA) which is a non-sulphated GAG present in the space of Disse. HA has been used in combination with other materials to develop conducting hydrogels and sponges for enhancing electrical communication between hepatocytes and for transplanting liver cells respectively (Katsuda *et al.*, 2010; Rad *et al.*, 2014). Being a hydrophilic molecule, they are often modified with cell adhesive peptides to improve cell attachment (Wang *et al.*, 2021). Chitosan is another popular polysaccharide that is used in LTE because of its resemblance to GAG (Arca and Şenel, 2008). Chitosan scaffolds of different topographies like foams, hydrogels, microcarriers, membranes and nanofibers have been used for LTE (Pan *et al.*, 2005). Presence of chitosan in hybrid scaffolds have shown to promote rapid hepatocyte spheroid formation by induction of genes coding E-cadherin and connexin-32 (Seo *et al.*, 2006).

Alginate is a polysaccharide that can form hydrogels through ionic crosslinking. It is an important biomaterial used in numerous applications, including drug delivery and tissue engineering (Lan, Safiejko-Mroczka and Starly, 2010). In liver tissue engineering, alginate-based scaffolds are mainly used for microencapsulation of hepatocytes to fabricate microbeads as implantable devices. Due to its hydrophilic nature the encapsulated hepatocytes form spheroids. High porosity of alginate microbeads has favored successful implantation of hepatocyte in animal models. However, during long-term implantation fibrotic capsules form around beads and prevent exchange of solutes between the cell and outside environment. In comparison to most widely used GelMA, alginate suffers from several limitations as a 3D scaffold. Primarily, the native form of the polymer lacks cell binding peptides and are irresponsive to proteolytic enzymes involved in tissue remodeling (Lee and Mooney, 2012). The other shortcomings of alginate include weak mechanical strength, and slow and uncontrollable degradation pattern resulting in loss of shape fidelity of the engineered tissue construct (Bouhadir *et al.*, 2001).

Recently, decellularized liver ECM has been examined for their potential as scaffold material. The decellularized matrix retains all the structural and functional components of liver ECM essential for liver cell growth and function (Croce *et al.*, 2019). Hepatic cell lines seeded on decellularized liver ECM cubes have shown to repopulate the scaffold while maintaining liver specific functions (Mazza *et al.*, 2015).

However, due to low mechanical strength, they are often blended with additives such as vitamin B2 or they are irradiated with UV light to induce covalent crosslinking (Choudhury *et al.*, 2018).

2.3.2 Synthetic polymers

Despite having a closer resemblance to native ECM composition and biological activity, it is difficult to fine tune the physico-chemical properties of natural polymers. In this effect, synthetic polymers were developed for LTE. The synthetic polymers have low immunogenicity and higher mechanical strength compared to the natural polymers. These properties qualify them as a suitable scaffolding material for long-term implantation studies. The popularly used synthetic polymers include poly (lactide-co-glycolide) (PLGA), poly L-lactic acid (PLLA), poly (ethylene glycol) (PEG), polycaprolactone (PCL) and stimuli-responsive polymers such as poly(N-isopropylacrylamide) (Jain, Damania and Kumar, 2014).

PLLA and PLGA are polyesters whose biodegradation rate can be controlled by changing the ratio of polymers, crystallinity of the polymer and molecular weight (Makadia and Siegel, 2011). Mostly, PLLA-PLGA composite scaffolds or scaffolds with surface coatings are used for hepatocyte culture and implantation. Collagen coated PLGA foams have been shown to be a promising scaffold for hepatocyte culture (Hasirci *et al.*, 2004). Nanoporous fibers of PLLA coated with collagen was demonstrated to be a superior substrate for hepatocyte adhesion and function compared to non-porous fibers (Wang *et al.*, 2012). A composite PLLA-PLGA sponge infiltrated with polyvinyl alcohol enabled successful engraftment of hepatocytes after implantation in the mesentery of a rat injury model (Mooney *et al.*, 1995). However, the PLGA suffer from an inherent disadvantage of acidic environment within the scaffold, resulting from their degradation products.

Another commonly used synthetic polymer is PEG, which is a hydrophilic linear polyether resistant to protein adsorption (Ngo and Grunlan, 2017). Micropatterned substrates consisting of PEG brushes have been used for developing implantable liver constructs. Primary hepatocytes and bovine endothelial cells cultured on these substrates formed heterospheroids which maintained the liver-specific functions for a month (Otsuka *et al.*, 2004). Mouse embryonic liver cells encapsulated in PEG hydrogels formed embryoid bodies and were able to differentiate into hepatic lineage (Underhill *et al.*, 2007). Addition of methacrylate or diacrylate groups to PEG has been shown to improve the mechanical strength of hydrogel after photocrosslinking.

Among other synthetic polymers PCL offers a better flexibility and strength to the scaffolds. Due to its non-immunogenicity and awfully slow degradation rate at physiological conditions they are often used as matrix for long-term implants and drug delivery. PCL have been used in combination with other biomaterials to enhance the mechanical properties of scaffolds used in LTE. Nanofibrous scaffolds fabricated using PCL and PCL-chitosan composites supported *in vitro* differentiation of human somatic stem cells into hepatocytes and maintained hepatocyte functions (Hashemi *et al.*, 2009; Semnani *et al.*, 2016).

Considering the lack of biological cues in synthetic polymers, immense research has been directed towards synthetic peptide-based biomaterials in the form of hydrogels. Peptide-based hydrogels have been proven to be an excellent biomaterial owing to its unique properties such as self-assembly, biocompatibility, biodegradability, tunable mechanical properties, ability to incorporate stimuli sensitivity and nano-fiber structure mimicking extracellular matrix (Koutsopoulos, 2016; Das and Das, 2021). The hydrogelation process involves two steps. In the first step, the peptides form a secondary structure like β-pleated sheet, α-helix, coiled-coil, β-turn etc. In the second step, either in the presence or absence of external stimuli these structures self-assemble in a hierarchical path through various non-covalent interactions to form higher order aggregates like hydrogels. Hence, while designing peptides one must identify the correct primary sequence that would eventually form desired secondary structure capable of triggering hydrogelation.

Studies on self-assembling peptides was initiated during the early 90's and Zang *et al* discovered that a peptide fragment (Ac-AEAEAKAKAEAEAKAK-$CONH_2$) of the yeast protein zuotin self-assembled to form nanofiber hydrogel in the presence of salt (Zhang *et al.*, 1993). Over the last two decades, several variants of self-assembling peptides have been designed for biomedical applications such as drug delivery, tissue engineering, antimicrobial coatings, etc (Koutsopoulos, 2016; Das and Das, 2021). The first generation of self-assembling peptides solely comprised of amino acid sequences that self-assemble and form a nanofiber hydrogel. While in the second generation a functional motif (e.g., RGD peptide) to promote cell specific biological functions were attached to the self-assembling peptides. The third generation of self-assembling peptides were developed by tethering soluble proteins to the peptide unit. Effector proteins like cytokines, growth factors and enzymes have been utilized for this purpose.

Peptide-based hydrogels have served as an ECM mimic for engineering various tissue types, including liver, bone, cartilage, neural, cardiac, and vascular tissue (Holmes *et al.*, 2000; Semino *et al.*, 2003; Narmoneva *et al.*, 2004, 2005; Misawa *et al.*, 2006; Florine *et al.*, 2013). In liver tissue engineering, peptide-based hydrogel has been proven to promote hepatic differentiation of progenitor cells and maintenance of adult hepatocyte functions. Semino *et al.*, (2003) utilized the Ac-(RADA)$_4$-CONH$_2$ self-assembling peptide hydrogel to culture rat hepatocyte progenitor cell line (Semino *et al.*, 2003). The cells encapsulated in the peptide hydrogel displayed non-exponential cell growth kinetics, formed spheroidal clusters, and produced progeny cells which when differentiated expressed mature hepatocyte phenotype. In contrast, cells cultured on petri dishes divided exponentially expressing endodermal and hepatocyte lineage markers but lacked mature hepatocyte properties.

Primary hepatocytes rapidly dedifferentiate when isolated from their natural microenvironment in the tissue. Wang *et al.*, (2008) investigated whether self-assembling peptide hydrogel Ac-(RADA)$_4$-CONH$_2$ could maintain the differentiated functions of primary rat hepatocytes *in vitro* (Wang *et al.*, 2008). Interestingly, the authors observed that the primary hepatocytes encapsulated in peptide hydrogel showed cell attachment, migration, and formation of 3D spheroids. The hepatocytes within the spheroids expressed apical membrane marker dipeptidyl peptidase IV at cell-cell contacts and exhibited higher secretion of urea and albumin compared to cells cultured on collagen matrix. Meanwhile, Genove *et al.* reported that hepatocytes cultured in the Ac-(RADA)$_4$-CONH$_2$ self-assembling peptide hydrogel functionalized with laminin receptor-binding sequence YIGSR, acquired parenchymal morphology and formed functional bile canaliculi-like structures (Genové *et al.*, 2009). The hepatocytes also displayed enhanced expression of liver-specific genes and secretion of urea and serum proteins.

Finally, thermoresponsive polymers such as poly(N-isopropylacrylamide) have been utilized for developing scaffold-free hepatic cell sheets (Ohashi *et al.*, 2007). The reversible phase transition property of the polymer with respect to temperature change is exploited to harvest intact hepatocyte sheets from a polymer coated culture dish without any enzymatic treatment. Primary hepatocyte cell sheets have shown better engrafting efficiency compared to individual cells in rodent models (Ohashi *et al.*, 2007).

2.4 Small molecules for liver tissue engineering

Stem cells are renewable cell sources for liver tissue engineering and their differentiation to hepatocyte lineage has been well established. In the conventional hepatocyte differentiation method, a monolayer culture of stem cells is exposed to a cocktail of recombinant growth factors and cytokines, including Activin A, Wnt3a, BMP4, FGF4, OSM, HGF, EGF and VEGF in a step-wise manner (Baxter *et al.*, 2015a). This approach is designed to stimulate the embryonic stages (definitive endoderm, liver bud, hepatoblast and hepatocyte) of hepatocyte lineage differentiation. However, this method is deficient in terms of low differentiation efficacy and phenotypic heterogeneity in differentiated cells. In this context, the role of small molecules and ECM in modulating hepatic differentiation of stem cells is studied thoroughly.

A wide collection of synthetic small molecules has been reported to modulate signaling pathways (Wnt, Notch & FGF) involved in hepatic fate determination

(Hosseini *et al.*, 2019). The small molecule analogues offer several advantages over using recombinant growth factor cocktails such as low cost, simplicity, reproducibility and stability. Currently, protocols for small molecule mediated hepatic differentiation of human ESCs, PSCs and MSCs are reported. Zhu *et al.*, (2009) identified a synthetic small molecule named stauprimide that increased the hepatic differentiation efficiency of ESCs by repressing c-Myc expression (Zhu *et al.*, 2009). c-Myc is the key factor in the preservation of ESC self-renewal. The authors discovered that stauprimide interacted with the transcription activator NME2 and inhibited its nuclear localization, which in turn suppressed c-Myc expression. Wnt/β-catenin signaling is another important regulator of pluripotency and it has been demonstrated to be suppressed during hepatic differentiation of human MSCs (Yoshida *et al.*, 2007). Based on this information, Itaba *et al.*, (2015) screened 23 different Wnt/ β-catenin small molecule inhibitors and identified IC-2, a derivative of IC-001 to be a potent inducer of hepatic differentiation of human MSCs (Itaba, Sakabe, *et al.*, 2015). IC-2 induced the expression of several liver-specific molecules such as albumin, urea, complement c3 and glycogen.

Meanwhile, Tasnim *et al.*, (2015) developed a cost-effective method to generate hepatocyte-like cells from human PSCs using small molecules (Tasnim *et al.*, 2015). The authors implemented a 3-step differentiation strategy that involved small molecules LY294002 and bromo-indirubin-3'-oxime (BIO) for the generation of definitive endoderm; sodium butyrate and dimethyl sulfoxide (DMSO) for the generation of hepatoblasts and SB431542 for differentiation into hepatocyte-like cells. Activin was the only growth factor utilized in this protocol and the results showed that the differentiated cells were morphologically and functionally better compared to the hepatocytes derived from the growth-factor induced differentiation. Later, an improved small molecule-driven protocol for hepatic differentiation of human PSCs devoid of any growth factors was reported (Mathapati *et al.*, 2016). The differentiation protocol consisted of three steps 1) differentiation of human PSCs to definitive endoderm (DE) using small molecule CHIR99021 (Wnt agonist); 2) differentiation of DE to hepatoblast-like cells in the presence of DMSO; 3) differentiation of hepatoblasts to hepatocyte-like cells with N-hexanoic-Tyr, Ile-6 aminohexanoic amide (HGF agonist) and dexamethasone. Interestingly, small molecules have also been demonstrated to replace the role of growth factors during the culture of bipotent liver organoids. Wang *et al.*, (2020) reported that a chemical- defined medium containing three small-molecule compounds CHIR-99021, blebbistatin, and forskolin together maintained the liver organoids in bipotential stage over 20 passages (4 months) (Wang *et al.*, 2020). In addition, the bipotent liver organoids treated with small molecules displayed enhanced capacity for further hepatocyte differentiation compared to the organoids treated with growth factors.

In summary, small molecules are increasingly suggested as an alternative to growth factors owing to its unique properties like high cell permeability, high specificity, high induction efficiency and low cost. The application of small molecules in tissue engineering field will allow better utilization of the stem cells as a cell source.

2.5 Liver tissue engineering approaches

There are two different approaches in tissue engineering namely top-down approach and bottom-up approach. Huge limitations of top-down approach pertaining to seeding cells on 3D scaffolds such as incomplete cell penetration, non-uniform cell distribution, low cell density, lack of vascularization and tissue organization, has diverted the attention towards bottom-up approaches. In this section various bottom-up approaches utilized in liver tissue engineering is reviewed along with two other recent approaches.

2.5.1 Cell sheet engineering

Cell sheet engineering is a bottom-up approach that utilizes a thermoresponsive culture substrate to harvest intact cell monolayer without any enzyme treatment. Thermoresponsive polymers having a lower critical solution temperature closer to physiological temperature have immense application in tissue engineering. The polymers exhibit a hydrophobic property at 37 °C and helps cells to adhere to the substrate. While on lowering the temperature they become hydrophilic and reduces cell adhesion. This makes them a suitable substrate for cell culture and cell detachment without any enzymatic treatment. The thermoresponsive polymer poly(N-isopropylacrylamide) (NIPAAm) and its derivatives are used as the substrate for cell sheet engineering. N-isopropylacrylamide-co-glycidylmethacrylate (NGMA) has been shown to be an excellent cytocompatible thermoresponsive culture substrate for cell sheet engineering (Joseph *et al.*, 2010; Joseph, Prasad and Joseph Sreenivasan K., 2011). Compared to NIPAAm, in NGMA the epoxy ring opening in the glycidylmethacrylate (GMA) moiety of the copolymer facilitates incorporation of biomolecules and thereby improves the interaction of cells with the substrate. Usually, thermoresponsive substrates are prepared by grafting thermoresponsive polymers on cell culture plates (Anil Kumar, Sreenivasan and Kumary, 2007).

Using cell sheet technology single layer or multilayer constructs can be generated from single cells. Ohashi *et al,* 2007 first demonstrated the application of poly-NIPAAm coated culture dish to generate uniformly continuous sheet of hepatic tissue using isolated primary hepatocytes (Ohashi *et al.*, 2007). The authors also showed that multilayered hepatic tissue can be fabricated by stacking individual cell sheets. Over the years, various improvisations have been made with respect to hepatic cell sheet engineering. Recently, composite cell sheets comprising patterned hepatocytes and endothelial cells were developed. In addition, hepatic cell sheet has been shown to provide better grafting efficiency in animal models compared to individual cells (Ohashi *et al.*, 2007). However, using cell sheet technology developing a 3D hepatic tissue of clinical scale remains challenging.

2.5.2 Three-dimensional culture of cellular aggregates

Three-dimensional (3D) culture of cells recreates the physiological microenvironment for cells by facilitating complex cell-cell and cell-matrix interactions in 3D space. They can be broadly classified into scaffold-free and scaffold-based culture systems. Scaffold-free systems encourages self-aggregation of cells by providing low adhesion culture conditions. While scaffold-based systems rely on natural or synthetic materials to induce aggregation and self-assembly of seeded cells. 3D cellular aggregates can recapitulate physiological gradients of nutrients, gases, growth factors and cytokines. Hence, modular assembly of these aggregates is considered as a bottom-up approach in tissue engineering. Spheroids and organoids are the two main types of 3D cellular aggregates and they have been shown to enhance and maintain liver cell functions for long-term *in vitro*.

2.5.2.1 *Spheroid culture*

Spheroids are simple spherical cellular clusters formed by self-aggregation of single or multiple cell types when cultured in low-adhesion environment. Spheroids can be established from primary cells, cell lines or tissue fragments. Epithelial cells like hepatocytes have an intrinsic ability to self-aggregate due to high-expression of cell adhesion molecule like E-cadherin (Takei *et al.*, 2005). This very property of hepatocytes has been exploited to develop homotypic and heterotypic liver spheroids. The latter one is developed by co-culturing hepatocytes with liver non-parenchymal cells or non-liver-derived cells. Heterotypic liver spheroid culture facilitates the three-dimensional homotypic and heterotypic intercellular interactions essential for maintaining the differentiated functions of hepatocytes *in vitro* (Otsuka *et al.*, 2013). Over the last few decades, numerous spheroid fabrication methods have been developed including hanging drop culture, culture of cells in non-adherent plates, rotating wall vessel culture, spinner flask culture and by magnetic levitation (Cui, Hartanto and Zhang, 2017). Liver spheroids have been utilized as models for high-throughput drug screening and as cell source for BAL devices. Recently, studies on rodent models showed that intraportally delivered hepatocyte spheroids were grafted efficiently and had better expansion potential compared to single hepatocytes (Okumura *et al.*, 2018; Shibuya *et al.*, 2021b). Meanwhile, macro-scale functional hepatic tissues were fabricated by stacking hepatocyte spheroids in hollow-fiber and on needles (Kenzan method) (Kizawa *et al.*, 2017; Okudaira *et al.*, 2017). However, the size of the spheroid is restricted to few hundred micrometers and therefore a large number of spheroids needs to be produced and assembled to generate macro-scale liver tissues.

2.5.2.1.1 Methods for hepatic spheroid production

Several methods have emerged during the last few decades with the intention to produce spheroids in a high-throughput manner. The spheroid culture methods basically rely on non-adherence of cells to the substratum to promote self -aggregation. Hepatic spheroids have been produced by both scaffold-free and scaffold-based methods.

Hanging drop method is a scaffold-free method that relies on gravitational force to promote cell aggregation inside a hanging drop of cell suspension. The method offers precise control over the cell number and composition of the spheroids and requires very low volumes of nutrient medium (Kelm *et al.*, 2003). To overcome the labour-intensive manual dispensing of cell suspension, automated liquid dispensing technology has been integrated with hanging drop array plates to scale-up the process (Tung *et al.*, 2011). However, the number of spheroids produced are limited to the number of wells in the array plate and it is very expensive and cannot be reused.

Dynamic culture systems such as rotating wall vessel and spinner flasks have been utilized for large-scale production of structurally polarized functional hepatocyte spheroids (Moscona, 1961; SF *et al.*, 2002). However, the random spheroid formation process leads to a huge variation in size of the spheroids and it is difficult to incorporate definite number of NPCs in the spheroid using the current system.

Various forms of non-adherent culture substrates or scaffolds have been widely used for hepatocyte spheroid production (Landry *et al.*, 1985; Okubo *et al.*, 2002). These include the ultra-low attachment (ULA) microwell plates, hydrogel overlay plates and patterned microwell arrays. Microencapsulation of hepatocytes within a suitable hydrogel matrix like alginate can also promote cell aggregation to form spheroid (Chan, Zhang and Leong, 2016). Recently the microfluidics technology has been leveraged for microencapsulation of cells based on double-emulsion principle (Chan, Zhang and Leong, 2016).However, encapsulation within these scaffolds may hinder adequate mass transfer of nutrients and oxygen to spheroids.

Recently, using magnetic levitation technology cells magnetized by uptake of paramagnetic iron oxide nanoparticles were subjected to mild magnetic forces to pull cells together. Spheroid formation occurred within few hours without affecting cellular activity. Desai *et al.,* (2017) first demonstrated the assembly of magnetized human hepatocytes to form spheroids in a 384 well plate (Desai, Tseng and Souza, 2017).

2.5.2.2 *Organoid culture*

Fatehullah *et al.*, (2016) defined organoids as "An *in vitro* 3D cellular cluster derived exclusively from primary tissue, ESCs or iPSCs, capable of self-renewal and self-organization, and exhibiting similar organ functionality (Fatehullah, Tan and Barker, 2016). Organoids are considered as miniature versions of organs as they often display organ-specific microanatomy. The *in vivo* developmental processes drive the formation of organoids from cells when cultured in suitable ECM scaffolds like Matrigel^{TM} supplemented with adequate growth factors. Presence of stem cell population in organoids facilitates long term *in vitro* expansion and they retain the genetic features of parent organ over several passages. The advancements in stem cell technology and an in-depth knowledge about niche factors involved in liver development process helped researchers to develop liver organoids of varying complexity. Liver organoids have been derived from various cell types such as primary hepatocytes and cholangiocyte, adult stem cells, iPSC-derived hepatic endoderm cells co-cultured with mesenchymal stem cells (MSCs) and umbilical cord-derived endothelial cells (HUVECs) (Zhu *et al.*, 2021). Liver organoids derived from cells of healthy donors are ideal models for studying liver development and regeneration (Takebe *et al.*, 2014). While patient derived liver organoids have been shown to serve as *in vitro* models for liver diseases like Alagille syndrome and Wilson's disease (Huch *et al.*, 2015; Akbari *et al.*, 2019). Application of liver organoids for drug screening and toxicity testing is still at the stage of infancy.

2.5.2.2.1 Matrices for liver organoid formation

Self-organization of the cell population plays a major role in the formation of organoids. The liver organoid formation is dependent on culture matrix, signaling molecules and the starting cell type. The most widely used matrix for generating liver organoids is the Matrigel, a natural ECM extracted from Engelbreth-Holm-Swarm (EHS) mouse sarcoma. Michalopoulos *et al.*, (1999) have demonstrated the self-organization and hepatic plate-like formation in a co-culture of primary rat hepatocytes and NPCs inside matrigel in the presence of growth factors like HGF and EGF (Michalopoulos *et al.*, 1999). However, since matrigel is derived from mouse sarcoma, there is possible transfer of tumor factors from the matrix, and this hinders the clinical application of organoids. Meanwhile, liver organoid culture has been tested with ECM hydrogel made from decellularized liver tissues. Vyas *et al.*, (2016) reported that the decellularized liver scaffolds provided biochemical and biophysical cue to liver progenitor cells enabling the cell to differentiate into hepatobiliary organoids (Vyas *et al.*, 2018). However, the undefined complex and variable composition of decellularized scaffolds affects the consistency and reproducibility of large-scale organoid production (Giobbe *et al.*, 2019).

Recently, chemically defined synthetic hydrogels have been introduced for liver organoid culture. The tunable mechanical characteristics, uniformity, reproducibility, and Good Manufacturing Practices (GMP) compliance are some of the merits of synthetic hydrogels. Sorrentino *et al.,* (2020) developed a RGD conjugated PEG hydrogel with tunable mechanical properties for derivation of primary mouse and human liver organoids (Sorrentino *et al.*, 2020). However, the retrieval of the organoids from the gel was cumbersome as it required enzymatic digestion. Meanwhile, Ye *et al.*, (2020) developed a novel thermosensitive hydrogel based on poly-iso-cyanopeptides (PIC) and laminin-111 for human liver organoid cultures (Ye *et al.*, 2020a). Due to the thermoresponsive nature of hydrogel, the organoids could easily be retrieved during passaging. The only limitation of synthetic hydrogel matrices for organoid culture is that they do not represent the complete repertoire of biological ligands present in native ECM and incorporating each of them into the hydrogel is challenging.

2.5.2.2.2 Types of liver organoids

Liver organoids can be broadly classified into two types, namely simple liver organoids and complex liver organoids based on the cellular composition. Simple liver organoids are derived from either hepatocytes or cholangiocytes. Hu *et al.*, demonstrated long-term expansion of primary hepatocytes as organoids after encapsulation in matrigel when supplemented with appropriate growth factors and

WNT/β-catenin pathway activators (Hu *et al.*, 2018). The organoids formed a solid aggregate having a bunch-of-grape-like appearance with well-patterned hepatocytes, accompanied with gain of hepatic polarities. However, the liver functions were two to four-fold lower than freshly isolated hepatocytes. To create cholangiocyte organoids, Tysoe *et al.*, (2019) isolated cholangiocytes from the common bile duct and were embedded in Matrigel with appropriate growth factors and WNT/β-catenin pathway antagonist to prevent amplification of adult stem cells (Tysoe *et al.*, 2019). The cholangiocyte organoids showed a cystic hollow structure and they performed fluid transport and cyst swelling. Similarly, iPSCs and Lgr5$^+$ adult stem cells, when embedded in matrigel, formed embryoid bodies that later differentiated into cholangiocyte and hepatocyte organoids respectively when grown in differentiation media (Huch *et al.*, 2015; Sampaziotis *et al.*, 2015).

Complex liver organoids are composed of multiple cell types such as hepatocytes, cholangiocytes and non-hepatic cells like HUVEC and MSC (Zhu *et al.*, 2021). Hepato-biliary organoids and vascularized hepatocyte organoids are examples of complex liver organoids. The inclusion of MSCs into the organoid culture system have revolutionized the field of organoid research. Takebe *et al.*, (2015) reported that co-culture of iPSC-derived endoderm cells with HUVECs and MSCs over pre-solidified Matrigel caused spontaneous self-organization of cells into macroscopically visible 3D cell aggregates named liver buds (Takebe, Enomura, Yoshizawa, Kimura, Koike, Ueno, Matsuzaki, Yamazaki, Toyohara, Osafune, Nakauchi, Hiroshi Y. Yoshikawa, *et al.*, 2015). The endothelial network and expression of hepatic-specific marker genes were visible in the liver buds. According to the study, MSC-driven contraction and the substrate matrix stiffness were crucial for self-condensation.

Hence, co-culture of MSCs with the liver cells imparts two benefits 1) augmentation of liver function and 2) induction of spontaneous cell organization.

2.5.2.2.3 Limitations of current organoid culture methods

Although, implantation of human liver organoids has shown improvement in liver defective rodent models, greater utilization of xenogeneic scaffolds like matrigel impedes their clinical use (Zhang *et al.*, 2018). In addition, iPSC-derived liver organoids cultured in Matrigel are immature and they exhibit fetal liver phenotype (Baxter *et al.*, 2015b). Furthermore, heterogeneity of organoids in terms of viability, size and shape within same culture conditions limits their use for high-throughput drug screening assays (Sun and Hui, 2020). To add to that relatively rigid ECM could limit drug penetration and organoid retrieval during toxicity analysis. Finally, the absence of liver NPCs in epithelial organoids reduces their physiological relevance (Ye *et al.*, 2020b; Hofer and Lutolf, 2021).

2.5.3 Three-dimensional bioprinting

Three-dimensional (3D) bioprinting is an extension of additive manufacturing technique 3D printing. In 1986, Charles W. Hull first introduced the 3D printing technology named stereolithography, wherein a computer-controlled laser beam was used to crosslink photocurable resin material in a layer-by-layer fashion to build solid 3D structures (Hull and Arcadia, no date). Later this technology was applied in the field of tissue engineering to build sacrificial resin mold for preparing 3D scaffolds. The advancements in material science and 3D printing technology lead to the emergence of next-generation technology known as 3D bioprinting. 3D bioprinting allows fabrication of customized tissue constructs by simultaneous deposition of cells and biomaterials in a layer-by-layer fashion with precise control over the spatial distribution of cells. It is one among the bottom-up approaches in tissue engineering.

The process of 3D bioprinting involves a pre-printing phase, printing phase and post-printing phase. Pre-printing phase is also known as the design phase in which a 3D model of the target tissue or organ is designed using computer aided designing software. The printing phase involves two critical steps, primarily development of bioink (a formulation of cells, biomaterials, and biomolecules) and secondly, bioprinting of tissue construct using optimal bioink formulation. Finally, in the post-printing phase, after a period of *in vitro* maturation, the bioprinted construct will be characterized and used for implantation or *in vitro* analysis.

Recently, 3D bioprinting technology has made tremendous advancements in LTE. One of the important aspects in 3D bioprinting of liver construct is the bioink that will maintain the hepatocyte functions. Liver-specific bioinks prepared using decellularized liver matrix have been shown to induce stem cell differentiation into hepatic lineage (Lee *et al.*, 2017). In addition, biomimetic design approaches have facilitated partial reconstruction of liver lobule structure in the bioprinted construct (Ma *et al.*, 2016). Recently, attention has been directed towards scaffold-free bioprinting approach that utilizes self-assembling hepatic spheroids as bioink particles to achieve tissue-like cell density and function (Kizawa *et al.*, 2017). Meanwhile, combinatorial approaches comprising microfluidics and 3D bioprinting technology are being explored to recapitulate physiological shear forces and biochemical gradients in bioprinted liver constructs (Lee *et al.*, 2019).

2.5.3.1 *Elements of 3D bioprinting*

2.5.3.1.1 Imaging and computer aided designing

Two different approaches have been utilized for the design of a 3D construct. In the first approach, medical images of the target tissue or organ acquired using computed tomography (CT) or magnetic resonance imaging (MRI) are processed in computer aided designing (CAD) software (3D doctor, Mimics, etc) to generate accurate 3D anatomical models (Bücking *et al.*, 2017). The CAD files are then translated to a mesh file in the STL (standard triangle language) file format and it is fed into a slicer software (BioCAM, Cura, slic3r, etc.) to generate horizontal layer-by-layer toolpath (Xie *et al.*, 2020). The toolpath is encoded as G-code (geometric code) which is a series of coordinate locations that the bioprinter will follow during printing. In the second approach, a 3D model is designed *de novo* using drawing tools in the CAD software (Thinkercad, FreeCAD, SolidWorks etc.). A G-code is then generated from CAD file in the same manner as described in the first approach and it is fed into a 3D bioprinter.

2.5.3.1.2 Bioink

The term bioink was first used by Mironov *et al*., (2003) in the context of organ printing along with the term biopaper (Mironov *et al.*, 2003). According to the authors, bioink referred to cellular component (cells or spheroids) which were positioned within a 3D printed hydrogel (biopaper). Thereafter, with the advancement in bioprinting technologies, two classes of bioinks emerged namely, scaffold-based bioinks (cells + biomaterial) and scaffold-free bioinks (cells alone). In this regard, Groll *et al.,* (2018) later defined bioink as "*a formulation of cells suitable for* *processing by an automated biofabrication technology that may also contain biologically active components and biomaterials"*(Groll *et al.*, 2018). Cell is the major constituent of bioink and selection of right cell source is detrimental for the long-term functional performance of bioprinted tissue. Various cell sources such as transformed cell lines, primary cells and differentiated cells from stem cells are used in different forms for 3D bioprinting.

2.5.3.1.2.1 Scaffold-based bioink

Scaffold-based bioinks are the commonly used bioinks in 3D bioprinting. In these bioinks, biomaterial serve as cell delivery medium during formulation and processing. The selection of appropriate bioink material is crucial in controlling the physical and chemical cues inside the bioprinted construct. An ideal bioink material should possess features such as printability, biocompatibility, biodegradability, mechanical stability and biomimicry (Murphy and Atala, 2014). In addition to the above features the bioink material should be easily manufactured and processed on a large scale in a cost-effective manner.

2.5.3.1.2.2 Hydrogel precursors as bioink material

Among the different forms of biomaterials, hydrogel is the most preferred one for bioink formulation due to its high hydration capacity, and tunable biological, chemical and mechanical properties that support cell encapsulation. Both natural and synthetic hydrogel precursors are used for bioink preparation. Hydrogels derived from natural polymers such as collagen, gelatin, and fibrin contain native ECM molecules that provide physiologically relevant cues for cells. But it is difficult to fine tune their mechanical properties. In contrast, hydrogels derived from synthetic polymers like PEG and Pluronic, allow fine tuning of mechanical properties but lack native ECM features (Tibbitt and Anseth, 2009). To address these individual limitations, functionalized polymer hydrogels have been developed either by covalent modification of natural polymers with chemical moieties (e.g.- GelMA) or by functionalizing synthetic polymers with bioactive molecules (e.g.- PEG-RGD) (Kim *et al.*, 2014; Lee *et al.*, 2016).

Hydrogel-based bioinks have been much beneficial to printing soft tissues such as liver. Various hydrogel-based bioinks of both natural and synthetic origin has been utilized for 3D bioprinting of liver construct as shown in Table 1.

Table 1. Properties of hydrogel precursors used as bioinks for liver 3D bioprinting

Polymer	Class	Cell adherence	Bio-degradability	Important properties	References
Natural polymers					
Gelatin	Protein	Yes	Yes	Quick gelation at low temperature	(Wang *et al.*, 2008; Colosi *et al.*, 2016)
Collagen	Protein	Yes	Yes	Slow gelation at 37° C	(Liu *et al.*, 2018; Mazzocchi *et al.*, 2018)
Alginate	Polysaccharide	No	Yes	Cationic gelation	(Liu *et al.*, 2018; Wu *et al.*, 2020)
Synthetic polymers					
PEG	Polyether	No	No	Tunable mechanical strength	(Grix *et al.*, 2018; Khati *et al.*, 2022)
Pluronic	Poloxamer	No	No	Quick gelation above 25°C	(Gori *et al.*, 2020)
Functionalized polymers					
GelMA	Protein	Yes	Yes	Photo-crosslinkable and tunable	(Bhise *et al.*, 2016; Pai, Ajit,

Polymer	Class	Cell adherence	Bio-degradability	Important properties	References
				mechanical strength	*et al.*, 2022)
Decellularized matrix (dECM)					
Liver dECM	Proteins, glycoproteins, proteoglycans	Yes	Yes	Retain native ECM components	(Lee *et al.*, 2017; Khati *et al.*, 2022)

2.5.3.1.2.3 Crosslinking mechanisms of hydrogel precursors

Another important aspect of most hydrogel-based bioink is that the precursor may not be stable at physiological conditions and require some secondary intervention like crosslinking. Crosslinking of hydrogel precursor can be achieved by different methods such as physical crosslinking, chemical crosslinking and enzymatic crosslinking (Hospodiuk *et al.*, 2017). Physical crosslinking method rely on non-covalent interactions between polymer chains to form stable hydrogel. Ionic crosslinking is a type of physical crosslinking that involves interaction of oppositely charged moieties of the polymer chains in the presence of an ionic crosslinker. Crosslinking of sodium alginate polymer is facilitated by calcium ions which form ionic bonds with carboxyl group of alginate. Phase transition is another mechanism of physical crosslinking which happen due to changes in hydrophilicity/hydrophobicity of material with respect to changes in environmental stimuli. Collagen forms hydrogel at physiological temperature by means of phase transition.

In chemical crosslinking hydrogels are stabilized by covalent bonds between polymer chains. The common methods utilized for chemical crosslinking are Schiff base formation and photo-crosslinking. Schiff base is formed by the nucleophilic addition of an amine group to a carbonyl functional group. Amine containing polypeptides, polysaccharides and synthetic polymers can be crosslinked in the presence of an aldehyde containing crosslinkers like glutaraldehyde. However, due to its cytotoxic nature, glutaraldehyde has been replaced with naturally derived crosslinker genipin (Hospodiuk *et al.*, 2017). Photocrosslinking or photocuring is a light-based reaction which is highly efficient, yielding minimal byproducts and provides better spatiotemporal control over crosslinking density. In this method light activated photoinitiator/photosensitizer initiates the crosslinking of low molecular weight monomers or oligomers. Various photoinitiators such as Irgacure-2959, lithium-acyl phosphinate (LAP), riboflavin, ruthenium/ sodium persulfate and Rose Bengal have been used for photocrosslinking (GhavamiNejad *et al.*, 2020). Three different photo-crosslinking reactions have been utilized during bioprinting process such as free-radical chain polymerization, thiol-ene photocrosslinking, and photomediated redox cross-linking (Lim *et al.*, 2020). Some of the commonly used photo-crosslinkable hydrogels include methacrylated form of gelatin, collagen, and hyaluronic acid, and di-arylated form of PEG.

Enzymatic cross-linking leverages the biological enzyme-mediated reaction to form peptide bond between amino acid residues of the polypeptide chains. Transglutaminase is one of the widely used enzyme for cross-linking protein-based hydrogels (Heck *et al.*, 2013). Various strategies have been implemented for crosslinking hydrogel precursors during the process of bioprinting. In most cases crosslinking is done post-printing. While in another strategy, pre-crosslinking of precursor solution to a state of higher viscosity followed by printing and complete crosslinking has also been explored. Interestingly, in a recent approach in-situ photocrosslinking has been performed during the final stage of extrusion process in the needle immediately before deposition for extrusion-based bioprinting (GhavamiNejad *et al.*, 2020).

2.5.3.1.2.4 Scaffold-free bioink

Scaffold-free bioinks are devoid of any biomaterial and are mainly composed of cells assembled in various forms such as spheroids, cell pellet and tissue strand. Scaffold-free bioinks will help to achieve tissue-like cell density and cellular self-assembly within bioprinted construct. Tissue spheroids having a diameter of 200-400 μm have been extruded one-by-one on an agarose mold according to a computer design to support spheroid fusion and generate larger scale tissue constructs (Norotte *et al.*, 2009). In a different approach based on traditional Kenzan method, Itoh *et al.*, (2015) demonstrated that spheroids can be bioprinted on a needle array to achieve spheroid fusion without any supporting scaffold. The cell pellet is another form of scaffold-free bioink which are formed by centrifugation of cells inside conical tube. The cell pellet can be extruded as filaments using a customized cartridge in a 3D bioprinter. However, cells within the pellet are devoid of proper nutrient and oxygen supply which may affect the cell viability. This approach suites well for cells like chondrocytes which require low oxygen levels for synthesis of ECM and other chondrogenic proteins (Schrobback *et al.*, 2012).

The third class of scaffold-free bioink is the tissue strand, a cylindrical neo-tissue formed by aggregation of cells injected inside a hollow tube made of alginate hydrogel. The semi-permeable alginate shell allows exchange of nutrients and oxygen to the cells. Once tissue formation is completed the hydrogel is dissolved using a decrosslinker solution and the tissue strand can be extruded using a custom-made bioprinter head to fabricate tissue constructs.

2.5.3.1.3 Bioprinting modalities

In 3D bioprinting, there are four main bioprinting modalities or technologies. Inkjet, laser assisted forward transfer (LAFT), direct light projection (DLP) and extrusion bioprinting are the four different bioprinting modalities Figure 4 (Pai, Anupama Sekar, *et al.*, 2022).

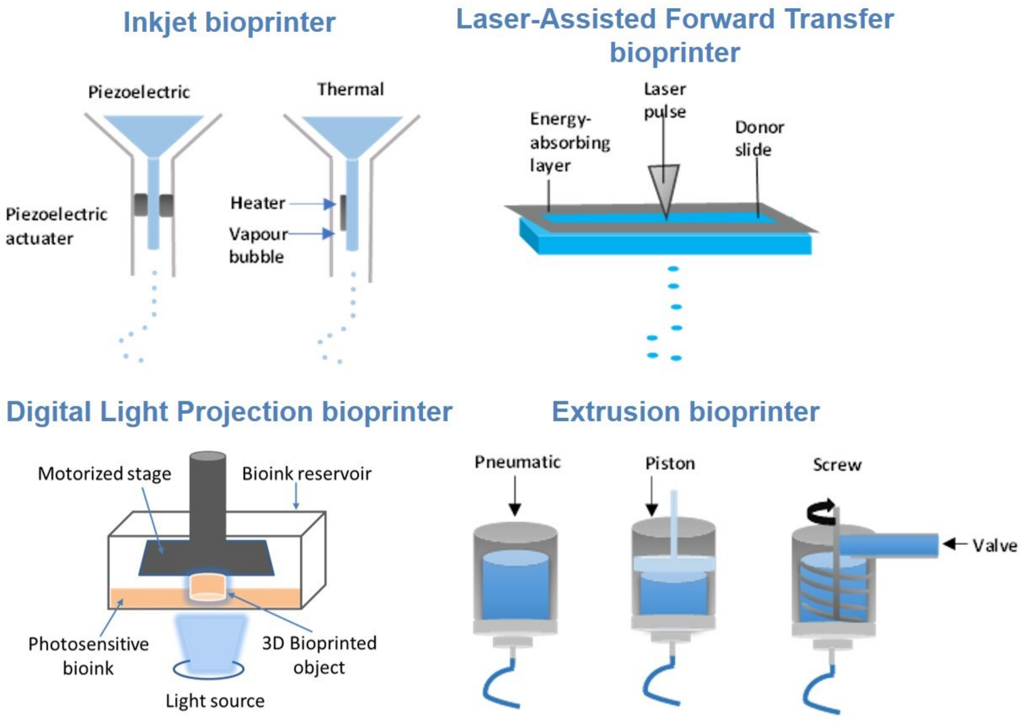

Figure 4.Illustration showing different 3D bioprinting technologies

Inkjet bioprinters are commonly used for low viscosity bioinks and it dispenses the bio-ink as a droplet to the collector plate. Ink-jet printers are classified as piezoelectric, thermal inkjet and microvalve-based printers based on droplet forming technology. Advantages of thermal ink-jet printers are low-cost, high-resolution, and high print speed. The limitations of inkjet modality include low droplet directionally, frequent clogging in the needle due to settling of cells, thermal or shear stress to cells, inability to print high cell density bioinks due to low viscosity and low mechanical strength of printed constructs (Murphy and Atala, 2014).

Laser-assisted forward transfer bioprinting is a nozzle-free bioprinting technology that functions on the basis of laser-induced forward transfer of bioink. During LAFT bioprinting a focused pulse of laser is directed on an absorbing ribbon that carry the bioink. The laser generates a high propelling pressure at the point of incidence and transfer the bioink to the collector plate. High-precision, absence of bioink clogging and ability to print high viscosity bioink are the merits of using LAFT (Pai, Anupama Sekar, *et al.*, 2022). However, lasers can cause damage to cells as they generate heat on collision with bioink (Murphy and Atala, 2014).

Digital light projection is another nozzle-free bioprinting technology developed from the traditional stereolithography method. Using a digital micro-mirror, DLP printers project light onto photocurable bioink that is placed inside a transparent ink reservoir. Then, a build plate in contact with the ink bed travels vertically while transporting crosslinked bioink layers one on top of the other. DLP offers a unique advantage of volumetric printing within a short time irrespective of the complexity of the structure. DLP has substantially superior printing resolution and reproductivity than other bioprinting technologies and it may produce smoother tissue structures (Pyo *et al.*, 2017). The limitation of DLP technology is that only photocurable bioinks can be used and excess volume of bioink is required for bioprinting.

Extrusion-based bioprinting is the most adaptable method for extruding biomaterials for 3D bioprinting applications. It functions by layer-by-layer deposition of pre-gelled bioink filament onto a substrate by robotically controlled extrusion print head. Extrusion print heads have been classified into three types, pneumatic, piston and screw driven, based on the method of force applied to extrude the bioink (Murphy and Atala, 2014). Extrusion based bioprinting suits to wide range of bioink viscosities with shear–thinning properties. Shear-thinning is a rheological property of non-Newtonian fluids, that describes the decrease in viscosity of a fluid with increase in shear rate and the ability to reverse back to the original state when the shear force is removed. This property of bioink rescue cells from damage due to high shear stress during extrusion and at the same time enables the bioink to recover the gel like property after deposition (Gillispie *et al.*, 2020). Shear thinning is also useful to retain the bioink shape fidelity and prevents collapsing of the printed construct (Gillispie *et al.*, 2020). Fabrication of multiple tissues like branched vascular trees, aortic valves and tumor models have been achieved using extrusion printers (Murphy and Atala, 2014). Compared to other technologies, extrusion bioprinting allows fabrication of high cell density constructs of clinically relevant size either using cells or cellular aggregates.

2.5.3.1.3.1 Printability

Rheological properties such as shear thinning, viscoelasticity, and yield stress control the printability of a bioink. The bioink may be fine-tuned to resist deformation when at rest and flow effortlessly when enough shear force is applied. The printability of the bioink can be assessed using a variety of criteria, depending on the bioprinting technology being employed. For inkjet bioprinting, two key factors droplet pinch-off duration and droplet breakdown type following pinch-off are used to define printability. These variables affect droplet size and velocity, which in turn affect printing resolution (Dong, Carr and Morris, 2006). In laser-assisted forward transfer bioprinting, bioink is expelled as a liquid jet with a jet velocity substantially higher than inkjet. The printability of LAFT printing is dependent on the type of liquid jet regime. When a well-defined liquid jet with a single breakdown impinges on the substrate, high-quality printing is generated (Zhang *et al.*, 2016). Photocurable bioink is spread across a build plate during digital light projection-based bioprinting to create 3D architecture. As a result, viscosity is the only factor that influences how well these bioinks print. Low viscosity bioink is advantageous for DLP-based bioprinting because it flows readily under the build plate, removing unreacted materials and enhancing resolution and minimizing printing artifacts (Schwab *et al.*, 2020). For extrusion bioprinting, printability is evaluated in two stages. In stage 1, rheological properties of the bioink such as flow initiation, shear thinning and post-printing recovery is analyzed. And in the second stage, extruded filament characteristics before and after deposition is analyzed. These include extrudability, filament spreading, filament uniformity and filament collapse. Furthermore, successful filament stacking and merging at crossover points are analyzed for 3D printed multilayer construct (Gillispie *et al.*, 2020). The ideal bioink can be extruded as uniform filaments with strand widths that closely match nozzle diameters and has enough storage modulus to permit layer stacking without merging.

2.5.3.1.4 Tissue maturation

The stage of tissue maturation is when the bioprinted tissues reach their mature structure and function. It needs a combination of physical and chemical elements known as maturogens (Passamai *et al.*, 2016). Utilizing bioreactors, tissue-specific physiological conditions are created for the tissue maturation of 3D bioprinted constructs. To preserve cell viability and function, the bioreactor maintains the tissue constructs in a moist environment with carefully monitored environmental factors (pH, temperature, gaseous exchange, nutrition delivery, and waste removal) (Castro *et al.*, 2020). Stirred tank bioreactors, bubble column bioreactors, airlift bioreactors, fluidized bed bioreactors, and packed bed bioreactors are the most frequently used bioreactors in the field of bioprocessing. Biomechanical signals, such as hydrostatic pressure and shear stress, are essential for developing the tissue functions during the maturation phase in addition to the ideal culture conditions (Guilak *et al.*, 2014). Following tissue maturation, the bioprinted constructs can be evaluated for their structural and functional integrity, and can be used for various applications such as drug testing, disease modelling and implantation.

2.5.4 Liver decellularization and recellularization

Liver decellularization and recellularization has emerged as a promising approach to engineer whole organ *ex vivo*. The decellularization method aims to eliminate resident cells from the liver while retaining the ECM components and architecture. It can be done by different methods including chemical, enzymatic, mechanical or in combination with each other and evidence suggest that ECM composition will vary for each method (Dai *et al.*, 2022). Therefore, a great body of qualitative and quantitative analysis is performed to check the efficiency of decellularization method. It mainly includes histological analysis of decellularized ECM for presence and distribution of ECM proteins, and quantification of DNA content to confirm complete removal of cellular components. To date, perfusion-based decellularization method seems to be the excellent option for obtaining clinical scale liver ECM scaffolds. Mazza *et al.,* (2015) first reported the perfusion-based decellularization protocol for human liver using a combination of trypsin + EDTA, Triton X-100 and SDS (Mazza *et al.*, 2015). The DCL scaffolds retained the major ECM proteins and were proven to be biocompatible.

Following decellularization, the matrix is sterilized and can be utilized for recellularization. The liver recellularization process involves perfusion-based cell seeding via portal vein or bile duct under control conditions. It has been shown that after recellularization, the matrix components can induce the differentiation of human induced pluripotent stem cells into hepatocyte-like cells but with incomplete liver functions (Jaramillo *et al.*, 2018). An advantage of this approach is that the intact macrovascular structure facilitates connection of the recellularized liver graft with the patient vasculature upon transplantation. However, regeneration of sinusoidal endothelium and biliary tree remains to be a major challenge in this approach. Efforts have been taken to conjugate anti-endothelial cell antibodies to the vascular network of porcine DCL scaffolds to enhance the endothelial cell adhesion (Ko *et al.*, 2015). Despite having great potential to reconstruct human liver at the macroscale, this approach is greatly depended on the availability of donor livers. Also, further refinement in the recellularization process is required to include all the non-parenchymal cells (NPCs) into the DCL scaffolds. The presence of residual detergents and the sterility of scaffold are the other important issues that needs to be addressed before transplantation of recellularized liver in humans.

2.5.5 Microfluidics-based culture

The microfluidics-based culture systems use technologies to pattern cells in a microfluidic chamber to stimulate *in vivo* cell assembly and fluid flow. Microfluidic devices have enabled generation of various aspects of liver lobules at a microscale. Yamada *et al.*, (2012) developed a hydrogel-based microfluidic platform to generate hepatic cord structures found in liver (Yamada *et al.*, 2012). Hepatocytes and 3T3 fibroblast cells were suspended in sodium alginate solution and were coaxially introduced into a microfluidic channel to produce hydrogel fibers. A heterotypic microtissue with 1 mm length and 50 µm diameter consisting of fibroblast cells lining the hepatocytes at the center was generated. Long-term cultures of microtissue showed high hepatocyte viability along with enhanced liver function and expression of hepatocyte-specific genes.

Meanwhile, Prodanov *et al.,* (2016) demonstrated a step-by-step method for building 3D microtissue resembling human liver sinusoid in a microfluidic chip consisting of dual chambers separated by a porous membrane (Prodanov *et al.*, 2016). Human hepatocytes were seeded in one chamber to form monolayer and were overlaid with collagen gel containing stellate cells. The endothelial cells (ECs) were seeded on the porous membrane confronting the second chamber to form monolayer and were cocultured with kupffer cells. The cells were cocultured under flow conditions. The hepatocytes showed cuboidal cell morphology with presence of bile canaliculi and maintained liver functionality for 28 days. A different strategy was used by Mi *et* *al.,*(2018) to construct liver sinusoid on a chip (Mi *et al.*, 2018). In this study, human hepatoma cell HepG2-laden collagen and human umbilical vein endothelial cell (HUVEC)-laden collagen was synchronously injected into the chip to form two layers with clear borderline. The HUVEC cells formed a monolayer and the construct maintained liver bioactivity for 7 days in culture.

Recent studies have also reported the metabolic zonation in liver-on-chip models (Kang *et al.*, 2018; Tonon *et al.*, 2019; Danoy *et al.*, 2020). Metabolic zonation was achieved by creating gradients of oxygen, hormones and inducers in the chip. Hepatocytes exposed to lower and higher concentration of metabolic modulators showed zone-specific gene expression and liver functions. Taken together the reports suggest that microfluidic-based 3D culture systems are useful for constructing micro-physiological hepatic tissues to study liver cell biology and drug toxicity. However, the low-throughput and limited volume of the engineered construct do not qualify this technology for regenerative therapy.

2.6 Reconstruction of biomimetic liver models by modular approaches

The regenerative function of liver can be destroyed by viral infection, drug poisoning and tumorigenesis, resulting in irreversible damage. Owing to the significant advantages in cell programming and bio-scaffold engineering, liver tissue engineering is the most promising alternative for mimicking liver microstructure, maintaining hepatic function or implanting whole liver. Recent advances in three-dimensional culture of liver cells have gained much attention due to their physiological resemblance. Several efforts have been directed towards reconstructing 3D liver tissue architecture by tissue engineering approaches at various scales.

2.6.1 3D stacked-up culture of cell sheets

Cell sheet engineering as proposed by Okano *et al* has been exploited as a method for constructing 3D tissue structures by stacking 2D cell sheets. Ohashi *et al.*, (2007) first demonstrated that hepatic sheets can be layered *in vivo*. In their study, the dual layered hepatocyte cell sheet was efficiently engrafted into a pre-vascularized subcutaneous site in mouse and it formed a functional 3D hepatic tissue mass that persisted stably for longer than 140 days (Ohashi *et al.*, 2007). Later, Itaba *et al.*, (2015) showed that orthotopic transplantation of a three-layered cell sheet construct derived from human mesenchymal stem cell-differentiated hepatocytes accelerated liver regeneration in mice with acute liver injury through activation of complement factor C3 and thioredoxin (Itaba, Matsumi, *et al.*, 2015).

Attempts have been also made to coculture hepatocyte cell sheet with the endothelial cell sheet to mimic the *in vivo* cellular assembly in 3D constructs. Kim *et al., (2017)* fabricated a triple-layered construct by sandwiching hepatocyte sheet between two endothelial cell sheets (Kim *et al.*, 2017). The construct attained *in vivo*-like hepatocyte polarity and highly preserved hepatocyte-specific functions. Recently, the application of hybrid hydrogel substrate for developing hepatocyte cell sheet was reported by Asadi *et al.,* (2021). In this study, a multilayered hepatic cell sheet was developed by the differentiation of human adipose-derived mesenchymal stem cells cultured on a hybrid hydrogel composed of rat dECM and PNIPAAm (Asadi *et al.*, 2021). The presence of dECM in the hybrid hydrogel caused upregulation of liver-specific genes compared to cells cultured on PNIPAAm alone. These studies suggest that multilayered hepatic cell sheets can mimic the tissue architecture and function and provide better engrafting efficiency. However, the inability to scale-up the three-dimensional volume of construct limits the translational potential of this technology. Although cell sheets can be stacked over each other, the thickness of the constructs remains in the range of few hundred microns which is insufficient for orthotopic transplantation in humans.

2.6.2 Self-assembly of liver cell aggregates

3D cellular aggregates such as spheroids and organoids are considered as building blocks for tissue engineering. However, only few attempts have been made to reconstruct liver tissue microarchitecture *in vitro* by self-assembly of 3D cellular aggregates. In an attempt to construct regularly vascularized liver tissue, Inamori *et al.*, (2009) packed HUVEC-covered hepatocyte spheroids in hollow fibers utilized for plasma separation. At day 9 post packing, the spheroids attached to each other forming a large cellular tissue and the HUVEC invaded the hepatocyte spheroids generating a dense vascular network within the tissue (Inamori, Mizumoto and Kajiwara, 2009). While, Hong *et al.,* (2021) combined a preset extrusion bioprinting technology with microfluidic emulsification system to generate spheroids with biomimetic hepatic lobule-like structure (Hong *et al.*, 2021). Collagen bioinks containing hepatocytes and endothelial cells were loaded individually into separate compartments of a preset bioprinting cartridge resembling hepatic lobule structure and were injected into the inner nozzle of the coaxial nozzle system as a disperse phase. Mineral oil was injected into the outer nozzle as a continuous phase. The fabricated structured spheroids showed improved functionality and lobule-mimetic structure compared to the conventional co-culture spheroids.

Recently, a new area of research focused on self-assembled hetero organoids, known as “Assembloid” has emerged. Sergiu Pasca, a physician-scientist at Stanford university, first coined the term “Assembloid” from his observation on self-assembly of cortical and striatal organoids derived from brain tissue. Of late, Nam *et al*., (2022) reported the development of endothelial cell-integrated liver assembloids. The authors combined induced hepatic stem cells organoids with induced endothelial cells to form assembloids. The assembloids exhibited enhanced functional maturity compared to hepatic stem cell organoids and improved therapeutic effects on cholestatic liver fibrosis mouse models.

2.6.3 Three-dimensional bioprinting of cells and cellular aggregate

Three-dimensional bioprinting has emerged as promising tool for biofabrication of functional liver constructs. In comparison to other approaches in liver tissue engineering, 3D bioprinting has several merits such as simultaneous cell/scaffold printing, fabrication of complex 3D constructs, high reproducibility and high spatio-temporal control positioning of cells (Agarwal, Banerjee, Konwarh, Esworthy, Kumari, Onesto, Das, Lee, Wagener, Makvandi, Mattoli, Ghosh, Maiti, Zhang and Ibrahim T Ozbolat, 2021). At present, the primary goal of 3D bioprinting research is to achieve biomimetic liver tissue architecture inside the printed construct. To achieve this goal efforts have been taken to improve the bioprinting strategies either my altering the bioink properties or by modulating the bioprinting technologies.

Matsusaki *et al*., (2013) fabricated an array of multi-layered liver 3D tissue architectures on a chip using inkjet printing. Each tissue consisted of three layers of cells, a layer HepG2 cells sandwiched between two layers of HUVEC. A thin nanosized film of fibronectin and gelatin was deposited between each layer to hold the cells in position. The sandwiched culture hepatic tissue exhibited higher levels of albumin secretion and xenobiotic metabolism compared to monolayer. This study also implies the importance of heterotypic cell interaction in liver tissue engineering.

Efforts have been also directed towards mimicking the *in vivo* patterning of liver cells within a hepatic lobule using digital light projection-based 3D printing and co-axial bioprinting. Ma *et al.*, (2016) executed DLP printing to develop a 3D hydrogel-based triculture system with adipose-derived stem cells, stem cell differentiated hepatocytes and HUVEC patterned in a microscale hexagonal geometry similar to liver lobule (Ma *et al.*, 2016). The bioprinted hepatic lobule model showed better structural organization, higher liver-specific gene expression, enhanced cytochrome P450 induction and increased metabolic product secretion.

In yet another study, Kang *et al.*, (2020) used a preset extrusion multi-material bioprinting process to create a hepatic lobule array (1 mm) that contained hepatocytes, endothelial cells, and a lumen inside a highly vascularized construct (Kang *et al.*, 2020). The method allowed for the spatial patterning of cellular components, allowing the endothelial cells to fence the construct's outside, form an endothelium-lined lumen, and subsequently integrate the exterior and lumen. The spatially patterned hepatic lobule displayed increased albumin secretion, urea production, CD31 expression (endothelial cell marker), and drug-metabolizing activity in comparison to hepatic cell/endothelial cell mixed cultures. The study also shown that cells organized more quickly under spatially constrained circumstances, finally maintaining their integrity and exhibiting improved responsiveness. Such pre-set extruded hepatic lobules could aid in the creation of both micro- and macro-scale tissues and encourage future multi-scale tissue engineering initiatives. However, these approaches can fail when multiple non-parenchymal cells need to be included in the bioprinted construct.

Engineering intrahepatic biliary tree inside bioprinted construct has not gained much attention compared to the hepatic tissue. In this backdrop, to create the intrahepatic biliary tree, cholangiocytes were embedded in PLECM hydrogel and were added inside a 3D printed pluronic F-127 channels (Lewis *et al.*, 2019). Computational 3D image analysis of duct alignment showed that via adjustment of the structural geometry of the sacrificial material, cells could be guided successfully to attain native cell assembly inside the construct.

Meanwhile, a scaffold-free approach was implemented by Yanagi *et al.* (2017), to 3D print spheroids based on the principles of Kenzan method (Yanagi *et al.*, 2017). The method uses a robotic arm to skewer discrete cell spheroids onto an array of needles in order to create 3D tissues constructs that are both medically and geometrically realistic. Hollow tube-shaped liver tissue was developed using multicellular spheroids containing human hepatocyte, HUVEC, and MSCs. The 3D liver tissue retained liver-specific functions and successful engraftment of constructs in nude rat led to secretion of human in rat serum. Although scalable tissue constructs with high cell density have been developed using scaffold-free bioprinting technology, there are limitations on spheroid dimensions because with the increase in size there will be higher chances for cell necrosis in the core (Achilli, Meyer and Morgan, 2012). Besides that, assembling smaller functional spheroids without supports into larger complex geometries to mimic organs is challenging.

Further to improve the structural organization of cells inside bioprinted liver construct, self-organized organ buds or organoids have been utilized recently. This approach of using organoids as the cell component in bioprinting will facilitate rapid tissue organization along with macroscale tissue fabrication. However, this area of research is still in the stage of infancy. Of late, Bouwmeester *et al.,* (2021) demonstrated that differentiated intrahepatic cholangiocyte organoids suspended in GelMA bioink could be bioprinted successfully (Bouwmeester *et al.*, 2021). The organoids were viable and showed evidence of structural reorganization inside the construct. However, the bioprinted organoids exhibited low levels of mature hepatocyte genes and expressed low levels of serum proteins like albumin. This study is highly promising but at the same time looking at the functional performance, further improvisations with respect to selection of organoid cell type and culture method is needed.

Chapter 3

MATERIALS AND METHODS

3.1 Synthesis of Gelatin Methacrylamide

Gelatin methacrylamide (GelMA) was synthesized by the substitution reaction between gelatin and methacrylic anhydride as previously reported (Lee, Shirahama, N.-J. Cho, *et al.*, 2015). Briefly, 10 g of Type A porcine skin gelatin (Merck-Sigma, Cat.#G-2625, Germany) with bloom value of 175 was dissolved in 100 mL of 0.1M carbonate-bicarbonate buffer (pH 10.5) at 60 °C on a magnetic stirrer with hot plate. The temperature of the solution was brought down to 50 °C and the pH was adjusted to 9. The solution was stirred at 500 rpm and 1ml methacrylic anhydride (MAA) (Merck-Sigma, Cat. #276685, Germany) was added in a stepwise manner, i.e., 167 µL at an interval of 30 min for 3 h. The molar ratio of MAA/amine was 2.2. The pH was adjusted to 9 before each addition. The GelMA formed in the solution was transferred into dialysis tubing with 12-14 kDa molecular weight cut-off (Merck-Sigma, Cat. # D9652, Germany). The GelMA solution was then dialyzed against water at 40 ºC for 72 h to remove un-reacted MAA and short chain polymers. The dialyzed GelMA was freeze-dried in a lyophilizer (CHRIST, Alpha 1-2 LD plus, Germany) at -80 °C for 72 h. The weight of the dried GelMA was measured and packed inside a glass vial and sterilized using ethylene oxide gas without the lid at 37 ºC. The caps were sterilized separately and the vials were closed aseptically inside a biosafety cabinet. The sterilized GelMA were stored in -20 ºC deep freezer (Sanyo, Model# MDF-U73V, Japan) until used.

The yield of GelMA synthesis was calculated using the equation 1 given below.

$$\text{Percentage Yield} = \frac{\text{Weight of GelMA}}{\text{Weight of Gelatin+Weight of MAA}} \times 100 \text{...........Equation 1}$$

The efficiency of GelMA synthesis was calculated from percentage yield obtained in different batches and presented it as Mean ± Standard Deviation.

3.2 Physico-chemical characterization of GelMA

3.2.1 ^{1}H Nuclear Magnetic Resonance Spectroscopy

The functionalization of gelatin by the methacrylamide group was verified by ^{1}H Nuclear Magnetic Resonance Spectroscopy (^{1}H NMR). Ten milligrams of GelMA and gelatin were dissolved separately in deuterium oxide (D_2O) at 40ºC, and their spectrum was recorded in a Fourier Transform-NMR spectrometer (Bruker, Model# Avance 400, USA) at 400 MHz using tetramethylsilane as the internal standard. The recorded spectrum was analyzed using TopSpin® software (Bruker, USA).

3.2.2 Degree of functionalization

The degree of functionalization in GelMA was determined by ninhydrin assay. Unmodified Type A gelatin was used as a control. Gelatin and GelMA was dissolved in deionized water at 60 ºC to obtain a 10% (wt/v) solution. The gelatin solution was diluted in water to prepare a series of standard solutions (8%, 6%, 4% and 2% wt/v). A solution mixture containing one part of 0.5 M sodium citrate monobasic (Merck-Sigma, Germany) and two parts of glycerol was prepared. The ninhydrin powder (Nice chemicals, India) was then dissolved in sodium citrate monobasic/glycerol mixture at a final concentration of 2.5 mg/ml. About 850 µL of the ninhydrin solution was transferred to a 1.5 mL tube. Multiple tubes were prepared and labelled for adding the blank, standards and sample solution. About 150 µL of water (Blank), gelatin (Standard) and GelMA (Test) were added into the tubes. The tubes were vortexed and incubated at 50 ºC in a water bath for 12 min. The tubes were allowed to cool to room temperature and 250 µL of the solution from the tubes were transferred to a 96-well plate. The absorbance of the sample and standards were recorded at 570 nm using a spectrophotometer (Biotek, Model# Powerwave XS, USA). A linear regression line was drawn using the absorbance values obtained from standards. The absorbance of GelMA sample corresponds to a gelatin concentration of X% on the standard curve. The degree of functionalization was calculated as per equation 2.

$$\text{Degree of Functionalization} = \frac{(10-\text{X}\%)}{10} \times 100 \ldots\ldots\ldots \text{ Equation 2}$$

Where X represents the concentration of unmodified gelatin in GelMA.

3.2.3 Photocrosslinking of GelMA

The GelMA polymer solution was crosslinked using UV light in the presence of a photoinitiator. Four different concentrations of GelMA hydrogel precursor solution (5 %, 10 %, 15 % & 25 % wt/v) were prepared by dissolving specific quantities of the lyophilized polymer in 1 mL Minimum Essential Medium (MEM, Merck-Sigma, Germany) at 37 ºC. A photoinitiator solution comprising 5% (wt/v) Irgacure-2959 (2-Hydroxy-4'-(2-hydroxyethoxy)-2-methylpropiophenone) (Merck-Sigma, Germany) was prepared in PBS by heating at 80 °C. About 0.2 mL of photoinitiator solution was added to the polymer solution obtain a final concentration of 1% (wt/v). The solution was mixed thoroughly by continuous pipetting and about 200 µL of each different GelMA solution was transferred to a cylindrical Teflon mold. The hydrogel precursor solution was exposed to UV light of 365 nm from a height of 1 cm from the sample. The polymer solutions were exposed to UV light for different duration (30 s, 60 s, 90 s and 120 s). The crosslinked hydrogels were then taken out and their morphology was examined. The hydrogels were then incubated 37°C in PBS for 24 h and their morphology was again examined.

3.2.4 GelMA hydrogel swelling

The swelling property of GelMA hydrogel was analyzed by incubating the crosslinked GelMA in PBS. Three different concentrations of GelMA hydrogel precursor solution (10 %, 15 % & 25 % wt/v) containing photoinitiator were prepared as described above. About 150 µL of each concentration was transferred to replicate wells (n=4) of 96-well plate. The solutions were then cross-linked by UV light of 365 nm. GelMA hydrogel samples with 6 mm diameter and 3 mm height were obtained. The hydrogel was weighed using an electronic balance (Sartorius, BSA 4202S-CW, Germany) and then transferred to a glass vial containing 1.5 mL PBS. The samples were incubated at 37 ºC for 24 h. The hydrogels were taken from the PBS, blotted on a paper, and the swollen weight was measured to estimate amount of water uptake. The percentage swelling of GelMA hydrogel was calculated using the equation 1. The results were represented as Mean ± Standard Deviation.

$$\text{Percentage Swelling (wt \%)} = \frac{\text{Swollen weight} - \text{Initial weight}}{\text{Initial weight}} \times 100. \text{ Equation 3}$$

3.2.5 Compressive modulus of GelMA hydrogel

The compressive modulus of GelMA hydrogel was determined by compression test using a universal testing machine (UTM) (Bioplus 3345, Instron, USA). Three different concentrations of GelMA hydrogel precursor solution (10 %, 15 % & 25 % wt/v) containing photoinitiator were prepared as described above. About 650 µL of each different GelMA solution was transferred to a well of 48-well plate in quadruplicate. The solution was crosslinked by UV-light and hydrogel samples with 10 mm diameter and 12 mm height were obtained from each well. The hydrogel samples were incubated in PBS at 37°C for 24 h for equilibrium swelling and the compression test was performed at 25 °C using a 100 N load having a diameter of 5 cm. The test was run at 10 mm/min strain rate until a maximum strain of 50 % was reached. The modulus values were then determined from the stress-strain curves.

3.3 Cytotoxicity evaluation of GelMA hydrogel

3.3.1 Culture of HepG2 cells

Human hepatocellular carcinoma cell line, (HepG2, National Centre for Cell Science, India), was cultured in Minimum Essential Medium (MEM, Merck-Sigma, Cat.# M0769, Germany) with 10 % Foetal Bovine Serum (FBS, Gibco, Cat.#10270106, USA) and 0.1 % Penicillin-Streptomycin antibiotic (Pen-Strep, Gibco, Cat.#15070-063, USA). Cells were incubated in CO^{-}_{2} incubator (New Brunswick, Galaxy 170 S, Canada) set at 37 ºC, 5 % CO_2 and >90 % relative humidity with medium change on every alternate day. The cells were subcultured at subconfluency in a split ratio of 1:2 using trypsin + 0.25 % EDTA solution.

3.3.2 Cell encapsulation in GelMA hydrogel and viability staining

A subconfluent culture of HepG2 cells were trypsinized and the total cell number was counted using a hemocytometer. A homogenous cell suspension containing 1×10^5 cells/mL was prepared in MEM and was equally aliquoted into three centrifuge tubes. Three different concentrations of sterile GelMA polymer solution (10 %, 15 % & 25 % w/v) containing photoinitiator was prepared as described above. The cell suspension was centrifuged at 1500 rpm for 2 min and equal volume of different concentration of GelMA solution was added to each cell pellet in assigned tubes. The cells were resuspended in GelMA solution by gentle pipetting. About 200 μL of the cell suspension was then transferred to each well of a chamber slide (Himedia, India) and was crosslinked by UV light of 365 nm for one minute. The cells encapsulated in GelMA hydrogel were supplemented with serum containing MEM and were incubated inside CO^{-}_{2} incubator for 7 days with medium change on every alternate day.

The viability of the encapsulated cells was assessed after one and seven days of culture by live-dead staining. The cell encapsulated hydrogel was washed with PBS and was incubated in serum-free medium containing 10 μg/mL fluorescein diacetate (FDA, Merck-Sigma, Germany) and 0.05 μg/mL propidium iodide (PI, HiMedia, Cat#TC252, India). After incubation for 2 min in the dark, the staining solution was removed, and the hydrogel was rinsed using fresh serum-free MEM. The viable and dead cells were visualized using a fluorescent microscope (Leica, DMI6000B, Switzerland) and images were captured using DML monochrome camera (DMC5400) and Leica Application Suite software (LAS V3.7).

3.3.3 In-vitro cytotoxicity evaluation of GelMA hydrogel

The in-vitro cytotoxicity of 10% (w/v) GelMA hydrogel was evaluated based on the ISO standard 10993, part 5. The mouse fibroblast cell line, L-929 (NCCS, Pune, India) was used for the cytotoxicity test. The cells were cultured in Minimum Essential Medium (MEM, Merck-Sigma, Germany) with 5 % Foetal Bovine Serum (FBS, Gibco, USA) and 0.1% Penicillin-Streptomycin antibiotic (Pen-Strep, USA) at 37 ºC, 5 % CO_2 and >90 % relative humidity. The cells were subcultured at subconfluency in a split ratio of 1:2 using trypsin + 0.25 % EDTA solution.

3.3.3.1 *Direct contact test*

The cytotoxicity test of GelMA hydrogel was performed by direct contact test method. GelMA hydrogel disc for direct contact test was casted by UV crosslinking 10% (w/v) GelMA prepolymer solution containing 1% (w/v) Irgacure in a teflon mold with 5 mm diameter and 3 mm thickness. L-929 cells were cultured in a 24-well plate (Eppendorf, USA) until subconfluency inside a CO_2 incubator. The GelMA hydrogel disc was allowed to swell in serum-free MEM for 30 min at 37 ºC. The culture medium from the L929 cells was removed and hydrogel discs were gently placed on the cell monolayer at the center of well. Ultra-high molecular weight polyethylene (UHMWPE) and polyvinyl chloride (PVC) discs were used as negative and positive cytotoxic controls respectively. Fresh culture medium was gently added into the well and cells were then incubated in contact with GelMA hydrogel and control samples for 24 h inside a CO_2 incubator. The cells beneath and around the sample were analyzed after 24 h using an inverted light microscope (Nikon Eclipse TS2, Japan) for evidences on cell detachment, cell lysis, vacuolization and morphology. The cell response was graded from 0 to 4 considering cytotoxicity reactivity indicating 0=None, 1=Slight, 2= Mild, 3= Moderate and 4=Severe.

3.3.3.2 *Test on extract and MTT assay*

The cytotoxicity due to potential eluants from the GelMA hydrogel was evaluated by test on extract method. L-929 cells were cultured in a 96-well plate (Eppendorf, USA) until subconfluency inside a CO_2 incubator. The extract of the sample was taken in complete medium with serum at an extraction ratio of 1.25 cm^2/ ml. For that GelMA hydrogel disc having 1 cm diameter and 0.1 cm thickness was casted and transferred to an extraction bottle containing 1.5 ml medium. The samples were then incubated inside a shaker incubator set at 37 ºC and 70 rpm speed for 24 h. Different dilutions of the hydrogel extract (50 %, 25 %, 12.5 % and 6.25 % (v/v)) were prepared by serial dilution with culture medium. Phenol was used as the positive control. A stock solution containing 13 mg/mL of phenol was prepared in serum-free MEM medium without sodium bicarbonate. The stock solution was then diluted 100 times in MEM complete medium containing serum. MEM complete medium with serum was used as the negative control. The spent media from the cells were removed and about 100 µL of the different dilutions of the extract and 100 % of the control samples were added to the cell monolayer. The cells were then incubated at 37 ºC inside a CO_2 incubator for 24 h. The cells were examined after 24 h using an inverted light microscope (Nikon Eclipse TS2, Japan) for evidences on cell detachment, cell lysis, vacuolization and morphology. The cell response was graded from 0 to 4 considering cytotoxicity reactivity indicating 0=None, 1=Slight 2= Mild, 3= Moderate and 4=Severe.

The metabolic activity of cells treated with extract of samples was evaluated by MTT assay. Metabolically active cells will reduce the tetrazolium salt to a chromogenic formazan crystal which can be solubilized and quantified. After 24 h incubation, the extract and control media were replaced with 100 μL MTT solution (1mg/ml in serum-free MEM) (Merck-Sigma, Cat.# M5655, Germany) and the cells were incubated at 37 ºC inside a CO_2 incubator for two hours. The MTT solution was then discarded and replaced with isopropanol to dissolve the formazan crystal. The plate was shaken well, and the absorbance was measured at 570 nm using a spectrophotometer (Biotek, Powerwave XS, USA). The metabolic activity of cells was expressed as the percentage activity of negative control, calculated using the equation 4.

$$\text{Metabolic activity} = \frac{\text{O.D of Test}}{\text{O.D of Control}} \times 100 \text{ ....Equation 4}$$

3.4 Hydrogel porosity analysis

The porosity of GelMA hydrogel was analyzed by scanning electron microscopy and micro-computed tomography.

3.4.1 Scanning Electron Microscopy

The surface morphology of the GelMA hydrogel was visualized using a scanning electron microscope (SEM) (HITACHI, S-2400, Japan). Cylindrical hydrogel samples (10 % w/v) having 8 mm diameter and 2 mm height were cast in a cylindrical Teflon mold by UV crosslinking. The hydrogel was then frozen at -80 °C and was lyophilized at -80 °C for 48 h. The lyophilized samples were sputter-coated with gold (HITACHI, E1010, Japan) and were examined under the microscope at an accelerating voltage of 15 kV.

3.4.2 Micro-Computed Tomography

The porosity of the GelMA hydrogel was analyzed using a micro-computed tomography (micro-CT) scanner (Scano Medical, Model# µCT 40, Switzerland). Lyophilized hydrogel samples having 12 mm diameter and 6 mm height were prepared as described in section 3.4.1. Freeze dried samples were scanned using a cone-beam X-ray source set at 70 kV and 160 µA having 5 µm spot size. The 2D images were processed using the software µCT V6.1 for 3D reconstruction. Morphometric analysis was also carried out to determine polymer volume (PV), total volume (TV) and pore size distribution. The percentage porosity of the hydrogel was calculated from the equation given below.

$$\text{Porosity (\%)} = \left(\frac{\text{PV}}{\text{TV}}\right) \times 100 \ldots\ldots\ldots\ldots\text{,Equation 5}$$

Where PV represents polymer volume and TV represents total sample volume.

3.5 High-throughput production and characterization of Liver Parenchymal Microtissues

3.5.1 Hanging-drop culture (conventional method)

A subconfluent culture of HepG2 cells were trypsinized and a uniform cell suspension containing 1×10^5 cells/ml was prepared in MEM. About 10 µL of cell suspension was then dispensed on the cover lid of a 90 mm polystyrene dish using a micropipette. Hundred drops were dispensed on a single lid with an inter-drop distance of 5 mm. The lid was gently inverted and placed over a dish containing PBS solution.

The cells were cultured in hanging drops at 37 ºC inside a CO_2 incubator for 72 h to form liver parenchymal microtissues (LPMTs). The microtissue formation efficiency was then determined by examining the entire drops from three different dishes under a phase-contrast microscope (Nikon TS100, Japan). The percentage efficiency of microtissue formation was calculated according to the equation given below.

$$\text{Microtissue Formation Efficiency} = \frac{\text{No.of microtissues formed}}{\text{No.of drops dispensed}} \times 100 \ldots\ldots \text{Equation 6}$$

3.5.2 Design and fabrication of hanging-drop culture chamber

Design of the Hanging drop Culture Chamber (HdCC) was prepared using an open-source general-purpose parametric 3D CAD modeler (FreeCAD Ver 0.18). The key internal component of HdCC is a base plate on which three vertical pillars are fixed in position along with a top plate on the other end. The vertical pillar has eight grooves of 2×4 mm size on the inner side that are accurately positioned to the grooves on the adjacent pillars. The grooves can accommodate eight substrates supporting hanging drops. The groove adjacent to the base plate is positioned at a height of 9 mm to accommodate a dish filled with water to maintain humidity inside chamber. A cubical cover lid is placed over the pillars to provide an aseptic environment to the cells. The cover lid is held in position by four rectangular frills attached to the periphery of the base plate. The overall dimensions of the chamber are 13.2 cm × 13.2 cm ×12.6 cm ($l \times b \times h$). Clear transparent acrylic sheets of 6 mm thickness were cut using a laser cutter (Han's Yueming; 100V) to predefined dimensions of the HdCC components. The components were then assembled manually according to the CAD design using chloroform-based adhesive.

3.5.3 Optimization of parameters for microvalve-based printing

Microvalve-based printing allows a user to generate arrays of droplets in a high-throughput manner. A template of droplet array (15×14 droplets) was created in BioCAD^{TM}1.1 version software (regenHU, Switzerland). The G-Code was generated from the CAD design and imported into the machine control software (HMI^{TM}, regenHU, Switzerland). A specialized nozzle with an electromagnetic dispensing valve (regenHu, Cat.#MVC-D0.3S0.1, Switzerland) having an inner diameter of 300 µm and 100 µm stroke was used to dispense the droplets. A cartridge containing water was loaded into cell-friendly print-head (regenHU, Cat.#CF-300N, Switzerland) of the bioprinter 3D Discovery^{TM} Evolution (regenHu, Switzerland) and the microvalve nozzle was connected to the cartridge through an adapter. A sterile polyethylene terephthalate (PET) sheet (Cat# CT100, Desmat^{TM}) having a size of 70×65×0.1 mm was used as the substrate for droplet printing. The optimum diameter of the droplet was calculated to be 2 mm, with inter-droplet space of 1.4 mm to accommodate 15 × 14 droplet array in one sheet. Since, the diameter of the droplet depends upon the volume of the dispensed droplet, the parameters that control the dispensed volume was analyzed. The volume dispensed by the microvalve nozzle, depends upon the print-head parameters such as valve opening time (VOT), valve closing time (VCT) and the cartridge pressure (CPr). To determine the optimum print-head parameters multiple arrays of water droplets were printed at a travel speed of 12 mm/s with variable VOT (10, 15, 20, 25 and 30 ms) and CPr (2, 4, 6, 8 and 10 kPa) while keeping the VCT constant at one millisecond.

The approximate volume of the printed droplet was estimated by comparing the diameter of the printed droplets with manually dispensed liquid drops. The printed droplet array was divided into top, middle and bottom section, each having 14×5 droplets. Multiple images (n=8) of the droplets were captured from each section using a 3D stereomicroscope (Leica S8 Apo, Switzerland). Similarly, liquid drops of different volumes (0.5 µL, 1.5 µL, 2.5 µL, 3.5 µL and 4.5 µL) were dispensed using a micropipette and the respective images were captured. The feret diameter of both the printed droplets and manually dispensed drops were measured using ImageJ software and were compared.

3.5.4 Microvalve-based bioprinting of HepG2 cells

A confluent culture of HepG2 cells were trypsinized using 0.25% trypsin-EDTA solution (Gibco, Cat.#25200072, USA) and different homogenous cell suspensions containing cell concentration (2×10^5, 4×10^5 and 10×10^5 cells/mL) were prepared in MEM. The cell suspensions were loaded separately into 3 mL cartridges assembled on the bioprinter head. A motorized cell agitator was inserted into the cartridge, and the cell suspension was agitated at the lowest speed for 5 s. A droplet array containing 15×14 droplets was bioprinted on the PET substrate at 8 kPa CPr, 20 milliseconds VOT and one millisecond VCT. The substrate was inverted carefully without disturbing the droplets and placed inside the HdCC. Eight bioprinted substrates were placed inside a single HdCC unit. The HdCC was covered and incubated inside CO_2 incubator for 72 h to form microtissues. The efficiency of microtissue formation was calculated using the equation mentioned in section 3.5.

3.5.5 LPMT harvesting efficiency, size distribution and stability

The LPMTs from each PET substrate (drop number = 210) were gently washed using culture medium (1mL) and the suspension was collected in a centrifuge tube. The microtissue suspension was then centrifuged at 11 g for 30 s. The supernatant was removed and 1mL fresh culture medium was added to the pellet. The suspension containing microtissues were transferred to a 12-well, non-treated plate (Eppendorf, Cat.#0030721012, Germany) and maintained inside a CO_2 incubator for 14 days with replenishment of media on alternate days.

LPMTs formed from three different cell concentrations were harvested separately. Phase-contrast images of the LPMTs (n=40) were captured using a digital camera (VUE, Model# US300, China) connected to the light microscope (Nikon Eclipse TS2-FL, Japan). The feret diameter of the LPMTs was measured using ImageJ analysis software.

3.5.6 LPMT cell viability

Viability of the LPMTs was assessed on 7thday after microtissue formation by live-dead staining. Microtissues collected from non-treated plates were pelleted down by centrifugation at 11 g for 30 s and the spent media was removed. The microtissues were washed with PBS once and were resuspended in serum-free medium containing 10 µg mL^{-1} fluorescein diacetate (FDA, Merck-Sigma, Germany) and 0.05 µg mL^{-1} propidium iodide (PI, HiMedia, Cat#TC252, India). After incubation for 2 min in the dark, the staining solution was removed, and microtissues were rinsed using fresh serum-free MEM. The viability was monitored and imaged using a confocal laser scanning microscope (Olympus, Model# FV3000, Japan).

Adenosine Tri Phosphate (ATP) content of LPMTs was quantified as a direct measure of metabolic activity in viable cells. The ATP content was measured using CellTiter-Glo® 3D cell viability assay kit (Promega, Cat.#G9681, USA) as per the manufacturer instructions. Briefly, 200 microtissues (n=3) cultured for day 1, 7 and 15 were collected from non-treated plate, pelleted and resuspended in 100 µL of culture medium. The suspension was transferred to a white opaque 96-well microplate (Thermo Scientific, Cat.#9502887, USA) in triplicates. The plate was equilibrated to room temperature (25ºC) for 25 min, and ATP assay reagent (100 µL) was added to each well. The plate was shaken vigorously on a microplate orbital shaker at 700 rpm for 10 min and was then incubated for 20 min at room temperature. The luminescence intensity was measured using a Multimode plate reader (Plate Chameleon V 425-106, Hidex, Finland). Percentage cell viability was calculated by normalizing the luminescence values at different time points to the value at the beginning of the culture.

3.5.7 Total protein content of LPMTs

The total protein content of LPMTs was estimated using the BCA Protein Assay Kit (Takara, Cat.#T9300A, Japan) as per the manufacturer instructions. Briefly, 210 microtissues were lysed in 500 µL of RIPA lysis buffer (Origin, Cat.#PB103-01, India). Serial dilutions of Bovine Serum Albumin standard were prepared in the lysis buffer. The standard dilutions and tissue lysate were transferred to a 96-well plate, and an equal volume of BCA working solution was added to each well. The content was mixed thoroughly by shaking at 500 rpm for 5 min using a microplate orbital shaker (MixMate 5353, Eppendrof, Germany), followed by incubation at 37 ºC for 1

h. The optical density of the solution was quantified by measuring absorbance at 562 nm using a microplate spectrophotometer (Power Wave HT, BioTek, USA). The concentration of protein in tissue lysate was estimated using the linear regression equation obtained from the standard curve.

3.5.8 Glucose uptake by LPMTs

Insulin-stimulated glucose uptake by LPMTs was monitored using fluorescent-tagged 2-deoxy-glucose analog, (2-deoxy-2-[(7-nitro-2,1,3-benzoxadiazol-4-yl) amino]-D- glucose) (2NDBG, Abcam, Cat.#146200, USA). Around, 210 microtissues (n=3) were collected and pelleted by centrifugation at 11 g for 30 s. The pellet was rinsed with PBS before resuspending in glucose-free DMEM (100 µL) (Himedia, Cat.#AT186, India). The microtissue suspension was transferred to a clear-bottom black 96-well microplate (Thermo Scientific Cat.#10281092, USA) and was incubated for 2 h at 37 ºC for glucose starvation. The microtissues were then treated with either zero or 32 IU/mL insulin (Huminsulin® R, Cat.#HI0240, Eli Lilly Company, India) in DMEM containing 2-NBD-Glucose probe (200 µg/mL) for 2 h at 37 ºC. The microtissues were washed twice with PBS with intermediate centrifugation at 500 rpm using a microplate centrifuge (Universal 32 R, Hettich, Germany). Microtissues were there suspended in PBS (100 µL), and fluorescence intensity was measured using a Multimode microplate reader (BioTek® Synergy H1, USA,) at an Ex/Em wavelength of 485/535 nm respectively. The concentration of glucose uptake by LPMTs was calculated using the linear regression equation obtained from the standard curve for 2-NBD-Glucose. The obtained values were normalized to the total protein content of spheroids before plotting.

3.5.9 Histological evaluation of LPMTs

LPMTs after seven days of culture were collected into a centrifuge tube and was centrifuged at 11 g for 30 s. The spent media was replaced with 2 % agarose solution prewarmed to 37 ºC. The suspension was transferred to a 96-well plate and allowed to cool to room temperature for gelation. The agarose embedded microtissues were then fixed in 10% neutral buffered formalin for 24 h. The sample was dehydrated using increasing concentrations of isopropanol (50 %, 70 %, 80 %, 90 % & 100 % v/v) for 10 min each followed by two-step clearing in xylene for 10 min and was embedded in paraffin wax at 56 ºC. Thin sections (5 µm) of embedded sample were cut using a microtome (Leica RM2245, Switzerland) and was mounted on charged glass slides. The sections were stained with hematoxylin and eosin stain. The stained sections were observed under the bright-field mode of a light microscope (Eclipse TS100, Nikon, Japan), and digital images were captured (Digital Sight camera # DS-Fi2, Nikon).

3.5.10 Immunofluorescence staining of LPMTs

Immunofluorescence staining was performed on paraffin sections of microtissues prepared as described in section 3.5.9. The sections were dewaxed at 60 ºC for 1 h and was cooled to room temperature. The sections were cleared by two xylene washes for 5 min and then rehydrated using decreasing concentrations of isopropanol (90% and 75% v/v) for 5 min and tap water for 3 min. Antigen retrieval of the section was performed at 60ºC in sodium citrate buffer (pH=6) for 20 min. The sections were permeabilized in 0.025% Triton X-100 for 10 min and was blocked using 1 % (w/v) BSA in tris-buffered saline (TBS) for 30 min. The sections were incubated with primary antibodies against Multidrug Resistance Protein 2 (MRP2)

(Abcam, Cat.#ab15603, 1:20 dilution) and Zonula Occludens 1 (ZO1) (Abcam, Cat.#ab214228, 1:250 dilution) overnight at 4 ºC. The sections were then washed twice with TBS and were incubated with secondary antibody tagged with the fluorescent probe Alexa 488 (Goat polyclonal antibody to rabbit IgG, Abcam, Cat.#ab150077 & Goat polyclonal antibody to mouse IgG, Abcam, Cat.#ab150113, 1:500 dilution). The cell nucleus was counterstained with propidium iodide, and sections were mounted using PBS: glycerol (1:1) solution. The samples were then observed under differential interference contrast mode, and fluorescence images were captured using a confocal laser scanning microscope (A1R si, Nikon, Japan).

3.5.11 Evaluation of GelMA using LPMTs

The influence of gelatin methacrylamide microenvironment on the structure and function of LPMTs was evaluated using a hydrogel sandwich culture model. The microtissues cultured in suspension were used as a control for studying the effects of GelMA on LPMTs.

3.5.11.1 *Preparation of GelMA and alginate sandwich culture*

The LPMTs were sandwiched between two layers of GelMA hydrogel (Figure 1). The GelMA polymer solution was prepared in serum-free MEM containing 10 % (w/v) GelMA and 1% (w/v) Irgacure-2959 (2-Hydroxy-4'-(2-hydroxyethoxy)-2-methylpropiophenone) (Merck-Sigma, Germany) as photoinitiator. The first layer of GelMA hydrogel was prepared by pouring 100 µL of the solution into a cylindrical gel casting tool (5 mm diameter) and was crosslinked with UV light of 365 nm for 5 min. A cylindrical well-shaped hydrogel was obtained. The hydrogel was then placed inside a 12-well plate, and approximately 200 spheroids (n = 3) were carefully transferred over the hydrogel. The plate was incubated inside a CO_2 incubator for 30 min allowing the microtissues to settle on the hydrogel. The second layer of GelMA solution (25 µL) was poured on the microtissues and crosslinked as mentioned above. One milliliter culture medium was added to each well containing the hydrogel sandwich, and the plate was incubated at 37ºC inside the humidified incubator with 5 % CO_2 for 15 days.

GelMA sandwich-cultured LPMTs (GelMA sw-LPMTs) and Alginate sandwich-cultured LPMTs (Alginate sw-LPMTs) were compared to examine how GelMA improved the tissue-specific functionalities of LPMTs. A 5% (w/v) GelMA hydrogel sandwich was made for comparison using the same procedure as described above. The sodium alginate powder (Merck-Sigma, Cat.#A2033, Germany) was first sterilized by exposing it to UV light for 30 min within a biosafety cabinet, and then it was pasteurized for 30 minutes at 60° C. Alginate was dissolved in serum free MEM to prepare a 5% (w/v) solution. In a cylindrical mold, the first layer of alginate hydrogel was prepared by crosslinking with a 20 mM calcium chloride solution for 10 min. About 200 LPMTs (n = 3) were carefully transferred over the hydrogel layer and the second layer of alginate solution was added on settled LPMTs. The second layer of alginate was crosslinked to form the hydrogel sandwich and 1 ml culture medium was added to each well. The sandwich culture was incubated at 37ºC inside the humidified incubator with 5% CO2 for 15 days.

3.5.11.2 *Functional analysis of LPMTs in GelMA sandwich culture*

Spent media from the LPMT suspension and sandwich culture were collected from triplicate samples at 48 h intervals for 15 days and stored at -80 ºC. The albumin and urea secreted by microtissues were estimated using Human Albumin ELISA kit (Bethyl Laboratories Inc., Cat.#E88-129, USA) and Urea assay kit (Biochain, Cat.#Z5030016, USA), respectively as per the manufacturer's protocol. The absorbance values were measured using a microplate spectrophotometer (BioTek® Model#, USA). The albumin and urea values estimated from the assay were normalized to the total protein content of LPMTs.

Cytochrome P450 3A4 (CYP3A4) enzyme activity in LPMTs was determined using P450-Glo™ CYP3A4 assay kit (Promega, Cat.#V9001, USA) as per manufacturers protocol. Briefly, microtissues from 210 droplets (n=3) were seeded into each well of a white opaque 96-well microplate. The microtissues were then incubated in 150 µL of luciferin-IPA substrate solution and incubated for 1 h at 37 ºC. The substrate solution was then replaced with 50 µL of luciferin detection reagent, and the plate was incubated at room temperature for 20 min. The luminescence intensity was measured using a multimode plate reader (Plate Chameleon V, Hidex Model#425-106, Finland). For sandwich-cultured LPMTs, to retrieve the microtissues, GelMA sw-LPMTs were treated with collagenase A enzyme (Cat.#10103586001, Merck-Sigma,) at a final concentration of 1mg/mL for 20 min and Alginate sw-LPMTs were treated with alginate dissolution solution (0.03M EDTA, 0.055 M sodium citrate and 0.15 M sodium chloride in water, pH 7) for 1 min. The microtissues were then separated by centrifugation at 11 g for 30 s and were seeded into the microplate for assay.

3.6 GelMA bioink formulation and rheological analysis

The bioink formulation was comprised of 7 % (w/v) GelMA, 3 % (w/v) gelatin and 1 % (w/v) Irgacure. To prepare 3 mL of the bioink 0.21 g of GelMA and 0.09 g of gelatin was initially dissolved in 2.4 mL serum-free medium by incubating at 37 °C. A photoinitiator stock solution containing 5 % (w/v) Irgacure was prepared in PBS by heating at 80 °C. About 0.6 mL of stock solution was added to the polymer solution and was mixed thoroughly by continuous pipetting. The bioink was incubated at 37 °C before analysis.

The rheological analysis of the polymer solution was performed using a rheometer (Physica MCR 301, Anton Paar, Germany) with cone-plate measuring geometry. All the analysis were performed using a 1°cone plate having 20 mm diameter and at a measuring distance of 0.5 mm.

3.6.1 Temperature sweep analysis

The temperature dependent sol-gel transition of GelMA bioink was analyzed by temperature sweep test in rotational mode. About 0.4 mL of the bioink was dispensed between the measuring plates and the temperature of the sample stage was decreased gradually from 30°C to 10°C at a cooling rate of 1°C/min. The viscosity of the solution was measured as a function of temperature. The precise gelation temperature was determined from the first derivative of the log viscosity curve by peak fitting using GuassAmp function in OriginPro software (Version 8.5, USA).

3.6.2 Dynamic viscosity analysis

The test for dynamic viscosity analysis was performed in rotational mode. About 0.4 mL of the GelMA bioink was dispensed beneath the measuring plate to cover the entire plate surface. A dynamic shear rate ranging from 0.1 to 1000 s^{-1} was applied for the analysis and the viscosity of the solution was determined at 19°C as a function of shear rate and shear stress. The changes in viscosity with respect to shear rate was analyzed to assess the shear thinning property of the polymer solution.

3.6.3 Amplitude sweep analysis

The amplitude sweep or strain sweep analysis of GelMA bioink was performed in oscillatory mode. About 0.4 mL of the bioink was dispensed between the cone plate and sample stage maintained at 19°C. A dynamic shear stress ranging from 0.01 to 1000 Pa (0.1-1000 % strain) was applied to the bioink by oscillating the cone plate at a constant angular frequency of 10 Hz. The dynamic shear storage modulus and loss modulus of the bioink was then measured and plotted on a graph as a function of percentage shear strain to obtain the strain-sweep curve. The linear viscoelastic region (LVER), the limit of LVER and the flow point of the bioink was determined from the strain-sweep curve.

3.6.4 Frequency sweep analysis

The frequency sweep analysis of GelMA bioink was performed in oscillatory mode. About 0.4 mL of the bioink was dispensed between the cone plate and sample stage maintained at 19°C. The cone plate was then oscillated at a dynamic angular frequency ranging from 0.1 to 100 rad/s by applying 10 % shear strain. The dynamic shear storage modulus and loss modulus of the bioink was then measured and plotted on a graph as a function of angular frequency to obtain the frequency-sweep curve.

3.6.5 UV curing analysis

The UV curing analysis was performed at 19 °C in the oscillatory mode at a constant frequency (10 Hz) and strain (1%). UV light source Omnicure 1000 (Lumen Dynamix LDGI) of wavelength 365 nm was routed through a 5 mm optical fiber to illuminate the sample through a quartz crystal stage. The changes in complex viscosity and storage modulus were monitored with respect to time of UV exposure.

3.7 Printability assessment of GelMA bioink formulation

The printability of GelMA bioink for extrusion-based bioprinting was assessed in three levels. In level 1 the extrudability of the bioink was evaluated. Level 2 comprised of single layer printing followed by assessing the shape fidelity of the printed filament. In level 3 multilayer structures were printed and the structural fidelity of the filament as well as the whole construct was assessed. All printability assessments were carried out after setting the room temperature at 19°C.

3.7.1 Level 1: Extrudability

The extrudability of GelMA bioink was assessed by filament drop test. Freshly prepared bioink solution was filled in a 3ml cartridge and was kept either at 25 °C or 18 °C for 5 min to undergo thermal gelation. A conical shaped printing nozzle having an inner diameter of 840 μm was connected to the cartridge. The cartridge was then loaded on the extrusion head of the 3D bioprinter (3D Discovery, RegenHU, Switzerland) and the bioink was extruded by applying increasing pneumatic pressure until continuous flow of bioink was achieved. Digital images of the extruded bioink at the nozzle tip was captured for assessment.

3.7.2 Level 2: Line printing and filament characterization

The path design for line printing was created using BioCAD software (RegenHU, Switzerland). The bioink was then printed in a polystyrene dish according to the design using the extrusion head of the 3D bioprinter at a nozzle height of 0.5 mm. The digital images and microscopic images of the printed structure were captured using a USB microscope camera (Dino-Lite) and a stereo microscope (Leica S8 Apo, Switzerland) respectively. All the measurements related to the analysis of the printed structure were   manually using ImageJ software.

Initially line printing was performed at four different print speed (10, 12, 14 and 16 mm/s) by applying two different extrusion pressure (33 kPa and 37 kPa). To analyze filament spreading, filament width was measured (n=18) and it was normalized to nozzle diameter to determine filament spreading ratio as reported by Daly *et al.*(Daly *et al.*, 2016) The uniformity of the printed filament was then evaluated (n=18) by determining the ratio between the perimeter and length of filament as reported by Gao *et al.*(Gao *et al.*, 2018) Thereafter, the versatility of the bioink for printing different shapes across various angles was assessed by angular pattern printing using optimal printing parameters. The line patterns consisted of square (angle at vertex: 90°), triangle (45°), circle (180°) and a zig-zag line. Finally, filament collapse test was done to analyze the mechanical stability of the printed filament while spanning over a large gap between underlying supporting structures. For the test, the bioink was printed as lines at a print speed of 18 mm/s and a pressure of 33 kPa, over a custom-made platform with vertical pillars positioned at various distances (1, 2, 3, 4 and 5 mm) from each other. The printed filament (n=3) was then closely observed for signs of collapse between the pillars. The collapse area factor (Cf), that is, the percentage of actual area under the suspended filament between pillars with respect to the theoretical area was determined using equation 7 as reported by Habib *et al* .(Habib *et al.*, 2018)

$$\text{Collapse area factor (Cf)} = \frac{\text{A}_\text{a}}{\text{A}_\text{t}} \times 100\% \text{ .... Equation 7}$$

Where A_a is the actual area under the suspended filament and A_t is the theoretical area when there is no deflection of suspended filament.

3.7.3 Level:3 Multilayer printing and shape fidelity of printed construct

For multilayer printing a CAD design consisting of a square construct with length and breadth 10 mm and having a rectilinear grid as in-fill pattern was created in BioCAD software. Construct with multiple layers (2, 4 and 6) were designed and printed with an inter-filament spacing of 1.5 mm following the optimal printing parameters. Subsequently, the dimensions of the construct were measured and compared to the CAD model. Digital images of the constructs were then captured to assess the shape. Further, the printability factor of the bioink was then calculated from the perimeter and area of the inter-filament pore formed within the printed construct using equation 8 as reported by Ouyang *et al.,* (Ouyang *et al.*, 2016).

$$\text{Printability factor (Pr)} = \frac{\text{L}^2}{16\text{ A}} \text{ ....Equation 8}$$

Where L is the perimeter and A is the area of the pore.

3.8 NGMA Synthesis

The copolymer poly (N-isopropylacrylamide-co-glycidyl methacrylate) (NGMA) was synthesized by free-radical copolymerization of N-isopropylacrylamide (NIPAAm) (Merck-Sigma, Germany) and glycidyl methacrylate (GMA) (Merck-Sigma, Germany) at a ratio 10:1 according to the procedure reported by Joseph et al. (Joseph, Prasad and Joseph Sreenivasan K., 2011). Briefly; a water bath was set at 60°C on a hot plate magnetic stirrer inside a fume hood. A 250 mL three-neck round bottom flask containing a magnetic stirrer bar was kept in a water bath to a level of half its volume and the center neck was connected to a water condenser. Nitrogen gas was passed through one of the side-neck. Through the other free neck, 20 ml of methanol was transferred into the flask. About four grams of NIPAAm and 400 µL of GMA were sequentially added into the flask while stirring. The free-radical polymerization reaction was initiated by adding 100 mg of Azo-iso-butyronitrile (AIBN) (Spectrochem, India) into the flask and all the openings of the flask were closed. The reaction mixture was stirred continuously at 100 rpm for six hours until a viscous copolymer solution was formed. The product was transferred to a glass beaker and precipitated by adding excess ice-cold distilled water. The water was decanted, and the precipitate was dissolved in 10 ml of tetrahydrofuran (THF) (Merck, USA) by stirring using a glass rod. The above two steps were repeated twice to ensure the complete removal of unreacted monomers and initiators. Finally, the precipitated copolymer was transferred to a Teflon sheet and was dried overnight inside a hot air oven set at 50 °C. The percentage yield of the synthesis was calculated from the weight of the monomer used and the copolymer formed as per the equation given below.

$$\text{Percentage yield} = \frac{\text{Weight of NGMA}}{\text{Weight of NIPAAm} + \text{Weight of GMA}} \times 100 \text{ ....Equation 9}$$

3.9 Physico-chemical characterization of NGMA

3.9.1 Attenuated Total Reflectance-Fourier Transform Infrared Spectroscopy

The functional groups in the copolymer corresponding to the NIPAAm and GMA moieties were identified by Fourier Transform Infrared (FTIR) spectroscopy. Briefly, 40 mg of the NGMA was dissolved in 1ml of isopropanol (Merck, USA). The solution was coated on a teflon mold, dried in an oven at 55 °C, and a thin film was peeled out. An attenuated total reflectance (ATR)-FTIR spectrometer (Thermo Nicolet 5700, Thermo Electron Scientific Instruments Corp., USA) was used to record the spectra of the film in the wavelength region from 400 $cm^{-1}$to 4000 cm^{-1} for 50 scans.

3.9.2 ^{1}H Nuclear Magnetic Resonance Spectroscopy

The copolymerization of the NIPAAm and GMA was evaluated by ^{1}H nuclear magnetic resonance spectroscopy. About six milligrams of the copolymer was dissolved in 1mL of deuterated chloroform ($CDCl_3$) (Merck, USA). The solution was then transferred into an NMR tube and was placed inside a Fourier Transform-NMR spectrometer (Bruker, Avance 400, USA). The ^{1}H NMR spectrum was recorded at 400 MHz using tetramethylsilane internal standard. The recorded spectrum was analyzed using TopSpin® software (Bruker, USA).

3.9.3 Differential Scanning Calorimetry

The LCST of NGMA was determined from the thermogram obtained using a differential scanning calorimeter (DSC Q20 V24.4, TA Instruments Inc, USA). About

10 mg of the copolymer was immersed in deionized water and allowed to swell for an hour. The swollen sample was kept inside a sealed hermetic pan, and thermal analysis was performed from -10 °C to +55 °C at a heating rate of 10 °C/min in a nitrogen atmosphere.

3.9.4 Gel Permeation Chromatography

The average molecular weight of the copolymer was determined by gel permeation chromatography. A high-performance liquid chromatography (HPLC) (Waters Inc. Milford, USA) system consisting of 600 series pump, 2414 refractive index detector and 7725 Rheodyne injector was used to estimate the molecular weight from 1% (w/v) copolymer solution in THF. The μ-styragel columns (HR5E/4E/2/0.5, Waters Inc. Milford, USA), connected in series in conjunction with THF at a flow rate of 1 mL/min were used for the separation. Polystyrene standards of molecular weight 250,000/34,300/1470/162 were used for calibration.

3.10 Coating NGMA on cell culture dish

A homogenous solution of 0.4% (w/v) NGMA was prepared in isopropanol (Merck Millipore, Germany). The solution was hand coated on a polystyrene tissue culture (PSTC) dish at room temperature (25°C). Briefly, NGMA solution was evenly spread on PSTC dishes. About 0.5 mL and 1mL of solution was used for hand-coating a 35 mm and a 60 mm dish, respectively. The dish was tilted to allow the solution to flow down and the excess solution was removed. The dishes were dried overnight inside a hot air oven set at 55 °C. The dishes coated with NGMA will be referred as NGMA dish hereafter.

3.11 Water contact angle of NGMA dish

The thermoresponsiveness of NGMA-coated surface was evaluated by measuring the water contact angle of the sessile drop at temperatures below and above LCST. The coated dishes were incubated at two different temperatures (37 ºC & 4 ºC) for 5 min and a water droplet was dispensed over the preincubated dish. Digital images of the sessile drop were immediately captured using an optical contact angle goniometer (OCA 15 PLUS, DataPhysics Instruments, Germany). The water contact angle was then measured using the SCA 20 software module. Contact angle measurements on PSTC were taken as control. Triplicate images were analyzed to measure the water contact angle for each group.

3.12 In-vitro cytotoxicity evaluation of NGMA

The cytotoxic effect of NGMA dish was tested using L-929 cells. The cells were cultured in Minimum Essential Medium (MEM, Merck-Sigma, Cat.# M0769, Germany) with 5 % Foetal Bovine Serum (FBS, Gibco, Cat.#10270106, USA) and 0.1% Penicillin-Streptomycin antibiotic (Pen-Strep, Cat.#15070-063, USA) at 37 ºC, 5 % CO_2 and >90 % relative humidity.

3.12.1 Cell adhesion and viability

The cell adhesion and viability on NGMA dish was evaluated using L929 cells. Cells were seeded at a density of 1×10^4 cells/cm^2 on NGMA dish and was incubated at 37 ºC inside a CO_2 incubator for 48 h. The cell adhesion was then examined by checking the morphology of the cells under an inverted light microscope (Nikon Eclipse TS2, Japan).

The viability of cells adhered to the NGMA dish was assessed by neutral red staining. The medium from the cells was replaced with 0.5 % (w/v) neutral red stain prepared in 0.8 % (w/v) sodium chloride solution. Th cells were incubated at 37 ºC, 5 % CO_2 for 30 min. The uptake of neutral red by the viable cells was examined under a microscope in bright-field mode.

3.12.2 Cell proliferation

The proliferation of cells on NGMA dish was determined from the metabolic activity of L929 cells by MTT assay. L-929 cells were seeded on NGMA dish and PSTC dish at a cell density of 1×10^4cells/cm^2. The assay was performed on cells cultured for 24 h and 72 h. Briefly, media was removed from the culture dish and was replaced with MTT solution (1mg/ml in serum free MEM). The culture dishes were incubated at 37 ºC inside CO_2 incubator for two hours. The formazan crystal formed were solubilized in isopropanol and transferred to a 96-well plate. Absorbance was read at 570 nm using a spectrophotometer (Biotek, Powerwave XS, USA). The data was represented as mean± standard deviation.

3.13 Isolation of parenchymal and non-parenchymal cells from rat liver

Hepatocytes and the non-parenchymal cell (NPC) fraction containing sinusoidal endothelial cells, kupffer cells and stellate cells were isolated from male Wistar rat (150-200 g) by a modified two-step perfusion method (Palakkan, P.R. and V, 2013). Prior approval (SCT/ABS/IAEC-107/16, 02-12-2020) was obtained from the Institutional Animal Ethics Committee for isolating the primary cells. Briefly, rats were anaesthetized by intramuscular administration of ketamine (10 mg/100 g body weight) and xylazine (1 mg/100g body weight). Heparin (0.25 mL/100 g body weight) was injected intraperitoneally to prevent blood clotting. The fur of the rat was thoroughly wiped with 70% ethanol, and the rat was placed on a bed inside a biosafety cabinet (ESCO, Labculture Type A2, Singapore). Laparotomy was performed, and the portal vein was cannulated with a 20-gauge blunt cannula connected to a perfusion system set at 37 °C. The liver was perfused with oxygenated calcium-free perfusion buffer at a 20 ml/min flow rate for 15 min. Perfusion was immediately switched without delay to calcium-containing perfusion buffer having 0.5 mg/mL Collagenase Type IV (Merck-Sigma, cat#.C4-BIOC, Germany), and the perfusion was continued for 10 min at a flow rate of 30 ml/min with continuous oxygenation. Immediately after canulation, the rat was euthanized by overdose of sodium thiopentone (25 mg/ml). The liver was excised from the carcass and transferred to a sterile petri dish containing cold (4 – 8 °C) serum-free Iscove's Modified Dulbecco's Medium (IMDM, Merck-Sigma, cat#.56479C, Germany) containing 100 µg/ml Penicillin and 100 IU/ml streptomycin. The Glisson's capsule was gently peeled off, and the liver cells were dislodged into the medium taken in 150 mm sterile Petri dish by gentle shaking. Released cells were passed through a sterile nylon mesh (70 µm) to remove tissue fragments and cell clumps. Cell suspension was incubated at 37 ºC inside a CO_2 incubator for 30 min. The cell suspension was then transferred to 50 ml centrifuge tubes and was immediately kept on an ice bath for 10 min.

Hepatocytes were separated by centrifuging the cell suspension at 50 g for 2 min at 4 ºC. The supernatant containing NPCs was collected and the hepatocyte pellet was washed twice in IMDM by centrifugation at 20 g, 4 ºC for 2 min. Cell viability was analyzed by trypan blue exclusion method and cells with greater than 85% viability were used for the experiments.

The NPC fraction collected during the hepatocyte separation was centrifuged at 350 g, for 3 min at 4 ºC. The supernatant was discarded, and the cell pellet was resuspended in fresh IMDM. Cell viability was estimated by trypan blue staining and appropriate number of cells were used for the experiments.

3.14 Culture of liver parenchymal and non-parenchymal cells

Freshly isolated hepatocytes and the non-parenchymal cell fraction were cultured on collagen-coated dishes. About 0.5 mL of alkali-neutralized type 1 bovine collagen solution (PureCol, Advanced BioMatrix, Germany) was hand-coated on a 35 mm cell culture dish, the excess solution was aspirated, and the dish was allowed to dry inside CO_2 incubator. The hepatocytes and NPC fraction were then seeded separately on collagen-coated dishes (35 mm) at a cell density of 5×10^5 cells/dish. The cells were cultured in IMDM containing 100 μg/ml Penicillin, 100 IU/mL streptomycin and 2% FBS (IMDM complete medium) at 37 ºC inside a CO_2 incubator. The hepatocyte and the non-parenchymal cells (Sinusoidal endothelial cell, Kupffer cell and Stellate cell) were observed under a phase-contrast microscope after 48 h to analyze their characteristic cell morphology.

3.15 Characterization of liver parenchymal and non-parenchymal cells

The hepatocytes and the non-parenchymal cells were characterized by immunofluorescence staining of cell-specific markers. Freshly isolated hepatocytes and NPCs were seeded on a sterile cover glass coated with collagen at a cell density of 1×10^3 cells/cm^2. The cells were then cultured in serum containing IMDM for 72h at 37 ºC inside a CO_2 incubator. The cells were washed thrice with 0.1 M PBS with each wash lasting for 5 min. The staining procedure was done at room temperature unless specified. Cells were then fixed in 4% paraformaldehyde (PFA) in PBS for 15 min. The cells were again rinsed with PBS and permeabilized by incubating with 0.1% Triton X-100 for 5 min. The non-specific binding sites were blocked with freshly prepared 1% (w/v) Bovine Serum Albumin (BSA) in PBS for 30 min at room temperature. The cells were then incubated at 4 ºC overnight in respective primary antibodies diluted in blocking buffer. The hepatocytes were treated with Rabbit Anti-Albumin (1:500; Abcam, ab207327, USA), Sinusoidal endothelial cells with Rabbit Anti-CD32 (1:100; ImmunoTag, ITT0754, USA) and Kupffer cells with Rabbit Anti-CD163 (1:100; ImmunoTag, ITT08235, USA). The primary antibody solution was removed, and the cells were rinsed thrice with PBS for 5 min each. The cells were then incubated in secondary antibody solution, Goat Anti-rabbit IgG tagged with Alexa Fluor 488 (Abcam, ab150077, USA) at a dilution of 1:500 in blocking buffer for one hour in dark at room temperature. After removing the secondary antibody, the cells were rinsed thrice with PBS. All samples were then counterstained with Hoechst 33258 (5 µg/mL in Hanks Balanced Salt Solution) for 1 min. The cells were given a final rinse with PBS and the cover glass was mounted on glass micro slides using an anti-fade medium (Dako, cat# CS703, USA). Cells were observed under a fluorescence microscope (Leica, DMI6000B, Switzerland) and images were captured using DML monochrome camera (Leica, DMC5400, Switzerland) and Leica Application Suite software (LAS V3.7).

The stellate cells exhibit fibroblast cell morphology and therefore, the cells were identified by F-actin cytoskeletal staining. The cells were washed thrice with 0.1 M PBS for 5 min each. Cells were then fixed in 4% paraformaldehyde (PFA) in PBS for 15 min. The cells were again rinsed with PBS and permeabilized by incubating with 0.1% Triton X-100 for 5 min. The cells were again rinsed with PBS and were incubated in Rhodamine Phalloidin stain (ThermoFisher Scientific, R415, USA) 1:200 diluted in PBS, for 20 min. The cells were rinsed thrice with PBS and were counterstained using Hoechst 33258 (5µg/mL in Hanks Balanced Salt Solution) for 1 min. The cells were given a final rinse with PBS and the cover glass was mounted on glass micro slides using an anti-fade medium (Dako, cat# CS703, USA). Cells were observed under a fluorescence microscope and images were captured.

3.16 Development of hepatic organoid on NGMA dish

The method for the development of hepatic organoids on NGMA dish was optimized after testing different strategies. The adhesion of cells on NGMA substrate and the swift retrieval of organoids from the dish by lowering the temperature was the critical steps during the process.

3.16.1 Strategy 1: Hepatocyte and NPC co-culture in NGMA dish

The first strategy to develop hepatic organoids was based on the co-culture of hepatocytes and NPCs in NGMA dish. Sterile NGMA dishes (35 mm) were rinsed with PBS. Freshly isolated rat hepatocyte and NPCs were seeded at a cell density of 7×10^5 cells/ dish and 3×10^5 cells/ dish, respectively. The cells were then co-cultured at 37 °C in IMDM complete medium for 5 days.

3.16.2 Strategy 2: Hepatocyte and NPC co-culture over MSC feeder layer in NGMA-coated dish

The second strategy was devised to improve adhesion of hepatocytes and NPCs on thermoresponsive dish. A mesenchymal stem cell feeder layer was opted to improve the cell adhesion. To prepare the feeder layer, mesenchymal stem cells from rat bone marrow were isolated and characterized for their stemness.

3.16.2.1 *Isolation and culture of mesenchymal stem cells from rat bone marrow*

Mesenchymal stem cells (MSCs) were isolated from the bone marrow of an eight-week-old male Wistar rat, after obtaining prior approval (SCT/ABS/IAEC-109/03) from the Institutional Animal Ethics Committee. The rat was euthanized, and the entire skin was thoroughly wiped with 70 % ethanol. The femur bones were exposed by incision on the skin and muscle tissue. The bones were aseptically dissected, and the unwanted soft tissues were removed. The bones were thoroughly washed with sterile 0.1 M phosphate buffered saline (PBS) containing 1 % Penicillin-Streptomycin antibiotic (Gibco, USA) and were cut below the epiphysis at both the ends. Sterile PBS was flushed through the bone cavity using a syringe connected to a 23-gauge blunt end needle and the contents were collected in a centrifuge tube. The tube was centrifuged at 650 g for 15 min and the pellet was then resuspended in α-MEM medium (Gibco, USA) supplemented with 10% FBS (Gibco, USA) and 1 % antibiotic (Gibco, USA). The cell suspension was filtered using a cell strainer (pore size 70 µm, Himedia) and were seeded into a tissue culture flask. The cells were then incubated at 37 ºC inside a CO_2 incubator. After 72 h, the media was replaced, and cells were cultured until subconfluency. The cells were subcultured using trypsin+ 0.25 % EDTA (Gibco, USA) at subconfluency.

3.16.2.2 *Characterization of Mesenchymal Stem Cells*

The MSCs were characterized for their stemness and lineage plasticity by immunofluorescence staining of stem cell markers and by differentiation into osteogenic cell lineage, respectively.

3.16.2.2.1 Expression of MSC markers- Immunostaining

The stemness and mesenchymal origin of the isolated MSCs was confirmed by immunofluorescence staining of the cell surface markers CD 90 and CD 34. The MSC suspension obtained from third passage were seeded on a cover glass (HiMedia, Cat.#TCP017, India) and were cultured for 48 h. The cells were washed thrice with 0.1 M PBS with each wash lasting for 5 min. The staining procedure was done at room temperature unless specified. Cells were then fixed in 4 % paraformaldehyde (PFA) in PBS for 15 min. The cells were again rinsed with PBS and permeabilized by incubating with 0.1% Triton X-100 for 5 min. The non-specific binding sites were blocked with freshly prepared 1 % (w/v) Bovine Serum Albumin (BSA) in PBS for 30 min at room temperature. The cells were then incubated in primary antibody solution (1:100) against respective CD markers for one hour. Primary antibodies used were Mouse Anti-CD 90/ Thy1- FITC (Abcam, ab226, USA), Mouse Anti-CD34 (Santa Cruz Biotechnology, sc-65261, USA) and Rat Anti-CD73 (Invitrogen, PA5-81614, USA). Primary antibody was removed and was rinsed thrice with PBS. The samples treated with anti- CD34 and anti-CD73 antibodies were incubated in respective secondary antibody solutions such containing Goat Anti-mouse IgG and

Goat Anti-rat IgG tagged with Alexa Fluor 488 at a dilution of 1:500 in PBS for one hour. The sample incubated with anti-CD90 antibody was kept in PBS since the primary antibody was FITC conjugated. After removing secondary antibody, all samples were incubated with Hoechst 33258 (5 µg/mL in Hanks Balanced Salt Solution) for 1 min to counter stain the nucleus of the cells. The cells were given a final rinse with PBS and the coverslips were mounted on glass microslides using an anti-fade medium (Dako, cat# CS703, USA). Cells were observed under a fluorescence microscope (Leica, DMI6000B, Switzerland) and images were captured using DML monochrome camera (Leica, DMC5400, Switzerland) and Leica Application Suite software (LAS V3.7).

3.16.2.2.2 Osteogenic lineage differentiation

The potency of MSCs to differentiate into osteocyte was evaluated. The MSC suspension obtained from third passage were seeded into three 12-well plates with a density of 5000 cells/ cm^2. The cells were cultured in alpha-MEM containing 10 % FBS for two days. After two days the spent media was replaced with osteocyte differentiation media (HiOsteoXL, cat#.AL522, Himedia, India) containing 1% Penicillin-Streptomycin antibiotic and 10 % FBS. The cells cultured in expansion media was used as a negative control. The culture was continued for 21 days with media replenishment after every two days. Each well-plate was taken on days 7, 14 and 21, and the cells were fixed in 4 % PFA. The fixed cells were then stained using Alizarin Red S stain (cat# TC255, Himedia, India) according to the manufacturer's instructions.

3.16.2.3 *Hepatic organoid development on MSC feeder layer*

After the characterization of MSCs, the cells were utilized for developing the feeder layer. Sterile NGMA dishes (60mm) were rinsed with PBS. Rat bone marrow mesenchymal stem cells from passage 2 to 5 were seeded in the dish at a density of 6×10^5 cells/ dish. The cells were cultured in α-MEM medium supplemented with 10% FBS and 1% antibiotic for seven days to form a monolayer. The culture medium was changed after every three days.

Freshly isolated rat hepatocytes and NPCs were suspended in IMDM medium containing 2% serum, 1% antibiotic, 20 ng/mL hepatocyte growth factor (HGF, Himedia, CF032, India) and 10 ng/mL epidermal growth factor (EGF, Himedia, CF023, India) at a cell density of 6.6×10^6 cells/ mL and $2.6\ \times10^6$ cells/ mL, respectively. The MSC culture medium was removed from the NGMA dish and about 3 mL of the liver cell suspension was seed over the MSC feeder layer. The cells were co-cultured for four days at 37 ºC inside a CO_2 incubator to form organoids. The self-organization of cells was closely observed on each day using a phase-contrast microscope and representative images showing the cellular assembly during organoid formation was captured. After four days of co-culture, the hepatic organoids formed on the NGMA dish were retrieved. The NGMA dish containing organoids were kept at 4 ºC for 10 min. The organoids were then gently flushed with ice-cold serum-free IMDM and the detached organoids were then collected in a centrifuge tube.

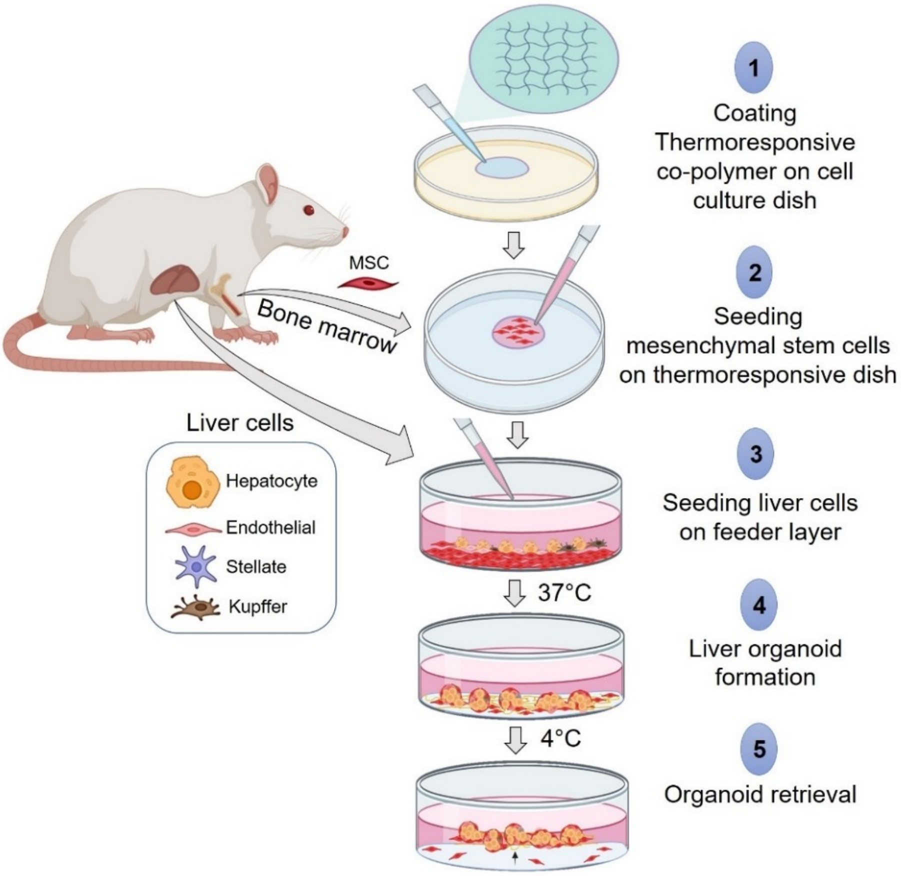

Figure 5. Illustration showing steps involved in rat hepatic organoid generation and retrieval from thermoresponsive dish.

3.17 Characterization of hepatic organoid

The structural and functional characteristics of hepatic organoids formed by co-culture of hepatocytes and NPCs on MSC feeder layer were analyzed during their culture in the NGMA dish for seven days.

3.17.1 Organoid size distribution

The size of rat hepatic organoids was determined on the third day after initiating the co-culture in NGMA dishes. Phase-contrast images of the hepatic organoids (n=20) were captured using a digital camera (VUE, Model# US300, China) connected to the light microscope (Nikon Eclipse TS2-FL, Japan). The feret diameter of the organoid was measured using ImageJ analysis software.

3.17.2 Cell viability

The cell viability of hepatic organoids was analyzed by quantifying the ATP content using the CellTiter-Glo® 3D cell viability assay kit (cat# G9681, Promega, USA). The organoids formed on NGMA-coated dishes (35 mm) were retrieved on days 3 and 7 after initiating co-culture. The organoids were resuspended in 100 µL of IMDM complete medium. The suspension was transferred to a white opaque 96-well microplate (Thermo Scientific, Cat.#9502887, USA) in triplicates. The plate was equilibrated to room temperature (25ºC) for 25 min, and an ATP assay reagent (100 µL) was added to each well. The plate was shaken vigorously on a microplate orbital shaker at 700 rpm for 10 min and was then incubated at room temperature for 20 min. The luminescence intensity was measured using a Multimode plate reader (Plate Chameleon V 425-106, Hidex, Finland). The unknown concentration of ATP in samples were calculated using the linear regression equation obtained from the ATP standard curve.

3.17.3 Multicellular distribution in organoids

The spatial distribution of multiple cell types within hepatic organoids was analyzed by labelling each cell type with different fluorescent dyes before initiating organoid culture. The MSCs were labelled after forming a monolayer in an NGMA dish. The spent media from the monolayer was removed and was rinsed with serum-free IMDM. A cell labelling solution containing DiD dye (Vybrant^{TM} Cell Labelling solution, Cat.# V22889, Invitrogen) was prepared by diluting 5 µL of the dye in one milliliter of serum-free media. The labelling solution was then added to the MSC monolayer culture and was incubated at 37 ºC for 20 min. The cells were then rinsed with warm (37 ºC) medium thrice for 10 min each. For labelling hepatocytes and NPCs, cells were individually suspended in a serum-free medium at a density of 6.6×10^6 cells/ mL and 2.6×10^6 cells/ mL respectively. The cell-labelling dyes, DiI and DiO were added to the hepatocyte and NPC suspension respectively, at a concentration of 5 µL per one million cells. The cells were then incubated at 37 ºC for 20 min and were centrifuged at 50×g, 2min (hepatocyte) and 350×g, 5 min (NPC) at 37 ºC. The supernatant was removed, and the cell pellet was washed twice with warm media. The cell pellet was then resuspended in 1.5 mL of organoid culture media. The cell suspensions were then mixed in a tube and were seeded over the labelled MSC monolayer. The cells were then co-cultured for 72 h to form organoids. The organoids were then retrieved from the dish and were transferred to a glass-bottom dish. Fluorescent Z-stack images of the labelled organoids were captured using laser-scanning confocal microscope (A1R si, Nikon, Japan) at the recommended excitation/emission wavelength specific to each dye (DiI- 549/565 nm, DiO- 484/501 nm & DiD- 644/665 nm).

3.17.4 Histological analysis

The histological analysis of hepatic organoids was performed according to the procedure reported by Fujii et al (2018) (E. Fujii et al., 2018). Hepatic organoids cultured for 7 days were retrieved and collected in a 15 mL centrifuge tube. The organoids were washed with PBS twice and were fixed in 4 % PFA for 30 min at 25 °C. The fixative was removed and the organoids were resuspended in warm 2 % (w/v) agarose solution. The suspension was allowed to form a gel at 4 °C and the hydrogel was transferred to a tissue cassette. The hydrogel was soaked in acetone stored at -20 °C for overnight and was again subjected to two changes of fresh acetone kept at 4 °C and 25 °C respectively for 15 min each. The hydrogel was then soaked in methyl benzoate and xylene for 30 min each at RT. The hydrogel was infiltrated with paraffin wax at 60 °C inside a vacuum oven (Sun Scientific, India) for 2 h and was embedded in fresh paraffin wax. Thin sections of the embedded sample having 10 μm thickness were cut using a microtome (Leica RM2245, Switzerland) and the sections were mounted on charged glass slides. The sections were stained with hematoxylin and eosin stain and mounted using DPX. The stained sections were observed under the bright-field mode of a light microscope (Eclipse TS100, Nikon, Japan), and digital images were captured (Digital Sight camera # DS-Fi2, Nikon).

3.17.5 Ultrastructural analysis -TEM

The ultrastructural features of hepatic organoids were visualized by transmission electron microscopy (TEM). Hepatic organoids retrieved from the NGMA dish were washed with 0.1 M PBS and fixed using 3% glutaraldehyde in phosphate buffer at 4°C for 24 h. The organoids were then washed with 0.1 M cold phosphate buffer (pH 7.4) and were incubated in 1 % osmium tetroxide at room temperature for 2 hours. The organoids were again washed and dehydrated in ascending grades of acetone (30%, 50%, 70%, 90%) for 15 min each and finally through three changes of 100% acetone for 30 min each. For resin infiltration the organoids were initially placed in propylene oxide (two changes for 5 min each) and were then transferred into propylene oxide-epoxy resin mixtures of ratio 3:1, 1:1 for 1 h each. The organoids were then kept overnight in propylene: epoxy resin mixture of ratio of 1:3 and final infiltration was carried out in pure resin prior to embedding. The samples were then embedded in molds containing the epoxy resin - Polybed 812 mixed with dodecenyl succinic anhydride (DDSA – Hardener), Nadic methyl anhydride (NMA -Hardener), Dimethylaminomethyl phenol (DMP - Accelerator) in appropriate ratios as per the kit instructions (Polysciences Inc., USA) and polymerized at 60°C in an oven for three days. For light microscopy semithin sections (~1µm) were cut using a glass knife in an ultramicrotome (Leica ultracut UCT). Once the area of interest was identified, the remaining areas of the block were trimmed off. Ultrathin sections (50-70 nm) were cut using a diamond knife (Diatome®) and collected onto the shiny side of the copper grids of 300 mesh size. Samples were then viewed in TEM (Hitachi H 7650, Japan) at 75-80 KV.

3.17.6 Immunofluorescence staining

The expression of protein markers specific to hepatocyte and NPCs in the hepatic organoids were analyzed by immunofluorescence staining. The hepatic organoids were washed with PBS (3 times) and were fixed in 4 % PFA for 45 min at 25 °C. The organoids were then permeabilized using in 0.1% Triton X-100 for 30 min. The non-specific binding sites were blocked with freshly prepared 1% (wt/v) Bovine Serum Albumin (BSA) in PBS for one hour at room temperature. The organoids were then incubated in respective primary antibodies, Rabbit Anti-Albumin (1:500; Abcam, ab207327, USA), Mouse anti-MRP2 (1:50; Abcam, ab15603, USA), Rabbit Anti-CD32 (1:100; ImmunoTag, ITT0754, USA), Rabbit Anti-CD163 (1:100; ImmunoTag, ITT08235, USA) diluted in blocking buffer at 4 ºC overnight. Subsequently, the organoids were washed with PBS (3 times) for 5 min and were incubated in respective secondary antibody solution, Goat Anti-rabbit IgG tagged with Alexa Fluor 488 (1:250; Abcam, ab150077, USA), Goat Anti-mouse IgG tagged with phycoerythrin (1:250; Abcam, ab74490, USA) for one hour at room temperature. The organoids were then washed with PBS and counterstained using DAPI (5µg/mL in PBS) for 10 min. The stained organoids were given a final wash with PBS and were mounted on a glass slide using an anti-fade medium (Dako, cat# CS703, USA). Images of the labelled organoids were captured using a fluorescence microscope (Leica, DMI6000B, Switzerland) and images were captured using DML monochrome camera (Leica, DMC5400, Switzerland) and Leica Application Suite software (LAS V3.7).

3.17.7 Evaluation of liver-specific functions

The liver-specific functions of rat hepatic organoids cultured in NGMA dishes were monitored for 7 days.

3.17.7.1 *Albumin synthesis*

Spent media from the organoid culture (n=3) were collected at 48 h intervals for 7 days and were stored at -80ºC. The secreted albumin in spent media was estimated using Rat Albumin ELISA kit (Bethyl Laboratories Inc., Cat.#E110-125, USA) as per the manufacturer's protocol. The absorbance values were measured using a microplate reader (PoweWave-XS, BioTek®, USA) and the concentration of albumin was estimated from the standard curve. The cumulative amount of albumin secreted every 48 h was presented as mean ± SD.

3.17.7.2 *Ammonia detoxification*

The ability of hepatic organoids to convert ammonia into urea was assessed by estimating the secreted urea after ammonium chloride treatment. About 10 mM ammonium chloride solution was prepared in serum-free IMDM. The organoids (n=3) were treated with ammonium chloride solution for 4 h on days 3 and 5 after initiating the culture. The organoids were then cultured in a serum-containing medium for 48 h and the spent media was collected. The spent media collected from the untreated groups were used as a control. The secreted urea in spent media was estimated using the Urea assay kit (Biochain, Cat.#Z5030016, USA), as per the manufacturer's protocol. The urea secreted by organoids was presented as mean ± SD.

3.17.7.3 *Biotransformation*

The biotransformation ability of hepatic organoids was analyzed by monitoring the ethoxy-resorufin-O-deethylase (EROD) activity of enzyme CYP1A1. A modified procedure based on an earlier report by Donato et al (1993) was followed.(Teresa Donato, José Gomez-Lechón and Castell, 1993) About 8 µM of the O^7-ethylresorufin (Merck-Sigma, cat#.E3763) solution was prepared in IMDM complete medium. The hepatic organoids were then incubated in the substrate solution for 4 h at 37 °C. The organoids were then retrieved from the dish and were collected in a centrifuge tube covered with aluminium foil. The organoids were then washed with warm PBS and were fixed in 4% PFA for 30 min at 25°C. The organoids were again washed with PBS twice and were transferred to a glass-bottom dish. The presence of resorufin within hepatic organoids was visualized using a confocal microscope in fluorescence mode at an excitation/emission wavelength of 535/590 nm and the Z-stack images of the organoids were captured.

3.18 Computer-Aided Designing of liver tissue Construct

A 3D design of the liver tissue construct was drawn using a freehand computer-aided designing software BioCAD (RegenHU, Switzerland). The design consisted of a 2-layered cuboidal structure with rectilinear infill pattern with 70 % infill density. The inter filament space was set as 1.2 mm to ensure sufficient mass transfer within the construct. The overall dimensions of the construct were 14×14×2 mm (length × breadth × height). A g-code was generated for the design using the same software.

3.19 Three-dimensional printing and characterization of hydrogel construct

A hydrogel construct was then fabricated by 3D printing according to the CAD design. Briefly, the GelMA-gelatin bioink was filled in a 3 mL cartridge and was incubated at 18 °C for 5 min to undergo thermal gelation. A conical printing nozzle having an inner diameter of 840 μm was connected to the cartridge and it was loaded on the extrusion head of the 3D bioprinter (3D Discovery, RegenHU, Switzerland). Multiple constructs of GelMA-gelatin hydrogel were printed by applying a pneumatic pressure of 33 kPa and at a feedrate of 16 mm/s. The constructs were crosslinked by irradiating UV light for 1 min.

To study the stability of the 3D printed hydrogel construct at physiological temperature, the constructs were incubated in IMDM complete medium at 37 °C inside a CO_2 incubator for two weeks. The weight of the construct (n=3) was measured before (day 0) and after incubation in media at different time points (days 1, 3, 7 &15). The percentage weight loss of the construct was calculated using the equation and the results were represented as mean ± standard deviation.

$$\text{Weight loss } (\%) = \frac{\text{Initial weight} - \text{Final weight}}{\text{Initial weight}} \times 100 \text{……………. Equation 10}$$

3.20 Three-dimensional bioprinting of liver tissue construct

Two different constructs were bioprinted during this study. An organoid construct using organoid-laden bioink and a cellular construct using cell-laden bioink. The cellular construct was used a control in this study.

3.20.1 Cell bioprinting

The GelMA bioink was prepared in serum-free IMDM as described in section 3.6. Freshly isolated rat hepatocytes (6×10^7 cells) and NPCs (24×10^7 cells) were suspended in 3 mL bioink. The MSC monolayer cultured in a flask was trypsinized and the cell pellet (3×10^6 cells) was also resuspended in the bioink. The cell number for each cell type was chosen based on the total cell number seeded in NGMA dishes (n=30) for organoid culture. The bioink was loaded inside a 3 ml cartridge and was allowed to undergo physical gelation at 18 °C for 5 min. A nozzle having an inner diameter of 840 µm was connected to the cartridge and was loaded on the extrusion head of the 3D bioprinter (3D Discovery, RegenHU, Switzerland). The needle length was calibrated automatically and the needle position was set at a distance of 0.5 mm from the stage. The pneumatic pressure was set to 35 kPa. The G-code for the construct design was uploaded into HMI software and the print job was initiated. The constructs were bioprinted at a feedrate of 12 mm/s into a 6 well plate. Post-printing the constructs were crosslinked by exposing to UV light of 365 nm for 1 min. Two milliliter media was added to each well containing construct and was incubated at 37 °C inside a CO_2 incubator.

3.20.2 Organoid bioprinting

Hepatic organoids were retrieved from NGMA dishes (n=30) and were collected in a 50 mL centrifuge tube. The organoid suspension was centrifuged at 50 ×g for 2 min and the pellet was resuspended uniformly in GelMA bioink by gentle pipetting. The organoid-laden bioink was loaded into a 3 ml cartridge and was allowed to undergo physical gelation at 18 °C for 5 min. Organoid bioprinting was performed using the same printing parameters as described in cell bioprinting.

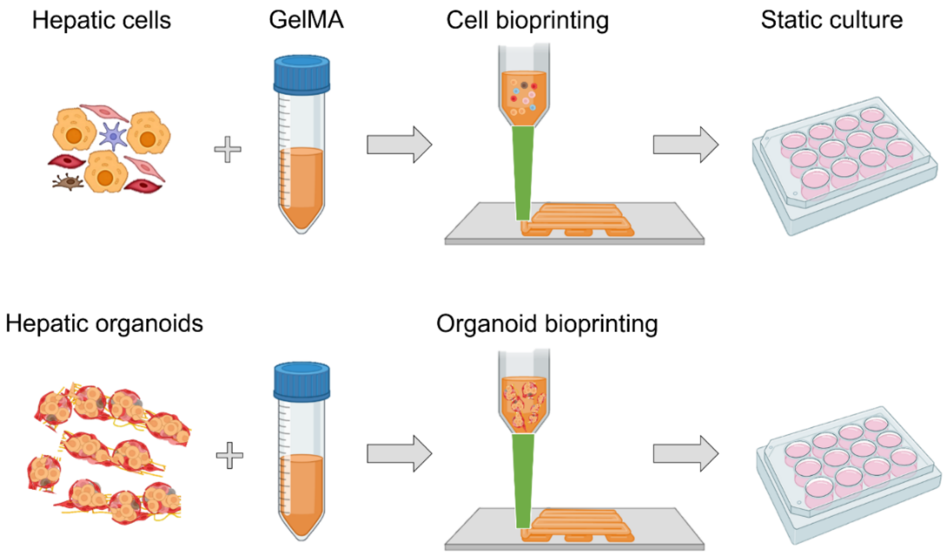

Figure 6 Illustration showing steps involved in 3D bioprinting of cell construct and organoid construct

3.21 Evaluation of 3D bioprinted liver construct

3.21.1 Morphological analysis

The morphology and distribution of the cells within different regions of the construct was examined using a light microscope under phase contrast mode. Images were captured from different regions of the construct for analysis.

3.21.2 Gene expression analysis

The relative changes in expression of liver-specific genes between the cellular and organoid construct were analyzed on days 7 and 15 post-printing by quantitative reverse transcription PCR. Briefly, the bioprinted constructs (n=3) were transferred to a centrifuge tube and were treated with collagenase A enzyme (Merck-Sigma, Germany) at a final concentration of 2 mg/mL in serum-free IMDM at 37 °C for 20 min. The cells and the organoids were then pelleted down by centrifugation at 100 ×*g* for 2 min and the pellet was homogenized using 0.5 mL RNAiso Plus reagent (TaKaRa, Cat#.9108/9109) as per manufacturer's instructions. The total RNA was extracted by conventional phenol-chloroform method (0.2 mL chloroform per mL lysate) and was quantified using Nanodrop (ND 1000, Thermo Scientific). The cDNA was synthesized by reverse transcriptase PCR using PrimeScript RT reagent kit (TaKaRa, Cat#.RR037A). About 500 ng of the RNA was used in 20 µL reaction mix for cDNA synthesis. The PCR reaction was run in a thermocycler (Eppendorf 5333, Master Cycler, Germany) according to the following steps, 1) 37 °C for 15 min, 2) 85 °C for 5 sec and 3) 4 °C for 10 min. The synthesized cDNA was diluted (1:4) in RNase-free water and was stored at -20 °C until further use. The cDNA amplification was performed using specific primer sequences (IDT, India) for liver-specific genes and house-keeping gene as detailed in the Table 2. About 1µL of the cDNA was used to prepare 20 µL reaction mix containing TB Green® Premix Ex Taq^{TM} II reagent (TaKaRa, Cat#.R820A) as per manufacturer's instructions. The reaction mix was transferred to a 96-well PCR plate in duplicates and the cDNA samples were amplified in a qPCR system (qTOWER^3, Analytik Jena, Germany) according to the cycling conditions as follows. 1) Initial denaturation at 95 °C for 30 s, 2) denaturation at 95 °C for 5 s, 3) primer annealing at 60 °C for 30 s, 4) primer extension at 60 °C for 15 s followed by plate scanning and melting curve analysis. The reaction was set for 40 cycles. The relative expression of liver-specific genes in bioprinted constructs with respect to housekeeping gene (18s RNA) was determined using $\Delta C(t)$ method. The fold change in gene expression by organoid construct and cell construct on day 15 with respect to the cell construct on day 7 were calculated using $2^{-\Delta\Delta C(t)}$ method. The fold change in gene expression was represented as mean ± standard deviation.

Table 2:List of rat liver genes and primer sequences.

Gene Name	Forward Primer Sequence 5'-3'	Reverse Primer Sequence 5'-3'
Transthyretin	CGGAAGGGGTGTACAGGGTA	GCTGTGAAAACCACCTCTGC
Cytochrome P450 3A1	AGTGGAAGACTCAAGGAGATGTT	CAGGTTTGCCTTTCTCTTGCCT
Cytochrome P450 1A2	GCTGTGGACTTCTTTCCGGT	TGTCCTGGATACTGTTCTTGTTGA
UDP-Glucuronosyl transferase 2B7	GACCCAATACTCGGGTGTTCA	GATGCCATTGGCTCCACCAT
Glutathione-s-transferase	ACAAGTAGGCCCTTGCTACAC	AAGGAGAGAGAACCACAGTGC
Multidrug resistance-associated protein 2	CAAGAACTTGCTGCGGTTCG	GTGACCACAGACACCAGGATT
Bile salt export pump	CCGATCAGGGAACTGTGATGA	CCGATGTTGGAACGGAGGAA
Fc fragment of IgG receptor IIb (SE-1)	CCATGTGCTCTCACGGACTT	TCCATGGGGGCTCAAGTTTC
Macrosialin	CTGGACTCAGCAGCTCTACC	TTTCCCTGTTCCTTGGGCTAC

Gene Name	Forward Primer Sequence 5’-3’	Reverse Primer Sequence 5’-3’
Desmin	CTCAAGGGCACCAACGACT	CGCGATGTTGTCCTGATAGC
Prominin 1(CD133)	ATTCCTGTCGAGGAGGTGCT	GCGACTCGTGGATGTACCTG
18s RNA (House-keeping)	TGCATGGCCGTTCTTAGTTG	AGTTAGCATGCCGAGAGTCT

3.21.3 Histological analysis

After seven days of culture, the bioprinted constructs were processed for histological analysis. The processing and staining procedures were performed at room temperature (25 °C) unless mentioned. Briefly, the bioprinted constructs were washed with warm PBS and were fixed using 4 % PFA in PBS for 2 h.The fixative was removed and the constructs were dehydrated in ascending grades of isopropanol (70%, 96% and 100%) for 2×30 min and were cleared by three xylene washes for 30 min each. The constructs were then infiltrated with molten paraffin wax for 45 min and were embedded in fresh paraffin wax in a vertical position. Thin cross-sections (10 μm) of the embedded construct were cut using a microtome (Leica, RM2245, Switzerland) and were mounted on charged glass slide. The sections were stained with hematoxylin and eosin stain following standard protocol. The stained sections were observed under the bright-field mode of a light microscope (Eclipse TS100, Nikon, Japan), and digital images were captured (Digital Sight camera # DS-Fi2, Nikon). The paraffin sections of rat liver tissue were used as a control for histological analysis.

3.21.4 Immunofluorescence staining

Immunofluorescence staining was performed on paraffin sections of bioprinted constructs. The paraffin sections were prepared as described above. The sections were then subjected to antigen retrieval process as described in section 3.5.10. After antigen retrieval the sections were permeabilized in 0.1% Triton X-100 for 10 min and was blocked using 1 % (wt/v) BSA in PBS for 30 min. The sections were then incubated with the primary antibody, rabbit anti-albumin (1:500; Abcam, ab207327, USA) for overnight at 4 ºC. The sections were washed thrice with PBS and were incubated with secondary antibody, goat polyclonal antibody to rabbit IgG tagged with the fluorescent probe Alexa 488 (1:500, Abcam, ab150077, USA). The sections were then washed thrice with PBS and were counterstained with DAPI (5µg/mL in PBS) for 10 min. A final rinse with PBS was given and the excess PBS was gently aspirated by pipetting. A cover glass was mounted on sections using an anti-fade medium (Dako, cat# CS703, USA). Images of the labelled sections were captured using a fluorescence microscope (Leica, DMI6000B, Switzerland) and images were captured using DML monochrome camera (Leica, DMC5400, Switzerland) and Leica Application Suite software (LAS V3.7).

3.21.5 Evaluation of liver-specific functions

The liver-specific functions of both the cell construct and organoid construct were analyzed and compared.

3.21.5.1 *Albumin synthesis*

Spent media from the cell and organoid constructs (n=3) were collected at 48 h intervals for 15 days and were stored at -80 ºC. The secreted albumin in spent media was estimated using Rat Albumin ELISA kit (Bethyl Laboratories Inc., Cat.#E110-125, USA) as per the manufacturer's protocol. The absorbance values were measured using a microplate reader (Power Wave-XS, BioTek®, USA) and the concentration of albumin was estimated from the standard curve. The obtained values were normalized to the number of hepatocyte (1×10^6 cells) and represented as mean ± standard deviation.

3.21.5.2 *Ammonia detoxification*

The detoxification ability of liver constructs was assessed by estimating the secreted urea after ammonium chloride treatment. About 20 mM ammonium chloride solution was prepared in serum-free IMDM. The cell and organoid constructs (n=3) were treated with ammonium chloride solution for 4 h on days 1,7 and 15. The constructs were then cultured in a serum-containing medium for 48 h and the spent media was collected. The spent media collected from the untreated groups were used as a control. The secreted urea in spent media was estimated using the Urea assay kit (Biochain, Cat.#Z5030016, USA), as per the manufacturer's protocol. The obtained values were normalized to the number of hepatocyte (1×10^6 cells) and represented as mean ± standard deviation.

3.21.5.3 *Drug-induced Cytochrome P450 activity*

The induction of CYP450 1A2 enzyme activity in the bioprinted liver constructs were analyzed after treating the constructs with the drug dexamethasone (cat#, Himedia, India). About 10 mM of the drug stock solution was prepared in DMSO and was diluted in IMDM complete medium to obtain a working solution having 10 µM concentration. Medium containing an equal concentration of DMSO was used as a vehicle control. The bioprinted constructs (n=3) were treated with the drug or vehicle solution on days 1, 3 and 7 for 48 h. After 48 h, the construct was digested using collagenase A enzyme (COLLA-RO, Merck-Sigma, Germany). An enzyme working solution was prepared in serum-free IMDM at a final concentration of 2 mg/mL and the constructs were incubated in the solution for 20 min at 37 °C. The cells or the organoids were then separated by centrifugation at 100 ×*g* (cells) and 50 ×*g* (organoids) for 3 min. The pellet was resuspended in cytochrome assay buffer provided in the CYP1A2 assay kit (Abcam, cat# ab211074, USA) and were sonicated in an ice bath using an ultrasonic probe sonicator (Soniprep 150, MSE, UK). The lysate was then centrifuged at 15000 ×*g* for 15 min at 4 °C and the supernatant was collected in a fresh tube. The CYP1A2 enzyme activity in the lysate was determined using the CYP1A2 assay kit according to the manufacturer's protocol. The relative fluorescence unit values were measured using a multimode microplate reader (Synergy, BioTek®, USA) and the concentration of product formed due to the enzyme activity was estimated from the standard curve. The obtained values were normalized to the total protein content of the lysate and represented as mean ± standard deviation.

3.21.5.4 *Glycogen storage*

After seven days of culture the bioprinted constructs were processed for paraffin embedding as described earlier and the paraffin sections of the construct were stained with Periodic acid-Schiff (PAS) stain to examine the glycogen content. Briefly, the sections were deparaffinized by incubating the slides at 45 °C inside an oven for 30 min, followed by two xylene washes for 15 min each. The sections were rehydrated by immersing the slides in decreasing concentrations of isopropanol (90 % and 70 %) and tap water for 5 min each. The sections were then oxidized by adding aqueous periodic acid (0.5 % w/v) (Himedia, Cat#. GRM1837, India) for 5 min and were washed several times with distilled water. The sections were then treated with Schiff's

Fuchsin-Sulphite reagent (Himedia, Cat#. S070, India) for 30 min and were washed in running tap water for 2 min. The sections were then counter stained using hematoxylin, differentiated in acid alcohol and blued in Scott's tap water for 5 min each. The sections were dehydrated using increasing concentrations of isopropanol (70 % and 100 %) and were cleared using xylene. Finally, the sections were mounted with a cover glass using DPX medium (Merck-Sigma, Cat#.06522). The stained sections were observed under a light microscope (Eclipse TS100, Nikon, Japan) in the bright-field mode and digital images were captured (Digital Sight camera # DS-Fi2, Nikon).

3.22 Statistical Analysis

Statistical analysis was performed using the GraphPad Prism software (Version 8, San Diego, USA), and all data were expressed as mean ± standard deviation. Student's t-tests analyzed differences between groups, and a p-value of <0.05 was considered significant.

Chapter 4

RESULTS AND DISCUSSION

4.1 Synthesis of Gelatin Methacrylamide

Fifteen batches of GelMA were synthesized and the percentage yield of each batch of GelMA is given in Table 3. Approximately 100 g of GelMA was synthesized in total and the overall efficiency of GelMA synthesis was 65 ± 1.6 %, which is closer to the reported value (70 ± 3%) (Lee, Shirahama, N.-J. Cho, *et al.*, 2015).

Table 3. Yield of GelMA synthesis

Batch No.	Amount of Gelatin (g)	Yield of GelMA (g)	Percentage Yield
1	10	6.4	64.0
2	10	6.4	64.0
3	10	6.3	63.0
4	10	6.8	68.0
5	10	6.5	65.3
6	10	6.4	64.0
7	10	6.4	64.5
8	10	6.7	67.0
9	10	6.6	66.2
10	10	6.4	64.3
11	10	6.6	66.6
12	10	6.8	68.1
13	10	6.5	65.4
14	10	6.6	66.3
15	10	6.3	63.0

GelMA is a photopolymerizable polymer formed by the substitution reaction of free amino groups in lysine/hydroxylysine residues of gelatin with the methacrylic anhydride (Van Den Bulcke *et al.*, 2000). It is extensively used as a scaffold material in tissue engineering applications including 3D bioprinting due its excellent biocompatibility, biodegradability and tunable mechanical strength (Piao *et al.*, 2021). Therefore, GelMA was chosen as the biomaterial for bioink preparation in this study. Type A gelatin was chosen for GelMA synthesis because it is less denatured and hydrolyzed compared to type B gelatin, and it is more similar to collagen in terms of amino acid composition and isoelectric point (IEP) (Lee, Shirahama, N.-J. Cho, *et al.*, 2015). GelMA was synthesized using a carbonate-bicarbonate buffer system with intermittent pH adjustment as reported by Lee, *et al* (2015) (Lee, Shirahama, N. J. Cho, *et al.*, 2015). This buffer system enabled us to use an appreciably smaller molar excess, 2- fold of MAA compared to conventional PBS system using 13-44-fold molar excess of MAA (Van *et al.*, 2000; Hutson *et al.*, 2011; Kim *et al.*, 2014).

4.2 Physico-chemical characterization of GelMA

4.2.1 ^{1}H Nuclear Magnetic Resonance Spectroscopy

The ^{1}H NMR spectrum of the GelMA confirmed the functionalization of gelatin with the methacrylamide group. Resonance signals in GelMA at 2 ppm, 5.5 ppm and 5.7 ppm corresponded to methyl protons of methacrylamide grafts and acrylic protons of methacrylamide grafts on hydroxyl lysine and lysine, respectively. The signal at 3.09 ppm corresponding to methylene protons of unreacted lysine was lower in GelMA than gelatin suggesting modification of lysine by methacrylamide groups. The ^{1}H NMR spectrum of GelMA matched well with the earlier reports (Lee, Shirahama, N.-J. Cho, *et al.*, 2015; Shirahama *et al.*, 2016).

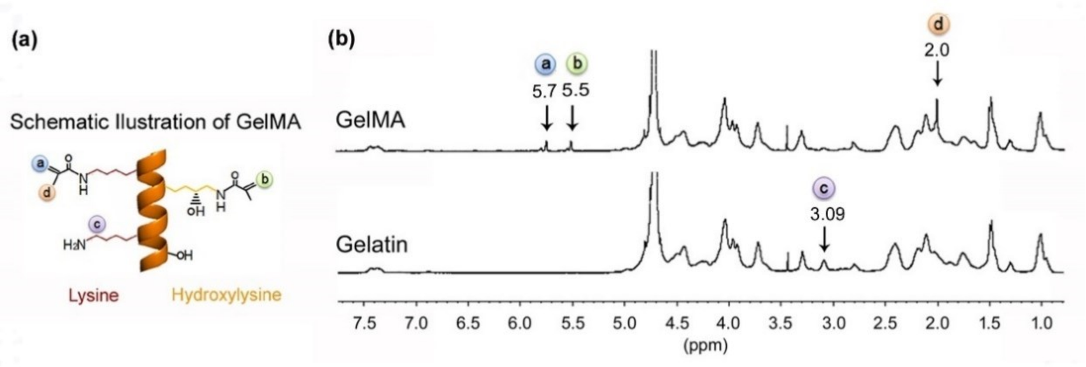

Figure 7. ^{1}H NMR spectrum of gelatin methacrylamide. a) Schematic molecular structure of GelMA showing methacrylated lysine and hydroxylysine residues. b) ^{1}H-NMR spectrum depicting peaks corresponding to acrylic protons (2H) of methacrylamide grafts of lysine groups (a) and those of hydroxyl lysine groups (b), methyl protons (3H) of methacrylamide grafts (d) in GelMA and methylene protons (2H) of unreacted lysine groups (c) in gelatin.

4.2.2 Degree of functionalization

The degree of functionalization in GelMA was estimated by ninhydrin assay. Different batches of GelMA B1, B2, B4, B5, B10 and B15 were evaluated and the degree of methacrylation was estimated to be 77.9 ± 0.2 %, 81.7 ± 0.4 %, 73.8 ± 0.2%, 74 ± 2.1 %, 79.9 ± 7.1 % and 74.4 % respectively (Figure 8). The mean value of percentage methacrylation in GelMA was found to be 76.87 ± 3 %. The coefficient of variation of percentage degree of methacrylation for the representative batches was only 4.5 %, the degree of methacrylation is expected to be similar for all the batches synthesized under similar conditions. The degree of methacrylation has profound effect on the mechanical properties of GelMA hydrogel. The storage modulus of the hydrogel increases with the increase in degree of methacrylation due to an increase in crosslinking density (Nichol *et al.*, 2010). According to the earlier reports, GelMA having a degree of methacrylation above 50 % yielded hydrogels with good shape fidelity and mechanical strength after UV- crosslinking (Nichol *et al.*, 2010; Lee, Shirahama, N. J. Cho, *et al.*, 2015). This suggests that the in-house synthesized

GelMA having a degree of functionalization above 70%, when used as bioink can provide adequate shape fidelity and strength to the 3D bioprinted construct after UV crosslinking.

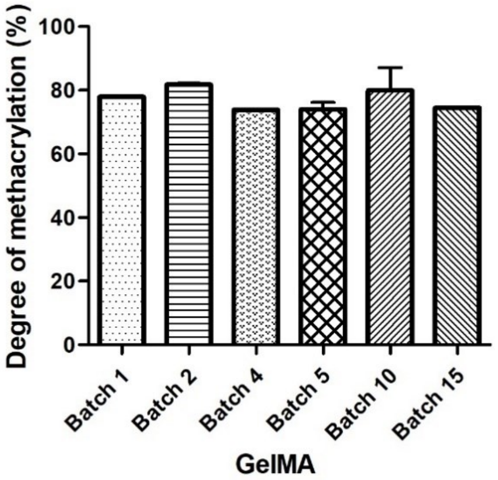

Figure 8. Degree of methacrylation. Graph showing the consistency in the percentage of gelatin methacrylated across different batches of GelMA.

4.2.3 Photocrosslinking of GelMA

The optimum crosslinking time for different concentrations of GelMA polymer solution was determined by analyzing the stability of hydrogel after UV irradiation for different duration. The 5% (w/v) GelMA solution required more than 120 s to form a stable hydrogel (Figure 9 a). Whereas GelMA solutions of a higher concentration, 10%, 15% and 25% (wt/v) formed hydrogels with definite size and shape after 30 s of UV-irradiation (Figure 9 b, c & d). The hydrogels were mechanically strong enough to be handled using forceps. However, the hydrogel samples exposed to UV for 30 s deformed after incubating in PBS at 37°C. While hydrogels exposed to more than 30 s were intact in PBS.

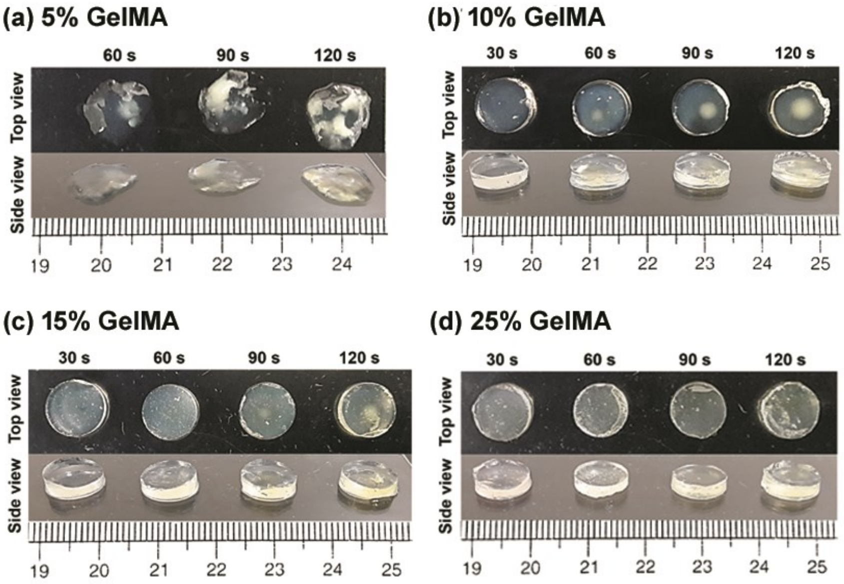

Figure 9.Photocrosslinking of GelMA. Representative images of UV crosslinked GelMA hydrogels (a) 5 % GelMA, (b) 10 % GelMA, (c) 15 % GelMA and (d) 25 % GelMA irradiated for 30 s, 60 s, 90 s and 120 s. Scale in cm.

The GelMA solution was crosslinked by UV light of 365 nm in the presence of the photoinitiator Irgacure 2959. About 1% (w/v) Irgacure was used as the photoinitiator, since it has been reported to be a safer concentration for cells encapsulated in photo-crosslinked GelMA (Jung and Oh,). An ideal photo-crosslinkable bioink should have a short UV-crosslinking time because prolonged UV exposure can be toxic to the cells (Mironi-Harpaz *et al.*, 2012a). At the same time, insufficient crosslinking may compromise their long-term stability (Saunders and Moussa, 2012). Earlier Nichol *et al*, (2010) have shown that UV light exposures for at least 60 s did not visibly influence the viability of cell-laden GelMA hydrogels (Nichol *et al.*, 2010). Further, Mironi-Harpaz *et al.*, (2012) has demonstrated that the short exposures (up to 5 min) to long-wave UV light irradiation (20 mW cm^{-2}, 365 nm) is not toxic to cells (Mironi-Harpaz *et al.*, 2012b). Hence, taking into consideration both the cell viability and mechanical stability, 60 s was chosen as the optimal UV-crosslinking time and GelMA hydrogel samples having concentrations of 10%, 15% and 25% (wt/v) were selected for further analysis. The ratio between volume of GelMA (0.2 ml) and the UV crosslinking time (1 min) was maintained throughout the following experiments.

4.2.4 GelMA hydrogel swelling

To determine the degree of swelling relative to various concentrations of GelMA hydrogel, the percentage weight gained by the hydrogel after incubation in PBS was calculated (Figure 10 a). The mean percentage swelling of 10 %, 15 % and 25 % (wt/v) GelMA hydrogels were 23.7 ± 9.8 %, 11.1 ± 4.1 % and 1.4 ± 2.8 % respectively. The hydrogel swelling increased with the decrease in polymer concentration. There was significant increase in size of the hydrogel with decrease in polymer concentration (Figure 10 b). Nevertheless, the swollen hydrogels retained their shape, were self-standing and exhibited sufficient handling stability.

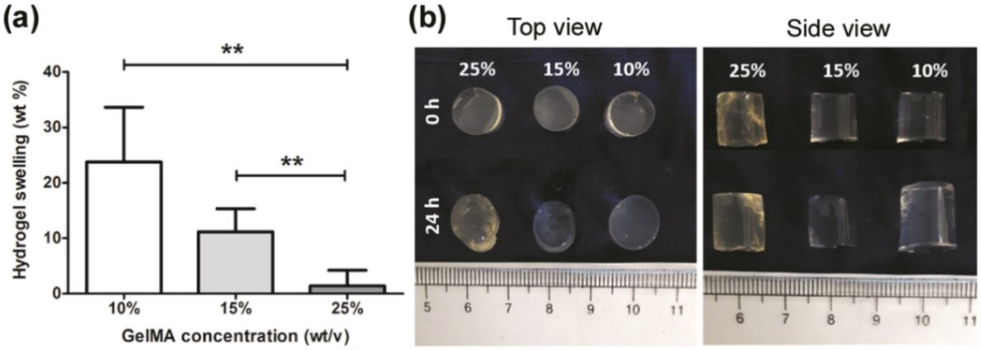

Figure 10. GelMA hydrogel swelling. (a) Graph showing percentage weight gain of different concentrations of GelMA hydrogel after 24 h incubation in PBS at 37°C, represented as percentage weight gain of the hydrogel. (n=4, **p-value < 0.01). (b) Digital images of GelMA hydrogels before (0 h) and after (24 h) incubation in PBS. Scale in cm.

Hydrogel swelling has a substantial effect on solute diffusion and shape fidelity of the 3D bioprinted construct (Peppas *et al.*, 2006). Swelling will allow sufficient mass transfer to encapsulated cells by simple diffusion. But uncontrolled swelling can reduce the mechanical strength of the hydrogel and thereby affecting the final shape. The variation in hydrogel swelling observed in this study was in line with the earlier study by Nichol *et al*, (2010) where it was reported that the degree of swelling for GelMA hydrogel was inversely proportional to the polymer concentration and cross-linking density (Nichol *et al.*, 2010). Qualitative analysis of the hydrogel after swelling also confirmed the earlier observation.

4.2.5 Compressive Modulus of GelMA Hydrogel

The compressive modulus of hydrogel is a measure of mechanical strength or stiffness. The mean modulus values of 10%, 15% and 25% (wt/v) GelMA hydrogels after equilibrium swelling were 6 kPa, 7.8 kPa and 12.7 kPa. The compressive modulus of the hydrogel increased with increase in polymer concentration (Figure 11). Such an increment in modulus value with respect to polymer concentration can be attributed to the surge in crosslinking density as reported by Nichol *et al*, (2010) (Nichol *et al.*, 2010). As a scaffolding material, hydrogel stiffness has great impact on cell viability, proliferation, migration, differentiation and function (Discher, Janmey and Wang, 2005). Earlier, studies have reported that soft hydrogel scaffolds (4-10 kPa) promoted better maintenance of hepatocyte phenotype in contrast to stiffer hydrogels (> 20 kPa) which facilitated epithelial-to-mesenchymal transition and induced apoptosis (You *et al.*, 2013; Xia *et al.*, 2020). Considering the above information, 10%

GelMA would be the most appropriate for 3D bioprinting liver construct, since it has a modulus value in the desirable range.

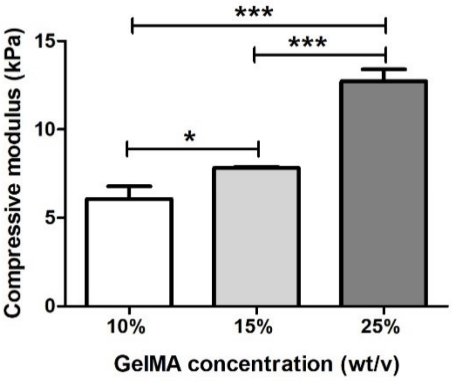

Figure 11. Compressive modulus of GelMA hydrogel. Graph showing compressive modulus of 10%, 15% and 25% GelMA hydrogel after equilibrium swelling in PBS at 37°C for 24 h. (n=4, *p-value < 0.05, **p-value < 0.01, ***p-value < 0.001)

4.3 Cytotoxicity evaluation of GelMA hydrogel

4.3.1 Cell encapsulation in GelMA hydrogel and viability staining

The cytocompatibility of various concentrations of GelMA hydrogel was tested by analyzing the viability of the encapsulated hepatocytes on days 1, 7 and 15 by live-dead staining. More than 90 % of the cells encapsulated in 10 % GelMA hydrogel were viable on days 1, 7 and 15 (Figure 12 b, f & j). The cells encapsulated in 15 % GelMA hydrogel displayed a similar percentage viability on days 1 and 7 (Figure 12 c & g). Whereas on day 15 more dead cells appeared inside the hydrogel. In contrast, to the above observation, cells encapsulated in 25 % GelMA were dead as early as on day 1 until day 15 (Figure 12 d, h & i). It was also observed that 10 % and 15% GelMA hydrogel supported cell aggregation and proliferation as evidenced by the presence of cellular aggregates on day 7 (Figure 12 f & g). The cellular aggregation was more prominent in 10 % GelMA and the size of the aggregates increased significantly from day 7 to 15 (Figure 12 f & j). As shown in Figure 12 e & f, the morphology of cellular aggregates in 10 % GelMA hydrogel resembled the expanding hepatic organoids cultured in matrigel.

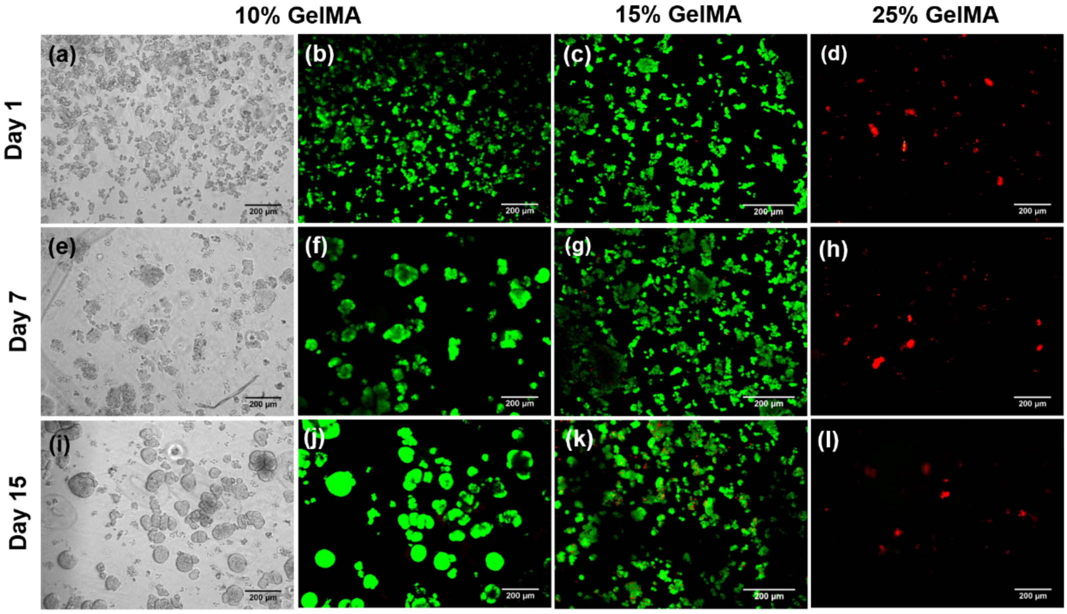

Figure 12. Cell viability after encapsulation in GelMA hydrogel. Live (green)/dead (red) staining images of HepG2 cells after days 1, 7 and 15 of encapsulation in 10% GelMA (b, f & j), 15% GelMA (c, g & k) and 25% GelMA (d, h & l). Phase-contrast images of cells encapsulated in 10 % GelMA hydrogel on days 1, 7 and 15 (a, e & i). Scale bar =200µm

Human hepatoma cell HepG2 is a commonly used liver cell line which is easily propagatable and can secrete liver-specific molecules (albumin & urea) which are routinely analysed during liver function test (Arzumanian, Kiseleva and Poverennaya, 2021). HepG2 cells being highly proliferative in nature, they were used to evaluate the ability of the GelMA bioink to support hepatocyte survival and proliferation after encapsulation. The variation in cell viability across different hydrogel concentrations can be explained based on the previous data on hydrogel swelling and compressive modulus. High cell viability and proliferation in 10 % GelMA hydrogel may be due to the low stiffness (compressive modulus) [Figure 11] and better nutrient diffusion facilitated by hydrogel swelling [Figure 10 a]. Whereas high stiffness and less nutrient diffusion in 25 % GelMA hydrogel must have resulted in complete cell death. While in 15 % GelMA hydrogel, cells might have experienced a stiffness value and nutrient diffusion rate lying between the other two concentrations of GelMA, which is very well reflected in the behaviour of cells. A similar correlation between hydrogel stiffness, cell viability and proliferation has been reported earlier by two different groups. Aparnathi and Patel, (2016) studied the effect of gel porosity and stiffness on HepG2 cells encapsulated in 5 % and 10 % GelMA hydrogel (Aparnathi and Patel, 2016). The authors observed that both cell viability and proliferation was negatively affected when the stiffness of the hydrogel was higher. Similarly, Xu *et al.*, (2021) examined the effect of GelMA hydrogel (5 %, 10 % & 15 %) stiffness on nucleus pulposus cells (NPCs) properties (Xu *et al.*, 2021). As the concentration of GelMA hydrogel increased the stiffness of the hydrogel also increased and the cell survival, proliferation and ECM deposition gradually decreased. Based on the above observation and published reports, 10 % GelMA was chosen for further experiments because it preserved cell viability for long-term and supported growth of 3D cellular aggregates which is beneficial for organoid culture.

4.3.2 In vitro cytotoxicity evaluation of GelMA hydrogel

4.3.2.1 *Direct contact test*

The direct cell contact test allows qualitative assessment of the cytotoxic potential of a test item in contact with cells. The cytotoxicity response of cells in contact with the GelMA hydrogel and control samples were graded as per the ISO standard 10993-5. The cells in contact with the hydrogel were intact without any sign of lysis, vacuolization, detachment, or membrane disintegration (Figure 13 a). There was no detectable zone of cytotoxic reactivity around or under the GelMA hydrogel and hence, the reactivity was graded as zero or non-toxic. Negative control gave no cytotoxic reactivity, while positive control exhibited severe cytotoxic reactivity (Figure 13 b & c). The above data indicate that cells exposed directly to the GelMA hydrogel were viable and healthy and therefore qualifies the hydrogel for 3D bioprinting application.

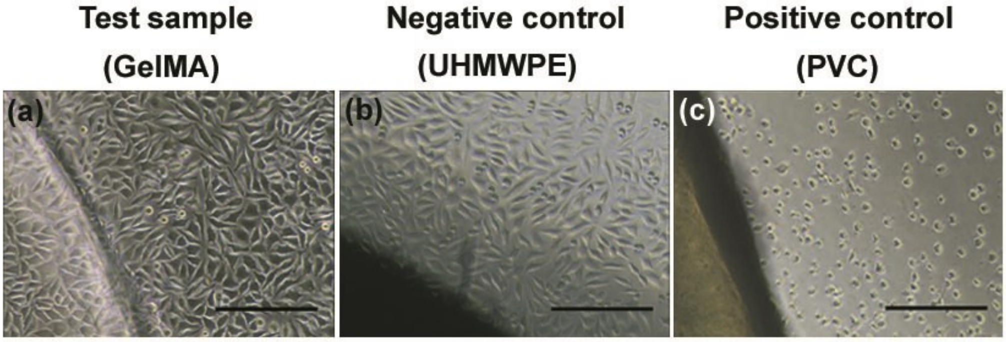

Figure 13.Direct contact test. Phase-contrast images showing L929 cells in contact with (a) GelMA hydrogel, (b) negative control (UHMWPE) and (c) positive control (PVC). Scale bar = 200µm.

4.3.2.2 *Test on extract and MTT assay*

The cytotoxicity response of cells treated with the GelMA hydrogel extract were graded as per the ISO standard 10993-5. The cells incubated with different dilutions of hydrogel extract (Figure 14 b-f) showed discrete intracytoplasmic granules without any cell lysis and a reduction of cell growth similar to cell control (culture media) (Figure 14 a). Hence, the cytotoxic reactivity was graded as zero for the GelMA hydrogel extract. Cell treated with the phenol (positive control) showed severe cytotoxic reactivity as evidenced by cell detachment and loss of cell morphology (Figure 14 g).

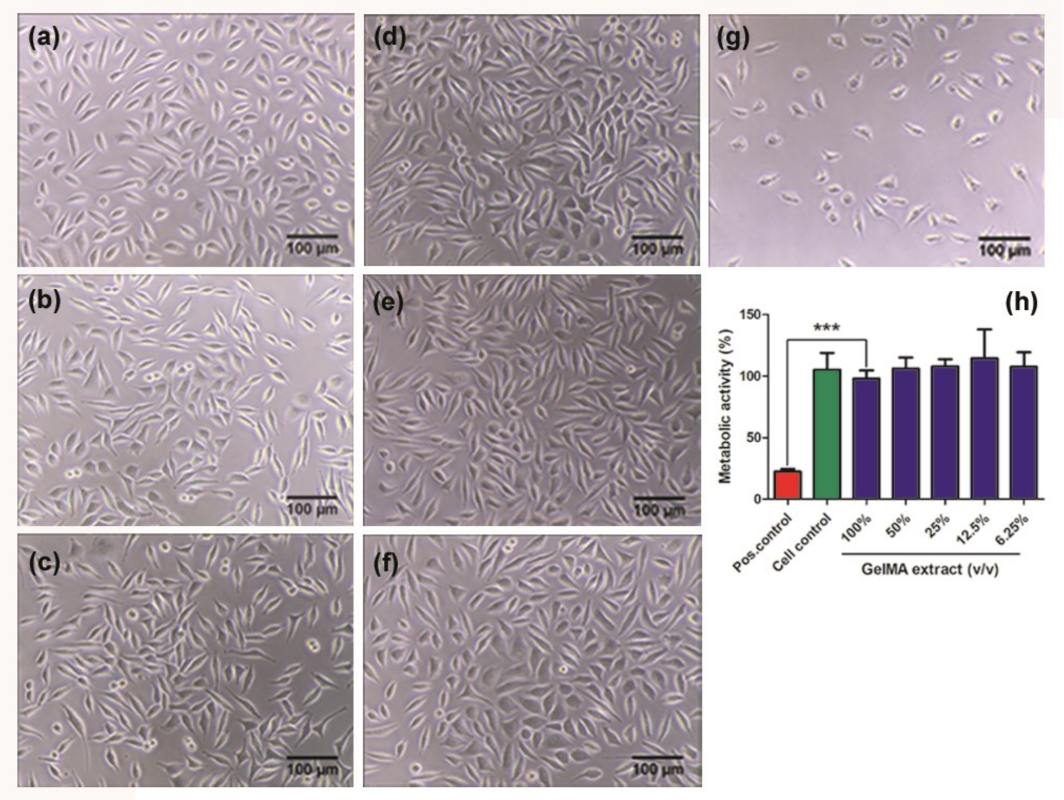

Figure 14. Test on extract and MTT assay. Phase-contrast images showing L929 cells incubated with (a) culture medium and dilutions of GelMA extract (b) 100% (c) 50%, (d) 25%, (e) 12.5% and (f) 6.25%. (g) Graph depicting percentage metabolic activity of cells treated with phenol and dilutions of GelMA hydrogel extract with respect to cell control.

The metabolic activity of cells treated with the GelMA hydrogel extract was analyzed by MTT assay (Figure 14 h). The percentage metabolic activity of cells treated with test and control media is shown in Figure 14 h. The cells treated with different dilutions of hydrogel extract 100%, 50%, 25% 12.5% and 6.25% (v/v) exhibited 98%, 106.3%, 107.9%, 114.4% and 107.6% metabolic activity respectively, with respect to cell control. The metabolic activity of cells treated with phenol was only 22.5% of the activity of cell control. According to ISO 10993-5 metabolic activity more than 75% is considered non-cytotoxic. Since, the metabolic activity of cells treated with GelMA hydrogel extract was more than 75%, GelMA hydrogel was proven to be non-cytotoxic. Hence, this data suggests that there are no potential toxic eluants released from the GelMA hydrogel and therefore GelMA can be considered safe for liver tissue bioprinting.

4.4 Hydrogel Porosity Analysis

4.4.1 Scanning Electron Microscopy

GelMA scaffolds showed a dense honeycomb-like porous network of polymer (Figure 15 a) with smooth walls separating the pores under scanning electron microscope. The pores were polygonal in shape with varying pore sizes distributed evenly across the surface of the hydrogel. The pores were not interconnected and appeared as distinct pockets within the hydrogel. The results obtained very well matched with the previous studies (Benton *et al.*, 2009).

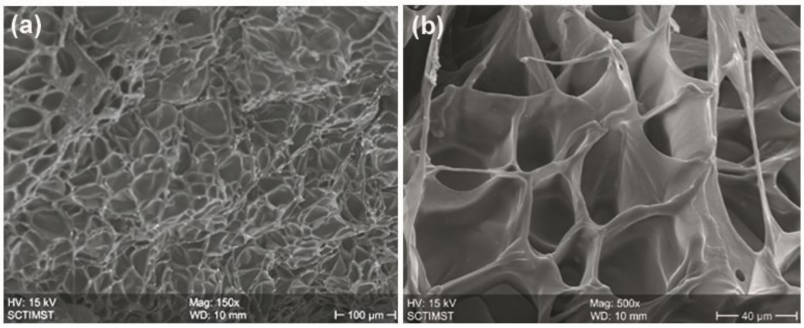

Figure 15.Surface morphology of GelMA hydrogel. SEM micrographs of GelMA hydrogel, (a) Low magnification and (b) high magnification depicting the porous network of polymer on the surface.

4.4.2 Micro-Computed Tomography

Micro-CT analysis provided the cross-sectional images of lyophilized GelMA depicting porous internal structure (Figure 16 a). The quantitative morphometric analysis yielded a PV/ TV ratio of 0.3867 and the percentage porosity was determined to be 61.33 %. The pore diameter of the lyophilized hydrogel ranged from 10 to 300 µm. The percentage pore volume occupied by pores having diameters of 10-100 µm, 100-200 µm and 200-300 µm were 67.2 %, 29.5 % and 3.2 %, respectively (Figure 16 b).

The morphological characterization of GelMA hydrogel has proved that it is highly porous. This characteristic property of hydrogel will facilitate sufficient diffusion of nutrient inward and thereby support the cells after encapsulation (Peppas *et al.*, 2006).

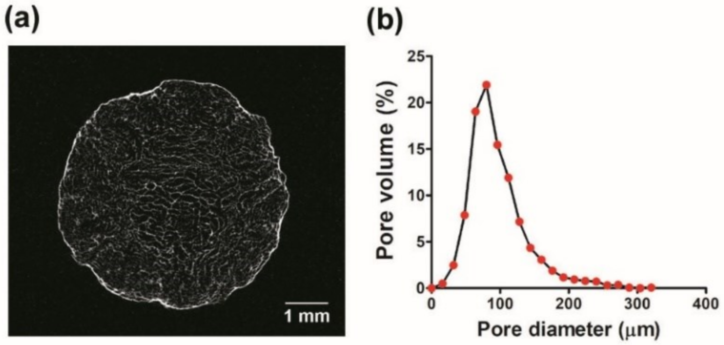

Figure 16.Porosity of GelMA hydrogel. (a) Micro-CT image showing cross-section of porous GelMA hydrogel. (b) Graph depicting pore size distribution within GelMA hydrogel.

4.5 High-throughput production and characterization of liver parenchymal microtissues

Liver parenchymal microtissues (LMPTs) are 3D multicellular aggregates of hepatocytes that form spontaneously through cell-cell adhesion. Although they are less complex 3D liver tissue models, they mimic some of the characteristics of liver organoids. Hence, LPMTs were chosen as a tissue model to evaluate the suitability of GelMA hydrogel as a biomaterial for preparation of organoid bioink.

4.5.1 Hanging-drop culture (Conventional method)

Manual cell dispensing was laborious, and the time required to dispense 100 drops was around 5 min. The cells in the hanging drop formed an aggregate after 24 h and attained a spherical morphology after 72 h. The efficiency of microtissue formation in the manual dispensing method was only 62.8 ± 2%.

4.5.2 Design and fabrication of hanging-drop culture chamber

A transparent portable hanging-drop culture chamber that is easy to assemble was designed (Figure 17). A single chamber could accommodate eight culture substrates carrying the hanging drops. Transparent, thin PET sheets with the size of 70 mm × 65 mm × 0.1 mm (length × width × height) was used as the substrate. It has been reported before that PET sheets can act as carriers for cell constructs (Joseph, Prasad and Joseph Sreenivasan K., 2011). Lightweight, optically clarity, and a high strength-to-weight ratio are the advantages of using PET sheet. The cover lid ensured an aseptic environment inside the chamber. The chamber was reused after thorough cleansing and ETO sterilization. The manufacturing cost of HdCC was approximately 30 US$ and the price for PET culture substrates required for one HdCC unit was only 100 center coin. Collectively, the total cost of the culture system was several times lesser than commercially available single-use hanging-drop culture plates. The chamber was designed to work with the microvalve-based printing technique in order to produce a consistent droplet array on the PET substrate.

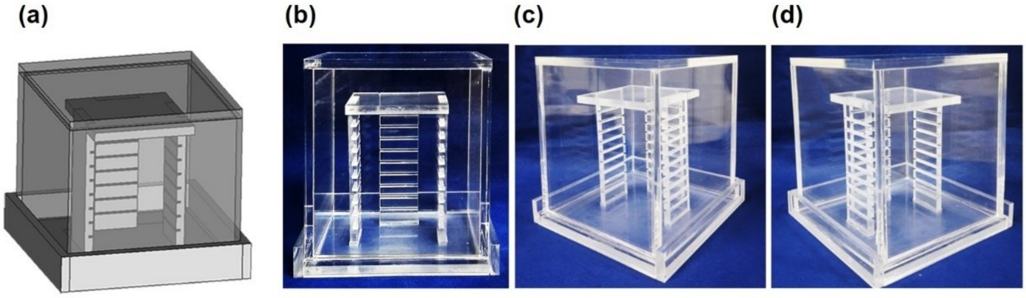

Figure 17. Design of the Hanging drop Culture Chamber. (a) The computer-aided design (CAD) model of the HdCC. Photograph showing different views of the chamber; (b) front view, (c) right side view and (d) left side view.

4.5.3 Optimization of parameters for microvalve-based printing

Using a microvalve nozzle (Figure 18 a), liquid droplets with volumes ranging from nanoliters to microliters were printed quickly and accurately. The desired droplet diameter of 2 mm was obtained with a droplet volume of 2.5 µl. To determine the optimal printing parameters for obtaining a droplet volume of 2.5 µl, the volume dispensed after applying 25 different combinations of VOT and CPr were measured and plotted into a matrix format as shown in Table 4. It was observed that the required volume of 2.5 µl was obtained at two settings (VOT = 15 ms, CPr =10 kPa & VOT = 20 ms, CPr = 8 kPa). The setting with lower cartridge pressure (8 kPa) and corresponding VOT (20 ms) were chosen for cell printing to reduce shear stress. Figure 18 b shows the array of 15×14 droplets printed on a PET substrate using optimized printing parameters. The droplets were positioned at equal distance from one another, and the time needed to finish one array was 45 s. Image analysis of the printed droplets revealed that there was no difference in droplet size (diameter) across different locations (top, middle and bottom) of the array and it matched with the manually dispensed droplet having a volume of 2.5 µl.

Table 4. Determining the optimum printhead parameters for microvalve-based printing

	Droplet volume (µL)				
Cartridge pressure (kPa) / **Valve opening time** (ms)	**10**	**15**	**20**	**25**	**30**
10	1.6	2.5	3	4	4.5
8	1.5	2	2.5	3.5	4
6	1	2	2.1	3	3.5
4	0.5	1	1.5	2	3
2	0	0	0	0	0

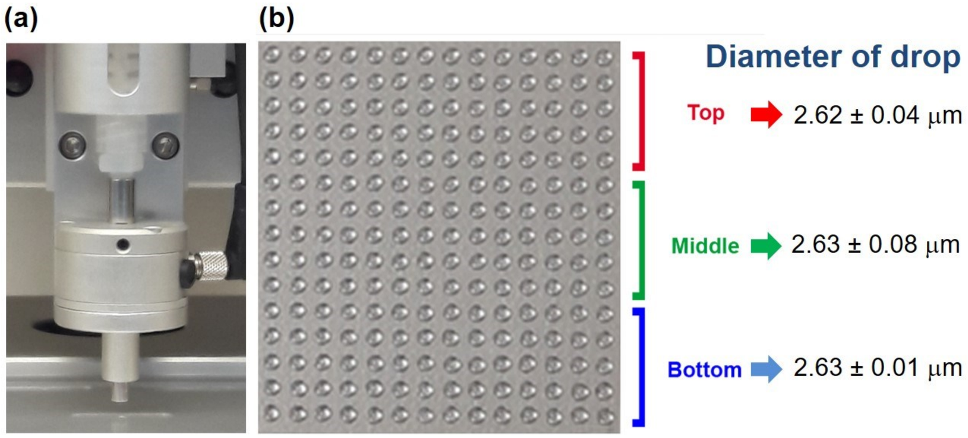

Figure 18. (a) Image of the cell-friendly microvalve connected to the printhead. (b) Photograph of droplet array printed using optimal printhead parameters.

For hanging drop culture, the manual dispensing of cell suspension is labor-intensive and needs to be replaced with an automated liquid dispensing system. Earlier, studies have demonstrated the application of automated liquid handling systems for dispensing cell suspension into a hanging-drop multiwell plate (Drewitz *et al.*, 2011; Tung *et al.*, 2011). Concurrently, valve-based drop-on-demand printing technology also emerged as handy tool for generating cell-laden hanging drops (Faulkner-Jones *et al.*, 2013; Gutzweiler *et al.*, 2017). The application of a valve-based cell printer to generate hanging drop array was first demonstrated by Faulkner-Jones *et al.,* (2013) (Faulkner-Jones *et al.*, 2013). Later, Gutzweiler *et al.*, (2017) reported the utilization of a disposable, electromagnetic dispensing valve for large-scale production of HUVEC spheroids (Gutzweiler *et al.*, 2017). The major advantage of using microvalve-based printing technique is that it offers a high degree of miniaturization in cell number, droplet volume and substrate area without compromising microtissue formation and viability. Hence, in this study, microvalve-based printing technique was chosen for preparing cell-laden hanging drop array on our PET substrate.

4.5.4 Microvalve-based bioprinting of HepG2 cells

The microvalve-based printing technique was combined with the in-house fabricated hanging-drop culture platform to produce vast numbers of 3D microtissues. Figure 19 a-c shows the steps involved in the microtissue production. A uniform 15×14 droplet array containing ~ 500 HepG2 cells/droplet was bioprinted on the PET substrate and was placed inside the HdCC device to form hanging drops (Figure 19 a & b). After 72 hours of incubation at 37 °C, the cells within the droplets formed compact spherical microtissues (Figure 19 c). The efficiency of microtissue formation via microvalve-based bioprinting (97.4%) was noticeably higher than the manual dispensing method (62.8%) (Figure 19 d). Meanwhile, we observed that the diameter of the microtissues generated on subsequent PET substrates varied significantly (Figure 19 e). Cell bioprinting following agitation helped to reduce the variation in diameter of microtissues across different substrates (Figure 19 e).

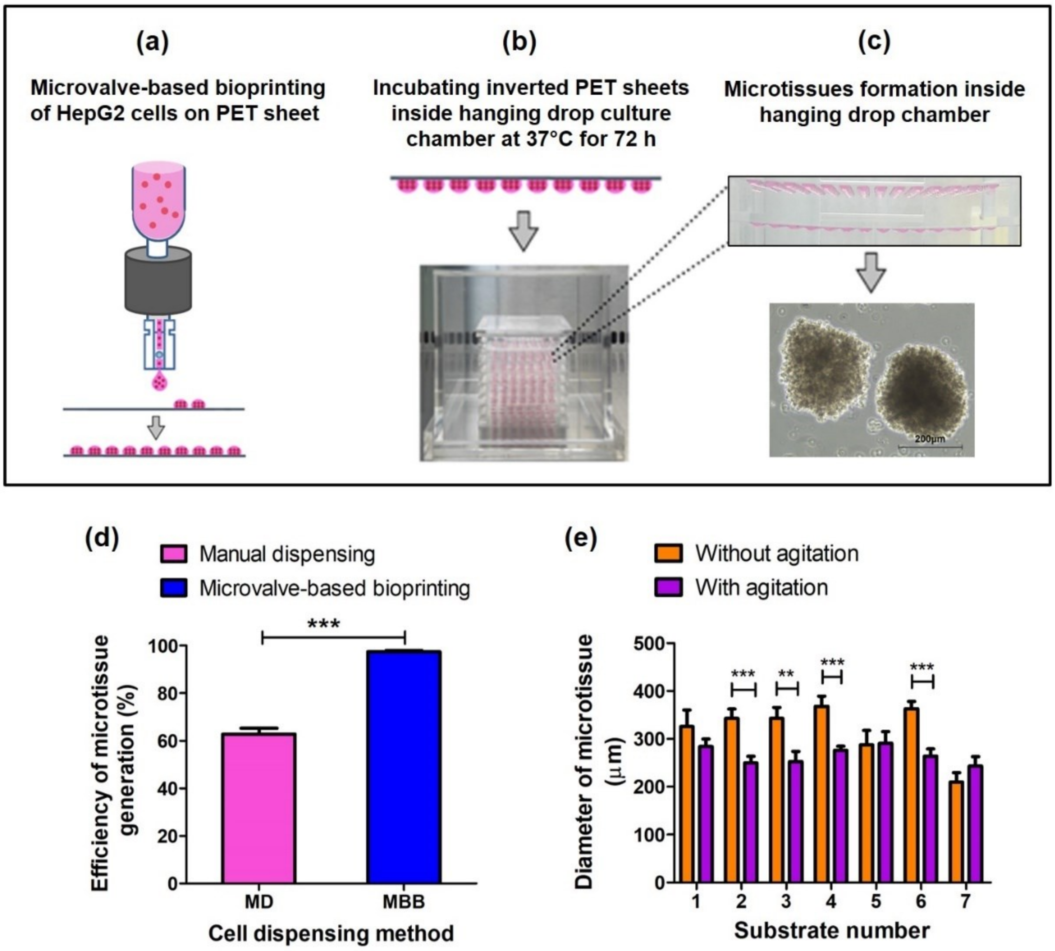

Figure 19. Production of LPMTs by microvalve-based bioprinting. Illustration showing (a) microvalve-based HepG2 cell bioprinting, b) Culture of cells in hanging drops inside HdCC (c) Formation of LPMTs inside HdCC. (d) Graph depicting difference in efficiency of microtissue production between manual dispensing and microvalve-based bioprinting method (n = 630, *** p-value < 0.001). (e) Graph showing variation in size of the microtissues formed with and without agitation during bioprinting.

The *in vitro* experiments were conducted using the hepatocarcinoma cell line (HepG2) since it has an infinite lifespan and is frequently used as a substitute for primary hepatocytes (Gómez-Lechón, Tolosa and Mt, 2014). HepG2 cells in traditional monolayer culture do not adequately express cytochrome P450 activity, whereas 3D microtissues show increased enzyme activity (Ramaiahgari *et al.*, 2014).

In comparison to the manual dispensing approach, microvalve-based bioprinting was shown to be a more efficient method for the high-throughput production of microtissues. But at the same time, continuous printing resulted in non-uniform microtissues. The non-uniformity among the microtissues was assumed to be due to the difference in cell number per droplet. It has been earlier reported that the cells tend to settle down during the printing due to low viscosity of cell suspension (Faulkner-Jones *et al.*, 2013). To address this problem, we introduced a brief agitation step using a cell-friendly agitator before initiating each print command. Such additions to the process methodology improved the effectiveness of our printing procedure and produced consistent microtissues. Previous studies have demonstrated the benefits of a combined strategy that incorporates platforms for hanging drop culture with automated cell dispensing. To create tumor microtissues, Popova *et al.*, (2019) created a miniaturized single spheroid hanging droplet microarray based on hydrophilic-superhydrophobic patterning (Popova *et al.*, 2019). However, compared to HdCC, which can produce 1600 microtissues in a single go, it requires a number of difficult fabrication steps to create the droplet microarray device, which can hold only 588 spheroids.

4.5.5 LPMT harvesting efficiency, size distribution and stability

Around 200 microtissues were harvested from a single PET sheet with an efficiency of 92.2 ± 3%, and a HdCC chamber produced roughly 1600 microtissues. The size of the microtissue and the number of cells dispensed per droplet were found to be positively correlated (Figure 20 a & c). The mean diameter of microtissues having a cell number of 0.5×10^3, 1×10^3 and 2.5×10^3 cells per microtissue were 297.15

± 11μm, 393.69 ± 16 μm and 557.71 ± 17 μm respectively. Considering efficient nutrient transfer to the core cells, the cell number (0.5×10^3) that yielded microtissues with smallest diameter were chosen for the later experiments. In suspension culture, the microtissues remained stable for two weeks without exhibiting any signs of disintegration (Figure 20 b). However, the diameter of microtissue increased over time with an increment of 28.8% and 35.6% on days 6 and 14 of culture compared to the second day (Figure 20 d).

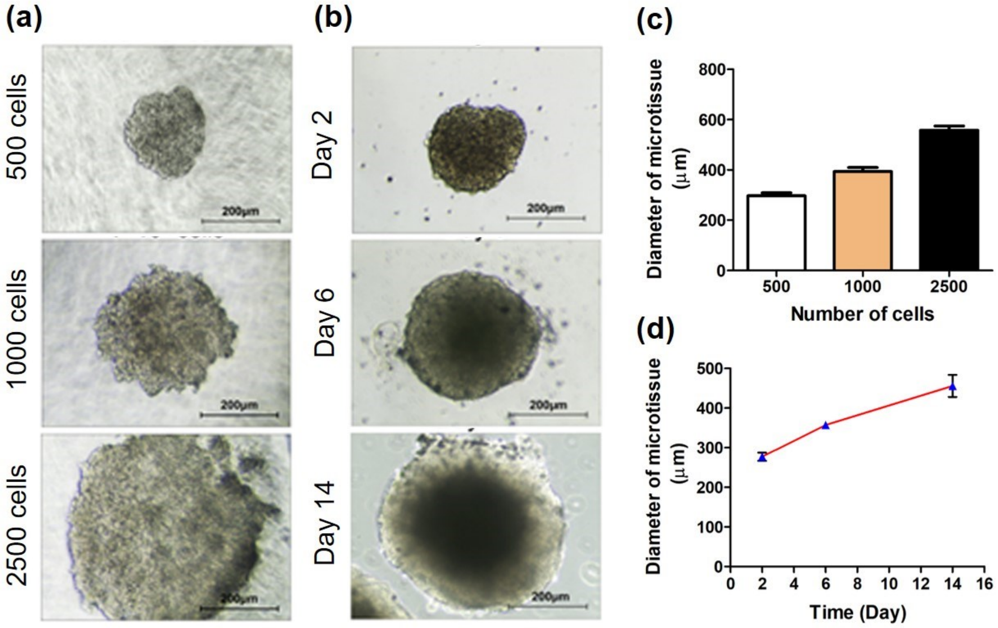

Figure 20. Size and stability of the LPMTs. Phase-contrast images of (a) representative microtissues generated from three different cell concentrations after 72 h and (b) Growth of the microtissue (500 cells) in suspension culture. Graphs depicting (c) average diameter of the microtissues (n=4) with different cell number after 72 h and (d) changes in diameter of microtissue (500 cells) over 14 days (n = 9). Scale bar = 200 μm.

The efficiency of harvesting the microtissues from the substrate is also a detrimental factor in assessing the reliability of high-throughput methods. Earlier, Gutzweiler *et al.,* (2017) reported a microvalve-based printing method to generate endothelial cell microtissues on polystyrene plates with a high efficiency of microtissue formation (~96%), while the efficiency of harvesting the microtissues was significantly less (~54%) (Gutzweiler *et al.*, 2017). The hydrophilic properties of the PET substrate in our study made it possible to easily collect microtissues with a harvesting efficiency of more than 90%.

When proliferating cell lines are used for microtissue culture, the cell multiplication increases cell number and thereby the size of LPMTs over the days. The increase in diameter of the microtissue could be attributed to the cell proliferation in the peripheral zone. However, with the increase in size there is a higher chance for development of hypoxia within microtissues due to the limited diffusion of oxygen and nutrients (Asthana and Kisaalita, 2012). As demonstrated by Gaskell *et al.*, (2016), a smaller cell number is therefore favored for seeding over a large cell number to prevent necrotic core formation (Gaskell *et al.*, 2016). Hence, 500 cells per droplet were opted as the optimum cell concentration since the radius of the spherical microtissue formed was well within the range of the diffusion limit.

4.5.6 LPMT cell viability

HepG2 cell bioprinting using microvalve technology produced viable LPMTs. In culture, the microtissues produced ATP consistently for up to two weeks Figure 21 a). On days 1, 7 and 15, the percentage of cell metabolic activity was 100 ± 11 %, 109 ± 20 % and 99.4 ± 2 % respectively. Further, live/dead staining of 7-day old LPMTs revealed that more than 95 % of cells inside the microtissue were viable and did not show a necrotic core (Figure 21 b).

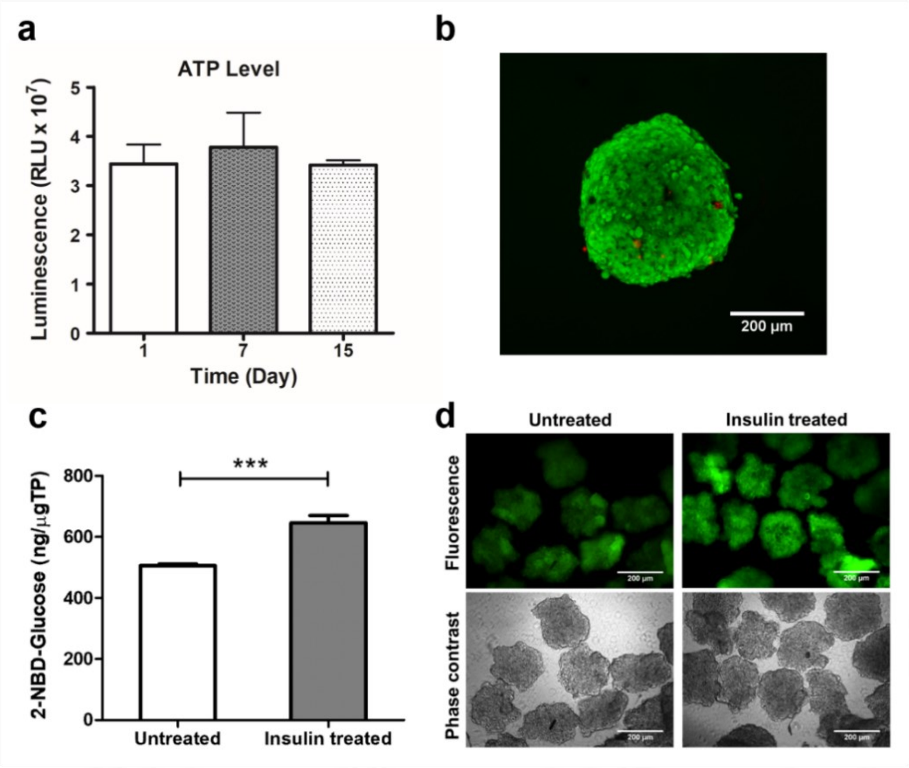

Figure 21. Cell viability and insulin-stimulated glucose uptake in LPMTs. (a) Graph showing levels of ATP in LPMTs (n=200) lysate collected on days 1, 7 and 15. (b) Confocal image showing live dead staining of 7-day old LPMT. Live (green) & dead (red) (c) Graph depicting the quantity of 2-NBD glucose absorbed by microtissues in the absence and presence of insulin. (d) Fluorescent image showing uptake of 2-NBD glucose by microtissues and phase-contrast images showing the integrity of the microtissues. Scale bar = 200 µm. ***p-value < 0.01). [Reproduced from Roopesh, et al. (2022), *Biotechnol Bioeng*. DOI: 10.1002/bit.28010]

Hepatocytes are highly metabolically active cells with around 1000-2000 mitochondria within each cell (Wiesner, Rüegg and Morano, 1992). Such a huge number of mitochondria are essential to produce an adequate amount of ATP for performing diverse liver functions. Hence, consistent levels of ATP production by LPMTs proves that hepatocytes are viable and metabolically active. In addition, production of intracellular fluorescein following live-dead staining ensured the esterase enzyme activity within hepatocytes. While absence of PI stain confirmed the integrity of cell membrane. The data also substantiates the fact that the size of the microtissue was optimal for proper mass transfer as evidenced by the absence of necrotic core.

4.5.7 Glucose uptake by LPMT

The ability of hepatocytes to respond to insulin partly determines the uptake and release of glucose from the liver. In the presence of insulin, the quantity of glucose uptake by LPMTs was significantly higher (646.6 ± 22 ng μg^{-1} total protein) compared to its absence (505.8 ± 5 ng μg^{-1} total protein) (Figure 21 c). The microtissues were intact, and visibly there were obvious differences in fluorescence intensity between the two groups indicating differences in absorption of labelled glucose (Figure 21 d).

By controlling the interconversion of glucose and glycogen, the liver contributes to glucose homeostasis in the human body. The hormone insulin partially regulates glucose absorption and glucose conversion to glucose-6-phosphate in hepatocytes.[37] To stimulate *in vivo* microenvironment, the LPMTs were starved for a short period before insulin treatment. Insulin treated LPMTs showed a significant increase in glucose uptake, indicating an active response of hepatocytes toward hormonal stimuli.

4.5.8 Histological evaluation of LPMT

The structural characteristics of 7-day-old LPMTs were analyzed by H&E staining of paraffin-embedded microtissue sections. Stained sections showed dense tissue-like cellular assembly mimicking the hepatic plates present *in vivo* (Figure 22 a). Previous research has demonstrated that, in comparison to traditional monolayer culture, the microtissues preserve native cell morphology and promote improved cell-to-cell interactions (Peshwa *et al.*, 1996; van Zijl and Mikulits, 2010). To the best knowledge, this is the first report that depicts a typical cellular arrangement resembling a hepatic plate within microtissues created via hanging drop culture.

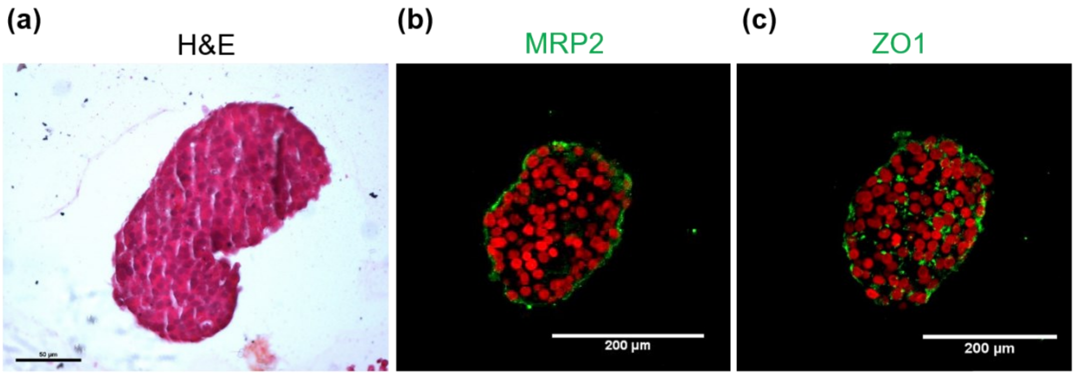

Figure 22. Histological and immunofluorescence staining of LPMTs. (a) Bright-field image of H&E stained LPMT showing hepatic plate-like cellular assembly. Scale bar = 50 µm. (b) & (c) Confocal images showing LMPTs stained for hepatocyte polarization markers MRP2 and ZO1. Cell nuclei were counterstained with PI (red). Scale bar = 200 µm.

4.5.9 Structural polarity of LPMT

The expression of hepatocyte polarization markers MRP2 (apical) and ZO1 (basolateral) by LPMTs was visualized by immunofluorescence staining. MRP2 expression was largely confined to the microtissue's periphery and was less abundant inward (Figure 22 b). Formation of tight junctions necessary for epithelialization was demonstrated by positive staining for the protein ZO1 throughout the microtissue (Figure 22 c).

Hepatocytes are polarized epithelial cells with distinct apical and basolateral domains having specified functions. MRP2 is a bile acid transporter protein situated on the apical canalicular membrane of hepatocyte. While ZO1 is a tight junction protein involved in segregation of the two membrane domains. Hepatocyte polarization is essential for performing liver functions like bile acid secretion, protein secretion and detoxification. HepG2 spheroids made on a PDMS mold have been shown to express MRP2 and ZO1 when encapsulated in GelMA, making them useful for the liver on a chip platform (Bhise *et al.*, 2016). The expression of MRP2 and ZO1 in LPMTs produced in HdCC confirms structural polarization and epithelialization of hepatocytes.

4.5.10 Evaluation of GelMA using LPMT

4.5.10.1 *Structural integrity of LPMTs in hydrogel sandwich and suspension culture*

The LPMTs were kept immobile by the sandwich culture, and the microtissues remained intact throughout a 15-day period without experiencing any significant size changes (Figure 23 c). The LPMTs in alginate showed irregular edges but with intact structure (Figure 23 d). However, in suspension culture, microtissues exhibited agglomeration and fusion (Figure 23 e).

4.5.10.2 *Functional analysis of LPMTs in hydrogel sandwich and suspension culture*

The primary liver functionality of LPMTs in GelMA sandwich and in suspension was evaluated to better understand the influence of the biomaterial GelMA on the microtissue function. Liver-specific functions such as protein synthesis, ammonia detoxification and phase I metabolism-related enzyme activity were analyzed for 15 days. The protein synthesis activity of the LPMT was represented by albumin secreted into the culture medium. Even though the synthesis of albumin was identical in both the groups on day 1, the synthesis increased over time for sandwich-LPMTs and was significantly higher than LPMTs in suspension on days 7 and 15 (Figure 23 f). The capability of LPMTs to detoxify ammonia was assessed by estimating the urea secreted into the culture medium. Similar to the albumin secretion, urea secreted by sandwich-LPMTs increased over time and was considerably higher on days 7 and 15 (Figure 23 g). However, urea secretion by LPMTs in suspension significantly decreased on days 7 and 15. The predominant liver enzyme responsible for phase I xenobiotic metabolism is cytochrome P450 3A4 monooxygenases. The CYP3A4 enzyme activity in sandwich-LPMTs increased significantly over time compared to LPMTs in suspension, where the activity was consistently less throughout the culture period (Figure 23 h).

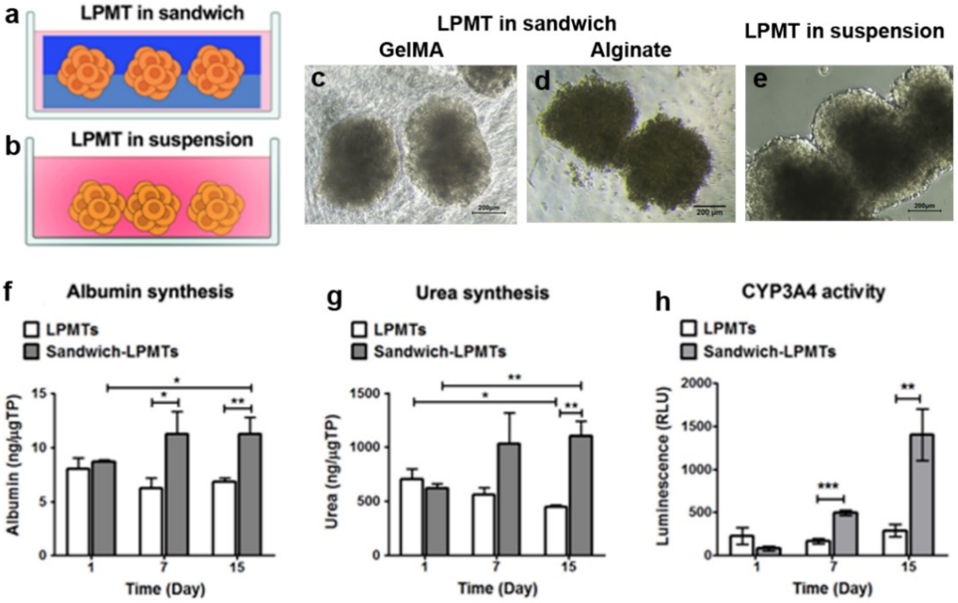

Figure 23. Structural and functional integrity of LPMTs in the sandwich and suspension culture. (a) & (b) Illustration showing LPMTs in sandwich culture and suspension culture. (c & d) Phase-contrast images of the microtissues sandwiched in GelMA and alginate hydrogel, respectively. (e) LPMTs in suspension. Graphs showing (f) levels of albumin secreted by GelMA sandwich-LPMTs and LPMTs in suspension, (g) levels of urea secreted by GelMA sandwich–LPMTs and LPMTs in suspension and (h) CYP3A4 enzyme activity of sandwich-cultured LPMTs and LPMTs in suspension. (a pooled sample of 210 microtissues were analyzed in triplicates for all the assays, *p-value < 0.05, **p-value < 0.01, ***p-value < 0.001). Scale bar = 200 µm. [Reproduced from Roopesh, et al. (2022), *Biotechnol Bioeng.* DOI: 10.1002/bit.28010]

Additionally, the organ-specific activities of LPMTs sandwiched in GelMA hydrogel were compared to LPMTs sandwiched in sodium alginate hydrogel. From day 1 to day 7, the albumin production dramatically increased in both sandwich systems and remained stable till day 15 (Figure 24 a). However, during the course of the culture period, GelMA sw-LPMTs produced significantly higher amount of albumin than Alginate sw-LPMTs (Figure 24 a). From day 1 to day 15, there was a large linear rise in the production of urea in both groups, while GelMA sw-LPMTs consistently produced much more urea than Alginate sw-LPMTs (Figure 24 b). In GelMA sw-LPMTs, the CYP3A4 enzyme activity was maintained from day 1 to day 15 of culture, whereas the enzyme activity in Alginate sw-LPMTs drastically dropped (Figure 24 c).

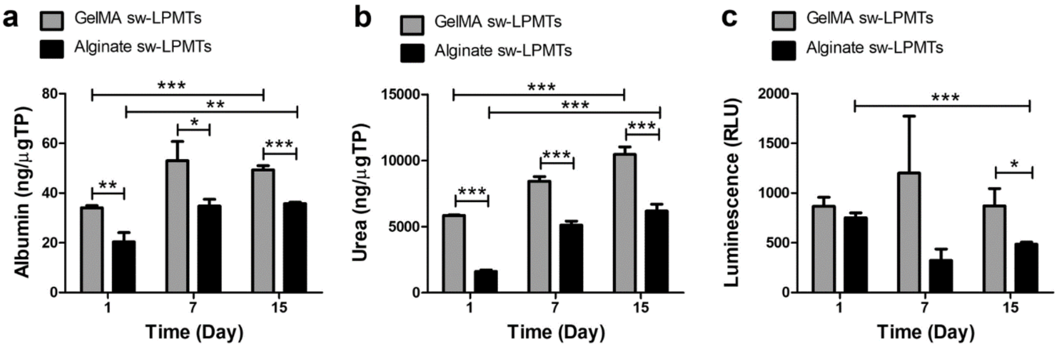

Figure 24. Comparative analysis of the liver functions between LPMTs in the GelMA and Alginate sandwich culture. Graphs showing (a) levels of albumin secretion (b) levels of urea synthesis and (c) levels of CYP3A4 enzyme activity in GelMA sandwich-cultured LPMTs and Alginate sandwich-cultured LPMTs. (a pooled sample of 210 microtissues were analyzed in triplicates for all the assays, *p-value < 0.05, **p-value < 0.01, ***p-value < 0.001). [Reproduced from Roopesh, et al. (2022), *Biotechnol Bioeng.* DOI: 10.1002/bit.28010]

Earlier reports on collagen sandwich culture of hepatocytes have proven the beneficial effect of extracellular matrix on hepatocyte survival and functions (Dunn *et al.*, 1989). Pinkse *et al.*, (2005) have demonstrated that the activation of the ILK-pAkt pathway by interactions between RGD peptides and integrins enhances hepatocyte survival (Pinkse *et al.*, 2005). In the present study, GelMA was chosen because it is a functionalized gelatin that is rich in RGD peptides. Hence, it is expected that the GelMA sandwich culture will provide *in vivo*-like extracellular cues to the microtissues. To study the advantages of GelMA as a biomatrix, comparison between the functions of LPMTs sandwiched in GelMA to the LPMTs in suspension culture was done. The data presented in Figure 23 clearly showcased the beneficial effect of GelMA on liver microtissue structure and function. Further to prove that the functional enhancement of LPMTs in GelMA sandwich is not just merely due to immobilization of microtissues within a hydrogel, the organ specific functions of GelMA sw-LPMTs with Alginate sw-LPMTs were compared.

Alginate is a polymer made of polysaccharides that can form hydrogels through ionic crosslinking. It is an important biomaterial used in numerous applications, including drug delivery and tissue engineering (Lan, Safiejko-Mroczka and Starly, 2010). However, the native form of the polymer has a limited long-term stability and lacks the bioactive components found in the native extracellular matrix (Lee and Mooney, 2012). Hence, alginate hydrogel was chosen as a control for evaluating our GelMA hydrogel. However, it was difficult to prepare sandwich culture using 10% (w/v) alginate solution. Hence, 5% (w/v) of GelMA and alginate was used for the experiment. Higher levels of liver function exhibited by GelMA sw-LPMTs confirmed that GelMA was a superior biomatrix. Taken together, it can be perceived form this study that GelMA is an excellent biomatrix for 3D hepatocyte culture and will be a suitable bioink material for hepatic organoid bioprinting.

4.6 GelMA bioink formulation and rheological analysis

The bioink formulation consisted of 7% (wt/v) GelMA, 3% (wt/v) gelatin and 1% (wt/v) Irgacure-2959 in serum-free culture medium. Although 10% (wt/v) GelMA was proven to be an excellent biomatrix for 3D hepatocyte culture, as a bioink it is not printable at room temperature. To enhance printability, 3% gelatin was added to the bioink based on earlier reports (Kang *et al.*, 2016; Pai, Ajit, *et al.*, 2022). It has been shown that addition of gelatin improves the thermosetting properties of low-concentration GelMA bioink, allowing one to print at temperatures between 15 and 25°C (Yin *et al.*, 2018). While to maintain the total polymer concentration at 10%, the concentration of GelMA was reduced to 7% (wt/v). Further, rheological analysis was carried out to study the sol-gel transition, shear-thinning behavior, and cross-linking kinetics of GelMA bioink.

4.6.1 Temperature sweep analysis

The gelation temperature of GelMA bioink was assessed by cooling the polymer solution from 30 °C to 10 °C at a cooling rate of 1 °C/min. It was observed that as the temperature decreased, the viscosity of the bioink gradually increased (Figure 25 a). A rapid surge in viscosity was observed at temperature below 20°C, suggesting the gelation of bioink. The precise gelling temperature of the GelMA bioink was determined from the derivative of the log viscosity curve. The gelation temperature of GelMA bioink was determined to be 18 °C. Sol-gel transition temperature is the temperature at which a solution transforms into gel form. During extrusion-based bioprinting sol-gel transition of the bioink is essential to extrude smooth regular filaments and to achieve high shape fidelity (Ouyang *et al.*, 2016). GelMA/Gelatin bioinks exhibit temperature-dependent sol-gel transition on cooling and enable stable filament extrusion (Yin *et al.*, 2018). Finding the sol-gel transition temperature of the bioink is critical for setting the printing temperature. Earlier Ouyang *et al.,*(2016) reported that the difference between the gelation temperature of bioink and the printing temperature should be minimum to maintain the shape fidelity of the extruded filament and the printed construct (Ouyang *et al.*, 2016). Hence, based on the above data 19°C was chosen as the printing temperature and the subsequent rheological analysis were done at 19°C.

4.6.2 Dynamic viscosity analysis

The dynamic or shear viscosity is the coefficient of proportionality between the shear stress and shear rate. Materials exhibiting a decrease in viscosity with respect to an increase in shear rate are considered to have shear thinning property. The viscosity of GelMA bioink decreased with an increase in shear rate confirming that it exhibited a shear thinning property (Figure 25 b). In rheology, shear-thinning refers to the non-Newtonian behavior of fluids where the viscosity decreases under shear stress and reverts back to original state when shear stress is not applied (Zołek-Tryznowska, 2016). This property is particularly relevant to the bioink as it ensures continuous extrudability, high shape fidelity and mechanical endurance (Miri *et al.*, 2019). Additionally, the shear-thinning bioink presents a high viscosity to settling cells to maintain suspensions, and a low viscosity during extrusion to aid in the reduction of shear stress which can otherwise lead to cell damage (Wilson *et al.*, 2017). Hence, this implies that GelMA bioink is well suited for high cell density bioprinting.

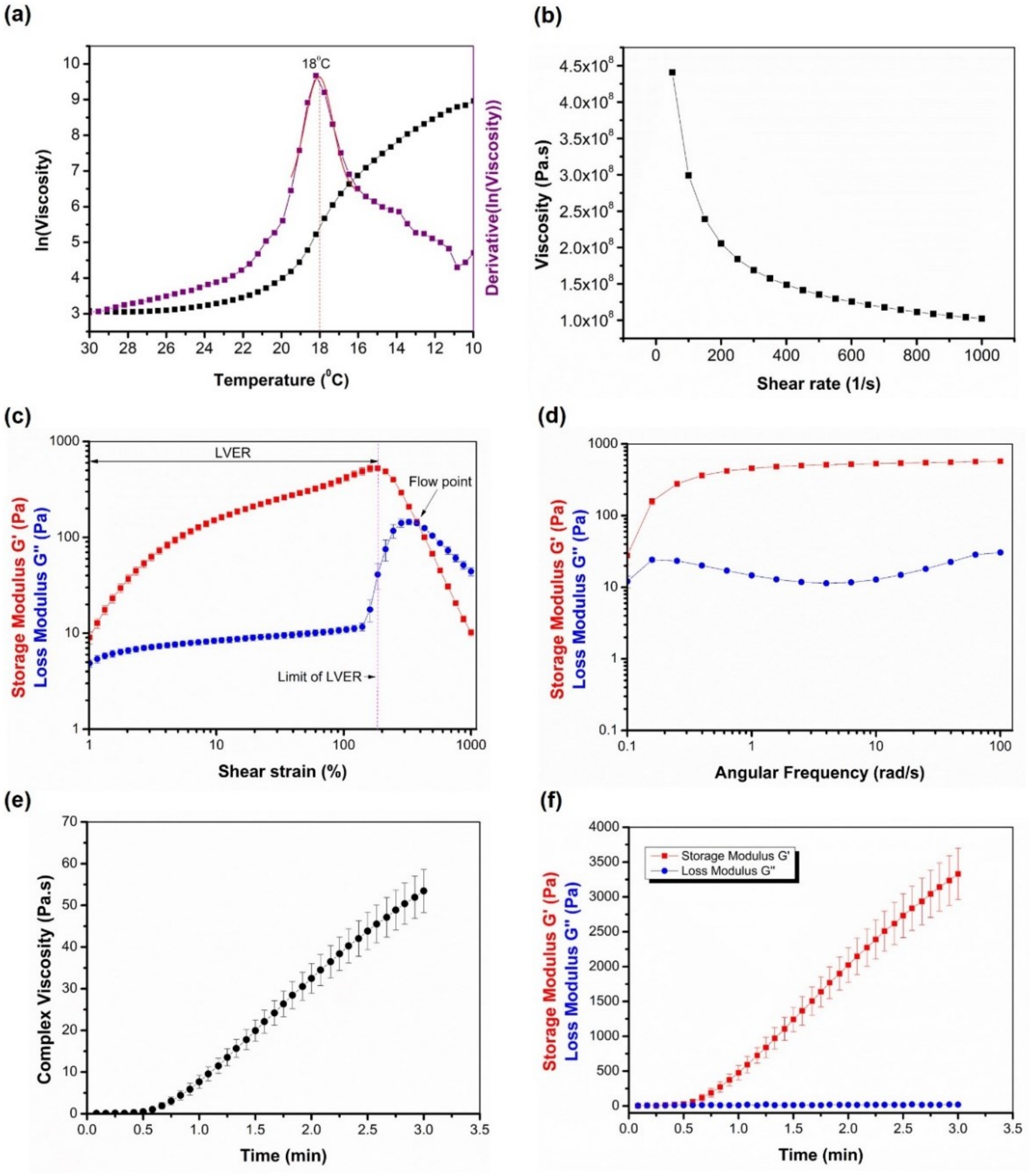

Figure 25. Rheological analysis of GelMA bioink. (a) Temperature sweep curve indicating the precise gelling temperature of GelMA bioink and (b) Viscosity curve depicting shear thinning behavior of GelMA bioink, (c) Strain sweep curve indicating LVER, limit of LVER and flow point of GelMA bioink (n=3), (d) Frequency sweep curve depicting viscoelastic behavior of GelMA bioink (n=3). (e & f) Graph depicting the variation in complex viscosity and storage modulus of GelMA bioink with UV crosslinking time (n=3).

4.6.3 Amplitude sweep analysis

To determine the linear viscoelastic region (LVER) of GelMA bioink, amplitude sweep test was performed. Figure 25 c depicts the strain-sweep curve of GelMA bioink. As indicated in the curve, with an increase in shear stress the storage modulus of the bioink initially increased linearly (until 10 % strain) and started to saturate until the stress value reached 878 Pa causing 185 % strain. However, the storage modulus value started to decrease with further increase in stress. Such a reduction in storage modulus is indicative of structural breakdown (yielding) of polymer chains and the stress value corresponding to this transition is the yield stress. Based on the above information, the region on the storage modulus curve lying between 1 % and 185 % strain can be considered as the LVER of GelMA bioink. In contrast, the values of loss modulus remained merely constant until the applied stress value reached 772 Pa causing 161 % strain and thereafter increased exponentially with further increase in shear stress. On reaching 375 % strain, the values of storage and loss modulus intersected and the loss modulus dominated over storage modulus. This crossover point is the flow point which indicates the oscillatory strain (or stress) above which the material will flow.

In the LVER, applied stresses are insufficient to cause structural breakdown of the material and therefore it is the ideal region to study the microstructural properties of the material. Ideally shear moduli remains independent of strain amplitude within the LVER of the material (Cooke and Rosenzweig, 2021). However, the storage modulus of GelMA bioink was increasing during the initial phase within LVER. This can be attributed to the progressive physical gelation of the bioink at 19 °C. The dominance of storage modulus within LVER is indicative of the elastic gel-like character of GelMA bioink which is a plus for extrusion bioprinting (Cooke and Rosenzweig, 2021). The yield stress value of the bioink can be referred to set the printing parameters required for extrusion bioprinting (Schwab *et al.*, 2020).

4.6.4 Frequency sweep analysis

Frequency sweep test was conducted to investigate the viscoelastic property of GelMA bioink. As shown in Figure 25 d, the storage modulus (G') of the bioink remained many folds higher than the loss modulus (G'') across the frequency range of 0.1 to 100 Hz. Dominance of storage modulus indicates that GelMA bioink at 19 °C have a predominantly elastic rather than viscous character within the LVER. This also indicates that GelMA bioink retains sufficient elastic recoil, which is essential for achieving good shape fidelity after extrusion during bioprinting (Schwab *et al.*, 2020). About 10 % strain was applied during this test, because the strain value was within the LVER of the bioink as determined from the amplitude sweep test.

4.6.5 UV curing analysis

The gelation characteristics of the GelMA bioink was investigated in the presence of UV irradiation at a constant temperature. The gelation kinetics was assessed based on the changes in complex viscosity and storage modulus of the bioink. Figure 25 (c & d) shows the variation in the complex viscosity and storage modulus of the bioink with time during the UV crosslinking process. The complex viscosity and storage modulus of GelMA increased linearly with the time of UV exposure. This clearly shows that the methacrylamide moieties have been consumed for crosslinking and bioink is getting more elastic with the UV exposure time. Since, 1min was opted as the optimal photocrosslinking time (section 4.2.3), the storage modulus of GelMA after 1 min of UV irradiation was noted and was found to be approximately 500 Pa. Earlier it has been reported that UV-crosslinked GelMA hydrogels having a storage moduli between 400 and 800 Pa were optimal for proliferation of encapsulated cells (Young *et al.*, 2020). Hence, it can be very well stated that the GelMA bioink will facilitate cell proliferation after UV crosslinking.

4.7 Printability assessment of GelMA Bioink

Depending on the bioprinting modality the printability of the respective bioink can be assessed based on various parameters. For extrusion-based 3D bioprinting, printability refers to the suitable extrudability, filament formation and shape fidelity of the filament and the printed construct as a whole (Gillispie *et al.*, 2020). A conical shaped printing nozzle having an inner diameter of 840 μm was selected for this study due to two reasons. Primarily, it has been earlier reported that conical printing nozzles deliver high cell viability compared to cylindrical needles (Billiet *et al.*, 2014). In addition, considering the size of the organoid, an inner diameter of 840 μm was selected to reduce the cell damage due to shear stress.

4.7.1 Level 1: Extrudability

The ability of the bioink to form a continuous filament on extrusion through a nozzle under given printing condition is defined as extrudability and it is the basic requirement for printability. GelMA bioink was extruded at two different temperatures to study the influence of printing temperature on extrudability. As shown in Figure 27 a, at 25 °C the bioink was extruded as drops when a dispensing pressure of 25 kPa was applied, whereas at 19 °C continuous filaments of bioink were extruded at 33 kPa. The extruded filament was regular and stable. This clearly showed that at 19°C the bioink achieved proper gelation and could be well extruded since the printing temperature was closer to the sol-gel transition temperature (18°C) of bioink. Whereas at 25°C, due to incomplete gelation the bioink was extruded as a drop.

A similar correlation was drawn between gelation temperature and printing temperature on the extrusion status of gelatin-based bioink by Ouyang *et al.*,(Ouyang *et al.*, 2016). Further the stability of the extruded filament demonstrates the shear recovery of GelMA bioink, which is a characteristic property of shear thinning materials essential for maintaining the shape fidelity of printed structure (Zołek-Tryznowska, 2016). Rheological properties like viscosity, sol-gel transition and shear thinning affects the extrudability of a bioink (Zołek-Tryznowska, 2016). At the same time, the extrudability of a bioink are also governed by printing parameters like temperature, applied pressure and nozzle diameter (Gillispie *et al.*, 2020).

The inner diameter and geometry of the printing nozzle also affects the extrudability of a bioink. It has been reported that, bioinks could be easily extruded when the diameter of the nozzle is increased and a conical nozzle is chosen over cylindrical nozzle (Hölzl *et al.*, 2016). This substantiates the easy extrusion of GelMA bioink through a conical printing nozzle having an inner diameter closer to 1 mm.

4.7.2 Level 2: Line printing and filament characterization

The second level of printability assessment involved characterization of the extruded bioink filament after printing on a substrate. Parameters such as filament spreading, uniformity and stability were analyzed to determine the shape fidelity of the printed filament.

In general, filament width and filament spreading ratio are analyzed to assess filament spreading. Since the extrusion pressure and print speed affects the filament spreading, filaments were printed by applying two different extrusion pressure and at various speed. Figure 27 b shows the images of the filaments printed at various extrusion pressure and print speed. The initial dispensing pressure was set at 33 kPa because that was the minimum pressure required to extrude GelMA bioink at 19 °C. Table 5 shows the mean values of filament width and filament spreading ratio corresponding to the printed filaments. The filament width decreased with an increase in print speed at both 33 kPa and 37 kPa pressure. However, at a particular print speed, the filament width was higher when the extrusion pressure was 37 kPa. The filament width was much closer to the nozzle diameter at a pressure of 33 kPa, and 16 and 18 mm/s print speed compared to the other printing conditions. The filament spreading ratio was above one at 10 mm/s print speed and 33 kPa pressure. However, the ratio decreased and approached to one at print speed 16 and 18 mm/s. While on applying a pressure of 37 kPa, the filament spreading ratio was far above one at all the print speed, although a reduction in value was observed with increasing print speed.

Table 5 Variation in filament width with respect to changes in print speed and dispensing pressure.

Print speed (mm/s)	Nozzle diameter (µm)	Filament width at 33 kPa (µm)	Filament spreading ratio at 33 kPa	Filament width at 37 kPa (µm)	Filament spreading ratio at 37 kPa
10	840	1183.6 ± 37.9	1.4	1781.7 ± 51.8	2.12
12	840	1199.5 ± 34.3	1.42	1606.3 ± 66.4	1.91
14	840	1039.6 ± 34.9	1.23	1515.1 ± 59.1	1.8
16	840	893.7 ± 114.6	1.06	1285.3 ± 81.8	1.53
18	840	893.8 ± 83.4	1.06	1169.6 ± 62.9	1.39

Filament spreading will have an impact on the inter-filament distance and layer height, which in turn will affect the shape fidelity and macroporosity of the 3D printed construct (Schwab *et al.*, 2020). Ideally, filament width should match the nozzle diameter and a spreading ratio equal to one is desirable to mimic the intended design. As observed in Table 5, a reduction in filament width with an increase in print speed is expected because the dwell time of the printer head decreases at higher print speed and therefore less bioink will be extruded at a point. Earlier Chang *et al.,* (2011) have reported that with increasing the print speed, the suspended filament experiences tension along the deposition direction and becomes thinner (Chang *et al.*, 2011). At the same time, rise in extrusion pressure could lead to deposition of excess amount of bioink yielding thicker filaments (Chen, Li and Ke, 2008). The same principle applies to the filament spreading ratio, since that is positively corelated to the filament width.

Filament uniformity is a measure of the regularity and continuity of a 3D printed filament and a uniformity ratio of one indicates regular continuous filament (Gao *et al.*, 2018). Filament uniformity affects the layer stacking and thereby the shape fidelity of a multilayer construct. Filament uniformity ratio was determined for all the filaments printed at different extrusion pressure and print speed. Table 6 shows the mean values of the filament uniformity ratio corresponding to the 3D printed filaments. The filament uniformity ratio was slightly above one at all printing conditions with a very small difference between different conditions suggesting that the filaments were a little irregular. Images of the printed filaments shown in Figure 27 b also reflects the above observation. At a given extrusion pressure, a print speed of 14 mm/s yielded a uniformity ratio closest to one compared to other printing conditions. This could be explained by the fact that at lower print speed excess bioink deposition may develop irregular boundaries, while at higher print speed the filament may break down due to high tension resulting in non-uniform deposition (Habib *et al.*, 2018). Taking into consideration both the filament spreading and uniformity, a feed rate of 16 mm/s and an extrusion pressure of 33 kPa was chosen for further printability studies.

Table 6. **Variation in filament uniformity ratio with respect to changes in print speed and extrusion pressure.**

Print speed (mm/s)	Filament uniformity ratio at 33 kPa	Filament uniformity ratio at 37 kPa
10	1.011 ± 0.005	1.016 ± 0.005
12	1.011 ± 0.003	1.014 ± 0.004
14	1.007 ± 0.002	1.009 ± 0.004
16	1.012 ± 0.005	1.01 ± 0.002
18	1.013 ± 0.005	1.008 ± 0.002

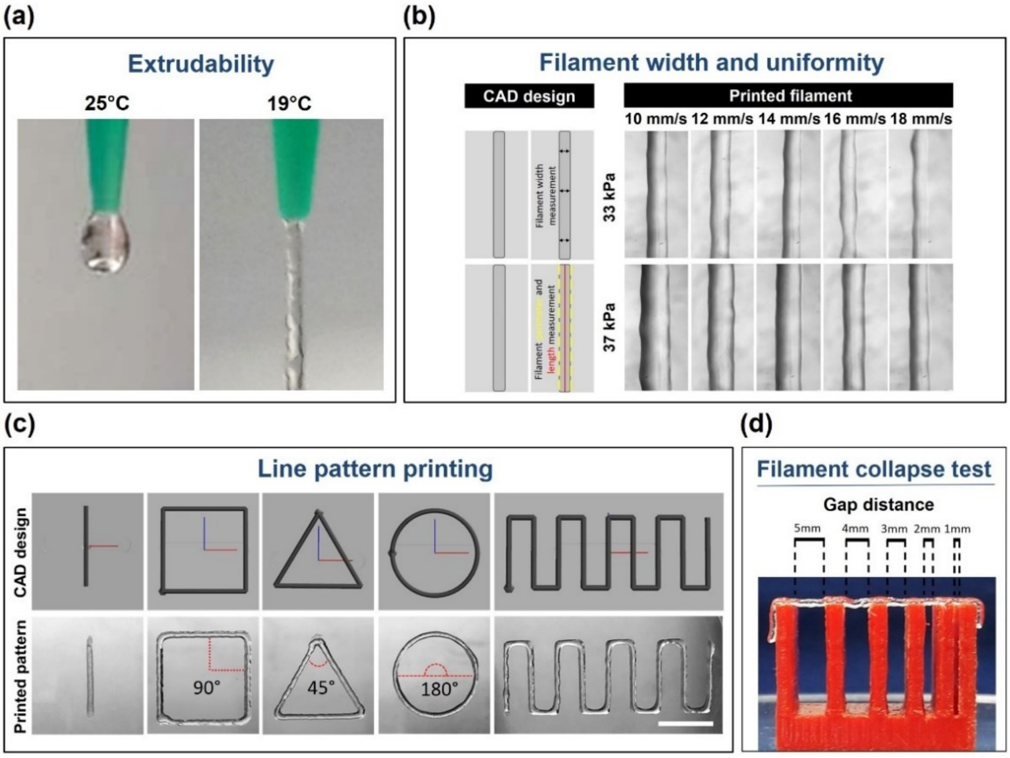

Figure 26.Printability assessment of GelMA bioink by filament characterization (a) Photographs showing extrudability of GelMA bioink. (b) Images showing width and uniformity of the filaments printed at different extrusion pressure and print speed in comparison to CAD design. (c) Photographs showing the CAD design and the corresponding 3D printed line pattern. (d) Photograph showing stability of 3D printed filament spanning over various gap distances.

Filament printing across various angles is a method to evaluate time-dependent flow (prior to stabilization via crosslinking) characterized by filament fusion at vertices. Filament fusion at sharp angles is a demerit for a bioink, as it reduces the printing resolution (He *et al.*, 2016). As shown in Figure 27 c different patterns of lines passing through various angles were printed successfully using the optimal printing parameters. The 3D printed patterns were very well matched with the CAD designs and filament fusion was not observed at vertices. The angle at the vertex of each pattern was closer to the intended angle. This suggest that GelMA bioink can be printed with high resolution by following the optimal printing parameters described earlier.

The shape fidelity of a multilayer construct depends on the mechanical strength of the 3D printed filament to support filament stacking in the vertical direction. Similarly, transversal porosity is essential to ensure proper mass transfer to the cells inside a multilayer construct. To achieve transversal porosity, the infill density of the construct is reduced by printing porous patterns such as a rectilinear grid. However, preventing filament collapse along the axial direction while spanning over a gap between underlying filaments is imperative. To analyze the ability of GelMA bioink to counter gravitational pull, a filament collapse test was performed, and collapse area factor was determined. As shown in Figure 27 d, there was only minimal sagging of the printed filaments with the increase in distance. The values of collapse area factor were approaching 100% with a decrease in inter-pillar distance suggesting a minimal deflection. The mean values of collapse area factor were 97.4 ± 0.9 %, 96.9 ± 0.9 %, 98.1± 0.7%, 100.8 ± 0.1% and 100.6 ± 0.3 % for gap distances 5 mm, 4 mm, 3 mm, 2 mm and 1 mm respectively. Earlier, Habib *et al.,* (2018) have demonstrated that the filament collapse depends on the mechanical strength of filament and the inter-filament distance of the underlying layer (Habib *et al.*, 2018). The authors reported that a collapse area factor of 100% is ideal for printing multilayer constructs. Correlating this information to our result suggest that the GelMA bioink filaments are mechanically stable and could very well counter gravitational pull when spanning over an inter-filament distance between 1 to 2 mm. Based on this data, an inter filament distance of 1.5 mm was selected for multilayer printing in the following experiment.

4.7.3 Level:3 Multilayer printing and shape fidelity of printed construct

Geometric accuracy, layer stacking and structural integrity are the important parameters that have been proposed for the assessment of shape fidelity in a 3D printed multilayered construct (Schwab *et al.*, 2020). To assess the geometric accuracy, dimensions of the multilayered construct was measured post-printing and was compared to the dimensions of the intended design. Figure 27 e gives the side view and top view of the 3D printed two-layered (2L), four-layered (4L) and six-layered (6L) constructs. As seen in the Figure 27 e the multilayered constructs displayed a square geometry over the *x-y* plane and maintained this geometry over the x-z plane. The dimensions (length × breadth × height) of the multilayered constructs are given in Table 7. The multilayered constructs exhibited a linear relationship between number of layers and the height of the construct. The intended heights of the constructs determined based on nozzle diameter are 1.68 mm (2 layers), 3.36 mm (4 layers) and 5.04 mm (6 layers). The measured height of the constructs closely matched with the intended values Table 7. Close examination of multilayered GelMA hydrogel construct under microscope revealed uniform distribution of printed filaments with a pore geometry closely matching a square shape Figure 27 b. The printability factor (*Pr*) for GelMA bioink was determined from the dimensions of the pore formed between filaments and the obtained mean value was 0.929 ± 0.029.

Table 7. Dimensions of the multi-layered constructs

No. of layers	Length (mm)	Breadth (mm)	Height (mm)
2	10.033 ± 0.06	10.07 ± 0.2	1.63 ± 0.01
4	10.03 ± 0.03	10.01 ± 0.06	3.32 ± 0.01
6	10.08 ±0.03	10.08 ± 0.05	4.92 ± 0.01

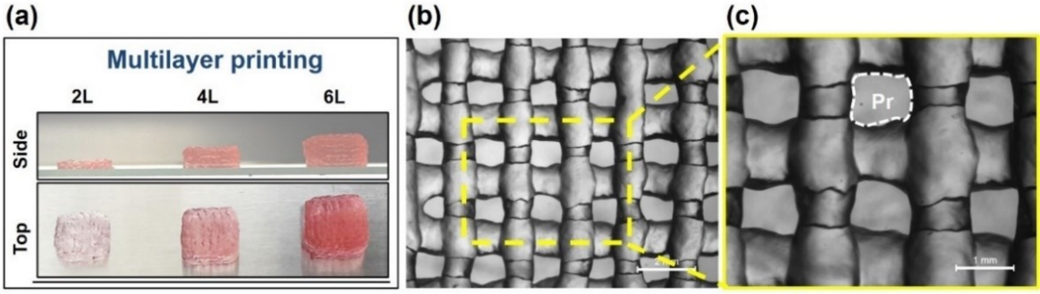

Figure 27. Printability of GelMA bioink during multilayer printing. (a) Photograph showing 3D printed multilayered constructs with 2, 4 and 6 layers. (b) Stereomicroscopic image of the 3D printed two-layered construct showing filament characteristics at cross-over points and inter-filament pores. (c) Image of the 3D printed two-layered construct showing pore perimeter and area (dash line) chosen for calculating printability factor (Pr).

Recapitulating the shape and height of the design in the bioprinted construct is very critical during 3D bioprinting of complex tissue construct. Liver tissue is a classic example of structure-function analog. Hence, while printing a liver tissue construct, it is very important to position cells in appropriate pattern as *in vivo*. As shown in Figure 27 a, the printed construct closely matched the geometry of the CAD design indicating that GelMA bioink can be patterned efficiently according to the design. Along with geometrical precision, the maximum height achieved when printing a specified geometry reflects the quality of layer stacking in multilayered constructs. A significant reduction in layer height indicates merging of the subsequent layers and this can negatively affect the shape fidelity (Schwab *et al.*, 2020). In this study, the height of the multilayered construct was in close proximity to the intended height and therefore this suggests that there was no significant layer merging after bioprinting. The ideal value for printability factor is one (Ouyang *et al.*, 2016). This value indicates the efficiency of the printed filament to generate square-shaped pore indicating absence of filament spreading at cross-over points. In this study the obtained value of 0.9 is close to 1 and therefore indicates good printability behavior of bioink.

Taken together, all the observation related to printability assessment suggest that GelMA bioink is printable and has adequate printability value at optimal printing conditions.

4.8 NGMA Synthesis

Two batches of NGMA were synthesized and the mean percentage yield of synthesis was 72.4 %. The unreacted monomers were completely removed by alternate washing with tetrahydrofuran and ice-cold water. A solid white pellet was obtained after drying. The pellet was powdered before dissolving in any solvents. The co-polymer NGMA has been shown to be an excellent cytocompatible thermoresponsive culture substrate for non-invasive retrieval of cell sheets (Joseph *et al.*, 2010; Joseph, Prasad and Joseph Sreenivasan K., 2011). In this study, NGMA was synthesized to prepare thermoresponsive culture dishes for hepatic organoid culture and easy retrieval.

4.9 Physico-chemical characterization of NGMA

4.9.1 Attenuated Total Reflectance-Fourier Transform Infrared Spectroscopy

The ATR–FTIR spectrum of NGMA showed characteristic peaks corresponding to PNIPAAm and GMA moieties in the copolymer (Figure 28). Peaks at 1637.6 cm^{-1}, 1533.3 cm^{-1}, and 1457.4 cm^{-1} represented the amide group in PNIPAAm. While the peak at 1725.1 cm^{-1} of C=O and peaks at 841.4 cm^{-1}, 913.8 cm^{-1}, and 992.7 cm^{-1} of epoxy groups confirmed the presence of GMA moieties in co-polymer. The FTIR spectrum compared well with the earlier report (Joseph *et al.*, 2010).

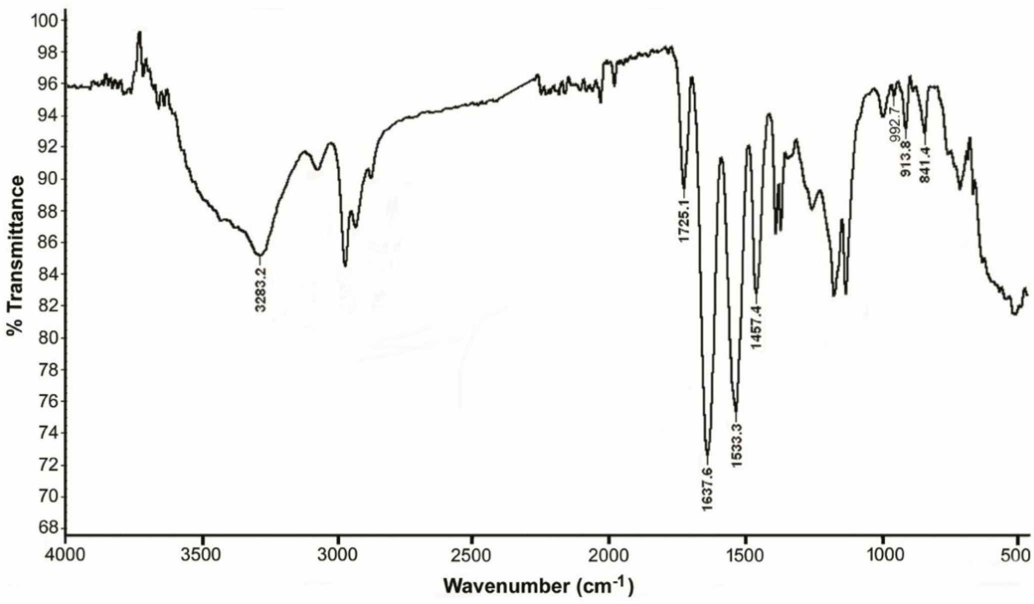

Figure 28. FTIR spectrum of NGMA copolymer. Peaks at 1637.6 cm^{-1}, 1533.3 cm^{-1}, and 1457.4 cm^{-1} represent amide group of PNIPAAm. The peak at 1725.1 cm^{-1} shows the presence of C=O and peaks at 841.4 cm^{-1}, 913.8 cm^{-1}, and 992.7 cm^{-1} indicate epoxy group GMA moieties.

4.9.2 ^{1}H Nuclear Magnetic Resonance Spectroscopy

The ^{1}H NMR spectrum of the NGMA confirmed the co-polymerization of PNIPAAm with glycidyl methacrylate (Figure 29). The broad peak at 6.7 ppm corresponded to the protons in amide groups of the NIPAAm units, whereas the resonance signals at 3.9 ppm corresponded to the methylidene protons next to the amide group. The signals for the methylene and methylidene protons of the epoxy groups of GMA units were detected at 2.7 and 3.3ppm, respectively. The NMR spectrum compared well with the previous report (Joseph *et al.*, 2010).

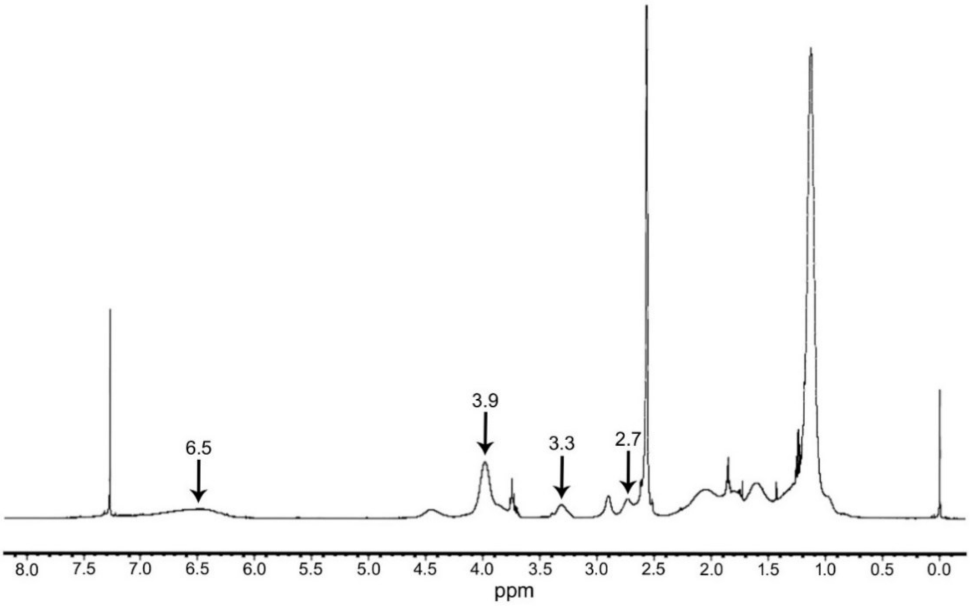

Figure 29. ^{1}H NMR spectrum of NGMA copolymer. Peaks at 3.9 ppm and 6.5 ppm correspond to the protons of NIPAAm units and peaks at 2.7 ppm and 3.3 ppm correspond to epoxy groups of GMA units.

4.9.3 Differential Scanning Calorimetry

Lower critical solution temperature (LCST) is the temperature below which the components of a solution are miscible in all proportions. The DSC thermogram of NGMA showed the LCST at 29.02°C (Figure 30). LCST of PNIPAAm was lowered from 32°C to 29.02°C as a result of copolymerization with hydrophobic monomer. The temperature at which the glass transition occurred closely matched with earlier report (Joseph *et al.*, 2010). Above LCST, the water molecules dissociate from the co-polymer because the hydrophobic interaction of the isopropyl groups of PNIPAAm surpasses the hydrophilic nature of the amide groups. While below LCST, due to the hydrogen bonding between water and hydrophilic amide groups of the PNIPAAm, co-polymer shows water-swollen property (Zhang, Wu and Chu, 2004). This very property of NGMA makes it suitable substrate for cell culture at 37°C, which is above LCST and enable swift cell retrieval below LCST.

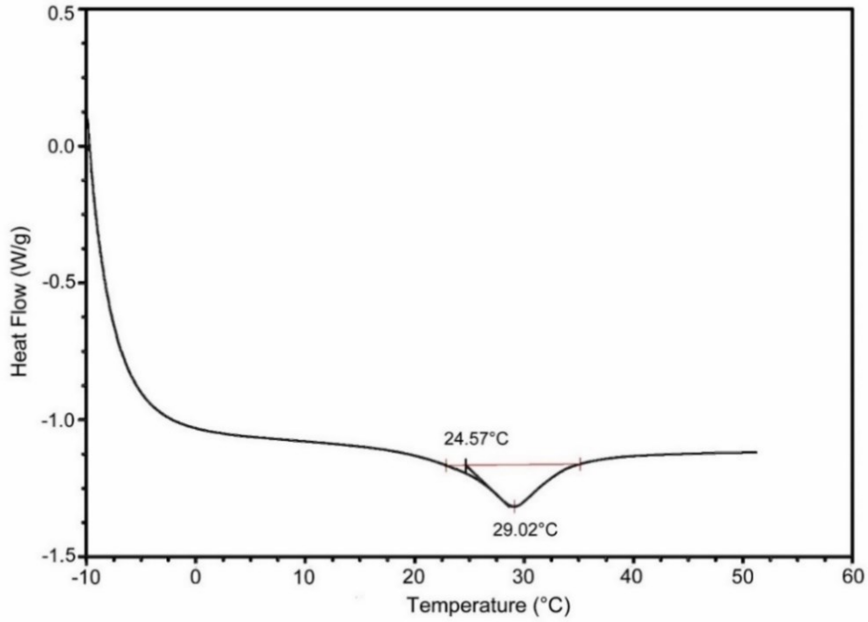

Figure 30. DSC thermogram of NGMA copolymer depicting LCST at 29.02°C.

4.9.4 Gel Permeation Chromatography

The gel permeation chromatogram of NGMA copolymer depicted the peak molecular weight (Mp) at 106498 (Figure 31). The molecular weight averages of NGMA were found to be 77,161 (number average, Mn) and 97,115 (weight average, Mw). The narrow dispersity value of 1.26 indicated that the synthesized polymer chains were nearly identical in length.

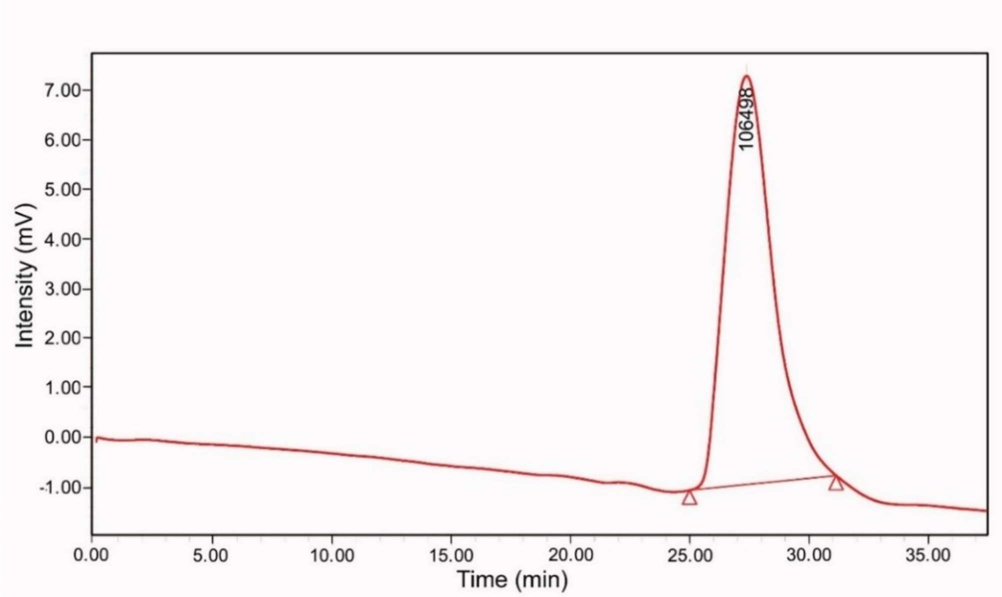

Figure 31. Gel permeation chromatogram of NGMA copolymer depicting peak molecular weight (Mp) at 106498. The single narrow peak indicated that the polymer chains formed are nearly identical in length.

4.10 Thermoresponsive property of NGMA dish

To assess the thermoresponsive property of NGMA dish, water contact angle was measured at temperature above and below LCST of NGMA and was compared to uncoated PSTC dish (Figure 32 a). Above LCST, the mean water contact angle of PSTC dish and NGMA dish were 75.4° ± 1.4 and 72.9° ± 1.6, respectively. While below LCST, the mean water contact angle of PSTC dish and NGMA dish were 76.9° ± 1 and 66.3° ± 0.6. The contact angles from different points of the coated surface were nearly identical showing the uniformity of the coating for the NGMA on PSTC (Figure 32 b). Above LCST, both the dishes exhibited similar hydrophobicity suitable for cell adhesion and proliferation (da Silva, Mano and Reis, 2007). Whereas below LCST, there was a reduction in contact angle of NGMA dish, indicating a temperature-dependent phase transition from hydrophobic to hydrophilic nature. This typical phase transition confirmed the thermoresponsive property of NGMA dish and will help in swift retrieval of cells from the dish as previously reported (Joseph *et al.*, 2010).

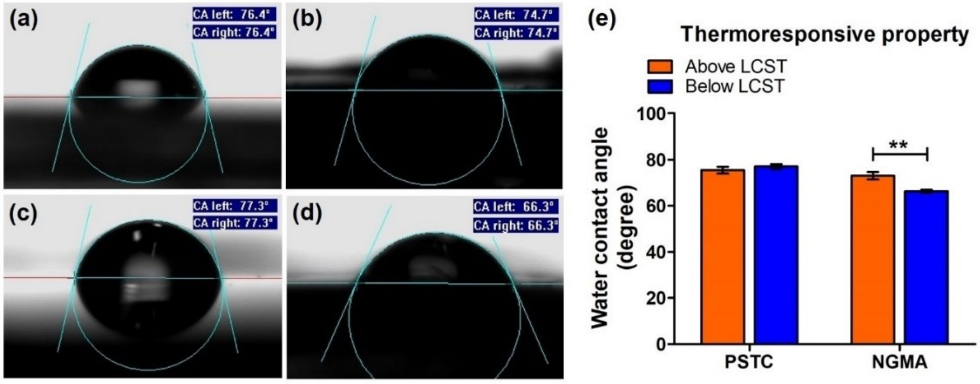

Figure 32.Thermoresponsive property of NGMA dish. Water contact angle measurement by sessile drop method for (a & b) PSTC dish and NGMA dish respectively at 37° C and (c & d) PSTC dish and NGMA dish respectively at 4° C. (e) Graph depicting the mean water contact angle measurements of PSTC dish and NGMA dish at 37°C (above LCST) and 4° C (below LCST).

4.11 In-vitro cytotoxicity evaluation of NGMA

4.11.1 Cell adhesion and viability

The L-929 cells seeded on NGMA dish adhered and attained a characteristic spindle morphology like PSTC (Figure 33 a & b). Neutral red staining of the cells adhered on NGMA dish revealed 100% cell viability at the end of 48 h similar to the cells on PSTC (Figure 33 c & d).

4.11.2 Cell proliferation

After 24 h of culture, the metabolic activity of L-929 cells cultured on NGMA and PSTC did not show any significant difference in cell proliferation. However, significant differences in cell proliferation were noted after 72 h. The lower cell proliferation on NGMA dish can be related to reduced surface roughness as reported earlier (Joseph *et al.*, 2010). It has been reported that a rough surface enhances cell proliferation and this substantiate the higher cell proliferation on PSTC dish (Lampin *et al.*, 1997).

Taken together, our data showed that the NGMA was non-cytotoxic, and it can be a suitable substrate for organoid culture.

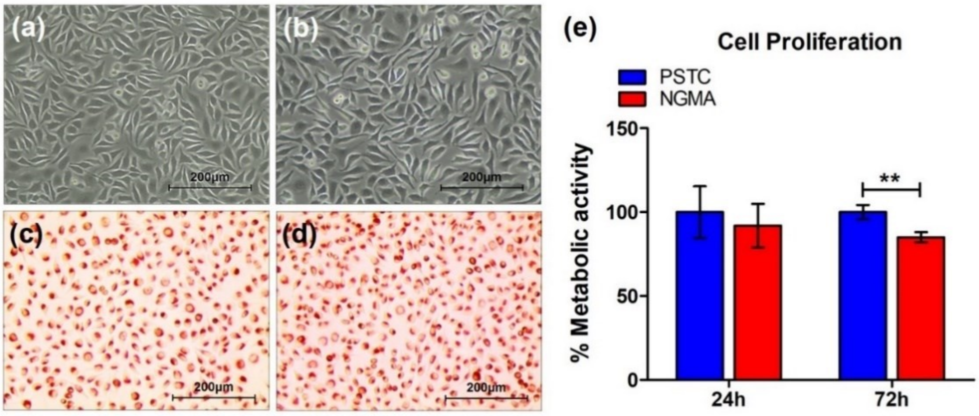

Figure 33. *In vitro* cytotoxicity evaluation of NGMA. (a & b) Phase-contrast images showing morphology of L929 cells adhered on PSTC dish and NGMA dish respectively. (c & d) Bright-field images showing neutral red staining of L929 cells cultured on PSTC dish and NGMA dish, respectively. (e) Graph depicting percentage metabolic activity of L929 cells cultured on PSTC dish and NGMA dish respectively, after 24 h and 72 h.

4.12 Isolation and culture of parenchymal and non-parenchymal cells from rat liver

As a preliminary step towards the development of hepatic organoid, rat liver cells were isolated and cultured *in vitro*. Figure 34 (a) shows the steps involved in isolation of rat liver cells. On an average, about 200 to 300 million cells having 80 to 90 % viability were obtained during each isolation. The isolated hepatocytes and NPCs were then segregated by differential centrifugation before culture to identify individual cell types and to enable mixing of cells in a definite ratio during organoid culture. Primary hepatocytes and non-parenchymal cells (NPCs) were chosen over induced pluripotent stem cells for organoid culture because they express mature liver phenotype compared to a fetal liver phenotype expressed by iPSC-differentiated liver cells (Baxter *et al.*, 2015b). Also, primary rat liver cell isolates have been reported to display histological-organization *in vitro* when co-cultured in the presence of growth factors HGF and EGF (George K Michalopoulos *et al.*, 2001). The high yield and viability of isolated cells can be attributed to the efficiency of the modified two-step perfusion method reported by Seglen *et al.*(Seglen, 1976).

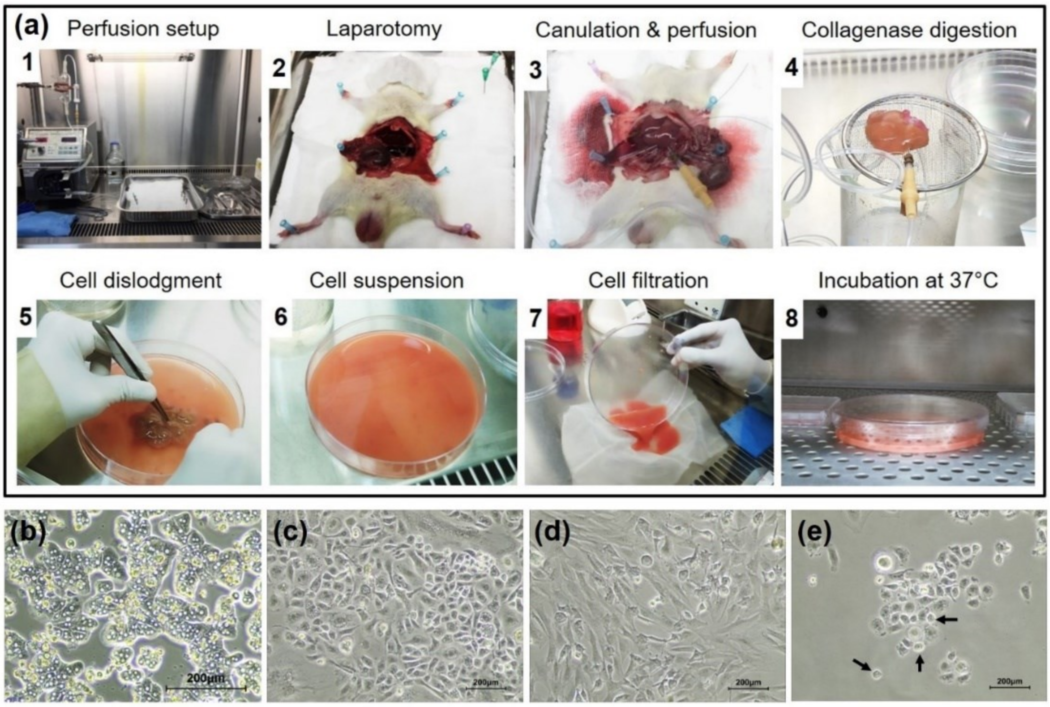

Figure 34. Isolation and culture of rat liver cells. (a) Photographs showing step-by-step procedure involved in isolation of rat liver cells. (b-e) Phase-contrast images of isolated hepatocytes, sinusoidal endothelial cells, stellate cells and kupffer cells (black arrows) respectively, after 48 h of culture on collagen-coated dishes.

The isolated liver cells adhered to the collagen-coated dishes, and they exhibited characteristic cell morphology. Single and binucleated hepatocytes with polygonal shapes were found in the hepatocyte monoculture (Figure 34 b). The NPC fraction consisted of sinusoidal endothelial cells (SEC) with cobblestone-like morphology (Figure 34 c), hepatic stellate cells (HSC) with elongated and flat cell morphology

(Figure 34 d), and kupffer cells (KC) which were small and round in morphology (Figure 34 e). The characteristic cell morphology observed in our culture system matched well with the earlier report (Bale *et al.*, 2016).

4.13 Characterization of rat liver parenchymal and non-parenchymal cells

The isolated hepatocytes and NPCs were characterized by immunofluorescence staining. The markers for cell identification was selected based on a previous report by Bale *et al* (Bale *et al.*, 2016). Figure 35 shows the isolated rat liver cells stained for their cell-specific markers. Hepatocytes were positively stained for albumin (Figure 35 a), confirming their protein synthesis functionality (Bale *et al.*, 2016). Sinusoidal endothelial cells were identified by the expression of CD32b (Figure 35 b) which is a low affinity Fc γ receptor essential for clearance of small circulating IgG complex from liver (Brech and Berg, 2000). Kupffer cells were identified by the expression of CD163 (Figure 35 c), a scavenger receptor involved in clearance of haptoglobin-hemoglobin complex from the circulation and helps in hemoglobin metabolism (Philippidis *et al.*, 2004). Stellate cells showed uniform distribution of highly organized F-actin network within the cells (Figure 35 d), which is a characteristic feature of in-activated stellate cells (Cui *et al.*, 2014).

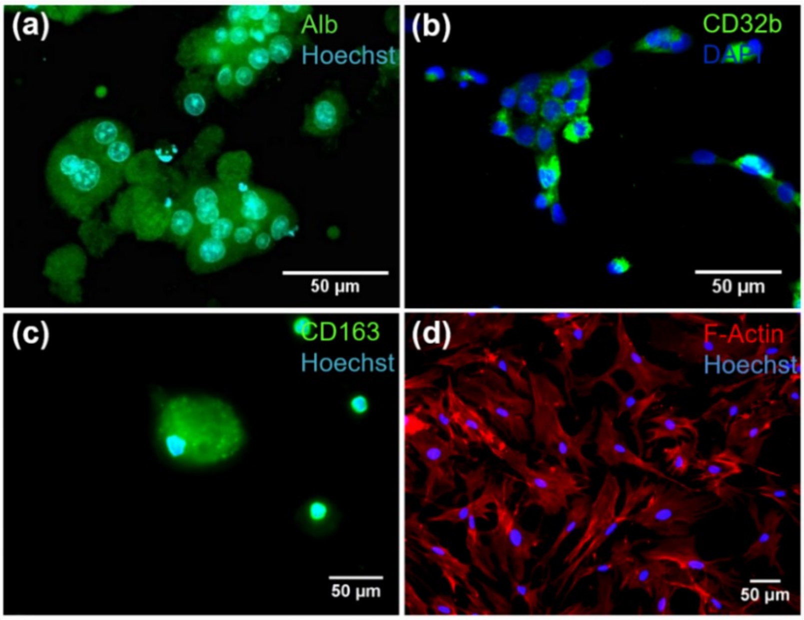

Figure 35. Characterization of rat liver cells. (a-d) Fluorescence images showing rat liver cells stained for markers hepatocytes (albumin), sinusoidal endothelial cells (CD32b), Kupffer cells (CD163) and stellate cells (F-actin) respectively.

4.14 Development of hepatic organoid on NGMA dish

The method for the development of hepatic organoids on NGMA dish was optimized after testing two different strategies. The adhesion of cells on an NGMA dish, self-organization of multiple cell types and the swift retrieval of organoids by the thermoresponsive nature of the culture dish were the critical parameters for selecting the strategy.

4.14.1 Strategy 1: Hepatocyte and NPC co-culture in NGMA dish

The first strategy to develop hepatic organoids was based on the co-culture of hepatocytes and NPCs in NGMA dish. The hepatocytes and NPCs were seeded in NGMA dishes at a ratio of 7:3 (Hep: NPCs) like the *in vivo* tissue. However, as shown in Figure 36 a, most of the cells particularly hepatocytes did not adhere to the dish even after 24 h and were seen as cell aggregates suspended in the media. The aggregates gradually became compact spherical microtissues after 3 days (Figure 36 b) and the size of the microtissues increased after 5 days in culture (Figure 36 c). At the same time, few cells were found attached to the dish. After 7 days of coculture, the cells started to disintegrate from microtissues (Figure 36 d). The non-adherence of hepatocytes to the thermoresponsive dish could be due to the lack of matrix proteins which is essential for anchoring primary hepatocytes. Earlier He *et al.,*(2010) have demonstrated the use of galactose-immobilized thermoresponsive culture surface for improving hepatocyte cell adhesion and proliferation (He *et al.*, 2010). However, the immobilization process increases the complexity and can have high batch-to-batch variation. From the above observation, it was clear that the strategy 1 was inefficient as there was a lack of complete cell attachment and cell organization. Hence, this strategy was not implemented for organoid development.

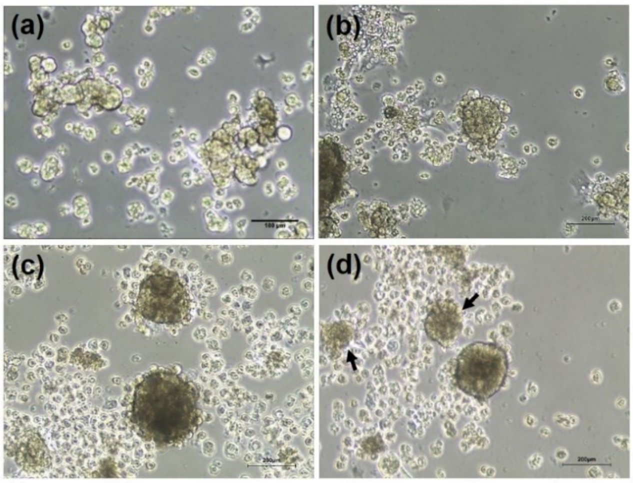

Figure 36. Hepatocyte and NPC coculture on NGMA dish. (a) Phase-contrast image showing unadhered rat liver cells and cellular aggregates after 24 h of co-culture on NGMA dish. (b) Image showing suspended compact spherical microtissues formed after 3 days of coculture on NGMA dish. Few NPCs are seen attached to the dish. (c) Image showing suspended enlarged spherical microtissues after 5 days of coculture on NGMA dish. (d) Image showing disintegrated microtissues (black arrow) after 7 days of coculture on NGMA dish.

4.14.2 Strategy 2: Hepatocyte and NPC co-culture on MSC feeder layer in NGMA dish

Primary hepatocytes are anchorage dependent epithelial cells that require an ECM to adhere and grow. Thermoresponsive dishes as such does not harbor any matrix ligands to adhere. In order to improve the primary liver cell adhesion and function, inclusion of a feeder layer on thermoresponsive dishes has been reported earlier (Sakai *et al.*, 2013; M. Fujii *et al.*, 2018). Sakai *et al.,* (2018) utilized skin fibroblast cell feeder layer to culture hepatocytes, while Fuji *et al*., (2018) utilized adipose derived mesenchymal stem cell (MSC) feederlayer to culture NPCs. The resultant multilayered cell sheet from both the studies possessed high liver-specific functions compared to their counterparts without feederlayer. Inspired from the above studies, use of MSC feeder layer was considered to develop hepatic organoids in this study.

4.14.2.1 *Isolation and Culture of Rat bone marrow Mesenchymal Stem Cells*

Mesenchymal stem cells (MSCs) were successfully isolated from rat bone marrow. The cells adhered to PSTC flask and formed multiple colonies after 3 days post seeding (Figure 37 a). After 5 days of culture, the cells exhibited an elongated spindle shape morphology resembling fibroblast cells (Figure 37 b) and started to spread out evenly. The cells reached sub-confluency by 7th day (Figure 37 c) and became confluent on 9th day (Figure 36 d). Bone marrow-derived MSCs were selected as the feeder layer for organoid development because it has been earlier reported that bone marrow MSC can induce rapid attachment and self-organization of hepatocytes, and enhance the liver-specific functions such as albumin secretion, urea synthesis and CYP3A1 activity (Gu *et al.*, 2009).

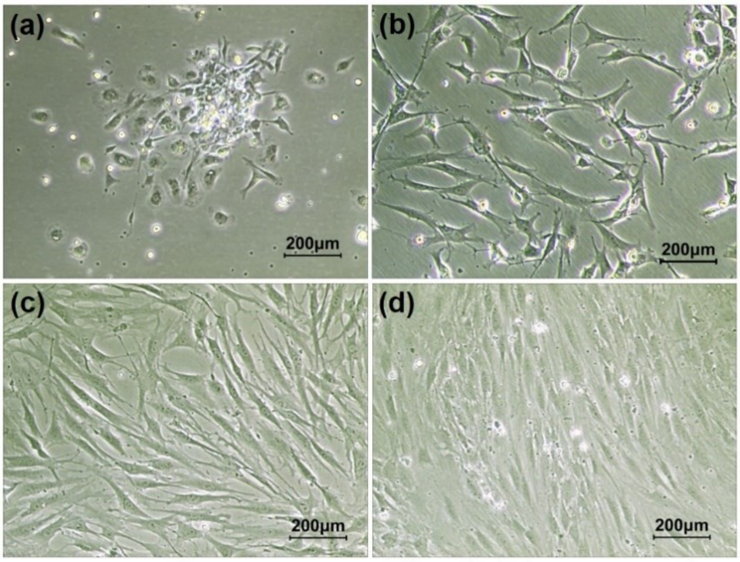

Figure 37. Culture of rat bone marrow MSCs. (a-d) Phase-contrast images showing cell morphology and density of rat bone marrow-derived MSCs cultured on PSTC flask after days 3, 5, 7 and 9 respectively.

4.14.2.2 *Characterization of Rat bone marrow Mesenchymal Stem Cells*

4.14.2.2.1 Expression of MSC markers- Immunostaining

The stemness and mesenchymal origin of the isolated rat bone marrow stromal cells were confirmed by immunostaining of the cell surface markers CD90, CD73 and CD34. As shown in Figure 38 a & b the isolated MSCs expressed CD90 and CD73 respectively. While the cells did not express CD34 (Figure 38 c). According to the International Society for Cell Therapy (ISCT) CD90 and CD73 are considered as positive markers and CD34 as negative marker for bone marrow-derived MSCs (Dominici *et al.*, 2006). CD34 is a positive marker for hematopoietic stem cells. The expression of CD90 and CD73 but not CD34 confirms the stemness and mesenchymal origin of isolated MSCs.

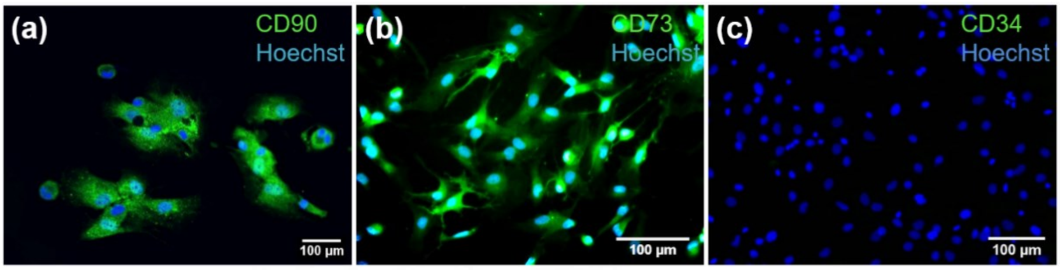

Figure 38. Immunophenotyping of MSCs. Fluorescence images showing rat bone marrow derived MSCs stained for mesenchymal markers (a) CD90 and (b) CD73, and (c) hematopoietic cell marker CD34.

4.14.2.2.2 Osteogenic Lineage Differentiation

Osteogenic differentiation is one among the tri-lineage differentiation studies conducted to evaluate the multipotency of MSCs (Ghasemzadeh-Hasankolaei *et al.*, 2016). The osteogenic differentiation potential of MSCs was evaluated after treating the cells with osteocyte differentiation media for 21 days. The presence of calcium deposit was considered the positive marker for osteocyte differentiation and was visualized by Alizarin red staining. As shown in Figure 39 b & d Alizarin red stained calcium deposits were observed around cells cultured in differentiation media on days 14 and 21 respectively. Whereas MSCs cultured in expansion media did not show any calcium deposition on day 14 and 21 as evidenced by negative staining (Figure 39 a & c). Since, there was no intention to differentiate the MSCs in the present study, only osteogenic lineage differentiation study was conducted as a minimal requirement. The study on osteogenic differentiation of MSCs was carried out until day 21 based on the protocol recommended by International Society for Cellular Therapy for defining the multipotent mesenchymal stromal cells (Dominici *et al.*, 2006).

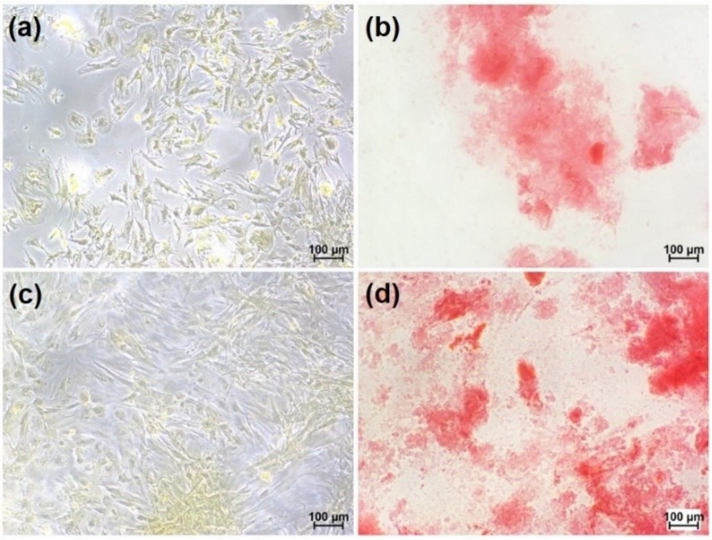

Figure 39. Osteogenic lineage differentiation of MSCs. (a & c) Brightfield images showing unstained MSCs cultured in expansion medium on days 14 and 21 respectively. (b & d) Brightfield images showing alizarin red stained MSCs treated with osteogenic differentiation medium on days 14 and 21 respectively.

4.14.2.3 *Hepatic organoid development on MSC feederlayer*

After the characterization of MSCs, the cells were cultured on NGMA dishes to form feeder-layer (Figure 40 a & b). Freshly isolated rat hepatocytes and NPCs were seeded on the feeder layer in a ratio of 7:3 (Figure 40 c). A ratio of 7:3 was selected because *in vivo,* hepatocytes form 70% of the total cell mass and the remaining is constituted by NPCs (Blouin, Bolender and Weibel, 1977b). As shown in Figure 40 d, hepatocytes and NPCs adhered to the MSC feeder layer and formed micron-sized aggregates within 24 h. Later, after 48 h the aggregates gathered (Figure 40 e) and condensed to form 3D organoid tissue after 72 h (Figure 40 f). As shown in (Figure 40 f) the organoids were often connected to each other by duct-like cellular connections. It was observed that MSCs were also driven into the organoid (Figure 40 e & f). After placing the culture dish at 4 °C for 10 min the organoids along with the deposited ECM started to detach from the dish as a sheet (Figure 40 g). The organoid sheet shrunk immediately after complete detachment (Figure 40 h & i).

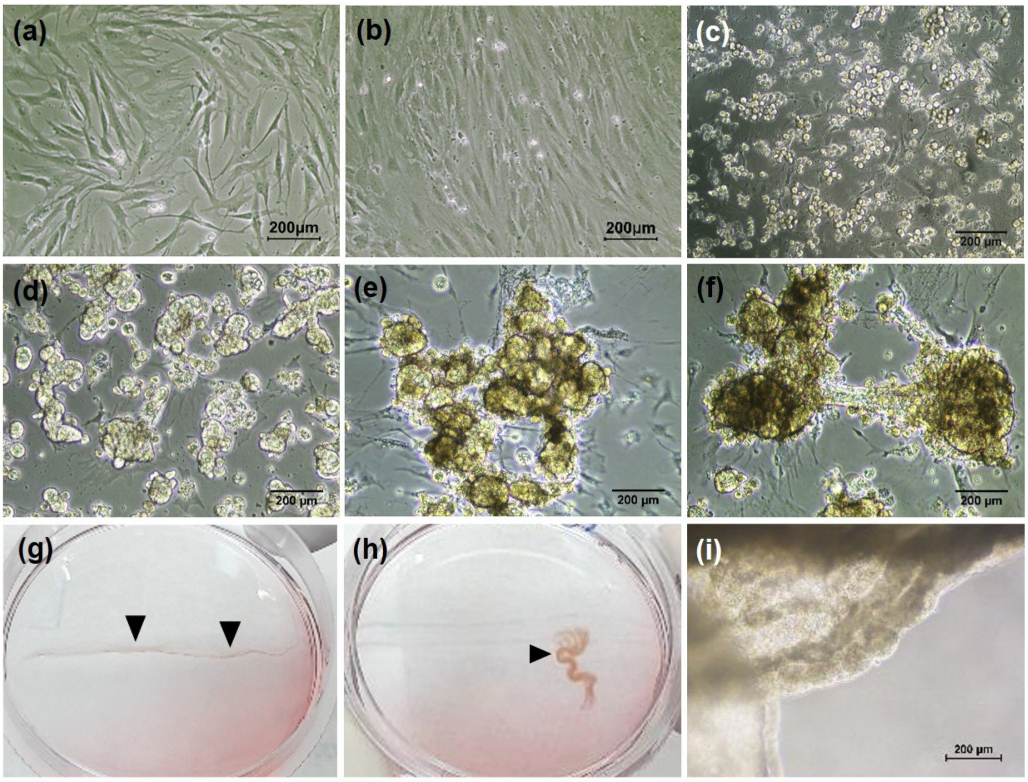

Figure 40. Development of hepatic organoid using MSC feeder layer on NGMA dish. Phase-contrast images showing (a & b) rat bone marrow MSC feeder layer cultured on NGMA dish on days 1 and 7 after seeding, (c) Rat hepatocytes and NPCs seeded on MSC feeder layer, (d) Rat liver cells forming cellular aggregates after 24 h of co-culture,(e) Cellular aggregates gathering after 48 h of co-culture, (f) Cellular aggregates undergoing condensation and self-organization to form 3D organoid tissue after 72 h, (g) Digital photograph showing organoid retrieval from the thermoresponsive dish as a sheet (black arrow heads), (h) Contracted organoid sheet after complete retrieval (black arrow head), (i) Organoid sheet observed under light microscope. Scale bar = 200µm.

Hepatocytes under appropriate conditions can form hepatic organoid sheets, cylindroids and clusteroids with better functional performance than cell monolayer (Ishihara *et al.*, 2006; Wang, Madden and Paunov, 2020). However, specific devices are required to create such organoid sheets and cylindroids. Hence another approach to develop hepatic organoids would be to utilize an ECM-based scaffold. It has been established beyond any doubt that hepatocytes cultured on extracellular matrices show enhanced growth and functions (Pinkse *et al.*, 2005; Roopesh *et al.*, 2022). In addition, ECM can also influence the spontaneous tissue organization. Recently, Hu *et al.*,(2018) have shown that primary hepatocytes encapsulated within mouse sarcoma-derived Matrigel proliferated and self-organized to form hepatocyte organoids and they retained key morphological, functional and gene expression features comparable to freshly isolated hepatocytes (Hu *et al.*, 2018). However, the retrieval of self-assembled cell aggregates or organoids from the matrix is difficult. The matrix has to be solubilized either with ionic switching (eg: alginate matrix) or introducing specific enzymes (eg: collagen, Matrigel) to retrieve the organoids. Meanwhile, in another approach, decellularized liver matrices (DLM) has been utilized as a scaffold for organoid culture. Vyas *et al.,* (2018) showed that human fetal liver progenitor cells self-assemble on acellular liver ECM discs to form 3D liver organoids that recapitulated several aspects of hepato-biliary organogenesis (Vyas *et al.*, 2018). However, the undefined complex and variable composition of decellularized scaffolds and its dependence on the donor liver affects the consistency and reproducibility of large-scale organoid production (Giobbe *et al.*, 2019).

In the present study, a unique approach was adopted to develop hepatic organoids. Primarily, MSC feeder layer was used to provide essential extracellular cues to direct self-organization of rat liver cells. In addition, a thermoresponsive substrate was utilized to co-culture these cells and facilitate easy retrieval of organoids. The motive for co-culturing parenchymal and non-parenchymal liver cells was acquired from the previous report by Michalopoulas, *et al.*(George K. Michalopoulos *et al.*, 2001). They reported that primary rat hepatocytes and NPCs seeded on collagen-coated roller bottles formed organoids with histological organization in the presence of growth factors like HGF and EGF. The present study slightly diverged from this approach by replacing collagen-coated substrate with MSC feeder layer on a thermoresponsive culture dish. Mesenchymal stem cells have been proposed as a potential feeder layer for variety of stem cells and differentiated cells. Induced pluripotent stem cells, cardiac stem cells, hepatocytes and NPCs are few examples that have shown enhanced tissue function when cultured on MSC feeder layer (Sakai *et al.*, 1996; Hatzistergos *et al.*, 2010; Havasi *et al.*, 2013; M. Fujii *et al.*, 2018). As a feeder layer MSC can promote hepatocyte growth by secreting ECM proteins like collagen, fibronectin and laminin, and paracrine factors like Hepatocyte Growth Factor (HGF) (Novoseletskaya *et al.*, 2020). In addition, they can perform immunomodulatory functions and has the potential to transdifferentiate into hepatocytes (Al Ghrbawy *et al.*, 2016; Yang *et al.*, 2021; Han *et al.*, 2022). This very property of MSC will help to reduce immuno rejection of organoids when utilized for transplantation.

As shown in Figure 40 d the spontaneous aggregation of liver cells on MSC feeder was evident in the present study. This can be attributed to the innate ability of hepatocytes to self-aggregate via E-cadherins (Luebke-Wheeler *et al.*, 2009). The self-assembly of cells into multicellular structures is an adaptation phenomenon of adherent dependent cells to its microenvironment through interactions with the mesenchymal cells and ECM. Studies by Takebe *et al.,* (2015) and Hughes *et al.,* (2018) have demonstrated that myosin II-dependent cytoskeletal contraction in mesenchymal cells induced cell condensation and ECM compaction during organ bud morphogenesis *in vitro* (Takebe, Enomura, Yoshizawa, Kimura, Koike, Ueno, Matsuzaki, Yamazaki, Toyohara, Osafune, Nakauchi, Hiroshi Y. Yoshikawa, *et al.*, 2015; Hughes *et al.*, 2018). In the present study, a similar process must have occurred during the formation of hepatic organoids as evidenced by the presence of constrained MSCs beneath the cell aggregate during self-assembly (Figure 40 e & f). The retrieval of hepatic organoids as a sheet can be considered beneficial to the primary hepatocyte, since it will support the maintenance of cuboidal cell morphology and liver-specific functions (Takagi *et al.*, 2012; Bual and Ijima, 2019).

4.15 Characterization of hepatic organoid

The structural and functional characteristics of hepatic organoids were analyzed to evaluate the reliability of the implemented organoid development strategy in this study.

4.15.1 Organoid size distribution and viability

The size of the hepatic organoid is detrimental for diffusion-dependent nutrient supply and waste removal (Akkerman and Defize, 2017). The feret diameter of the organoids ranged from 300 to 600 μm (Figure 41 a) and the mean diameter was 503.5 ± 64.8 μm. Since the average radius of the organoid was approximately 250 μm, it was well within the diffusion limit and sufficient enough to keep the organoids viable and functional. Previously, Gamboa *et al.,* (2021) have shown that donor-derived hepatic cell organoids with a diameter of 400-500 μm were viable and could be used as a model for liver metabolic assay (Gamboa *et al.*, 2021).

Hepatocytes are highly metabolically active cells which require an adequate amount of ATP to survive and perform diverse liver functions (Wiesner, Rüegg and Morano, 1992). The intracellular ATP content in organoids on days 3 and 7 were 35.7 ± 6 μM and 37.4 ± 7 μM respectively. The total amount of ATP present in organoids did not change significantly until day 7 (Figure 41 b), suggesting that the number of viable cells remained the same throughout the culture period. A similar observation was made by Messner *et al*, wherein they showed that human 3D liver microtissues having a diameter between 200 and 300 μm produced similar amount of ATP over a period of 35 days (Messner *et al.*, 2018). This clearly indicate that the size of the organoid is critical to maintain cell viability.

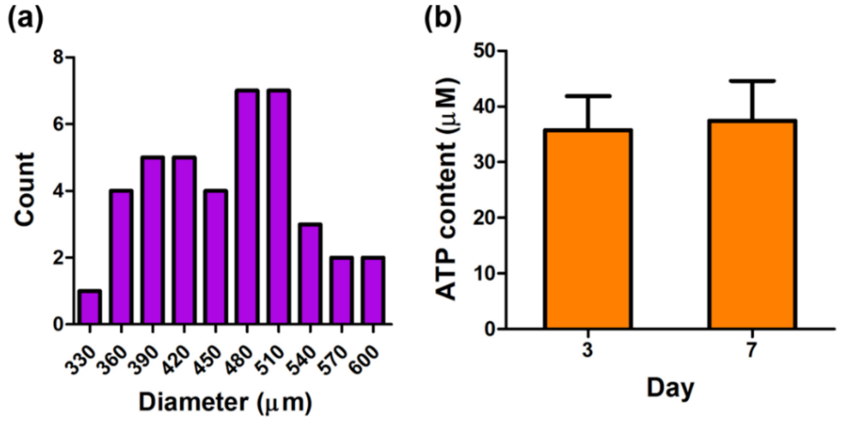

Figure 41. Hepatic organoid size and viability (a) Size distribution of rat hepatic organoids (n=40) formed on thermoresponsive dishes. (b) Intracellular ATP content in rat hepatic organoids (n=3) on days 3 and 7 during culture on thermoresponsive dishes. Data represented as mean ± SD.

4.15.2 Multicellular distribution in organoids

To confirm the presence and distribution of hepatocytes, NPCs and MSCs within the organoid, the cells were prelabelled before initiating the co-culture and the labelled organoids were visualized by confocal microscopy. Figure 42 a show the fluorescent maximum intensity Z-projection image of the labelled hepatic organoid comprising hepatocytes (red), NPCs (green) and MSCs (blue). The hepatic organoids were compact with a typical “bunch-of-grapes-like” appearance (Figure 42 a & b) as reported by Hu *et al.*(Hu *et al.*, 2018). Figure 42 c & d shows the top view and side view of the 3D projected image of the labelled hepatic organoid respectively. The hepatocytes occupied the major volume of the organoid and were located in the core. While the NPCs and MSCs were less in number and were found distributed on the surface and intercalated between hepatocytes. The difference in cell number between hepatocytes and NPCs can be justified by the cell seeding ratio (7:3) we have used during organoid formation. It was also observed that the tissue thickness (x/z plane) was around 30 μm which is well within the diffusion limits *in vivo*. Taken together, the data confirms the self-organization of cells within hepatic organoid.

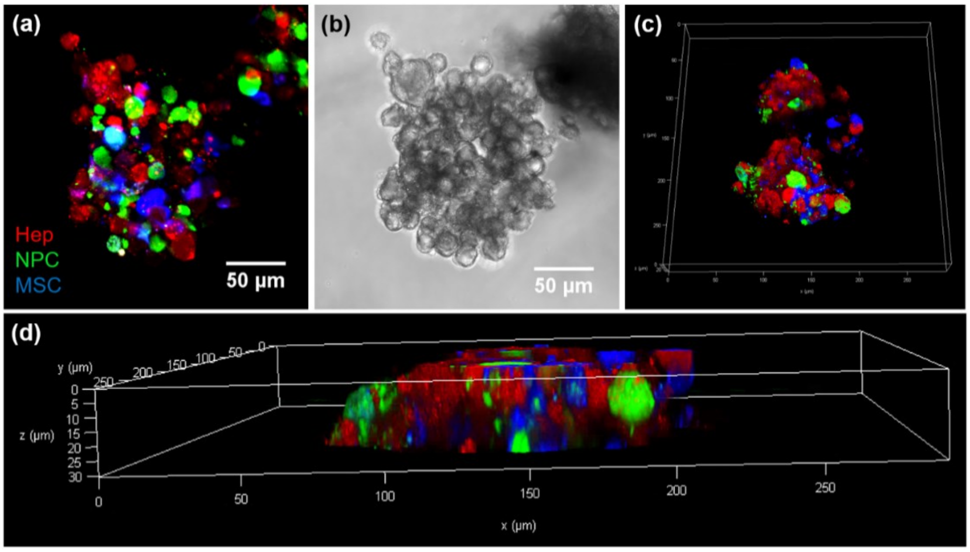

Figure 42. Multicellular distribution in hepatic organoid. (a) Fluorescent maximum intensity Z-projection image of the labelled hepatic organoid showing hepatocytes (red), NPCs (green) and MSCs (blue), (b) Transmitted light maximum intensity Z-projection image of the labelled hepatic organoid, (c) & (d) top view and side view of the 3D projected image of the labelled hepatic organoid respectively.

4.15.3 Histological analysis

Histological analysis of hepatic organoid was done to examine the cell morphology and cellular organization. Figure 43 shows the H&E-stained tissue section derived from a 7-day old hepatic organoid. Hepatocytes were polygonal in shape and were seen as cellular clusters deep in the organoids. They occupied a major volume of the organoid. Secretory cells were found at the periphery of the organoid as identified from their typical staining of cytoplasmic secretory granules by hematoxylin. The secretory cells intervened the hepatocyte clusters in the core forming microlumen-like structures. The organoids were also lined by elongated fibroblast-like cells at the periphery suggesting the presence of either stellate cells or MSCs.

Earlier Mitaka *et al.,* (1999) has shown that during co-culture of rat liver cells on collagen coated surface, the cells piled up forming structurally organized organoids with hepatocytes in the core and NPC in the periphery (Mitaka *et al.*, 1999). A similar cellular organization was observed in our organoids with hepatocytes occupying the core of the organoid. The presence of secretory cells within hepatic organoids has been observed earlier by Michalopoulos *et al.*2002 (Michalopoulos *et al.*, 2002). The authors demonstrated that hepatocytes on the surface of the organoid undergo phenotypic transition to biliary epithelial cells after five days of culture in the presence of medium containing growth factors like EGF and HGF. Since, an organoid culture medium having identical concentration of these growth factors were utilized in the present study, it is assumed that a similar phenotypic transition has occurred in the hepatic organoids developed in thermoresponsive dish.

The formation of microlumen and the presence of elongated cells lining the liver microtissue has been reported by Landry *et al.,*1985 (Landry *et al.*, 1985). The authors reported sorting out and histotypical organization of different cell types during spheroidal aggregate culture of rat liver cells. Cells of the first type formed a monolayer cell lining on the surface of the aggregate; while hepatocytes regrouped in small islands defining a central lumen. A third group of cells rearranged to form bile duct-like structures. A similar kind of microchannels or microlumens and peripheral cell lining were also obtained in the hepatic organoids developed in this study as presented in the Figure 43. Hence, close examination of the organoid histomorphology provided evidence for tissue-like cellular organization.

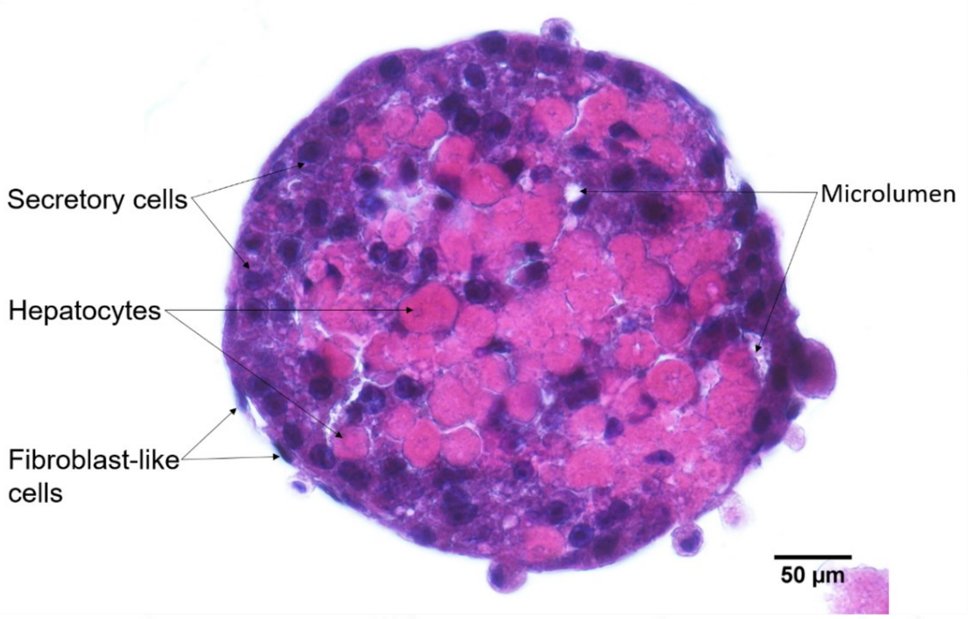

Figure 43. Histological analysis of hepatic organoid. Hematoxylin and eosin staining of paraffin embedded tissue section of hepatic organoid showing distribution of hepatocytes, secretory cells and fibroblast-like cells along with the secondary structure like microlumen.

4.15.4 Ultrastructural analysis -TEM

The ultrastructural features of hepatic organoid were visualized using TEM. Figure 44 a show the intracellular elements of a mature hepatocyte within organoid including abundant glycogen granules (G), numerous mitochondria (M) and vacuolar inclusions (V) distributed around an intact nucleus (N) containing chromatin material (C). Higher magnification images of intercellular contact between neighboring hepatocytes showed electron dense membrane domains forming tight junctions (TJ) on the basolateral side (Figure 44 b).

Glycogen storage is one among the important functions of hepatocyte (Hijmans *et al.*, 2017) and the presence of abundant glycogen granules suggest that glucose metabolism is active in hepatic organoids. Hepatocytes are high-energy demanding cells and therefore a large number of mitochondria are required to meet the energy demand (Wiesner, Rüegg and Morano, 1992). As seen in Figure 44 a & b, huge number of mitochondria were present in the cytoplasm and this substantiate the above fact that hepatocytes inside the organoid were metabolically active. Exposure of chromatin material by rupture of nuclear membrane can threaten cell viability (De Magistris and Antonin, 2018). The intact nuclear membrane and chromatin material in the organoids indicate that the cells were viable. Tight junction proteins play a pivotal role in maintaining apico-basal polarity of hepatocytes (Tocan *et al.*, 2021). Hence, presence of intact tight junctions (Figure 44 b) indicate that the hepatocytes were polarized inside the hepatic organoid.

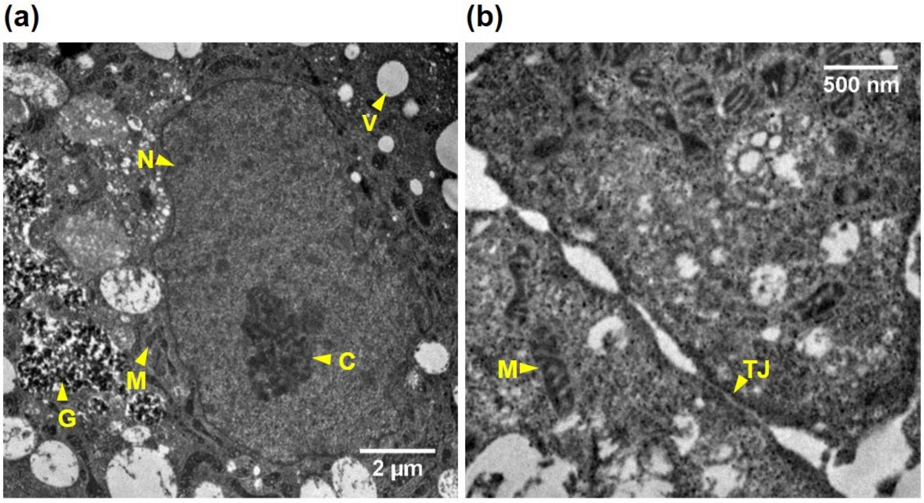

Figure 44. Ultrastructural analysis of hepatic organoid. (a) TEM image showing intracellular elements glycogen granules (G), mitochondria (M), Vacuolar inclusions (V), nucleus (N) and chromatin material (C) of hepatocytes within organoids. (b) Image showing tight junction (TJ) formed between neighboring hepatocytes within organoid. The hepatocytes contain numerous mitochondria which is a typical feature of mature hepatocytes.

4.15.5 Immunofluorescence staining

The expression of tissue-specific markers of hepatocyte polarization and liver function along with phenotypic markers of NPCs within hepatic organoids were analyzed by immunofluorescence staining liver cell specific markers. As shown in Figure 45 a & b, the hepatic organoids expressed both MRP2 and albumin. MRP2 was localized in the intermembrane regions shared by hepatocytes and formed an interconnected channel-like network inside the organoid (Figure 45 a). The hepatocytes expressed albumin in the cytoplasm (b). The positive staining for non-parenchymal cell markers CD32b and CD163 confirmed the presence of sinusoidal endothelial cells and kupffer cells respectively inside the organoid (Figure 45 f & j). The endothelial cells were found dispersed inside the organoid.

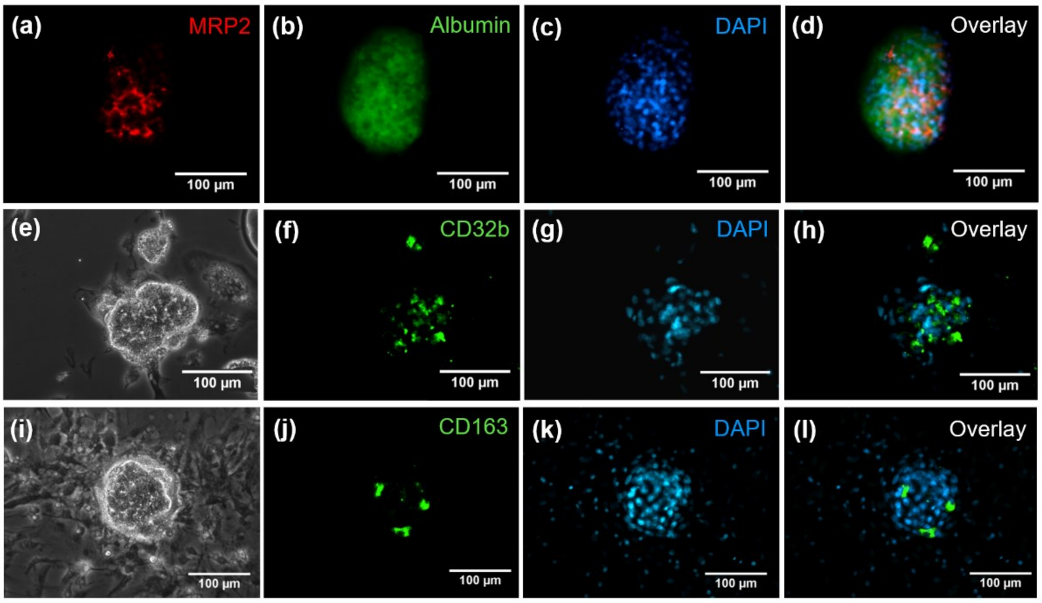

Figure 45. Immunofluorescence staining of hepatic organoids. Fluorescence images of the hepatic organoid showing expression of proteins (a) MRP2, (b) albumin, (f) CD32b & (j) CD163. (c), (g) & (k) shows the nuclear staining corresponding to the organoid in each row. (d), (h) and (l) shows the overlay of the respective fluorescent images in each row. (e) & (i) shows the phase contrast image of the organoid stained for CD32b and CD163 respectively. Scale bar = 100µm.

The tissue-like organization is an essential feature of organoids to exhibit and maintain tissue-like functions for the long-term *in vitro*. MRP2 is a transporter protein expressed on the apical membrane of the hepatocyte forming bile-canaliculi. Impaired trafficking of MRP2 proteins to canalicular membrane can depolarize the hepatocyte. (Fu *et al.*, 2019). While albumin is one of the major serum proteins synthesized by hepatocytes and it is essential to maintain plasma oncotic pressure (Valerio *et al.*, 2016). Positive staining of these two markers confirms that the hepatocytes in the organoids were polarized and functional. The expression of CD32b by sinusoidal endothelial cells has been associated to the vascular capillary-forming ability (Dingle *et al.*, 2018). Hence, the dispersed CD32b positive sinusoidal endothelial cells in the hepatic organoid (Figure 45 f) indicate that the SE cells might form intra-organoid vascular capillaries on further maturation. CD163 is a Kupffer cell marker involved in scavenging haptoglobin-hemoglobin complex from blood circulation in liver (Philippidis *et al.*, 2004). Hence, it is expected that the presence of CD163 positive kupffer cells inside the organoid (Figure 45 j) will enable hemoglobin scavenging function similar to the liver.

4.15.6 Evaluation of liver-specific functions

4.15.6.1 *Albumin synthesis*

Albumin is one of the major serum proteins synthesized by the liver which performs a wide range of functions such as transportation of small molecules, free radical scavenging, anticoagulation and modulation of plasma oncotic pressure (Moman, Gupta and Varacallo, 2022). The secretion of albumin by hepatic organoids was evident over a period of 7 days (Figure 46 a). The cumulative secretion of albumin by organoids showed a linear increase over a period of 7 days. Earlier, Soto-Gutierrez *et al.,* (2010) has also reported a similar trend in albumin production by liver organoids developed from co-culture of mouse hepatocytes and human NPCs in matrigel (Soto-Gutierrez *et al.*, 2010). The authors also showed that co-cultured organoids were secreting more albumin than organoids containing solely hepatocytes. Hence, this confirms that the organoids developed by co-culture of rat liver cells and MSCs on NGMA dish can match the performance of organoids produced using conventional Matrigel® matrix.

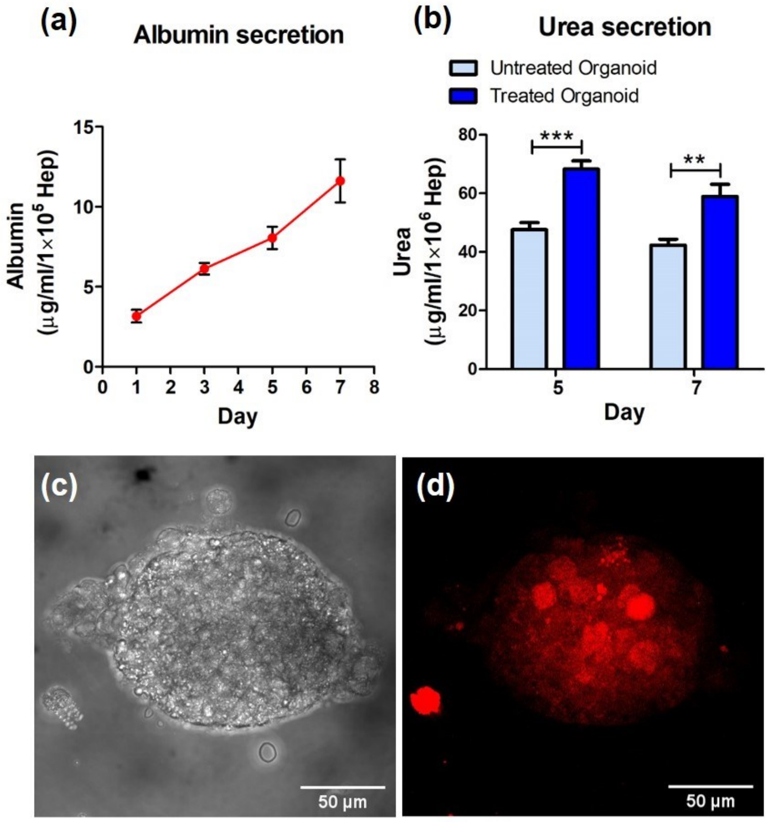

Figure 46. Functional evaluation of hepatic organoid. Graph showing (a) Albumin secretion by hepatic organoids and (b) Urea secretion by hepatic organoids either untreated or treated with ammonium chloride. All data represented as mean ± SD. (n=3, $^{**}p\text{-value} < 0.01$, $^{***}p\text{-value} < 0.001$). (c) Transmitted light image of hepatic organoid treated with the substrate O^7-ethylresorufin (d) Z-stacked fluorescence image of hepatic organoid showing intracellular CYP1A1 enzyme mediated conversion of substrate O^7-ethylresorufin to fluorescent product resorufin (red). Scale bar = 50 µm.

4.15.6.2 *Ammonia detoxification*

Ammonia detoxification is one of the vital functions of the liver in which ammonia generated during the deamination of amino acids is converted into urea through the urea cycle (Blanding and Tremblay, 1982). The functional capability of hepatic organoids to convert ammonia into urea was evaluated by quantifying the urea secreted by organoids with and without ammonium chloride treatment. As shown in

Figure 46 b, in comparison to untreated organoids, the treated one showed significantly higher secretion of urea on day 5 and 7. Although there was a slight reduction in urea secretion on day 7 irrespective of the treatment group, there was a significant difference between the treated and untreated organoids. Similar to the albumin secretion, Soto-Gutierrez *et al.,*(2010) also reported a significantly higher removal of ammonia in co-cultured organoids than hepatocyte organoids (Soto-Gutierrez *et al.*, 2010). This data again substantiates the earlier claim that organoids developed in the present study are equally performing with the conventional organoid culture models.

4.15.6.3 *Biotransformation*

The enzyme-mediated biotransformation is an important function of the liver that helps in drug metabolism and clearance of toxic metabolites (Phang-Lyn and Llerena, 2022). CYP450 1A1 is an important enzyme involved in biotransformation process. EROD activity of enzyme CYP450 1A1 within hepatic organoid was evaluated after incubating with the substrate O^7-ethylresorufin. As shown in Figure 46 d, after the incubation the hepatic organoid emitted fluorescence specific to the product resorufin. This suggests that CYP450 1A1 enzyme were active inside the hepatic organoid. EROD activity has been monitored to study the induction of enzyme CYP450 1A1 by drugs and to evaluate the chemical toxicity caused by drug metabolites in primary hepatocytes cultured on microphysiological systems (Chang *et al.*, 2017). This suggests that the hepatic organoids developed in this study can be used as an *in vitro* model to study CYP450 1A1 mediated biotransformation and related liver toxicity.

4.16 Computer-aided designing of liver tissue construct

The process of tissue bioprinting involves three phases, namely the pre-printing phase, printing phase and post-printing phase. In the pre-printing phase, a 3D model of the construct is designed *in silico* for bioprinting. The model can be either developed by 3D reconstruction of anatomical data such as CT scans or it can be created *de novo* using various CAD software. In this study, the second approach was employed to custom design a 3D model of the liver tissue construct. The model consisted of a two-layered square grid structure (Figure 47 a & b). As shown in Figure 47 c & d, an array of continuous horizontal and vertical filaments was used as an infill on layer one and two respectively, to achieve a rectilinear grid pattern within the construct. To ensure transversal porosity within the construct the filaments were positioned at a horizontal distance of 1.2 mm from each other. Three-dimensional bioprinting of uniform and geometrically repetitive patterns allows better recapitulation of repetitive microstructure of liver in bioprinted construct (Kang *et al.*, 2020). Of late, Lewis *et al.*, (2018) demonstrated that hepatocytes when seeded on 3D printed gelatin scaffolds with more interconnected filaments exhibited higher hepatocyte-specific functions compared to cells seeded on scaffolds with less interconnected geometry (Lewis, Green and Shah, 2018). Hence, a rectilinear infill pattern with a minimal inter-filament distance was designed for liver tissue bioprinting in this study.

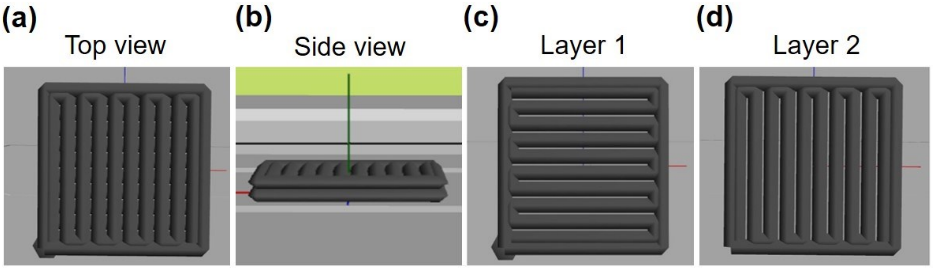

Figure 47. Computer-aided designing of tissue construct. Images showing 3D design of the tissue construct viewed from (a) Top and (b) side. (c & d) CAD image depicting the infill filament orientation in layer 1 and layer 2 of the tissue construct.

4.17 Three-dimensional printing and stability of hydrogel construct

The feasibility of printing the designed construct was initially tested using GelMA bioink without cells. A hydrogel construct was 3D printed, was stabilized by UV crosslinking and incubated in culture medium at 37°C. The percentage weight loss over 15 days was analyzed. The printed construct exhibited a minimal weight loss which was less than 2 % of the initial weight. The percentage weight loss on days 1, 3, 7 and 15 were 0.4 %, 0.7 %, 1.1% and 1% respectively. The results convey that the design of the construct was reliable enough to fabricate a stable tissue construct.

4.18 Three-dimensional bioprinting of liver tissue construct

Liver tissue constructs were fabricated by extrusion-based bioprinting using cell-laden GelMA bioink and organoid-laden GelMA bioink. Figure 48 a & e shows the printing cartridge loaded with cell-laden bioink and organoid-laden bioink respectively. Figure 48 b and f show the 3D bioprinting of cell construct and extrusion of organoid-laden bioink respectively. To establish the importance of tissue organization in organoid bioprinting, we used suspended liver cells in the bioink (cell-laden bioink) as in conventional method of 3D bioprinting. The cell-laden GelMA bioink was used to bioprint cell construct and it was utilized as a control for 3D bioprinted organoid construct. The addition of organoids to the GelMA bioink did not affect the extrudability of the bioink as witnessed in Figure 48 f. As shown in Figure 48 c & g both the constructs mimicked the intended design of the construct and were structurally stable after 24 h incubation in culture medium.

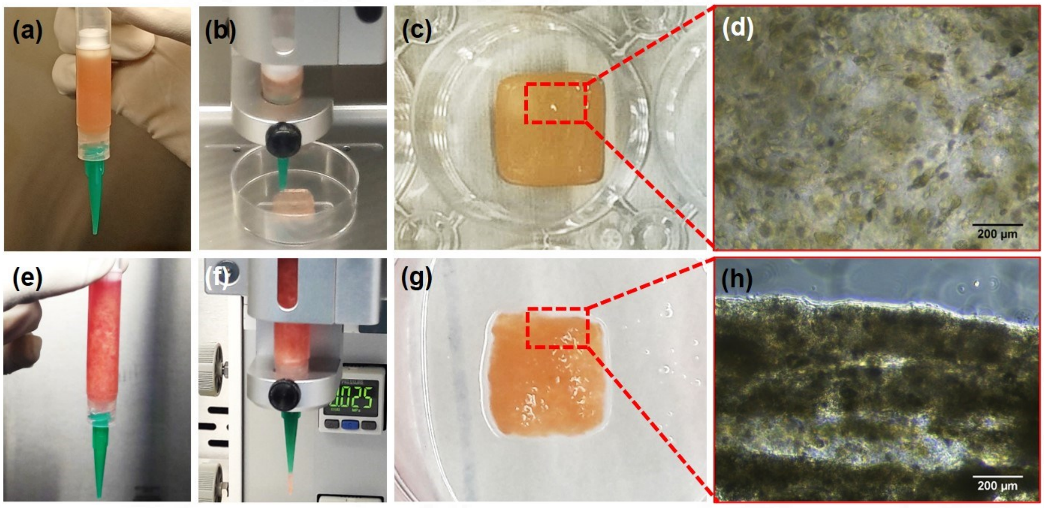

Figure 48. 3D Bioprinting of liver tissue construct. (a & e) Photographs showing the cell-laden bioink and organoid-laden bioink loaded in the cartridge respectively. (b & f) Photographs showing 3D bioprinting of cell construct and extrusion of organoid-laden bioink respectively. (c & f) Photographs of the 3D bioprinted cell construct and organoid construct after 24 h of culture in medium, (d) & (h) Phase contrast images showing the distribution of cells and organoids within cell construct and organoid construct respectively. Scale bar = 200 µm.

The second phase of this study involved 3D bioprinting of hepatic organoids aiming at achieving liver tissue organization inside bioprinted construct. The concept of using cell aggregates as building blocks for generating 3D tissues has been proposed a decade ago (Mironov *et al.*, 2009). Jakab *et al.,* (2004) reported the formation of tissue construct with predetermined shape by manually packing the cell aggregates in 3D gel (Jakab *et al.*, 2004). However, the selection of the hydrogel matrix for 3D culture of cell aggregates is critical in determining the functional output of the cells

(Roopesh *et al.*, 2022). In the present study, GelMA was used as the bioink for organoid bioprinting because it was proven to enhance the liver-specific functions of liver microtissues as presented earlier in the section 4.5.10.2. Moreover, Bhise *et al.,* (2016) have used GelMA bioink containing HepG2 spheroids for extrusion bioprinting and showed that the printed hepatic construct remained functional during the 30 days culture period (Bhise *et al.*, 2016). In addition, a recent study by Bouwmeester *et al.,* (2021) demonstrated that 3D bioprinted human liver-derived epithelial organoids encapsulated in GelMA bioink showed signs of tissue reorganization (Bouwmeester *et al.*, 2021). However, the authors used mechanically fragmented liver organoids in the bioink, since the organoids were formed inside the Matrigel. This very approach can affect the viability and limits the scalability of organoid production method.

In contrast, the approach followed in this study allows non-invasive retrieval of hepatic organoids from NGMA dish. Hepatic organoids retrieved from the thermoresponsive dish were resuspended in GelMA bioink and the organoid-laden bioink expressed thixotropic property when pneumatic pressure was applied for extrusion. Hence, the printing parameters need to be changed in the presence of organoids. The applied pneumatic pressure ranged from 35 to 40 kPa and the feed rate was decreased to 12 mm/s to obtain the continuous deposition of bioink. The applied pressure during extrusion printing has a great impact on cell viability. The more the pressure required to extrude a material, the greater the shear stress the cells will endure, and the greater the damage the extrusion process will cause to the cells (Ouyang *et al.*, 2016; Roehm and Madihally, 2017). Since the applied pressure was well within the acceptable limit (< 100 kPa) (Ouyang *et al.*, 2016) and the diameter of the printing nozzle was higher than that of the organoid, it is expected to cause less shear damage to the cells. The stability of the 3D bioprinted construct post 24 h culture indicate that the UV-crosslinking time was optimal.

4.19 Evaluation of 3D bioprinted liver construct

4.19.1 Morphological analysis

The bioprinted liver constructs were observed under a light microscope to assess the cell morphology and distribution within the construct. As shown in Figure 48 d, hepatocytes in the cellular construct exhibited a spherical morphology while the other cell types exhibited ellipsoid morphology. The cells were uniformly distributed across different regions of the construct with minimal cell-cell contacts. Whereas, in the organoid construct Figure 48 h, the organoids were found tightly packed as tissue strands aligned in the direction of bioprinted hydrogel filament. It was difficult to make out the cell morphology as observed in the cell construct. The organoids were also distributed uniformly across the entire area of the bioprinted construct.

Attaining *in vivo* cell morphology and tissue organization inside a bioprinted construct is a difficult task. The inability of hepatocytes within cell construct to exhibit characteristic cell morphology may be due to lack of cell-cell interaction. Polygonal morphology of hepatocytes have been mostly reported in 3D hepatocyte aggregate models like spheroids and organoids wherein the intercellular interactions are predominantly high (Messner *et al.*, 2018). Hence it is expected that within the organoid construct, the hepatocytes and other cells may attain native cell morphology. The advantage of using cell-laden bioink is the uniform distribution of cells within construct as seen in Figure 48 d. Whereas it is often difficult to achieve uniform distribution of organoids within the total volume of bioprinted construct. Previously, Bouwmeester *et al.,* (2021) reported a very less coverage area of organoids within bioprinted construct and it was only 6.4% of the total area of the bioprinted strand. Whereas, in the present study the coverage area of organoids was more than 50 % as seen in Figure 48 h. This could be due to the sheet-like structure of the hepatic organoids harvested from the NGMA dish. Hence, this organoid culture method seems to be advantageous for organoid bioprinting.

4.19.2 Gene expression analysis

The relative expression of genes specific to hepatocyte functions such as serum protein synthesis, enzyme-mediated drug metabolism, bile transport and cell-specific markers for NPCs of organoid bioprinted construct was compared with conventional cell construct. The expression of genes coding serum protein transthyretin was similar in both the constructs (Figure 49 a). While the expression of genes coding Phase I enzymes CYP3A1 and CYP1A2 was approximately two-fold higher in organoid construct compared to cell construct (Figure 49 b). The expression of genes coding Phase II enzymes GST and UGT2B7 were about six-fold higher in organoid construct compared to cell construct (Figure 49 c). The expression of genes coding for bile transport proteins MRP2 and BSEP were about two-fold higher in organoid construct compared to cell construct (Figure 49 d). A similar trend was observed for the genes specific to NPCs. The gene expression of sinusoidal endothelial cell marker- SE1, kupffer cell marker- CD68 and stellate cell marker- Desmin was four-fold, five-fold and ten-fold higher respectively in organoid construct compared to cell construct (Figure 49 e). CD 133 is liver stem cell marker and the expression of gene encoding this marker was identical in both the constructs (Figure 49 e).

The results confirmed that the organoid constructs expressed significantly higher levels of mature liver-specific genes compared to the cell construct. Higher expression of Phase I and Phase II enzymes in organoid construct confirms higher biotransformation potential of the hepatic organoids (Phang-Lyn and Llerena, 2022). MRP2 and BSEP are apical membrane proteins which are considered as markers of hepatocyte polarity (Treyer and Müsch, 2013). Significantly higher expression of these genes in organoid construct suggests the polarization of hepatocytes and this is expected due to the extensive cell-cell interactions and cellular organization. Since NPCs play an important role in enhancing liver-specific functions of hepatocytes, it is necessary to track their presence with bioprinted construct. Higher levels of expression of NPC markers SE1, CD68 and Desmin in organoid construct suggest that the heterotypic cell interactions between liver cells inside organoid must have promoted the survival and gene expression of NPCs as reported by Khetani *et al.*(Khetani *et al.*, 2004). Whereas, in cell construct due to weak inter-cellular connections, cells tend to dedifferentiate. Of late, Bouwmeester *et al.*, (2021) attempted to evaluate the expression of mature hepatocyte genes of 3D bioprinted intra-hepatic cholangiocyte organoids after culturing the organoids in hepatocyte differentiation media (Bouwmeester *et al.*, 2021). The analysis showed that the expression was very low and was similar to the immature organoids cultured in Matrigel. In the present study organoids were developed from the differentiated primary liver cells and this could be the probable reason for adequate expression of mature liver genes in organoid construct and cell construct.

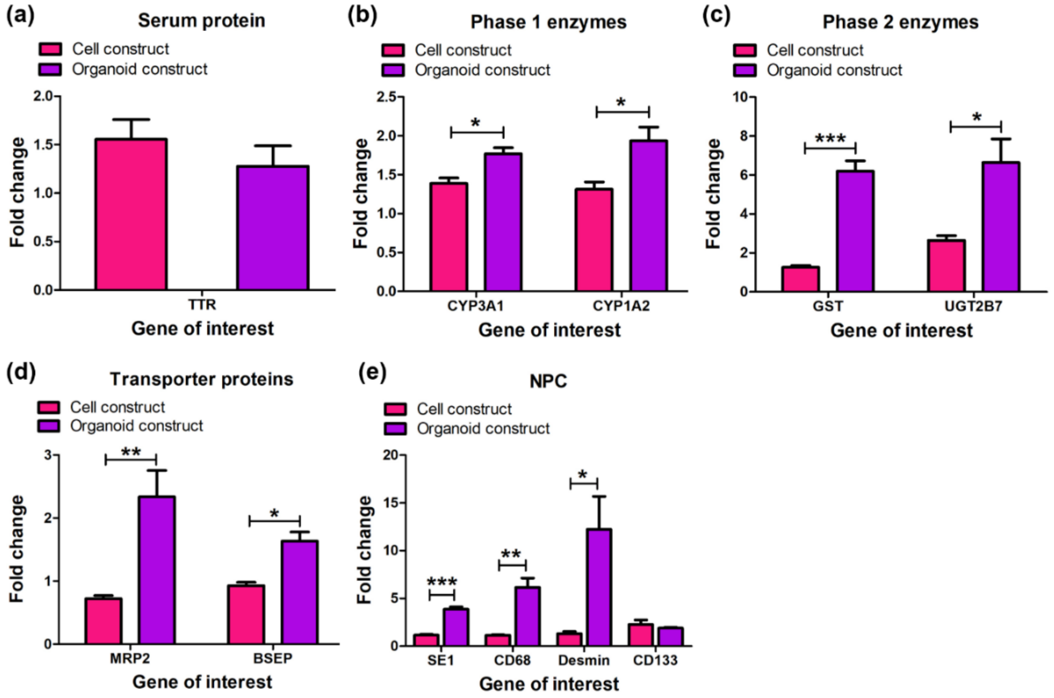

Figure 49. Gene expression analysis of liver tissue construct. (a-e) qRT-PCR data showing fold-change in expression of liver-specific genes in 3D bioprinted cell construct and organoid construct on day 15 relative to cell construct on day 7. All data represented as mean ± SD. (n=3, *p-value < 0.05, **p-value < 0.01, ***p-value < 0.001)

4.19.3 Histological analysis

Tissue organization is the key to long-term maintenance of liver cell function *in vitro*. The preliminary evidence for tissue organization within bioprinted liver construct was obtained from the histological analysis. It was observed that the cells inside the organoid construct were arranged as a continuous multi-layered tissue sheets (Figure 50 e and f). The cells were tightly bound to each other with minimal ECM between them. In contrast, cells inside cell construct were randomly distributed without any sign of tissue organization and with large quantity of ECM between cells (Figure 50 a & b). Cell-cell interaction was limited to few regions of the cell construct where cell clusters were present. A comparison between the histological sections of rat liver tissue and organoid construct showed similarities in cell morphology and cell distribution (Figure 50 c & f). The hepatocytes in organoid construct showed polygonal cell morphology (yellow line) and the distribution of NPC (yellow arrow) with respect to hepatocytes was similar to the rat liver tissue. However, the rat liver cells were much more compact due to high cell density.

Histological analysis confirms tissue-organization within organoid construct. The utilization of intact hepatic organoids during bioprinting ensured uniform and continuous distribution of liver cells within organoid construct. The multi-layered sheet-like appearance of hepatic organoids can be attributed to the innate reorganizing ability of hepatocyte to form hepatic plates under proper culture conditions as reported by Michalopoulos *et al.,* (Michalopoulos *et al.*, 1999).

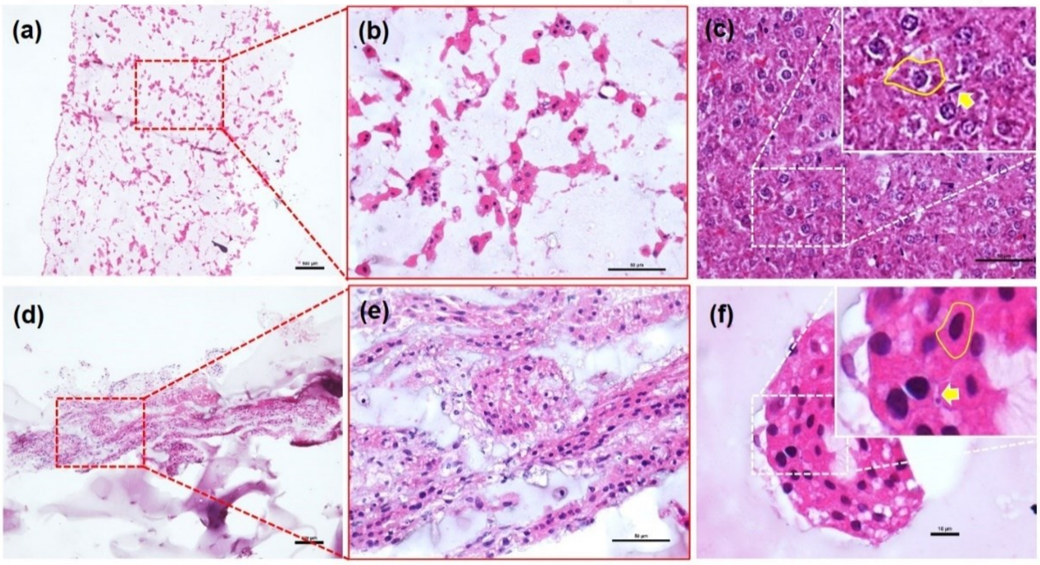

Figure 50. Histological analysis of liver tissue construct. Hematoxylin (blue) and eosin (pink) stained cross-sections of 3D bioprinted cell construct (a) & (b), rat liver (c) and organoid construct (d), (e) & (f) showing cellular distribution and organization. Images (a) & (d) were captured using 10x objective (scale bar =100μm) and (b) & (e) using 40x objective (scale bar= 100 μm & 50 μm)

The typical cellular arrangement inside organoid construct also indicate that organoids retrieved from NGMA dish are better building blocks for 3D bioprinting structurally organized liver tissue construct compared to the conventional cell bioprinting. In addition, the resemblance between the organoid construct and rat liver tissue implicates the potential application of hepatic organoid construct as an alternative *in vitro* liver model.

4.19.4 Immunofluorescence staining

The expression of albumin inside 3D bioprinted constructs were evaluated by immunofluorescence staining. Immunostained sections of 7-day cultured cell construct and organoid construct revealed positive staining of albumin in both the constructs (Figure 51 a & b). The data suggest that the hepatocytes inside bioprinted constructs were viable and functional even after 7 days of culture *in vitro*. Albumin is a serum protein synthesized by hepatocytes and it is considered as an important biomarker of hepatocyte functionality. Recently, Bouwmeester *et al.*, (2021) also showed the expression of albumin in 3D bioprinted and differentiated intra hepatic cholangiocyte organoids (Bouwmeester *et al.*, 2021). However, the expression of albumin was significantly lower compared to the hepatic organoid construct shown in Figure 51 b. This could be due to the incomplete differentiation of cholangiocyte organoids. Whereas, in this study differentiated primary liver cells were used for organoid development. Hence, the choice of cell source for liver organoid bioprinting is very critical when it comes to functional output.

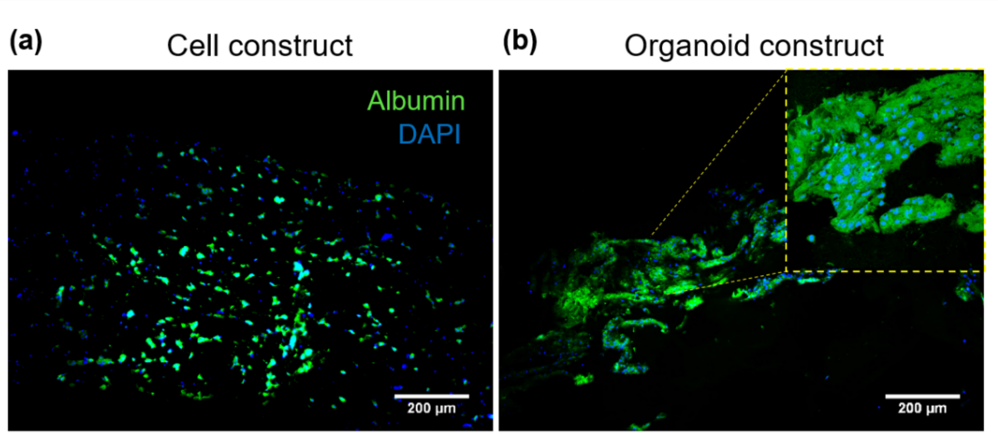

Figure 51. Immunofluorescence staining of liver construct. Fluorescent images showing expression of albumin in (a) cell construct and (b) organoid construct. Inset magnified image of the 3D bioprinted hepatic organoids expressing albumin. Scale bar = 200 μm.

4.19.5 Evaluation of liver-specific functions

The liver-specific functions of both the cell construct and organoid construct were analyzed and compared. The 3D bioprinted cell construct and the organoid construct was compared with respect to its albumin secretion, urea synthesis, drug-induced cytochrome P450 activity and glycogen storage ability.

4.19.5.1 *Albumin secretion*

Albumin is the most abundant serum protein synthesized by liver and it acts as the most significant modulator of plasma oncotic pressure and functions to transport a variety of ligands (Moman, Gupta and Varacallo, 2022). The quantity of albumin in serum is estimated as part of liver function test. The amount of albumin secreted by 3D bioprinted liver constructs were monitored over a period of 15 days to evaluate their protein synthesis function. Figure 52 a show the trend of albumin secretion by the bioprinted constructs over 15 days of culture. Although the amount of albumin secreted by the organoid construct was significantly lower than the cell construct during the initial days, the level of secretion increased linearly from day 1 to 5 and remained stable until day 15. In contrast, the amount of albumin secreted by the cell construct decreased exponentially after day 5 and was significantly lower than the organoid construct till day 15.

The initial dip in albumin secretion by organoid construct may be due to the development of diffusion barrier inside the hydrogel construct. Organoids are 3D tissues that exhibit a gradient diffusion of nutrients and other molecules both inward and outward of the tissue (McMurtrey, 2016). After the bioprinting process the organoids are encapsulated inside the hydrogel and this creates a further diffusion barrier to the movement of albumin. Earlier, it has been reported that collagen hydrogels can slow down the diffusion of bovine serum albumin outside the gel and it is dependent on the polymer weight content (Hettiaratchi *et al.*,). Over the days due to equilibrium swelling and gradual degradation of hydrogel, the polymer weight content may decrease allowing more albumin to diffuse outside the bioprinted organoid construct. Whereas in case of cell construct albumin can be easily secreted outside the cells due to its small size and larger surface area to volume ratio. And this justifies the higher albumin secretion by cell construct during initial days. However, an exponential reduction in albumin by cell construct can be attributed to the lack of cellular contacts in cell construct which is a prerequisite for normal functioning of hepatocytes. Evidence suggests that cell junctions between hepatocytes including tight junctions, adherens junction, desmosomes and gap junctions play a key role in performance of liver-specific functionality (Vinken *et al.*, 2008). In addition, the dedifferentiation of hepatocytes can occur due to lack of heterotypic cell interactions as reported by Bhatia *et al.*,(Bhatia *et al.*, 1999b).

4.19.5.2 *Ammonia detoxification*

Ammonia produced during the deamination of amino acids is transformed into urea through the urea cycle by hepatocytes (Blanding and Tremblay, 1982). To evaluate the ammonia detoxification ability of the bioprinted constructs, urea secreted by the constructs was estimated after ammonium chloride treatment Figure 52 b shows the secretion of urea by the bioprinted constructs on days 1, 7 and 15. The organoid construct treated with ammonium chloride secreted higher amount of urea compared to the untreated group on days 1, 7 and 15. While there was no significant difference between the two groups of cell construct (Figure 52 b). The amount of urea secreted by the cell construct linearly decreased after day one irrespective of the treatment group. In contrast, the organoid construct maintained the levels of secreted urea and was significantly higher than the cell construct on day 15.

Heterotypic cell interactions have important role in regulating hepatocyte functions like urea synthesis. Natarajan *et al.,* (2021) have observed that urea synthesis by rat hepatocyte was dependent on its interaction with non-parenchymal cell (Natarajan, Moeun and Kidambi, 2021). This information justifies the higher levels of urea secretion by organoid construct where both hepatocytes and NPCs are in close proximity with each other allowing relevant heterotypic cell interactions. Whereas due to weak interactions in cell construct only basal levels of urea were secreted. From the Figure 52 b it is also very clear that the organoids had a better response towards ammonium chloride treatment which was lacking in cell construct.

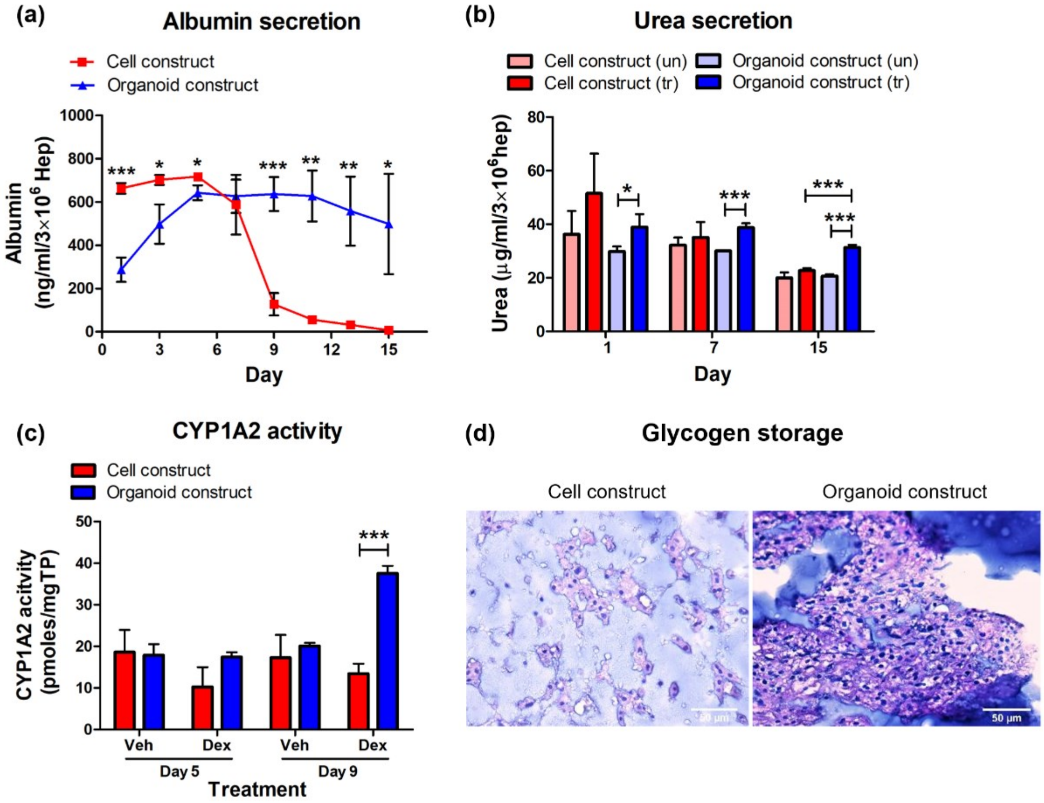

Figure 52.Functional evaluation of 3D bioprinted liver tissue construct. (a) Albumin secretion by 3D bioprinted cell construct and organoid construct. (b) Urea secretion by 3D bioprinted cell construct and organoid construct either untreated or treated with ammonium chloride. (c) CYP1A2 activity in 3D bioprinted cell construct and organoid construct either treated with dexamethasone (Dex) or DMSO (Veh). All data represented as mean ± SD (n=3, *p-value < 0.05, **p-value < 0.01, ***p-value < 0.001). (d) PAS staining (dark pink) showing glycogen accumulation in cells within 3D bioprinted cell construct and organoid construct. Nuclei were counterstained with hematoxylin (blue). Scale bar = 50 µm.

4.19.5.3 *Drug-induced Cytochrome P450 activity*

Liver is the central metabolic hub wherein biotransformation of xenobiotics occurs. Cytochrome P450 enzymes play a key role in biotransformation and elimination of drugs upon induction. To evaluate the drug-induced CYP450 1A2 enzyme activity in organoid and cell construct, they were treated with the inducer drug dexamethasone on days 3 and 7 during culture. The enzyme activity was analyzed after 48 h incubation with the drug. Figure 52 c shows the CYP 1A2 enzyme activity corresponding to cell construct and organoid construct with and without drug treatment. On day 5 the cellular and organoid construct exhibited an equal level of CYP450 1A2 enzyme activity without any difference between the treated and vehicle control. Whereas, on day 9 the enzyme activity of the dexamethasone-treated organoid construct increased two-fold and was significantly higher than all other groups. At the same time, the cellular construct showed the same basal activity as on day 5 irrespective of the drug treatment.

Since, the albumin and urea secretion function of cell construct was shown to reduce significantly after 7 days, the CYP1A2 induction study was conducted during the initial days of culture after bioprinting. Dexamethasone is a corticosteroid that has been shown to induce the activity of the CYP1A family of enzymes in rat hepatocytes (Monostory *et al.*, 2005). Hence, optimal concentration of dexamethasone was used to induce the enzyme activity in the bioprinted constructs. It has been reported that the cytochrome P450 1A enzyme activity in hepatocytes were enhanced during coculture of hepatocyte and NPCs on PDMS substrate (Natarajan, Moeun and Kidambi, 2021). Hence, the induction of CYP1A2 in organoid construct on day 9 is justified by the strong heterotypic cell interactions. However, during the initial time point, even the organoid construct did not respond to dexamethasone. This may be due to low copy number of enzyme during the initial days of culture and has to be examined further by molecular techniques.

4.19.5.4 *Glycogen storage*

Glycogen is a main source of energy and it is stored in the liver by hepatocytes (Hijmans *et al.*, 2017). The presence of glycogen is an indicative of the carbohydrate metabolism function of hepatocyte. The stored glycogen content within the bioprinted liver tissue construct was examined by PAS staining. Figure 52 d shows the PAS-stained sections of 3D bioprinted cell construct and organoid construct. The hepatocytes within the bioprinted organoid and cell construct stained positive for glycogen. However, the organoid construct exhibited intense staining for glycogen compared to the cell construct suggesting higher glycogen content within the organoid construct. A similar pattern of PAS staining was observed by Bouwmeester *et al.*, (Bouwmeester *et al.*, 2021). Earlier, the presence of abundant glycogen granules inside the hepatic organoids were observed in the TEM analysis (Figure 44 a). The PAS staining reconfirms that the bioprinting process did not affect the glycogen storage capability of primary hepatocytes inside the construct. Collectively, the above results indicate that liver tissue constructs fabricated by organoid bioprinting technique will recapitulate tissue-like cellular organization and exhibit higher levels of liver functions compared to the traditional cell bioprinting method.

Chapter 5

SUMMARY AND CONCLUSION

5.1 Summary

Liver tissue engineering encompasses several approaches to fabricate liver tissue substitutes for replacing or restoring lost tissue functions. The key to developing a fully functional liver tissue substitute is by recapitulating tissue microarchitecture in the bioengineered construct. The present study puts forward a novel methodology to develop hepatic organoids using a thermoresponsive culture substrate and provides insight into the fabrication of histomimetic liver tissue constructs by 3D organoid bioprinting.

Towards achieving this goal, various objectives were formulated and were successfully accomplished. The first objective was to develop a suitable bioink for organoid bioprinting. To meet this objective, Gelatin methacrylamide (GelMA) was synthesized and characterized for its suitability as a biomatrix for 3D microtissue culture. In this regard, a high-throughput method to produce viable and functional liver parenchymal microtissues (LPMTs) was also developed. On successfully meeting the requisite properties as a biomatrix, GelMA was utilized to prepare a bioink formulation with excellent printability and shape fidelity. The second objective was to develop hepatic organoids using a thermoresponsive culture substrate. To meet this purpose, a thermoresponsive copolymer NGMA was synthesized and characterized for its physicochemical and biological properties.

NGMA coated culture dishes were cytocompatible and exhibited thermoresponsive property making it a suitable substrate for organoid culture. Thereafter, a novel approach for development of rat hepatic organoids on thermoresponsive dish was established, based on self-assembly of rat liver cells driven by self-condensation of mesenchymal stem cell feederlayer. Viable, structurally organized and functional hepatic organoids were retrieved non-invasively from thermoresponsive dish. The third objective was to design and bioprint the liver construct. An optimum design for 3D bioprinting of organoid construct was developed using a BioCAD software and the bioprinting parameters were optimized for extrusion bioprinting of organoids as well as cells suspended in GelMA bioink. A cell construct and an organoid construct was bioprinted successfully. The final objective of the study was to evaluate the functions and histoarchitecture of bioprinted liver construct. The bioprinted organoid construct exhibited histomimetic cellular organization of hepatocytes and non-parenchymal cells. Whereas in the cell construct there was no evidence of tissue organization. Interestingly, the organoid construct showed higher expression of liver specific genes and exhibited enhanced liver functionalities compared to the cell construct. The results indicate that heterotypic cell interaction and cellular organization are key to achieving functional liver tissue substitutes.

The following points highlights the outcomes of the study.

1. A simple, cost effective and efficient hanging drop culture platform for high-throughput production of microtissues was developed.
2. Novel methodology for hepatic organoid production using thermoresponsive culture dish was developed.

3. Histomimetic functional liver tissue construct was biofabricated by 3D organoid bioprinting.

5.2 Conclusion

Depending on the results and the inferences from the study, it can be concluded that

1. GelMA bioink is an excellent biomatrix for the 3D culture of liver microtissues and for the 3D bioprinting of hepatic organoids.
2. The hanging-drop culture chamber developed in this study is a simple, cost effective and efficient platform for high-throughput fabrication of microtissues.
3. NGMA is an excellent thermoresponsive cell culture substrate for the non-invasive harvest of hepatic organoids.
4. Bone marrow-derived mesenchymal stem cells (MSCs) can be used as a supporting feeder layer for the formation and non-invasive harvest of hepatic organoids.
5. The hepatic organoids formed by the coculture of liver cells with MSCs can be used as an *in vitro* model for drug screening and as a cell source for the biofabrication of a histomimetic functional liver tissue construct.

5.3 Future perspectives

The future perspective of the work is to lead *in vitro* drug screening utilizing 3D bioprinted organoid constructs, which are more efficient than other cell culture systems. Various aspects of drug-induced hepatoxicity can be studied using the organoid construct. The presence of bile transporter protein (MRP2) within hepatic organoids may allow a user to study drug-induced cholestasis. While presence of immune cells like kupffer cell will enable a user to investigate inflammatory reactions associated with drug metabolites. Moving on to the pre-clinical level, implantation studies of the bioprinted organoid construct on rat liver disease models will further the understanding of its regenerative capabilities and about its potential to be used as an alternative to donor organs for liver transplantation. Furthermore, the methodology presented in this study can be implemented for human liver organoid development and bioprinting which will open up new avenues in the field of drug screening and regenerative therapy. With the use of human liver cells, the bioprinted human liver organoid constructs can become an *in vitro* alternative drug screening system before clinical trials.

Further improvements can be made to the bioprinted organoid construct with respect to the bioink composition, vascularization and culture condition. Mimicking the biochemical and biomechanical cues of native tissue ECM is crucial for modulating the proliferation and differentiation of cells within organoids. In this regard, a decellularized liver ECM bioink can be used for organoid bioprinting. Vascularization of the *in vitro* construct is one of the major challenges faced in liver tissue engineering. In the absence of a vascular network, the passive diffusion for delivering nutrients, growth factors, oxygen and removal of metabolic waste will be limited to few hundred microns within the bioprinted construct. To overcome this limitation microchannels could be created within organoid construct by printing sacrificial material. After stabilization of the bioprinted construct, the sacrificial material can be replaced with endothelial cells to form lumen like structures. In addition, culturing the organoid construct within a flow perfusion bioreactor may help to bypass the nutrient diffusion limits and will allow long-term culture of larger tissue constructs inside a highly controlled environment.

BIBLIOGRAPHY

1. Abdel-Misih, S. R. Z. and Bloomston, M. (2010) ‘Liver Anatomy’, The Surgical clinics of North America, 90(4), p. 643. doi: 10.1016/J.SUC.2010.04.017.
2. Acharya, S. K. (2021) ‘Acute Liver Failure: Indian Perspective’, Clinical Liver Disease, 18(3), pp. 143–149. doi: 10.1002/CLD.1135.
3. Achilli, T.-M., Meyer, J. and Morgan, J. R. (2012) ‘Advances in the formation, use and understanding of multi-cellular spheroids’, Expert opinion on biological therapy. 2012/07/12, 12(10), pp. 1347–1360. doi: 10.1517/14712598.2012.707181.
4. Agarwal, T., Banerjee, D., Konwarh, R., Esworthy, T., Kumari, J., Onesto, V., Das, P., Lee, B. H., Wagener, F. A. D. T. G., Makvandi, P., Mattoli, V., Ghosh, S. K., Maiti, T. K., Zhang, L. G. and Ozbolat, Ibrahim T (2021) ‘Recent advances in bioprinting technologies for engineering hepatic tissue’, Materials Science and Engineering: C, 123, p. 112013. doi: 10.1016/J.MSEC.2021.112013.
5. Agarwal, T., Banerjee, D., Konwarh, R., Esworthy, T., Kumari, J., Onesto, V., Das, P., Lee, B. H., Wagener, F. A. D. T. G., Makvandi, P., Mattoli, V., Ghosh, S. K., Maiti, T. K., Zhang, L. G. and Ozbolat, Ibrahim T. (2021) ‘Recent advances in bioprinting technologies for engineering hepatic tissue’, Materials Science and Engineering: C, 123, p. 112013. doi: 10.1016/J.MSEC.2021.112013.
6. Agarwal, T., Subramanian, B. and Maiti, T. K. (2019) ‘Liver Tissue Engineering: Challenges and Opportunities’, ACS Biomaterials Science and Engineering, 5(9), pp. 4167–4182. doi: 10.1021/ACSBIOMATERIALS.9B00745/ASSET/IMAGES/LARGE/AB9B00745_0001.JPEG.
7. Akbari, S. et al. (2019) ‘Robust, Long-Term Culture of Endoderm-Derived Hepatic Organoids for Disease Modeling’, Stem cell reports, 13(4), pp. 627–641. doi: 10.1016/J.STEMCR.2019.08.007.
8. Akkerman, N. and Defize, L. H. K. (2017) ‘Dawn of the organoid era’, BioEssays, 39(4), p. 1600244. doi: 10.1002/BIES.201600244.
9. Ang, C. H. et al. (2019) ‘Lgr5(+) pericentral hepatocytes are self-maintained in normal liver regeneration and susceptible to hepatocarcinogenesis.’, Proceedings of the National Academy of Sciences of the United States of America, 116(39), pp. 19530–19540. doi: 10.1073/pnas.1908099116.
10. Anil Kumar, P. R., Sreenivasan, K. and Kumary, T. V. (2007) ‘Alternate method for grafting thermoresponsive polymer for transferring in vitro cell sheet structures’, Journal of Applied Polymer Science, 105(4), pp. 2245–2251. doi: 10.1002/APP.26221.
11. Aparnathi, M. K. and Patel, J. S. (2016) ‘Effect of gel porosity and stiffness on culture of HepG2 cells encapsulated in gelatin methacrylate hydrogels’, Bioscience Biotechnology Research Communications, 9(3), pp. 463–470. doi: 10.21786/BBRC/9.3/18.
12. Arca, H. Ç. and Şenel, S. (2008) ‘Chitosan Based Systems for Tissue

Engineering Part II: Soft Tissues', J. Pharm. Sci, 33, pp. 211–216.

13. Arzumanian, V. A., Kiseleva, O. I. and Poverennaya, E. V. (2021) 'The Curious Case of the HepG2 Cell Line: 40 Years of Expertise', International journal of molecular sciences, 22(23). doi: 10.3390/IJMS222313135.
14. Asadi, M. et al. (2021) 'Hepatic cell-sheet fabrication of differentiated mesenchymal stem cells using decellularized extracellular matrix and thermoresponsive polymer', Biomedicine & Pharmacotherapy, 134, p. 111096. doi: 10.1016/J.BIOPHA.2020.111096.
15. Asrani, S. K. et al. (2019) 'Burden of liver diseases in the world', J Hepatol. 2018/09/30, 70(1), pp. 151–171. doi: S0168-8278(18)32388-2 [pii]10.1016/j.jhep.2018.09.014.
16. Asthana, A. and Kisaalita, W. S. (2012) 'Microtissue size and hypoxia in HTS with 3D cultures', Drug Discov Today, 17(15–16), pp. 810–817.
17. Baccarani, U. et al. (2004) 'First Report of Cryopreserved Human Hepatocytes Based Bioartificial Liver Successfully Used as a Bridge to Liver Transplantation', American Journal of Transplantation, 4(2), pp. 286–289. doi: 10.1046/J.1600-6143.2003.00310.X.
18. Bale, S. S. et al. (2016) 'Isolation and co-culture of rat parenchymal and non-parenchymal liver cells to evaluate cellular interactions and response', Scientific Reports, 6. doi: 10.1038/SREP25329.
19. Baxter, M. et al. (2015a) 'Phenotypic and functional analyses show stem cell-derived hepatocyte-like cells better mimic fetal rather than adult hepatocytes', Journal of Hepatology, 62(3), pp. 581–589. doi: 10.1016/J.JHEP.2014.10.016.
20. Baxter, M. et al. (2015b) 'Phenotypic and functional analyses show stem cell-derived hepatocyte-like cells better mimic fetal rather than adult hepatocytes', Journal of Hepatology, 62(3), pp. 581–589. doi: 10.1016/j.jhep.2014.10.016.
21. Benton, J. A. et al. (2009) 'Photocrosslinking of gelatin macromers to synthesize porous hydrogels that promote valvular interstitial cell function.', Tissue engineering. Part A, 15(11), pp. 3221–3230. doi: 10.1089/ten.TEA.2008.0545.
22. Bhatia, S. N. et al. (1999a) 'Effect of cell–cell interactions in preservation of cellular phenotype: cocultivation of hepatocytes and nonparenchymal cells', The FASEB Journal, 13(14), pp. 1883–1900. doi: 10.1096/FASEBJ.13.14.1883.
23. Bhatia, S. N. et al. (1999b) 'Effect of cell–cell interactions in preservation of cellular phenotype: cocultivation of hepatocytes and nonparenchymal cells', The FASEB Journal, 13(14), pp. 1883–1900. doi: 10.1096/FASEBJ.13.14.1883.
24. Bhise, N. S. et al. (2016) 'A liver-on-a-chip platform with bioprinted hepatic spheroids', Biofabrication, 8(1), p. 14101. doi: 10.1088/1758-5090/8/1/014101.
25. Billiet, T. et al. (2014) 'The 3D printing of gelatin methacrylamide cell-laden tissue-engineered constructs with high cell viability', Biomaterials, 35(1), pp. 49–62. doi: 10.1016/J.BIOMATERIALS.2013.09.078.
26. Blanding, J. H. and Tremblay, G. C. (1982) 'Ammonia detoxification in the fatty liver', Biochemical and Biophysical Research Communications, 107(4), pp. 1440–1445. doi: 10.1016/S0006-291X(82)80160-5.

27. Blouin, A., Bolender, R. P. and Weibel, E. R. (1977a) 'Distribution of organelles and membranes between hepatocytes and nonhepatocytes in the rat liver parenchyma. A stereological study', Journal of Cell Biology, 72(2), pp. 441–455. doi: 10.1083/jcb.72.2.441.
28. Blouin, A., Bolender, R. P. and Weibel, E. R. (1977b) 'Distribution of organelles and membranes between hepatocytes and nonhepatocytes in the rat liver parenchyma. A stereological study', Journal of Cell Biology, 72(2), pp. 441–455. doi: 10.1083/jcb.72.2.441.
29. Bouhadir, K. H. et al. (2001) 'Degradation of partially oxidized alginate and its potential application for tissue engineering.', Biotechnology progress, 17(5), pp. 945–950. doi: 10.1021/bp010070p.
30. Bouwmeester, M. C. et al. (2021) 'Bioprinting of Human Liver-Derived Epithelial Organoids for Toxicity Studies', Macromolecular bioscience, 21(12). doi: 10.1002/MABI.202100327.
31. Brech, A. and Berg, T. (2000) 'Fc receptor mediated endocytosis of small soluble immunoglobulin G immune complexes in Kupffer and endothelial cells from rat liver Education and Differentiation Determine Functional Hierarchies of CAR Modified Primary NK Cells View project Tankyrase inhibition View project', Article in Journal of Cell Science. doi: 10.1242/jcs.113.18.3255.
32. Bual, R. P. and Ijima, H. (2019) 'Intact extracellular matrix component promotes maintenance of liver-specific functions and larger aggregates formation of primary rat hepatocytes', Regenerative Therapy, 11, pp. 258–268. doi: 10.1016/J.RETH.2019.08.006.
33. Bücking, T. M. et al. (2017) 'From medical imaging data to 3D printed anatomical models', PLOS ONE, 12(5), p. e0178540. doi: 10.1371/JOURNAL.PONE.0178540.
34. Van Den Bulcke, A. I. et al. (2000) 'Structural and rheological properties of methacrylamide modified gelatin hydrogels', Biomacromolecules, 1(1), pp. 31–38. doi: 10.1021/BM990017D.
35. Castro, N. et al. (2020) 'Physically Active Bioreactors for Tissue Engineering Applications', Advanced Biosystems, 4(10), p. 2000125. doi: 10.1002/ADBI.202000125.
36. Chamuleau, R. A. (2009) 'Future of bioartificial liver support', World Journal of Gastrointestinal Surgery, 1(1), p. 21. doi: 10.4240/WJGS.V1.I1.21.
37. Chan, H. F., Zhang, Y. and Leong, K. W. (2016) 'Efficient One-Step Production of Microencapsulated Hepatocyte Spheroids with Enhanced Functions', Small, 12(20), pp. 2720–2730. doi: 10.1002/SMLL.201502932.
38. Chang, C. C. et al. (2011) 'Direct-write bioprinting three-dimensional biohybrid systems for future regenerative therapies', Journal of Biomedical Materials Research Part B: Applied Biomaterials, 98B(1), pp. 160–170. doi: 10.1002/JBM.B.31831.
39. Chang, S.-Y. et al. (2017) 'Characterization of rat or human hepatocytes cultured in microphysiological systems (MPS) to identify hepatotoxicity'. doi: 10.1016/j.tiv.2017.01.007.
40. Cheemerla, S. and Balakrishnan, M. (2021) 'Global Epidemiology of Chronic Liver Disease', Clinical Liver Disease, 17(5), pp. 365–370. doi:

10.1002/CLD.1061.

41. Chen, X. B., Li, M. G. and Ke, H. (2008) ‘Modeling of the flow rate in the dispensing-based process for fabricating tissue scaffolds’, Journal of Manufacturing Science and Engineering, 130(2), pp. 0210031–0210037. doi: 10.1115/1.2789725/462176.
42. Choudhury, D. et al. (2018) ‘Organ-Derived Decellularized Extracellular Matrix: A Game Changer for Bioink Manufacturing?’, Trends in Biotechnology, 36(8), pp. 787–805. doi: 10.1016/J.TIBTECH.2018.03.003.
43. Colosi, Cristina et al. (2016) ‘Microfluidic Bioprinting of Heterogeneous 3D Tissue Constructs Using Low-Viscosity Bioink’, Advanced Materials, 28(4), pp. 677–684. doi: 10.1002/ADMA.201503310.
44. Cooke, M. E. and Rosenzweig, D. H. (2021) ‘The rheology of direct and suspended extrusion bioprinting’, APL Bioengineering, 5(1). doi: 10.1063/5.0031475/1021206.
45. Croce, S. et al. (2019) ‘A Hepatic Scaffold from Decellularized Liver Tissue: Food for Thought’, Biomolecules, 9(12). doi: 10.3390/BIOM9120813.
46. Cui, X. et al. (2014) ‘F-actin cytoskeleton reorganization is associated with hepatic stellate cell activation’, Molecular Medicine Reports, 9(5), p. 1641. doi: 10.3892/MMR.2014.2036.
47. Cui, X., Hartanto, Y. and Zhang, H. (2017) ‘Advances in multicellular spheroids formation’, Journal of The Royal Society Interface, 14(127). doi: 10.1098/RSIF.2016.0877.
48. Cunningham, R. P. and Porat-Shliom, N. (2021) ‘Liver Zonation – Revisiting Old Questions With New Technologies’, Frontiers in Physiology, 12, p. 732929. doi: 10.3389/FPHYS.2021.732929.
49. Dai, Q. et al. (2022) ‘Recent Advances in Liver Engineering With Decellularized Scaffold’, Frontiers in Bioengineering and Biotechnology, 10, p. 142. doi: 10.3389/FBIOE.2022.831477/BIBTEX.
50. Daly, A. C. et al. (2016) ‘A comparison of different bioinks for 3D bioprinting of fibrocartilage and hyaline cartilage’, Biofabrication, 8(4). doi: 10.1088/1758-5090/8/4/045002.
51. Damania, A., Jain, E. and Kumar, A. (2014) ‘Advancements in in vitro hepatic models: Application for drug screening and therapeutics’, Hepatology International, 8(1), pp. 23–38. doi: 10.1007/S12072-013-9490-8.
52. Danoy, M. et al. (2020) ‘Characterization of liver zonation-like transcriptomic patterns in HLCs derived from hiPSCs in a microfluidic biochip environment’, Biotechnology Progress, 36(5), p. e3013. doi: 10.1002/BTPR.3013.
53. Das, P. et al. (2020) ‘Collagen-I and fibronectin modified three-dimensional electrospun PLGA scaffolds for long-term in vitro maintenance of functional hepatocytes’, Materials Science and Engineering: C, 111, p. 110723. doi: 10.1016/J.MSEC.2020.110723.
54. Das, S. and Das, D. (2021) ‘Rational Design of Peptide-based Smart Hydrogels for Therapeutic Applications’, Frontiers in Chemistry, 9, p. 980. doi: 10.3389/FCHEM.2021.770102/BIBTEX.
55. Desai, P. K., Tseng, H. and Souza, G. R. (2017) ‘Assembly of Hepatocyte Spheroids Using Magnetic 3D Cell Culture for CYP450 Inhibition/Induction’, International Journal of Molecular Sciences, 18(5). doi:

10.3390/IJMS18051085.

56. Dhawan, A. (2015) ‘Clinical human hepatocyte transplantation: Current status and challenges’, Liver Transplantation, 21, pp. S39–S44. doi: 10.1002/LT.24226.
57. Dingle, A. M. et al. (2018) ‘Characterization of isolated liver sinusoidal endothelial cells for liver bioengineering’, Angiogenesis, 21(3), pp. 581–597. doi: 10.1007/S10456-018-9610-0/FIGURES/7.
58. Discher, D. E., Janmey, P. and Wang, Y. L. (2005) ‘Tissue cells feel and respond to the stiffness of their substrate’, Science, 310(5751), pp. 1139–1143. doi: 10.1126/SCIENCE.1116995/ASSET/9FD0A405-058F-4F6E-B5B4-F55BB0CF5F4A/ASSETS/GRAPHIC/310_1139_F4.JPEG.
59. Dominici, M. et al. (2006) ‘Minimal criteria for defining multipotent mesenchymal stromal cells. The International Society for Cellular Therapy position statement’, Cytotherapy, 8(4), pp. 315–317. doi: 10.1080/14653240600855905.
60. Dong, C. and Lv, Y. (2016) ‘Application of Collagen Scaffold in Tissue Engineering: Recent Advances and New Perspectives’, Polymers, 8(2). doi: 10.3390/POLYM8020042.
61. Dong, H., Carr, W. W. and Morris, J. F. (2006) ‘Visualization of drop-on-demand inkjet: Drop formation and deposition’, Review of Scientific Instruments, 77(8), p. 085101. doi: 10.1063/1.2234853.
62. Drewitz, M. et al. (2011) ‘Towards automated production and drug sensitivity testing using scaffold-free spherical tumor microtissues’, Biotechnol J, 6(12), pp. 1488–1496.
63. Dunn, J. C. Y. et al. (1989) ‘Hepatocyte Function and Extracellular-Matrix Geometry - Long-Term Culture in a Sandwich Configuration’, FASEB Journal, 3(2), pp. 174–177.
64. Fatehullah, A., Tan, S. H. and Barker, N. (2016) ‘Organoids as an in vitro model of human development and disease’, Nature Cell Biology 2016 18:3, 18(3), pp. 246–254. doi: 10.1038/ncb3312.
65. Faulkner-Jones, A. et al. (2013) ‘Development of a valve-based cell printer for the formation of human embryonic stem cell spheroid aggregates’, Biofabrication, 5(1), pp. 1758–5082.
66. Florine, E. M. et al. (2013) ‘Effects of Dexamethasone on Mesenchymal Stromal Cell Chondrogenesis and Aggrecanase Activity: Comparison of Agarose and Self-Assembling Peptide Scaffolds’, Cartilage, 4(1), pp. 63–74. doi: 10.1177/1947603512455196.
67. Forbes, S. J., Gupta, S. and Dhawan, A. (2015) ‘Cell therapy for liver disease: From liver transplantation to cell factory’, Journal of hepatology, 62(1 Suppl), pp. S157–S169. doi: 10.1016/J.JHEP.2015.02.040.
68. Fu, D. et al. (2019) ‘Novel Mechanisms of Valproate Hepatotoxicity: Impaired Mrp2 Trafficking and Hepatocyte Depolarization’, Toxicological sciences : an official journal of the Society of Toxicology, 171(2), pp. 431–442. doi: 10.1093/TOXSCI/KFZ154.
69. Fujii, E. et al. (2018) ‘A simple method for histopathological evaluation of organoids’, Journal of Toxicologic Pathology, 31(1), pp. 81–85. doi: 10.1293/TOX.2017-0060.

70. Fujii, M. et al. (2018) ‘In vivo construction of liver tissue by implantation of a hepatic non-parenchymal/adipose-derived stem cell sheet’, Journal of Tissue Engineering and Regenerative Medicine, 12(1), pp. e287–e295. doi: 10.1002/TERM.2424.
71. Gamboa, C. M. et al. (2021) ‘Optimized 3d culture of hepatic cells for liver organoid metabolic assays’, Cells, 10(12). doi: 10.3390/CELLS10123280/S1.
72. Gao, F. et al. (2016) ‘Mesenchymal stem cells and immunomodulation: current status and future prospects’, Cell Death & Disease 2016 7:1, 7(1), pp. e2062–e2062. doi: 10.1038/cddis.2015.327.
73. Gao, T. et al. (2018) ‘Optimization of gelatin–alginate composite bioink printability using rheological parameters: a systematic approach’, Biofabrication, 10(3), p. 034106. doi: 10.1088/1758-5090/AACDC7.
74. Gaskell, H. et al. (2016) ‘Characterization of a Functional C3A Liver Spheroid Model’, Toxicol. Res., 5. doi: 10.1039/c6tx00101g.
75. Genové, E. et al. (2009) ‘Functionalized self-assembling peptide hydrogel enhance maintenance of hepatocyte activity in vitro’, Journal of cellular and molecular medicine, 13(9B), pp. 3387–3397. doi: 10.1111/J.1582-4934.2009.00970.X.
76. Ghasemi-Mobarakeh, L. et al. (2019) ‘Key terminology in biomaterials and biocompatibility’, Current Opinion in Biomedical Engineering, 10, pp. 45–50. doi: 10.1016/J.COBME.2019.02.004.
77. Ghasemzadeh-Hasankolaei, M. et al. (2016) ‘Transplantation of Autologous Bone Marrow Mesenchymal Stem Cells into the Testes of Infertile Male Rats and New Germ Cell Formation’, International Journal of Stem Cells, 9(2), pp. 250–263. doi: 10.15283/IJSC16010.
78. GhavamiNejad, A. et al. (2020) ‘Crosslinking Strategies for Three-Dimensional Bioprinting of Polymeric Hydrogels’, Small (Weinheim an der Bergstrasse, Germany), 16(35), p. e2002931. doi: 10.1002/SMLL.202002931.
79. Al Ghrbawy, N. M. et al. (2016) ‘Differentiation of Bone Marrow: Derived Mesenchymal Stem Cells into Hepatocyte-like Cells’, Indian Journal of Hematology & Blood Transfusion, 32(3), p. 276. doi: 10.1007/S12288-015-0581-7.
80. Gijbels, E., Vanhaecke, T. and Vinken, M. (2019) ‘Establishment of Sandwich Cultures of Primary Human Hepatocytes’, Methods in molecular biology (Clifton, N.J.), 1981, pp. 325–333. doi: 10.1007/978-1-4939-9420-5_21.
81. Gillispie, G. et al. (2020) ‘Assessment methodologies for extrusion-based bioink printability’, Biofabrication, 12(2), p. 022003. doi: 10.1088/1758-5090/AB6F0D.
82. Giobbe, G. G. et al. (2019) ‘Extracellular matrix hydrogel derived from decellularized tissues enables endodermal organoid culture’, Nature Communications 2019 10:1, 10(1), pp. 1–14. doi: 10.1038/s41467-019-13605-4.
83. Gómez-Lechón, M. J., Tolosa, L. and Mt, D. (2014) ‘Cell-based models to predict human hepatotoxicity of drugs’, Revista de Toxicología, 31(2), pp. 149–156. Available at: https://www.redalyc.org/articulo.oa?id=91932969007.
84. Gori, M. et al. (2020) ‘Biofabrication of Hepatic Constructs by 3D Bioprinting of a Cell-Laden Thermogel: An Effective Tool to Assess Drug-Induced

Hepatotoxic Response', Advanced Healthcare Materials, 9(21), p. 2001163. doi: 10.1002/ADHM.202001163.

85. Grix, T. et al. (2018) 'Bioprinting Perfusion-Enabled Liver Equivalents for Advanced Organ-on-a-Chip Applications', Genes, 9(4). doi: 10.3390/GENES9040176.
86. Groll, J. et al. (2018) 'A definition of bioinks and their distinction from biomaterial inks', Biofabrication, 11(1), p. 013001. doi: 10.1088/1758-5090/AAEC52.
87. Gu, J. et al. (2009) 'Establishment of a three-dimensional co-culture system by porcine hepatocytes and bone marrow mesenchymal stem cells in vitro', Hepatology research : the official journal of the Japan Society of Hepatology, 39(4), pp. 398–407. doi: 10.1111/J.1872-034X.2008.00472.X.
88. Guilak, F. et al. (2014) 'Biomechanics and mechanobiology in functional tissue engineering', Journal of biomechanics, 47(9), pp. 1933–1940. doi: 10.1016/J.JBIOMECH.2014.04.019.
89. Gutzweiler, L. et al. (2017) 'Large scale production and controlled deposition of single HUVEC spheroids for bioprinting applications', Biofabrication, 9(2), pp. 1758–5090.
90. Habib, A. et al. (2018) '3D Printability of Alginate-Carboxymethyl Cellulose Hydrogel', Materials 2018, Vol. 11, Page 454, 11(3), p. 454. doi: 10.3390/MA11030454.
91. Hall, C. et al. (2017) 'Regulators of Cholangiocyte Proliferation', Gene Expression, 17(2), p. 155. doi: 10.3727/105221616X692568.
92. Han, Y. et al. (2022) 'The secretion profile of mesenchymal stem cells and potential applications in treating human diseases', Signal Transduction and Targeted Therapy 2022 7:1, 7(1), pp. 1–19. doi: 10.1038/s41392-022-00932-0.
93. Harwate, N. et al. (2021) 'Gelatin–chitosan macroporous scaffolds integrated with customizable hollow channels for liver tissue engineering', Food, Medical, and Environmental Applications of Polysaccharides, pp. 667–685. doi: 10.1016/B978-0-12-819239-9.00009-9.
94. Hashemi, S. M. et al. (2009) 'In vitro differentiation of human cord blood-derived unrestricted somatic stem cells into hepatocyte-like cells on poly(epsilon-caprolactone) nanofiber scaffolds', Cells, tissues, organs, 190(3), pp. 135–149. doi: 10.1159/000187716.
95. Hasirci, V. et al. (2004) 'Expression of Liver-Specific Functions by Rat Hepatocytes Seeded in Treated Poly(Lactic-co-Glycolic) Acid Biodegradable Foams', https://home.liebertpub.com/ten, 7(4), pp. 385–394. doi: 10.1089/10763270152436445.
96. Hatzistergos, K. E. et al. (2010) 'Bone Marrow Mesenchymal Stem Cells Stimulate Cardiac Stem Cell Proliferation and Differentiation', Circulation Research, 107(7), pp. 913–922. doi: 10.1161/CIRCRESAHA.110.222703.
97. Havasi, P. et al. (2013) 'Mesenchymal stem cells as an appropriate feeder layer for prolonged in vitro culture of human induced pluripotent stem cells', Molecular biology reports, 40(4), pp. 3023–3031. doi: 10.1007/S11033-012-2376-3.
98. He, X. L. et al. (2010) 'Immobilization of galactose ligands on

thermoresponsive culture surface and its influence on cell adhesion/detachment', Journal of Colloid and Interface Science, 350(2), pp. 471–479. doi: 10.1016/J.JCIS.2010.07.013.

99. He, Y. et al. (2016) 'Research on the printability of hydrogels in 3D bioprinting', Scientific Reports 2016 6:1, 6(1), pp. 1–13. doi: 10.1038/srep29977.
100. Heck, T. et al. (2013) 'Enzyme-catalyzed protein crosslinking', Applied Microbiology and Biotechnology, 97(2), p. 461. doi: 10.1007/S00253-012-4569-Z.
101. Hettiaratchi, M. H. et al. (no date) 'A rapid method for determining protein diffusion through hydrogels for regenerative medicine applications'. doi: 10.1063/1.4999925.
102. Hijmans, B. S. et al. (2017) 'Hepatocytes contribute to residual glucose production in a mouse model for glycogen storage disease type Ia', Hepatology, 66(6), pp. 2042–2054. doi: 10.1002/HEP.29389.
103. Hirata, K. et al. (1983) 'Effects of laminin, fibronectin and type IV collagen on liver cell cultures', Experimental cell biology, 51(3), pp. 121–129. doi: 10.1159/000163182.
104. Hirode, G., Saab, S. and Wong, R. J. (2020) 'Trends in the Burden of Chronic Liver Disease Among Hospitalized US Adults', JAMA Network Open, 3(4), pp. e201997–e201997. doi: 10.1001/JAMANETWORKOPEN.2020.1997.
105. Hirsch, D. et al. (2014) 'LGR5 positivity defines stem-like cells in colorectal cancer', Carcinogenesis, 35(4), p. 849. doi: 10.1093/CARCIN/BGT377.
106. Hoekstra, R. and Chamuleau, R. A. F. M. (2002) 'Recent developments on human cell lines for the bioartificial liver', International Journal of Artificial Organs, 25(3), pp. 182–191. doi: 10.1177/039139880202500304.
107. Hofer, M. and Lutolf, M. P. (2021) 'Engineering organoids', Nature Reviews Materials 2021 6:5, 6(5), pp. 402–420. doi: 10.1038/s41578-021-00279-y.
108. Holmes, T. C. et al. (2000) 'Extensive neurite outgrowth and active synapse formation on self-assembling peptide scaffolds', Proceedings of the National Academy of Sciences of the United States of America, 97(12), pp. 6728–6733. doi: 10.1073/PNAS.97.12.6728.
109. Hölzl, K. et al. (2016) 'Bioink properties before, during and after 3D bioprinting', Biofabrication, 8(3), p. 032002. doi: 10.1088/1758-5090/8/3/032002.
110. Hong, G. et al. (2021) 'Production of Multiple Cell-Laden Microtissue Spheroids with a Biomimetic Hepatic-Lobule-Like Structure', Advanced Materials, 33(36), p. 2102624. doi: 10.1002/ADMA.202102624.
111. Hospodiuk, M. et al. (2017) 'The bioink: A comprehensive review on bioprintable materials', Biotechnology Advances, 35(2), pp. 217–239. doi: 10.1016/J.BIOTECHADV.2016.12.006.
112. Hosseini, V. et al. (2019) 'Current progress in hepatic tissue regeneration by tissue engineering', Journal of Translational Medicine 2019 17:1, 17(1), pp. 1–24. doi: 10.1186/S12967-019-02137-6.
113. Hu, C. and Li, L. (2015) 'In vitro culture of isolated primary hepatocytes and stem cell-derived hepatocyte-like cells for liver regeneration', Protein & Cell, 6(8), p. 562. doi: 10.1007/S13238-015-0180-2.

114. Hu, H. et al. (2018) 'Long-Term Expansion of Functional Mouse and Human Hepatocytes as 3D Organoids', Cell, 175(6), pp. 1591-1606.e19. doi: 10.1016/J.CELL.2018.11.013.
115. Huch, M. et al. (2015) 'Long-Term Culture of Genome-Stable Bipotent Stem Cells from Adult Human Liver', Cell, 160(1–2), p. 299. doi: 10.1016/J.CELL.2014.11.050.
116. Hughes, A. J. et al. (2018) 'Engineered Tissue Folding by Mechanical Compaction of the Mesenchyme', Developmental Cell, 44(2), pp. 165-178.e6. doi: 10.1016/J.DEVCEL.2017.12.004.
117. Hull, C. W. and Arcadia, C. (no date) 'United States Patent (19) Hull (54) (75) (73) 21) 22 (51) 52) (58) (56) APPARATUS FOR PRODUCTION OF THREE-DMENSONAL OBJECTS BY STEREO THOGRAPHY'.
118. Hutson, C. B. et al. (2011) 'Synthesis and Characterization of Tunable Poly(Ethylene Glycol): Gelatin Methacrylate Composite Hydrogels', Tissue Engineering. Part A, 17(13–14), p. 1713. doi: 10.1089/TEN.TEA.2010.0666.
119. Iansante, V. et al. (2017) 'Human hepatocyte transplantation for liver disease: current status and future perspectives', Pediatric Research 2018 83:1, 83(1), pp. 232–240. doi: 10.1038/pr.2017.284.
120. Inamori, M., Mizumoto, H. and Kajiwara, T. (2009) 'An Approach for Formation of Vascularized Liver Tissue by Endothelial Cell–Covered Hepatocyte Spheroid Integration', https://home.liebertpub.com/tea, 15(8), pp. 2029–2037. doi: 10.1089/TEN.TEA.2008.0403.
121. Ishihara, K. et al. (2006) 'Formation of a sheet-shaped organoid using rat primary hepatocytes for long-term maintenance of liver-specific functions', The International journal of artificial organs, 29(3), pp. 318–328. doi: 10.1177/039139880602900310.
122. Itaba, N., Matsumi, Y., et al. (2015) 'Human mesenchymal stem cell-engineered hepatic cell sheets accelerate liver regeneration in mice', Scientific Reports 2015 5:1, 5(1), pp. 1–17. doi: 10.1038/srep16169.
123. Itaba, N., Sakabe, T., et al. (2015) 'Identification of the small molecule compound which induces hepatic differentiation of human mesenchymal stem cells', Regenerative Therapy, 2, p. 32. doi: 10.1016/J.RETH.2015.10.001.
124. Jain, E., Damania, A. and Kumar, A. (2014) 'Biomaterials for liver tissue engineering', Hepatology International, 8(2), pp. 185–197. doi: 10.1007/S12072-013-9503-7/FIGURES/3.
125. Jakab, K. et al. (2004) 'Engineering biological structures of prescribed shaped using self-assembling multicellular systems', Proceedings of the National Academy of Sciences of the United States of America, 101(9), pp. 2864–2869. doi: 10.1073/PNAS.0400164101/ASSET/8CE52A28-BA68-4123-8E9B-1953C1F2AF30/ASSETS/GRAPHIC/ZPQ0080439610005.JPEG.
126. James, S. L. et al. (2018) 'Global, regional, and national incidence, prevalence, and years lived with disability for 354 Diseases and Injuries for 195 countries and territories, 1990-2017: A systematic analysis for the Global Burden of Disease Study 2017', The Lancet, 392(10159), pp. 1789–1858. doi: 10.1016/S0140-6736(18)32279-7/ATTACHMENT/DB6E3413-74DC-43AE-B7CC-CA155C28589E/MMC2.PDF.
127. Jaramillo, M. et al. (2018) 'Decellularized Human Liver Extracellular Matrix

(hDLM) Mediated Hepatic Differentiation of Human Induced Pluripotent Stem Cells (hIPSc)', Journal of tissue engineering and regenerative medicine, 12(4), p. e1962. doi: 10.1002/TERM.2627.

128. Joseph, N. et al. (2010) 'A Cytocompatible Poly(N-isopropylacrylamide-co-glycidylmethacrylate) Coated Surface as New Substrate for Corneal Tissue Engineering':, http://dx.doi.org/10.1177/0883911509353481, 25(1), pp. 58–74. doi: 10.1177/0883911509353481.
129. Joseph, N., Prasad, T. and Joseph Sreenivasan K., L. (2011) 'Intelligent Thermoresponsive Substrate from Modified Overhead Projection Sheet as a Tool for Construction and Support of Cell Sheets In Vitro', Tissue Engineering Part C: Methods, 17(2), pp. 181–191. doi: 10.1089/ten.tec.2009.0783.
130. Jung, J. and Oh, J. (no date) 'INFLUENCE OF PHOTO-INITIATOR CONCENTRATION ON THE VIABILITY OF CELLS ENCAPSULATED IN PHOTO-CROSSLINKED MICROGELS FABRICATED BY MICROFLUIDICS', Digest Journal of Nanomaterials and Biostructures, 9(2), pp. 503–509.
131. Kalra, A. et al. (2022) 'Physiology, Liver', StatPearls. Available at: https://www.ncbi.nlm.nih.gov/books/NBK535438/ (Accessed: 19 November 2022).
132. Kang, D. et al. (2020) 'Bioprinting of Multiscaled Hepatic Lobules within a Highly Vascularized Construct', Small, 16(13), p. 1905505. doi: 10.1002/SMLL.201905505.
133. Kang, H. W. et al. (2016) 'A 3D bioprinting system to produce human-scale tissue constructs with structural integrity', Nature Biotechnology 2016 34:3, 34(3), pp. 312–319. doi: 10.1038/nbt.3413.
134. Kang, Y. B. A. et al. (2018) 'Metabolic Patterning on a Chip: Towards in vitro Liver Zonation of Primary Rat and Human Hepatocytes', Scientific Reports 2018 8:1, 8(1), pp. 1–13. doi: 10.1038/s41598-018-27179-6.
135. Kanninen, L. K. et al. (2016) 'Laminin-511 and laminin-521-based matrices for efficient hepatic specification of human pluripotent stem cells.', Biomaterials, 103, pp. 86–100. doi: 10.1016/j.biomaterials.2016.06.054.
136. Katsuda, T. et al. (2010) 'Transplantation of a fetal liver cell-loaded hyaluronic acid sponge onto the mesentery recovers a Wilson's disease model rat', The Journal of Biochemistry, 148(3), pp. 281–288. doi: 10.1093/JB/MVQ063.
137. Kelm, J. M. et al. (2003) 'Method for generation of homogeneous multicellular tumor spheroids applicable to a wide variety of cell types', Biotechnology and Bioengineering, 83(2), pp. 173–180. doi: 10.1002/BIT.10655.
138. Khati, V. et al. (2022) '3D Bioprinting of Multi-Material Decellularized Liver Matrix Hydrogel at Physiological Temperatures', Biosensors, 12(7). doi: 10.3390/BIOS12070521.
139. Khetani, S. R. et al. (2004) 'Exploring interactions between rat hepatocytes and nonparenchymal cells using gene expression profiling', Hepatology, 40(3), pp. 545–554. doi: 10.1002/HEP.20351.
140. Khonsary, S. A. (2017) 'Guyton and Hall: Textbook of Medical Physiology', Surgical Neurology International, 8(1), p. 275. doi: 10.4103/SNI.SNI_327_17.
141. Kim, K. et al. (2017) 'Fabrication of functional 3D hepatic tissues with polarized hepatocytes by stacking endothelial cell sheets in vitro', Journal of

Tissue Engineering and Regenerative Medicine, 11(7), pp. 2071–2080. doi: 10.1002/TERM.2102.

142. Kim, P. et al. (2014) ‘Fabrication of poly(ethylene glycol): gelatin methacrylate composite nanostructures with tunable stiffness and degradation for vascular tissue engineering’, Biofabrication, 6(2), p. 024112. doi: 10.1088/1758-5082/6/2/024112.
143. Kizawa, H. et al. (2017) ‘Scaffold-free 3D bio-printed human liver tissue stably maintains metabolic functions useful for drug discovery’, Biochemistry and Biophysics Reports, 10, pp. 186–191. doi: 10.1016/J.BBREP.2017.04.004.
144. Ko, I. K. et al. (2015) ‘Bioengineered transplantable porcine livers with re-endothelialized vasculature’, Biomaterials, 40, pp. 72–79. doi: 10.1016/J.BIOMATERIALS.2014.11.027.
145. Kobayashi, N. et al. (2000) ‘Establishment of a reversibly immortalized human hepatocyte cell line by using Cre/loxP site-specific recombination’, Transplantation proceedings, 32(5), pp. 1121–1122. doi: 10.1016/S0041-1345(00)01154-4.
146. Koui, Y. et al. (2017) ‘An In Vitro Human Liver Model by iPSC-Derived Parenchymal and Non-parenchymal Cells’, Stem cell reports, 9(2), pp. 490–498. doi: 10.1016/J.STEMCR.2017.06.010.
147. Koutsopoulos, S. (2016) ‘Self-assembling peptide nanofiber hydrogels in tissue engineering and regenerative medicine: Progress, design guidelines, and applications’, Journal of Biomedical Materials Research Part A, 104(4), pp. 1002–1016. doi: 10.1002/JBM.A.35638.
148. Krishna, M. (2013) ‘Microscopic anatomy of the liver’, Clinical Liver Disease, 2(Suppl 1), p. S4. doi: 10.1002/CLD.147.
149. Lampin, M. et al. (1997) ‘Correlation between substratum roughness and wettability, cell adhesion, and cell migration’. doi: 10.1002/(SICI)1097-4636(199707)36:1.
150. Lan, S. F., Safiejko-Mroczka, B. and Starly, B. (2010) ‘Long-term cultivation of HepG2 liver cells encapsulated in alginate hydrogels: A study of cell viability, morphology and drug metabolism’, Toxicology in Vitro, 24(4), pp. 1314–1323. doi: 10.1016/J.TIV.2010.02.015.
151. Landry, J. et al. (1985) ‘Spheroidal aggregate culture of rat liver cells: histotypic reorganization, biomatrix deposition, and maintenance of functional activities.’, Journal of Cell Biology, 101(3), pp. 914–923. doi: 10.1083/JCB.101.3.914.
152. Langer, R. and Vacanti, J. P. (1993) ‘Tissue Engineering’, Science, 260(5110), pp. 920–926. doi: 10.1126/SCIENCE.8493529.
153. Lee, B. H., Shirahama, H., Cho, N.-J., et al. (2015) ‘Efficient and controllable synthesis of highly substituted gelatin methacrylamide for mechanically stiff hydrogels’, RSC Advances, 5(128), pp. 106094–106097. doi: 10.1039/c5ra22028a.
154. Lee, B. H., Shirahama, H., Cho, N. J., et al. (2015) ‘Efficient and controllable synthesis of highly substituted gelatin methacrylamide for mechanically stiff hydrogels’, RSC Advances, 5(128), pp. 106094–106097. doi: 10.1039/C5RA22028A.

155. Lee, B. H. et al. (2016) ‘Synthesis and Characterization of Types A and B Gelatin Methacryloyl for Bioink Applications’, Materials, 9(10), p. 797. doi: 10.3390/MA9100797.
156. Lee, H. et al. (2017) ‘Development of Liver Decellularized Extracellular Matrix Bioink for Three-Dimensional Cell Printing-Based Liver Tissue Engineering’, Biomacromolecules, 18(4), pp. 1229–1237. doi: 10.1021/ACS.BIOMAC.6B01908/ASSET/IMAGES/MEDIUM/BM-2016-01908B_0007.GIF.
157. Lee, H. et al. (2019) ‘Cell-printed 3D liver-on-a-chip possessing a liver microenvironment and biliary system’, Biofabrication, 11(2), p. 025001. doi: 10.1088/1758-5090/AAF9FA.
158. Lee, K. Y. and Mooney, D. J. (2012) ‘Alginate: properties and biomedical applications’, Progress in polymer science, 37(1), p. 106. doi: 10.1016/J.PROGPOLYMSCI.2011.06.003.
159. Lee, W. M. (2003) ‘Drug-Induced Hepatotoxicity’, https://doi.org/10.1056/NEJMra021844, 349(5), pp. 474–485. doi: 10.1056/NEJMRA021844.
160. Lewis, P. L. et al. (2019) ‘Directing the growth and alignment of biliary epithelium within extracellular matrix hydrogels’, Acta Biomaterialia, 85, pp. 84–93. doi: 10.1016/J.ACTBIO.2018.12.039.
161. Lewis, P. L., Green, R. M. and Shah, R. N. (2018) ‘3D-Printed Gelatin Scaffolds of Differing Pore Geometry Modulate Hepatocyte Function and Gene Expression’, Acta biomaterialia, 69, p. 63. doi: 10.1016/J.ACTBIO.2017.12.042.
162. Li, R. et al. (2022) ‘Fibrinogen improves liver function via promoting cell aggregation and fibronectin assembly in hepatic spheroids’, Biomaterials, 280, p. 121266. doi: 10.1016/J.BIOMATERIALS.2021.121266.
163. Lim, K. S. et al. (2020) ‘Fundamentals and Applications of Photo-Cross-Linking in Bioprinting’, Chemical Reviews, 120(19), pp. 10662–10694. doi: 10.1021/ACS.CHEMREV.9B00812.
164. Liu, F. et al. (2018) ‘Natural Polymers for Organ 3D Bioprinting’, Polymers 2018, Vol. 10, Page 1278, 10(11), p. 1278. doi: 10.3390/POLYM10111278.
165. Liver Disease in India (no date). Available at: https://www.worldlifeexpectancy.com/india-liver-disease (Accessed: 15 March 2022).
166. Luebke-Wheeler, J. L. et al. (2009) ‘E-cadherin protects primary hepatocyte spheroids from cell death by a caspase-independent mechanism’, Cell Transplantation, 18(12), pp. 1281–1287. doi: 10.3727/096368909X474258.
167. Ma, X. et al. (2016) ‘Deterministically patterned biomimetic human iPSC-derived hepatic model via rapid 3D bioprinting’, Proceedings of the National Academy of Sciences of the United States of America, 113(8), pp. 2206–2211. doi: 10.1073/PNAS.1524510113.
168. De Magistris, P. and Antonin, W. (2018) ‘The Dynamic Nature of the Nuclear Envelope’, Current Biology, 28(8), pp. R487–R497. doi: 10.1016/J.CUB.2018.01.073.
169. Mahillo, B. et al. (2018) ‘Worldwide distribution of solid organ transplantation and access of population to those practices’, Transplantation, 102(Supplement

7), pp. S71–S72. doi: 10.1097/01.TP.0000542650.33995.B3.

170. Makadia, H. K. and Siegel, S. J. (2011) 'Poly Lactic-co-Glycolic Acid (PLGA) as Biodegradable Controlled Drug Delivery Carrier', Polymers, 3(3), p. 1377. doi: 10.3390/POLYM3031377.
171. Manco, R. and Itzkovitz, S. (2021) 'Liver zonation', Journal of Hepatology. Elsevier B.V., pp. 466–468. doi: 10.1016/j.jhep.2020.09.003.
172. Manne, V., Handa, P. and Kowdley, K. V. (2018) 'Pathophysiology of Nonalcoholic Fatty Liver Disease/Nonalcoholic Steatohepatitis', Clinics in liver disease, 22(1), pp. 23–37. doi: 10.1016/J.CLD.2017.08.007.
173. Mathapati, S. et al. (2016) 'Small-Molecule-Directed Hepatocyte-Like Cell Differentiation of Human Pluripotent Stem Cells.', Current protocols in stem cell biology, 38, pp. 1G.6.1-1G.6.18. doi: 10.1002/cpsc.13.
174. Mazza, G. et al. (2015) 'Decellularized human liver as a natural 3D-scaffold for liver bioengineering and transplantation', Scientific reports, 5. doi: 10.1038/SREP13079.
175. Mazza, G. et al. (2018) 'Liver tissue engineering: From implantable tissue to whole organ engineering', Hepatology Communications, 2(2), pp. 131–141. doi: 10.1002/HEP4.1136.
176. Mazzocchi, A. et al. (2018) 'Optimization of collagen type I-hyaluronan hybrid bioink for 3D bioprinted liver microenvironments', Biofabrication, 11(1). doi: 10.1088/1758-5090/AAE543.
177. McMurtrey, R. J. (2016) 'Analytic Models of Oxygen and Nutrient Diffusion, Metabolism Dynamics, and Architecture Optimization in Three-Dimensional Tissue Constructs with Applications and Insights in Cerebral Organoids', Tissue Engineering. Part C, Methods, 22(3), p. 221. doi: 10.1089/TEN.TEC.2015.0375.
178. Messner, S. et al. (2018) 'Transcriptomic, Proteomic, and Functional Long-Term Characterization of Multicellular Three-Dimensional Human Liver Microtissues', Applied In Vitro Toxicology, 4(1), pp. 1–12. doi: 10.1089/AIVT.2017.0022/ASSET/IMAGES/LARGE/FIGURE5.JPEG.
179. Mi, S. et al. (2018) 'Construction of a liver sinusoid based on the laminar flow on chip and self-assembly of endothelial cells', Biofabrication, 10(2), p. 025010. doi: 10.1088/1758-5090/AAA97E.
180. Michalopoulos, G. K. et al. (1999) 'Morphogenetic events in mixed cultures of rat hepatocytes and nonparenchymal cells maintained in biological matrices in the presence of hepatocyte growth factor and epidermal growth factor', Hepatology (Baltimore, Md.), 29(1), pp. 90–100. doi: 10.1002/HEP.510290149.
181. Michalopoulos, George K et al. (2001) 'Histological Organization in Hepatocyte Organoid Cultures', The American Journal of Pathology, 159(5), p. 1877. doi: 10.1016/S0002-9440(10)63034-9.
182. Michalopoulos, George K. et al. (2001) 'Histological Organization in Hepatocyte Organoid Cultures', The American Journal of Pathology, 159(5), p. 1877. doi: 10.1016/S0002-9440(10)63034-9.
183. Michalopoulos, G. K. et al. (2002) 'Hepatocytes Undergo Phenotypic Transformation to Biliary Epithelium in Organoid Cultures', Hepatology (Baltimore, Md.), 36(2), p. 278. doi: 10.1053/JHEP.2002.34858.

184. Miri, A. K. et al. (2019) ‘Effective bioprinting resolution in tissue model fabrication’, Lab on a Chip, 19(11), pp. 2019–2037. doi: 10.1039/C8LC01037D.
185. Mironi-Harpaz, I. et al. (2012a) ‘Photopolymerization of cell-encapsulating hydrogels: crosslinking efficiency versus cytotoxicity’, Acta biomaterialia, 8(5), pp. 1838–1848. doi: 10.1016/J.ACTBIO.2011.12.034.
186. Mironi-Harpaz, I. et al. (2012b) ‘Photopolymerization of cell-encapsulating hydrogels: Crosslinking efficiency versus cytotoxicity’, Acta Biomaterialia, 8(5), pp. 1838–1848. doi: 10.1016/J.ACTBIO.2011.12.034.
187. Mironov, V. et al. (2003) ‘Organ printing: computer-aided jet-based 3D tissue engineering’, Trends in Biotechnology, 21(4), pp. 157–161. doi: 10.1016/S0167-7799(03)00033-7.
188. Mironov, V. et al. (2009) ‘Organ printing: Tissue spheroids as building blocks’, Biomaterials, 30(12), p. 2164. doi: 10.1016/J.BIOMATERIALS.2008.12.084.
189. Misawa, H. et al. (2006) ‘PuraMatrix facilitates bone regeneration in bone defects of calvaria in mice’, Cell transplantation, 15(10), pp. 903–910. doi: 10.3727/000000006783981369.
190. Mitaka, T. et al. (1999) ‘Reconstruction of hepatic organoid by rat small hepatocytes and hepatic nonparenchymal cells’, Hepatology, 29(1), pp. 111–125. doi: 10.1002/HEP.510290103.
191. Mohammadpour, A. et al. (2018) ‘Promoting hepatogenic differentiation of human mesenchymal stem cells using a novel laminin-containing gelatin cryogel scaffold’, Biochemical and Biophysical Research Communications, 507(1–4), pp. 15–21. doi: 10.1016/J.BBRC.2018.10.121.
192. Moman, R. N., Gupta, N. and Varacallo, M. (2022) ‘Physiology, Albumin’, StatPearls. Available at: https://www.ncbi.nlm.nih.gov/books/NBK459198/ (Accessed: 17 November 2022).
193. Monostory, K. et al. (2005) ‘The effect of synthetic glucocorticoid, dexamethasone on CYP1A1 inducibility in adult rat and human hepatocytes’, FEBS Letters, 579(1), pp. 229–235. doi: 10.1016/J.FEBSLET.2004.11.080.
194. Mooney, D. J. et al. (1995) ‘Biodegradable sponges for hepatocyte transplantation’, Journal of biomedical materials research, 29(8), pp. 959–965. doi: 10.1002/JBM.820290807.
195. Moriya, K. et al. (2012) ‘Fibronectin is essential for survival but is dispensable for proliferation of hepatocytes in acute liver injury’, Hepatology (Baltimore, Md.), 56(1), p. 311. doi: 10.1002/HEP.25624.
196. Moscona, A. (1961) ‘Rotation-mediated histogenetic aggregation of dissociated cells: A quantifiable approach to cell interactions in vitro’, Experimental Cell Research, 22(C), pp. 455–475. doi: 10.1016/0014-4827(61)90122-7.
197. Mukherjee, P. S. et al. (2017) ‘Etiology and mode of presentation of chronic liver diseases in India: A multi centric study’, PloS one, 12(10). doi: 10.1371/JOURNAL.PONE.0187033.
198. Murphy, S. V. and Atala, A. (2014) ‘3D bioprinting of tissues and organs’, Nature Biotechnology 2014 32:8, 32(8), pp. 773–785. doi: 10.1038/nbt.2958.
199. Narasimhan, G., Kota, V. and Rela, M. (2016) ‘Liver transplantation in India’,

Liver Transplantation, 22(7), pp. 1019–1024. doi: 10.1002/LT.24459.

200. Narmoneva, D. A. et al. (2004) ‘Endothelial cells promote cardiac myocyte survival and spatial reorganization: implications for cardiac regeneration’, Circulation, 110(8), pp. 962–968. doi: 10.1161/01.CIR.0000140667.37070.07.
201. Narmoneva, D. A. et al. (2005) ‘Self-assembling short oligopeptides and the promotion of angiogenesis’, Biomaterials, 26(23), pp. 4837–4846. doi: 10.1016/J.BIOMATERIALS.2005.01.005.
202. Natarajan, V., Moeun, Y. and Kidambi, S. (2021) ‘Exploring Interactions between Primary Hepatocytes and Non-Parenchymal Cells on Physiological and Pathological Liver Stiffness’. doi: 10.3390/biology.
203. Ngo, B. K. D. and Grunlan, M. A. (2017) ‘Protein Resistant Polymeric Biomaterials’, ACS Macro Letters, 6(9), pp. 992–1000. doi: 10.1021/ACSMACROLETT.7B00448/ASSET/IMAGES/LARGE/MZ-2017-004485_0007.JPEG.
204. Nichol, J. W. et al. (2010) ‘Cell-laden microengineered gelatin methacrylate hydrogels’, Biomaterials, 31(21), p. 5536. doi: 10.1016/J.BIOMATERIALS.2010.03.064.
205. Noguchi, H. et al. (2002) ‘Controlled expansion of human endothelial cell populations by Cre-loxP-based reversible immortalization’, Human gene therapy, 13(2), pp. 321–334. doi: 10.1089/10430340252769833.
206. Norotte, C. et al. (2009) ‘Scaffold-free vascular tissue engineering using bioprinting’, Biomaterials, 30(30), pp. 5910–5917. doi: 10.1016/J.BIOMATERIALS.2009.06.034.
207. Novoseletskaya, E. et al. (2020) ‘Mesenchymal Stromal Cell-Produced Components of Extracellular Matrix Potentiate Multipotent Stem Cell Response to Differentiation Stimuli’, Frontiers in Cell and Developmental Biology, 8, p. 983. doi: 10.3389/FCELL.2020.555378/BIBTEX.
208. Ohashi, K. et al. (2007) ‘Engineering functional two- and three-dimensional liver systems in vivo using hepatic tissue sheets’, Nature Medicine 2007 13:7, 13(7), pp. 880–885. doi: 10.1038/nm1576.
209. Okubo, H. et al. (2002) ‘A Novel Method for Faster Formation of Rat Liver Cell Spheroids’, Artificial Organs, 26(6), pp. 497–505. doi: 10.1046/J.1525-1594.2002.06836.X.
210. Okudaira, T. et al. (2017) ‘Fabrication of a fiber-type hepatic tissue by bottom-up method using multilayer spheroids’, Journal of Bioscience and Bioengineering, 123(6), pp. 739–747. doi: 10.1016/J.JBIOSC.2017.01.002.
211. Okumura, H. et al. (2018) ‘Effective Transplantation of 2D and 3D Cultured Hepatocyte Spheroids Confirmed by Quantum Dot Imaging’, Advanced Biosystems, 2(8), p. 1800137. doi: 10.1002/ADBI.201800137.
212. Orge, I. D. et al. (2020) ‘Phenotype instability of hepatocyte-like cells produced by direct reprogramming of mesenchymal stromal cells’, Stem Cell Research and Therapy, 11(1), pp. 1–15. doi: 10.1186/S13287-020-01665-Z/FIGURES/7.
213. Osna, N. A., Donohue, T. M. and Kharbanda, K. K. (2017) ‘Alcoholic Liver Disease: Pathogenesis and Current Management’, Alcohol Research : Current Reviews, 38(2), p. 147. Available at: /pmc/articles/PMC5513682/ (Accessed: 19 April 2022).

214. Otsuka, H. et al. (2004) ‘Two-Dimensional Multiarray Formation of Hepatocyte Spheroids on a Microfabricated PEG-Brush Surface’, ChemBioChem, 5(6), pp. 850–855. doi: 10.1002/CBIC.200300822.
215. Otsuka, H. et al. (2013) ‘Micropatterned co-culture of hepatocyte spheroids layered on non-parenchymal cells to understand heterotypic cellular interactions’, Science and Technology of Advanced Materials, 14(6), pp. 65003–65013. doi: 10.1088/1468-6996/14/6/065003.
216. Ouyang, L. et al. (2016) ‘Effect of bioink properties on printability and cell viability for 3D bioplotting of embryonic stem cells’, Biofabrication, 8(3). doi: 10.1088/1758-5090/8/3/035020.
217. P Sharma, O. (2014) ‘Clinical Biochemistry of Hepatotoxicity’, Journal of Clinical Toxicology, 04(01). doi: 10.4172/2161-0495.S4-001.
218. Pai, R. R., Ajit, S., et al. (2022) ‘Radical scavenging gelatin methacrylamide based bioink formulation for three dimensional bioprinting of parenchymal liver construct’, Bioprinting, 27, p. e00214. doi: 10.1016/J.BPRINT.2022.E00214.
219. Pai, R. R., Anupama Sekar, J., et al. (2022) ‘Three-dimensional bioprinting of tissues and organs’, Biomedical Product and Materials Evaluation, pp. 135–150. doi: 10.1016/B978-0-12-823966-7.00018-9.
220. Palakkan, A. A., P.R., A. K. and V, K. T. (2013) ‘An in vitro fluorometric assay for evaluating functional polarity of hepatocyte’, International Journal of Bioassays, 3(1), pp. 1630–1636. Available at: https://www.ijbio.com/abstract/an-in-vitro-fluorometric-assay-for-evaluating-functional-polarity-of-hepatocyte-13490.html (Accessed: 16 November 2022).
221. Pan, J. L. et al. (2005) ‘Chitosan-Based Scaffolds for Hepatocyte Culture’, Key Engineering Materials, 288–289, pp. 91–96. doi: 10.4028/WWW.SCIENTIFIC.NET/KEM.288-289.91.
222. Passamai, V. E. et al. (2016) ‘From 3D Bioprinters to a fully integrated Organ Biofabrication Line’, Journal of Physics: Conference Series, 705(1), p. 012010. doi: 10.1088/1742-6596/705/1/012010.
223. Payne, C. M. et al. (2011) ‘Persistence of functional hepatocyte-like cells in immune-compromised mice’, Liver international : official journal of the International Association for the Study of the Liver, 31(2), pp. 254–262. doi: 10.1111/J.1478-3231.2010.02414.X.
224. Peppas, N. A. et al. (2006) ‘Hydrogels in Biology and Medicine: From Molecular Principles to Bionanotechnology’, Advanced Materials, 18(11), pp. 1345–1360. doi: 10.1002/ADMA.200501612.
225. Peshwa, M. V et al. (1996) ‘Mechanistics of formation and ultrastructural evaluation of hepatocyte spheroids’, In Vitro Cell. Dev. Biol. Anim., 32(4), p. 197. doi: 10.1007/bf02722946.
226. Phang-Lyn, S. and Llerena, V. A. (2022) ‘Biochemistry, Biotransformation’, StatPearls. Available at: https://www.ncbi.nlm.nih.gov/books/NBK544353/ (Accessed: 17 November 2022).
227. Philippidis, P. et al. (2004) ‘Hemoglobin Scavenger Receptor CD163 Mediates Interleukin-10 Release and Heme Oxygenase-1 Synthesis’, Circulation Research, 94(1), pp. 119–126. doi: 10.1161/01.RES.0000109414.78907.F9.

228. Piao, Y. et al. (2021) 'Biomedical applications of gelatin methacryloyl hydrogels', Engineered Regeneration, 2, pp. 47–56. doi: 10.1016/J.ENGREG.2021.03.002.
229. Pinkse, G. G. et al. (2005) 'RGD peptides confer survival to hepatocytes via the beta1-integrin-ILK-pAkt pathway', Journal of Hepatology. 2005/01/05, 42(1), pp. 87–93. doi: S0168-8278(04)00432-5 [pii]10.1016/j.jhep.2004.09.010.
230. Popova, Anna A et al. (2019) 'Facile One Step Formation and Screening of Tumor Spheroids Using Droplet-Microarray Platform', Small, 15(25), p. 1901299. doi: 10.1002/SMLL.201901299.
231. Prinja, S. et al. (2018) 'Cost of Intensive Care Treatment for Liver Disorders at Tertiary Care Level in India', PharmacoEconomics - open, 2(2), pp. 179–190. doi: 10.1007/S41669-017-0041-4.
232. Prodanov, L. et al. (2016) 'Long-term maintenance of a microfluidic 3D human liver sinusoid', Biotechnology and Bioengineering, 113(1), pp. 241–246. doi: 10.1002/BIT.25700.
233. Pyo, S. H. et al. (2017) 'Continuous optical 3D printing of green aliphatic polyurethanes', ACS Applied Materials and Interfaces, 9(1), pp. 836–844. doi: 10.1021/ACSAMI.6B12500/ASSET/IMAGES/LARGE/AM-2016-12500J_0005.JPEG.
234. Rad, A. T. et al. (2014) 'Conducting scaffolds for liver tissue engineering', Journal of Biomedical Materials Research Part A, 102(11), pp. 4169–4181. doi: 10.1002/JBM.A.35080.
235. Ramaiahgari, S. C. et al. (2014) 'A 3D in vitro model of differentiated HepG2 cell spheroids with improved liver-like properties for repeated dose high-throughput toxicity studies', Archives of Toxicology, 88(5), pp. 1083–1095. doi: 10.1007/s00204-014-1215-9.
236. Rela, M., Kaliamoorthy, I. and Reddy, M. S. (2016) 'Current status of auxiliary partial orthotopic liver transplantation for acute liver failure', Liver Transplantation, 22(9), pp. 1265–1274. doi: 10.1002/LT.24509.
237. Reuben, A., Koch, D. G. and Lee, W. M. (2010) 'Drug-induced acute liver failure: results of a U.S. multicenter, prospective study', Hepatology (Baltimore, Md.), 52(6), pp. 2065–2076. doi: 10.1002/HEP.23937.
238. Roehm, K. D. and Madihally, S. V. (2017) 'Bioprinted chitosan-gelatin thermosensitive hydrogels using an inexpensive 3D printer.', Biofabrication, 10(1), pp. 015002–015002. doi: 10.1088/1758-5090/AA96DD.
239. Roopesh, R. P. et al. (2022) 'High-throughput production of liver parenchymal microtissues and enrichment of organ-specific functions in gelatin methacrylamide microenvironment', Biotechnology and Bioengineering. doi: 10.1002/BIT.28010.
240. Sakai, Y. et al. (1996) 'Large-scale preparation and function of porcine hepatocyte spheroids', International Journal of Artificial Organs, 19(5), pp. 294–301. doi: 10.1177/039139889601900507.
241. Sakai, Y. et al. (2013) 'Rapid fabricating technique for multi-layered human hepatic cell sheets by forceful contraction of the fibroblast monolayer', PloS one, 8(7). doi: 10.1371/JOURNAL.PONE.0070970.
242. Sampaziotis, F. et al. (2015) 'Cholangiocytes derived from human induced

pluripotent stem cells for disease modeling and drug validation', Nature Biotechnology 2015 33:8, 33(8), pp. 845–852. doi: 10.1038/nbt.3275.

243. Sánchez, A. et al. (2000) 'Fibronectin regulates morphology, cell organization and gene expression of rat fetal hepatocytes in primary culture', Journal of Hepatology, 32(2), pp. 242–250. doi: 10.1016/S0168-8278(00)80069-0.
244. Saunders, J. R. and Moussa, W. (2012) 'Dynamic mechanical properties and swelling of UV-photopolymerized anionic hydrogels', Journal of Polymer Science Part B: Polymer Physics, 50(16), pp. 1198–1208. doi: 10.1002/POLB.23114.
245. Scalone, L. et al. (2015) 'The societal burden of chronic liver diseases: results from the COME study', BMJ Open Gastroenterology, 2(1), p. e000025. doi: 10.1136/BMJGAST-2014-000025.
246. Schmidt, T. et al. (2021) 'A Paradigm Shift in Tissue Engineering: From a Top–Down to a Bottom–Up Strategy', Processes 2021, Vol. 9, Page 935, 9(6), p. 935. doi: 10.3390/PR9060935.
247. Schneeberger, K. et al. (2020) 'Large-Scale Production of LGR5-Positive Bipotential Human Liver Stem Cells', Hepatology, 72(1), pp. 257–270. doi: 10.1002/HEP.31037.
248. Schrobback, K. et al. (2012) 'Effects of oxygen and culture system on in vitro propagation and redifferentiation of osteoarthritic human articular chondrocytes', Cell and tissue research, 347(3), pp. 649–663. doi: 10.1007/S00441-011-1193-7.
249. Schwab, A. et al. (2020) 'Printability and Shape Fidelity of Bioinks in 3D Bioprinting', Chemical Reviews, 120(19), pp. 11028–11055. doi: 10.1021/ACS.CHEMREV.0C00084/ASSET/IMAGES/ACS.CHEMREV.0C00084.SOCIAL.JPEG_V03.
250. Schwartz, R. E. et al. (2014) 'Pluripotent stem cell-derived hepatocyte-like cells', Biotechnology advances, 32(2), pp. 504–513. doi: 10.1016/J.BIOTECHADV.2014.01.003.
251. Seglen, P. O. (1976) 'Chapter 4 Preparation of Isolated Rat Liver Cells', Methods in Cell Biology, 13(C), pp. 29–83. doi: 10.1016/S0091-679X(08)61797-5.
252. Semino, C. E. et al. (2003) 'Functional differentiation of hepatocyte-like spheroid structures from putative liver progenitor cells in three-dimensional peptide scaffolds.', Differentiation; research in biological diversity, 71(4–5), pp. 262–270. doi: 10.1046/j.1432-0436.2003.7104503.x.
253. Semnani, D. et al. (2016) 'Evaluation of PCL/chitosan electrospun nanofibers for liver tissue engineering', https://doi.org/10.1080/00914037.2016.1190931, 66(3), pp. 149–157. doi: 10.1080/00914037.2016.1190931.
254. Seo, S. J. et al. (2006) 'Alginate/Galactosylated Chitosan/Heparin Scaffold As a New Synthetic Extracellular Matrix for Hepatocytes', https://home.liebertpub.com/ten, 12(1), pp. 33–44. doi: 10.1089/TEN.2006.12.33.
255. SF, A.-A. et al. (2002) 'Structural polarity and functional bile canaliculi in rat hepatocyte spheroids', Experimental cell research, 274(1). doi: 10.1006/EXCR.2001.5467.
256. Shibuya, K. et al. (2021a) 'The Efficacy of the Hepatocyte Spheroids for

Hepatocyte Transplantation’, Cell Transplantation, 30. doi: 10.1177/09636897211000014.

257. Shibuya, K. et al. (2021b) ‘The Efficacy of the Hepatocyte Spheroids for Hepatocyte Transplantation’, Cell Transplantation, 30. doi: 10.1177/09636897211000014.
258. Shirahama, H. et al. (2016) ‘Precise Tuning of Facile One-Pot Gelatin Methacryloyl (GelMA) Synthesis’, Scientific Reports 2016 6:1, 6(1), pp. 1–11. doi: 10.1038/srep31036.
259. da Silva, R. M. P., Mano, J. F. and Reis, R. L. (2007) ‘Smart thermoresponsive coatings and surfaces for tissue engineering: switching cell-material boundaries’, Trends in biotechnology, 25(12), pp. 577–583. doi: 10.1016/J.TIBTECH.2007.08.014.
260. Sohlenius-Sternbeck, A. K. (2006) ‘Determination of the hepatocellularity number for human, dog, rabbit, rat and mouse livers from protein concentration measurements’, Toxicology in vitro : an international journal published in association with BIBRA, 20(8), pp. 1582–1586. doi: 10.1016/J.TIV.2006.06.003.
261. Soltys, K. A. et al. (2017) ‘Host conditioning and rejection monitoring in hepatocyte transplantation in humans’, Journal of hepatology, 66(5), pp. 987–1000. doi: 10.1016/J.JHEP.2016.12.017.
262. Sorrentino, G. et al. (2020) ‘Mechano-modulatory synthetic niches for liver organoid derivation’, Nature Communications 2020 11:1, 11(1), pp. 1–10. doi: 10.1038/s41467-020-17161-0.
263. Soto-Gutierrez, A. et al. (2010) ‘Engineering of an Hepatic Organoid to Develop Liver Assist Devices’, Cell transplantation, 19(6), p. 815. doi: 10.3727/096368910X508933.
264. Stock, P. et al. (2008) ‘Hepatocytes derived from adult stem cells’, Transplantation proceedings, 40(2), pp. 620–623. doi: 10.1016/J.TRANSPROCEED.2008.01.058.
265. Sun, L. and Hui, L. (2020) ‘Progress in human liver organoids’, Journal of Molecular Cell Biology, 12(8), pp. 607–617. doi: 10.1093/JMCB/MJAA013.
266. Tagle, M., Lemon, S. M. and Schiff, E. R. (2006) ‘Viral Hepatitis’, Tropical Infectious Diseases, 1, pp. 694–725. doi: 10.1016/B978-0-443-06668-9.50069-7.
267. Tajir, K. and Shimizu, Y. (2013) ‘Liver physiology and liver diseases in the elderly’, World Journal of Gastroenterology : WJG, 19(46), p. 8459. doi: 10.3748/WJG.V19.I46.8459.
268. Takagi, S. et al. (2012) ‘Cell shape regulation based on hepatocyte sheet engineering technologies’, Cell Transplantation, 21(2–3), pp. 411–420. doi: 10.3727/096368911X605312.
269. Takebe, T. et al. (2014) ‘Generation of a vascularized and functional human liver from an iPSC-derived organ bud transplant’, Nature Protocols 2014 9:2, 9(2), pp. 396–409. doi: 10.1038/nprot.2014.020.
270. Takebe, T., Enomura, M., Yoshizawa, E., Kimura, M., Koike, H., Ueno, Y., Matsuzaki, T., Yamazaki, T., Toyohara, T., Osafune, K., Nakauchi, H., Yoshikawa, Hiroshi Y., et al. (2015) ‘Vascularized and complex organ buds from diverse tissues via mesenchymal cell-driven condensation’, Cell Stem

Cell, 16(5), pp. 556–565. doi: 10.1016/J.STEM.2015.03.004.

271. Takebe, T., Enomura, M., Yoshizawa, E., Kimura, M., Koike, H., Ueno, Y., Matsuzaki, T., Yamazaki, T., Toyohara, T., Osafune, K., Nakauchi, H., Yoshikawa, Hiroshi Y., et al. (2015) 'Vascularized and Complex Organ Buds from Diverse Tissues via Mesenchymal Cell-Driven Condensation', Cell Stem Cell, 16(5), pp. 556–565. doi: 10.1016/J.STEM.2015.03.004.
272. Takei, R. et al. (2005) 'Role of E-cadherin Molecules in Spheroid Formation of Hepatocytes Adhered on Galactose-Carrying Polymer as an Artificial Asialoglycoprotein Model', Biotechnology Letters 2005 27:16, 27(16), pp. 1149–1156. doi: 10.1007/S10529-005-8652-8.
273. Tas, R. P. et al. (2021) 'From the freezer to the clinic', EMBO reports, 22(3). doi: 10.15252/EMBR.202052162.
274. Tasnim, F. et al. (2015) 'Cost-effective differentiation of hepatocyte-like cells from human pluripotent stem cells using small molecules', Biomaterials, 70, pp. 115–125. doi: 10.1016/J.BIOMATERIALS.2015.08.002.
275. Teresa Donato, M., José Gomez-Lechón, M. and Castell, J. V. (1993) 'A microassay for measuring cytochrome P450IA1 and P450IIB1 activities in intact human and rat hepatocytes cultured on 96-well plates', Analytical biochemistry, 213(1), pp. 29–33. doi: 10.1006/ABIO.1993.1381.
276. Thuluvath, P. J., Saraya, A. and Rela, M. (2021) 'An Introduction to Liver Disease in India', Clinical Liver Disease, 18(3), pp. 105–107. doi: 10.1002/CLD.1149.
277. Tibbitt, M. W. and Anseth, K. S. (2009) 'Hydrogels as extracellular matrix mimics for 3D cell culture', Biotechnology and Bioengineering, 103(4), pp. 655–663. doi: 10.1002/BIT.22361.
278. Tiruvannamalai-Annamalai, R., Armant, D. R. and Matthew, H. W. T. (2014) 'A glycosaminoglycan based, modular tissue scaffold system for rapid assembly of perfusable, high cell density, engineered tissues', PLoS ONE, 9(1). doi: 10.1371/JOURNAL.PONE.0084287.
279. Tocan, V. et al. (2021) 'Hepatocyte polarity establishment and apical lumen formation are organized by Par3, Cdc42, and aPKC in conjunction with Lgl', Journal of Biological Chemistry, 297(6). doi: 10.1016/j.jbc.2021.101354.
280. Tonon, F. et al. (2019) 'In vitro metabolic zonation through oxygen gradient on a chip', Scientific Reports 2019 9:1, 9(1), pp. 1–10. doi: 10.1038/s41598-019-49412-6.
281. Treyer, A. and Müsch, A. (2013) 'Hepatocyte Polarity', Comprehensive Physiology, 3(1), p. 243. doi: 10.1002/CPHY.C120009.
282. Tung, Y. C. et al. (2011) 'High-throughput 3D spheroid culture and drug testing using a 384 hanging drop array', The Analyst, 136(3), pp. 473–478. doi: 10.1039/C0AN00609B.
283. Tysoe, O. C. et al. (2019) 'Isolation and propagation of primary human cholangiocyte organoids for the generation of bioengineered biliary tissue', Nature protocols, 14(6), pp. 1884–1925. doi: 10.1038/S41596-019-0168-0.
284. Underhill, G. H. et al. (2007) 'Assessment of hepatocellular function within PEG hydrogels', Biomaterials, 28, pp. 256–270. doi: 10.1016/j.biomaterials.2006.08.043.
285. Valerio, C. et al. (2016) 'Human albumin solution for patients with cirrhosis

and acute on chronic liver failure: Beyond simple volume expansion', World Journal of Hepatology, 8(7), p. 345. doi: 10.4254/WJH.V8.I7.345.

286. Van, A. I. et al. (2000) 'Structural and Rheological Properties of Methacrylamide Modified Gelatin Hydrogels'. doi: 10.1021/bm990017d.
287. Vernon, H., Wehrle, C. J. and Kasi, A. (2021) 'Anatomy, Abdomen and Pelvis, Liver', StatPearls. Available at: https://www.ncbi.nlm.nih.gov/books/NBK500014/ (Accessed: 19 April 2022).
288. Vinken, M. et al. (2008) 'Involvement of Cell Junctions in Hepatocyte Culture Functionality', http://dx.doi.org/10.1080/10408440600599273, 36(4), pp. 299–318. doi: 10.1080/10408440600599273.
289. Vyas, D. et al. (2018) 'Self-assembled liver organoids recapitulate hepatobiliary organogenesis in vitro', Hepatology (Baltimore, Md.), 67(2), pp. 750–761. doi: 10.1002/HEP.29483.
290. Wang, A., Madden, L. A. and Paunov, V. N. (2020) 'High-throughput fabrication of hepatic cell clusteroids with enhanced growth and functionality for tissue engineering applications', Materials Advances, 1(8), pp. 3022–3032. doi: 10.1039/D0MA00635A.
291. Wang, C. et al. (2021) 'High-throughput hyaluronic acid hydrogel arrays for cell selective adhesion screening', Journal of Materials Chemistry B, 9(19), pp. 4024–4030. doi: 10.1039/D1TB00429H.
292. Wang, S. et al. (no date) 'Three-Dimensional Primary Hepatocyte Culture in Synthetic Self-Assembling Peptide Hydrogel'. doi: 10.1089/tea.2007.0143.
293. Wang, T. et al. (2012) 'Nanoporous fibers of type-I collagen coated poly(L-lactic acid) for enhancing primary hepatocyte growth and function', Journal of Materials Chemistry B, 1(3), pp. 339–346. doi: 10.1039/C2TB00195K.
294. Wang, X. et al. (2006) 'Generation of Three-Dimensional Hepatocyte/Gelatin Structures with Rapid Prototyping System', https://home.liebertpub.com/ten, 12(1), pp. 83–90. doi: 10.1089/TEN.2006.12.83.
295. Wang, X. et al. (2008) 'Liver tissue responses to gelatin and gelatin/chitosan gels', Journal of Biomedical Materials Research Part A, 87A(1), pp. 62–68. doi: 10.1002/JBM.A.31712.
296. Wang, X. et al. (2020) 'Generation of liver bipotential organoids with a small-molecule cocktail', Journal of Molecular Cell Biology, 12(8), pp. 618–629. doi: 10.1093/JMCB/MJAA010.
297. Wang, Y. et al. (2016) 'ECM proteins in a microporous scaffold influence hepatocyte morphology, function, and gene expression', Scientific Reports, 6. doi: 10.1038/SREP37427.
298. Wang, Z. and Liu, C. (2015) 'Lgr5-Positive Cells are Cancer-Stem-Cell-Like Cells in Gastric Cancer', Cellular Physiology and Biochemistry, 36(6), pp. 2447–2455. doi: 10.1159/000430205.
299. Watanabe, T. et al. (2003) 'Establishment of immortalized human hepatic stellate scavenger cells to develop bioartificial livers', Transplantation, 75(11), pp. 1873–1880. doi: 10.1097/01.TP.0000064621.50907.A6.
300. Wei, G. et al. (2007) 'Acute liver failure in Sweden: etiology and outcome', Journal of internal medicine, 262(3), pp. 393–401. doi: 10.1111/J.1365-2796.2007.01818.X.

301. Wei, Y. et al. (2021) ‘Liver homeostasis is maintained by midlobular zone 2 hepatocytes’, Science, 371(6532). doi: 10.1126/SCIENCE.ABB1625/SUPPL_FILE/SCIENCE.ABB1625_WEI_SM.PDF.
302. Wiesner, R. J., Rüegg, J. C. and Morano, I. (1992) ‘Counting target molecules by exponential polymerase chain reaction: Copy number of mitochondrial DNA in rat tissues’, Biochemical and Biophysical Research Communications, 183(2), pp. 553–559. doi: 10.1016/0006-291X(92)90517-O.
303. Wilson, S. A. et al. (2017) ‘Shear-Thinning and Thermo-Reversible Nanoengineered Inks for 3D Bioprinting’, ACS Applied Materials and Interfaces, 9(50), pp. 43449–43458. doi: 10.1021/ACSAMI.7B13602/ASSET/IMAGES/LARGE/AM-2017-13602D_0006.JPEG.
304. Wu, Y. et al. (2020) ‘3D bioprinting of bicellular liver lobule-mimetic structures via microextrusion of cellulose nanocrystal-incorporated shear-thinning bioink’, Scientific Reports 2020 10:1, 10(1), pp. 1–12. doi: 10.1038/s41598-020-77146-3.
305. Xia, T. et al. (2020) ‘The Effect of Matrix Stiffness on Human Hepatocyte Migration and Function—An In Vitro Research’, Polymers, 12(9). doi: 10.3390/POLYM12091903.
306. Xie, Z. et al. (2020) ‘3D Bioprinting in Tissue Engineering for Medical Applications: The Classic and the Hybrid’, Polymers 2020, Vol. 12, Page 1717, 12(8), p. 1717. doi: 10.3390/POLYM12081717.
307. Xu, P. et al. (2021) ‘Stiffness of photocrosslinkable gelatin hydrogel influences nucleus pulposus cell propertiesin vitro’, Journal of Cellular and Molecular Medicine, 25(2), pp. 880–891. doi: 10.1111/JCMM.16141.
308. Yamada, M. et al. (2012) ‘Controlled formation of heterotypic hepatic micro-organoids in anisotropic hydrogel microfibers for long-term preservation of liver-specific functions’, Biomaterials, 33(33), pp. 8304–8315. doi: 10.1016/J.BIOMATERIALS.2012.07.068.
309. Yanagi, Y. et al. (2017) ‘In vivo and ex vivo methods of growing a liver bud through tissue connection’, Scientific Reports 2017 7:1, 7(1), pp. 1–15. doi: 10.1038/s41598-017-14542-2.
310. Yang, Y. et al. (2021) ‘The Application of Mesenchymal Stem Cells in the Treatment of Liver Diseases: Mechanism, Efficacy, and Safety Issues’, Frontiers in Medicine, 8, p. 642. doi: 10.3389/FMED.2021.655268/BIBTEX.
311. Yang, Z. et al. (2012) ‘In vitro and in vivo characterization of silk fibroin/gelatin composite scaffolds for liver tissue engineering’, Journal of digestive diseases, 13(3), pp. 168–178. doi: 10.1111/J.1751-2980.2011.00566.X.
312. Ye, S. et al. (2020a) ‘A Chemically Defined Hydrogel for Human Liver Organoid Culture’, Advanced Functional Materials, 30(48). doi: 10.1002/ADFM.202000893.
313. Ye, S. et al. (2020b) ‘A Chemically Defined Hydrogel for Human Liver Organoid Culture’, Advanced Functional Materials, 30(48), p. 2000893. doi: 10.1002/ADFM.202000893.
314. Yin, J. et al. (2018) ‘3D Bioprinting of Low-Concentration Cell-Laden Gelatin

Methacrylate (GelMA) Bioinks with a Two-Step Cross-linking Strategy', ACS Applied Materials and Interfaces, 10(8), pp. 6849–6857. doi: 10.1021/ACSAMI.7B16059/SUPPL_FILE/AM7B16059_SI_001.PDF.

315. Yoshida, Y. et al. (2007) 'A role of Wnt/beta-catenin signals in hepatic fate specification of human umbilical cord blood-derived mesenchymal stem cells', American journal of physiology. Gastrointestinal and liver physiology, 293(5). doi: 10.1152/AJPGI.00187.2007.
316. You, J. et al. (2013) 'Characterizing the Effects of Heparin Gel Stiffness on Function of Primary Hepatocytes', Tissue Engineering. Part A, 19(23–24), p. 2655. doi: 10.1089/TEN.TEA.2012.0681.
317. Young, Ashlyn T et al. (2020) 'Rheological Properties of Coordinated Physical Gelation and Chemical Crosslinking in Gelatin Methacryloyl (GelMA) Hydrogels', Macromolecular Bioscience, 20(12), p. 2000183. doi: 10.1002/MABI.202000183.
318. Yue, K. et al. (2015) 'Synthesis, properties, and biomedical applications of gelatin methacryloyl (GelMA) hydrogels', Biomaterials. Elsevier Ltd, pp. 254–271. doi: 10.1016/j.biomaterials.2015.08.045.
319. Zhang, K. et al. (2018) 'In Vitro Expansion of Primary Human Hepatocytes with Efficient Liver Repopulation Capacity', Cell Stem Cell, 23(6), pp. 806-819.e4. doi: 10.1016/J.STEM.2018.10.018.
320. Zhang, S. et al. (1993) 'Spontaneous assembly of a self-complementary oligopeptide to form a stable macroscopic membrane.', Proceedings of the National Academy of Sciences of the United States of America, 90(8), p. 3334. doi: 10.1073/PNAS.90.8.3334.
321. Zhang, X. Z., Wu, D. Q. and Chu, C. C. (2004) 'Synthesis, characterization and controlled drug release of thermosensitive IPN-PNIPAAm hydrogels', Biomaterials, 25(17), pp. 3793–3805. doi: 10.1016/J.BIOMATERIALS.2003.10.065.
322. Zhang, Z. et al. (2016) 'Study of Impingement Types and Printing Quality during Laser Printing of Viscoelastic Alginate Solutions', Langmuir, 32(12), pp. 3004–3014. doi: 10.1021/ACS.LANGMUIR.6B00220/ASSET/IMAGES/MEDIUM/LA-2016-002202_0010.GIF.
323. Zheng, Y. B. et al. (2008) 'Characterization and hepatogenic differentiation of mesenchymal stem cells from human amniotic fluid and human bone marrow: a comparative study', Cell biology international, 32(11), pp. 1439–1448. doi: 10.1016/J.CELLBI.2008.08.015.
324. Zhu, S. et al. (2009) 'A small molecule primes embryonic stem cells for differentiation.', Cell stem cell, 4(5), pp. 416–426. doi: 10.1016/j.stem.2009.04.001.
325. Zhu, X. et al. (2021) 'Liver Organoids: Formation Strategies and Biomedical Applications', Tissue Engineering and Regenerative Medicine, 18(4), p. 573. doi: 10.1007/S13770-021-00357-W.
326. van Zijl, F. and Mikulits, W. (2010) 'Hepatospheres: Three dimensional cell cultures resemble physiological conditions of the liver', World journal of hepatology, 2(1), pp. 1–7. doi: 10.4254/wjh.v2.i1.1.
327. Zołek-Tryznowska, Z. (2016) 'Rheology of Printing Inks', Printing on

Polymers: Fundamentals and Applications, pp. 87–99. doi: 10.1016/B978-0-323-37468-2.00006-3.

Annexure

List of publications

Research articles

1. Roopesh, R. P. et al. High-throughput production of liver parenchymal microtissues and enrichment of organ-specific functions in gelatin methacrylamide microenvironment. Biotechnol. Bioeng. (2022) doi:10.1002/BIT.28010. (Impact factor: 4.395)
2. Pai, R. R. et al. Radical scavenging gelatin methacrylamide based bioink formulation for three dimensional bioprinting of parenchymal liver construct. Bioprinting 27, e00214 (2022). (Cite score: 7.2)

Book chapters

1. Pai, R. R. et al. Three-dimensional bioprinting of tissues and organs. Biomed. Prod. Mater. Eval. 135–150 (2022) doi:10.1016/B978-0-12-823966-7.00018-9.

Received: 23 April 2021 | Revised: 11 November 2021 | Accepted: 8 December 2021

DOI: 10.1002/bit.28010

ARTICLE

BIOTECHNOLOGY AND BIOENGINEERING WILEY

High-throughput production of liver parenchymal microtissues and enrichment of organ-specific functions in gelatin methacrylamide microenvironment

Ramesh Pai Roopesh[1] | **Senthilkumar Muthusamy**[1] | **Shiny Velayudhan**[2] | **Arumugham Sabareeswaran**[3] | **Pallickaveedu RajanAsari Anil Kumar**[1]

[1]Division of Tissue Culture, Department of Applied Biology, Biomedical Technology Wing, Sree Chitra Tirunal Institute for Medical Sciences and Technology, Thiruvananthapuram, Kerala, India

[2]Division of Dental Products, Department of Biomaterial Science and Technology, Biomedical Technology Wing, Sree Chitra Tirunal Institute for Medical Sciences and Technology, Thiruvananthapuram, Kerala, India

[3]Division of Experimental Pathology, Department of Applied Biology, Biomedical Technology Wing, Sree Chitra Tirunal Institute for Medical Sciences and Technology, Thiruvananthapuram, Kerala, India

Correspondence

Pallickaveedu RajanAsari Anil Kumar, Division of Tissue Culture, Department of Applied Biology, Biomedical Technology Wing, Sree Chitra Tirunal Institute for Medical Sciences and Technology, Poojapura, Thiruvananthapuram - 695 012, Kerala, India.
Email: anilkumarpr@sctimst.ac.in

Funding information

Department of Biotechnology, Ministry of Science and Technology, Grant/Award Number: BT/RLF/Re-entry/48/2016; Department of Science and Technology, Ministry of Science and Technology, Grant/Award Number: TRC/8141/PSN

Abstract

Liver parenchymal microtissues (LPMTs) are three-dimensional (3D) aggregates of hepatocytes that recapitulate in vivo-like cellular assembly. They are considered as a valuable model to study drug metabolism, disease biology, and serve as ideal building blocks for liver tissue engineering. However, their integration into the mainstream drug screening process has been hindered due to the lack of simple, rapid techniques to produce a large number of uniform microtissues and preserve their structural–functional integrity over the long term. Here, we present a high-throughput methodology to produce LPMTs in a novel, economic, and reusable Hanging-drop Culture Chamber (HdCC). A drop-on-demand bioprinting approach was optimized to generate droplets of HepG2 cell suspension on a polyethylene terephthalate substrate. The substrates carrying droplets were placed inside a novel HdCC and incubated to obtain 1600 LPMTs having a size of 200–300 μm. Tissue size, cell viability, cellular arrangement and polarity, and insulin-mediated glucose uptake by LPMTs were analyzed. The microtissues were viable and exhibited an active response to insulin stimulation. Cells within the microtissue reorganized to form hepatic plate-like structures and expressed apical (Multidrug Resistance Protein 2 [MRP2]) and epithelial (Zonula Occludens 1 [ZO1]) markers. Further to maintain the structural integrity and enhance the functional capabilities, LPMTs were sandwiched within gelatin methacrylamide (GelMA) hydrogel and the liver-specific functions were monitored for 2 weeks. The results showed that the 3D structure of LPMTs in GelMA sandwich was maintained while the albumin secretion, urea synthesis, and cytochrome P450 activity were enhanced compared with LPMTs in suspension. In conclusion, this study presents a novel culture chamber for mass production of microtissues and a method for enhancing organ-specific functions of LPMTs in vitro.

KEYWORDS

bioprinting, gelatin methacrylamide, hanging-drop culture, microtissues, sandwich culture

1 | INTRODUCTION

The liver is the largest gland in the body, performing a plethora of endocrine and exocrine functions. As a major organ involved in xenobiotic metabolism, it is highly susceptible to drug-induced liver injury (DILI). Therefore, it is critical to identify the toxicity of new chemical entities during drug development. However, despite having strict evaluation strategies in the preclinical phase, DILI remains the leading cause of drug failures in the clinical trials and postmarketing withdrawals (Watkins, 2011). The limitations of conventional hepatocyte monolayer culture to express mature liver phenotype and the interspecies difference in enzyme-mediated drug metabolism related to animal models are the primary cause of unprecedented complications due to DILI (Martignoni et al., 2006). Meanwhile, the global burden of liver diseases accounts for approximately two million deaths per year and liver transplantation is the only treatment strategy for end-stage liver diseases (Asrani et al., 2019). Hence, alternative physiologically relevant human liver models are needed for toxicity testing and engineering liver tissue grafts. Of late, three-dimensional (3D) liver models such as hepatocyte spheroids or microtissues, liver organoids, and 3D bioprinted liver constructs have exhibited enhanced efficiency in predicting human DILI and restoring functions in liver failure models (Jin et al., 2018; Nguyen et al., 2016; Ramaiahgari et al., 2014; Yang et al., 2021). Among these, hepatocyte microtissues are easy to prepare and amenable for high-throughput analysis (Hiemstra et al., 2019). Hepatocyte microtissues are self-organized aggregates of hepatocytes that exhibit complex cell-to-cell interaction and hepatic polarity, and they develop physiological gradients within the tissue (Glicklis et al., 2004).

Methods to generate microtissues can be broadly classified into two: scaffold-based and scaffold-free methods. Scaffold-based methods include culturing cells on scaffolds synthesized from natural polymers (agarose, collagen, etc.) or synthetic polymers (PEG, NIPAM, PLA, etc.; Lee, Kim, et al., 2015; Liao et al., 2019; Polonio-Alcalá et al., 2019; Wang et al., 2011). Scaffold-free methods include hanging-drop culture, culture in nonadherent wells, spinner flask, rotary flask, magnetic levitation, and microfluidics (Haisler et al., 2013; Manley & Lelkes, 2006; Okuyama et al., 2010; Shri et al., 2017). Among these, hanging-drop culture is the most common and straightforward method for generating microtissues. In this method, a cell suspension is transferred to a substrate as droplets, and the substrate is inverted to hang the suspension under gravity. The gravitational force induces cell aggregation and microtissue formation. Although microtissues of defined size, cell number, and composition can be generated using this method, manual dispensing of cells is extremely labor intensive. Recently use of automated liquid handling systems along with multiwell hanging-drop microplates has addressed the limitations to some extent (Drewitz et al., 2011). But at the same time, the microplates are expensive and the restriction in the number of microtissues produced per plate limits their use at the industrial scale. Apart from these limitations, preserving the structural integrity of microtissues during in vitro culture is important to maintain its differentiated functions (Chang & Hughes-Fulford, 2009). Earlier studies have shown that the sandwich culture of hepatocyte monolayer preserved hepatic polarity and improved differentiated functions (Berthiaume et al., 1996; Du et al., 2008). However, such a 3D matrix configuration has not been yet evaluated for the culture of hepatocyte microtissues.

To address these shortcomings, we developed a cost-effective and high-throughput method to produce hepatocyte microtissues, hereafter referred to as liver parenchymal microtissues (LPMTs). In this methodology, we used microvalve-based bioprinting technique to generate a high density of low-volume cell-laden droplets on polyethylene terephthalate (PET) substrate. Multiple substrates were then placed inside a novel, economic, and reusable Hanging-drop Culture Chamber (HdCC) to form microtissues. High efficiency of LPMT formation and harvesting was achieved using our culture platform. An in-depth characterization of LPMTs revealed that the microtissues were structurally and functionally mature. Further, we explored the potential of the gelatin methacrylamide (GelMA) hydrogel sandwich system to enhance the differentiated functions of LPMTs during in vitro culture.

2 | MATERIALS AND METHODS

2.1 | Culture of hepatocytes

Human hepatocellular carcinoma cell line, HepG2 (National Center for Cell Science), was cultured in Minimum Essential Medium (MEM, Merck-Sigma, Cat.# M0769) with 10% Fetal Bovine Serum (FBS, Gibco, Cat.#10270106) and 0.1% Penicillin–Streptomycin antibiotic (Pen-Strep, Gibco, Cat.#15070-063). Cells were incubated in CO_2 incubator (New Brunswick, Galaxy 170S) set at 37°C, 5% CO_2 and >90% relative humidity with medium change on every alternate day.

2.2 | Design and fabrication of an HdCC

Design of the HdCC was prepared using an open-source general-purpose parametric 3D computer-aided design (CAD) modeler (FreeCAD Ver 0.18). Clear transparent acrylic sheets of 6 mm thickness were cut using a laser cutter (Han's Yueming; 100 V) to predefined dimensions. The key internal component of HdCC is a base plate on which three vertically placed pillars fixed in position with a top plate. The vertical pillar has grooves of 2 × 4 mm size on the inner side that is accurately positioned to adjacent pillars. The vertical pillars can accommodate eight substrates supporting hanging drops.

2.3 | Optimization of microvalve-based printing

Microvalve-based printing allows a user to generate arrays of droplets in a high-throughput manner. We used an electromagnetic dispensing valve (regenHu, Cat.#MVC-D0.3S0.1) having an inner diameter of 300 and 100 µm stroke to dispense the droplets.

The microvalve was connected to a cartridge containing water and loaded into a cell-friendly printhead (regenHU, Cat.#CF-300N) of the bioprinter 3D Discovery Evolution (regenHu). The template to print a droplet array (15 × 14 droplets) was created in BioCAD 1.1 version software (regenHU). The G-Code was generated from the CAD design and imported into the machine control software (HMI regenHU). A PET sheet (Model#CT100, Desmat) of 70 × 65 mm size and a thickness of 100 µm were used as the substrate for hanging drop. The optimum diameter of the sitting droplet was calculated to be 2 mm, and a pitch of 1.4 mm between the droplets was required to accommodate a 15 × 14 droplet array within the print area. However, the diameter of the droplet depends upon the volume of the dispensed droplet. The volume dispensed by the microvalve, in turn, depends upon the printhead parameters, such as valve opening time (VOT), valve closing time (VCT), and the cartridge pressure (CPR). To determine the optimum printhead parameters multiple arrays of water droplets were printed at a travel speed of 12 mm/s with variable VOT (10, 15, 20, 25, and 30 s) and CPR (2, 4, 6, 8, and 10 kPa) while keeping the VCT constant at 10 milliseconds. The diameter and the weight of randomly selected droplet were measured to estimate the volume (1 mg = 1 µl).

The volume of the printed drops was analyzed indirectly from the diameter of the printed drops measured using ImageJ software. The droplet array was divided into top, middle, and bottom parts each section having 14 × 5 droplets. Random images from each section were captured using a 3D stereomicroscope (Leica S8 Apo) and the feret diameter of the drops were measured. Further, the approximate volume of printed drop was estimated by comparing with liquid drops of different volumes (0.5, 1.5, 2.5, 3.5, and 4.5 µl) manually dispensed using a micropipette. The diameter of the printed drops was and compared with manually dispensed drops.

2.4 | Microvalve-based drop-on-demand bioprinting of hepatocytes

HepG2 cells from a confluent culture were harvested using 0.25% trypsin-ethylenediaminetetraacetic acid (EDTA) solution (Gibco, Cat.#25200072) and different homogeneous cell suspensions containing cell concentration (2×10^5, 4×10^5, and 10×10^5 cells/ml) were prepared in MEM. The cell suspension was loaded into a 3 ml cartridge assembled on the bioprinter head. A motorized cell agitator was inserted into the cell suspension in the cartridge, and the cell suspension was agitated at the lowest speed for 5 s. A droplet array containing 15 × 14 droplets was bioprinted on the PET culture substrate at 8 kPa CPR, 20 ms VOT, and 10 ms VCT. The substrate was inverted carefully without disturbing the droplets and placed inside the HdCC. Bioprinted substrates were placed inside multiple HdCC with each unit having eight substrates each. The HdCC was closed and incubated inside CO_2 incubator for 72 h. The accuracy and the high-throughput nature of microvalve-based bioprinting were compared with the manually dispensing method and their culture in HdCC. In the manual method, 10 µl of cell suspension containing 500 cells was dispensed ($n = 200$) using a micropipette on PET sheets, was inverted and incubated inside the HdCC at 37°C for 72 h.

The efficiency of microtissue formation in both methods was determined by examining entire droplets from three different sheets under a phase-contrast microscope (Nikon TS100). The efficiency of microtissue generation was calculated using the equation given below and the results were presented as mean ± standard deviation.

$$\text{Efficiency of microtissue generation (\%)} = \frac{\text{Total no. of microtissues formed}}{\text{Total no. of drops dispensed}} \times 100.$$

2.4.1 | LPMT harvesting, culture, and size analysis

The microtissues from each PET substrate (drop number = 210) were gently washed out using culture medium (1 ml) and allowed to flow into a centrifuge tube. The microtissue suspension was centrifuged at 11*g* for 30 s. The supernatant was aspirated and 1 ml fresh culture medium was added to the pellet. The suspension containing microtissues were transferred to a 12-well, nontreated plate (Eppendorf, Cat.#0030721012) and maintained inside a CO_2 incubator. Phase-contrast images of the LPMT ($n = 40$) were captured using a digital camera (VUE, Model# US300) connected to the light microscope (Nikon Eclipse TS2-FL). The feret diameter of the microtissues was measured using ImageJ analysis software.

2.4.2 | Assessment of cell viability

Viability of LPMT was assessed on the 7th day by live–dead staining. Microtissues were pelleted by centrifuging and dispersed in serum-free medium containing 10 µg/ml fluorescein diacetate (FDA, Sigma Cat# F7378) and 0.05 µg/ml propidium iodide (PI; HiMedia, Cat#TC252). After incubation for 2 min in the dark, the stain was removed, and LPMT was rinsed using fresh serum-free MEM. The viability was monitored and imaged using a confocal laser scanning microscope (Olympus, Model# FV3000).

Adenosine TriPhosphate (ATP) content is a direct indicator of metabolic activity in viable cells. The ATP content of LPMTs was quantified using CellTiter-Glo 3D cell viability assay kit (Promega, Cat.#G9681) as per the product instructions. Around 200 LPMTs ($n = 3$) cultured for days 1, 7, and 15 were analyzed for measuring ATP. Briefly, LPMTs were collected, pelleted, and resuspended in 100 µl of culture medium. The suspension was transferred to a white opaque 96-well microplate (Thermo Scientific, Cat.#9502887) in triplicates. The plate was equilibrated to room temperature (25°C) for 25 min, and ATP assay reagent (100 µl) was added to each well. The plate was shaken vigorously on a microplate orbital shaker at 1000 rpm for 10 min and was then incubated for 20 min at room temperature. The luminescence intensity was measured using a Multimode plate reader (Plate Chameleon V 425-106, Hidex). Percentage of viable cells was calculated by normalizing the luminescence values at different time points to the value at the beginning of the culture.

2.4.3 | Protein estimation

The total protein content of LPMTs was quantified using the BCA protein assay kit (TaKaRa Cat.#T9300A) as per manufacturer instructions. Briefly, about 200 microtissues were lysed in a RIPA lysis buffer (500 µl; Origin, Cat.#PB103-01). Before lysis, the LPMTs from sandwich-cultured microtissues were isolated by collagenase A treatment. The standard solution was prepared by linear dilutions of Bovine Serum Albumin (BSA) dissolved in the lysis buffer. The tissue lysate and the standard dilutions were transferred to a 96-well plate, and an equal volume of BCA working solution was added to each well. The content was mixed thoroughly by shaking using a microplate orbital shaker (MixMate 5353, Eppendrof) at 1000 rpm for 5 min, followed by incubation at 37°C for 1 h. The optical density was quantified by measuring absorbance at 562 nm using a microplate spectrophotometer (Power Wave HT, BioTek). The concentration of protein was calculated from a standard curve.

2.4.4 | Glucose uptake assay

Insulin-stimulated glucose uptake by LPMTs was estimated using fluorescent-tagged 2-deoxy-glucose analog (2-deoxy-2-[(7-nitro-2,1,3-benzoxadiazol-4-yl)amino]-D-glucose, 2NDBG; Abcam Cat. #146200). Briefly, 210 LPMTs (*n* = 3) were collected and pelleted by centrifugation at 11*g* for 30 s. The pellet was rinsed with phosphate-buffered saline (PBS) and again pelleted before resuspending in glucose-free DMEM (100 µl; Himedia, Cat.#AT186). The LPMT suspension was transferred to a clear-bottom black 96-well microplate (Thermo Scientific Cat.#10281092) and incubated for 2 h at 37°C for starving. The LPMTs were then treated with 0 or 32 IU/ml insulin (Cat.#HI0240, Huminsulin R, Eli Lilly Company) in DMEM containing 2-[N-(7-nitrobenz-2-oxa-1,3-diazol-4-yl) amino]-2-deoxy-D-Glucose (200 µg/ml) for 2 h at 37°C. The LPMTs were washed twice with PBS with intermediate centrifugation using a microplate centrifuge (Universal 32R, Hettich). Microtissues were there suspended in PBS (100 µl), and fluorescence intensity was measured using a multimode microplate reader (BioTek Synergy H1) at an Ex/Em wavelength of 485/535 nm, respectively. The total protein of LPMTs was estimated using the BCA Protein Assay Kit (Takara, Cat.#T9300A). The glucose uptake by LPMTs was determined from a standard curve for 2-NBD-Glucose and was normalized to the total cellular protein content.

2.4.5 | Histomorphology analysis and immunostaining

LPMTs after 7 days of culture were embedded in 2% agarose solution prewarmed to 37°C. The suspension was transferred to a 96-well plate and allowed to cool to room temperature for gelation. The agarose embedded LPMTs were then fixed in 10% neutral buffered formalin for 24 h. The samples were dehydrated and processed for paraffin embedding. Embedded samples were cut into 5 µm thick sections using a microtome (Leica RM2245) and mounted on charged glass slides. The sections were stained with haematoxylin and eosin stain. The stained sections were observed under the bright-field mode of a light microscope (Eclipse TS100, Nikon), and digital images were captured (Digital Sight camera # DS-Fi2, Nikon).

Paraffin sections of LPMTs were used for immunofluorescence staining. The sections were dewaxed at 60°C, cleared by two xylene washes and then rehydrated using decreasing concentrations of isopropanol (90% and 75%) and tap water. Antigen retrieval was performed at 60°C in sodium citrate buffer (pH = 6). The sections were permeabilized in 0.025% Triton X-100, nonspecific binding sites were blocked using 1% BSA. The sections were incubated with primary antibodies against MRP2 (Abcam, Cat.#ab15603, 1:20 dilution) and ZO1 (Abcam, Cat.#ab214228, 1:250 dilution). They were detected using a secondary antibody tagged with the fluorescent probe Alexa 488. The cell nucleus was counterstained with PI, and sections were mounted using PBS:glycerol (1:1) solution. The samples were then observed under differential interference contrast mode, and fluorescence images were captured using a confocal laser scanning microscope (Nikon).

2.5 | LPMT sandwich culture

2.5.1 | GelMA synthesis

GelMA was synthesized, as previously reported (Lee, Shirahama, et al., 2015). Briefly, 10 g of Type A porcine skin gelatin (Merck-Sigma, Cat.#G-2625) dissolved in 100 ml of 0.1 M carbonate buffer (pH-10.5) and 1 ml methacrylic anhydride (MAA; Merck-Sigma, Cat. #276685) was added stepwise. The solution was stirred at 50°C for 3 h while keeping the pH stable at 10.5. The GelMA thus formed was dialyzed against water using 12–14 kDa cutoff dialysis tubing (Merck-Sigma, Cat. # D9652) for 72 h at 40°C. The dialyzed GelMA was lyophilized, sterilized by ethylene oxide (ETO) gas and stored at −20°C until use.

2.5.2 | Characterization of GelMA

Nuclear magnetic resonance (NMR) spectroscopy

The functionalization of gelatin by the methacrylamide group was verified by ^{1}H NMR spectroscopy. Five milligrams of gelatin and GelMA polymer was dissolved separately in deuterium oxide (D_2O) at 40°C, and their spectrum was recorded in a Fourier Transform-NMR spectrometer (Bruker, Model# Avance 400) at 400 MHz using tetramethylsilane as the internal standard.

Scanning electron microscopy

The surface morphology of lyophilized GelMA was visualized using a scanning electron microscope (SEM). Cylindrical hydrogel samples having 8 mm diameter and 2 mm height were lyophilized for 48 h and sputter-coated with gold (HITACHI, E1010). The images were then captured using an SEM (HITACHI, S-2400) set at 15 kV.

Microcomputed tomography (micro-CT)

The porosity of lyophilized GelMA was analyzed using a micro-CT scanner (Scano Medical, Model# µCT 40). Cylindrical hydrogel samples having 12 mm diameter and 6 mm height were cast and lyophilized for 48 h. Lyophilized samples were scanned using a cone-beam X-ray source set at 70 kV and 160 µA having a 5 µm spot size. Three-dimensional reconstruction of the 2D images was done using the software µCT V6.1. Morphometric analysis was carried out to determine polymer volume/total volume ratio (PV/TV) and pore size distribution. Percentage porosity of the hydrogel was calculated from Equation (1).

$$\text{Porosity (\%)} = 1 - \left(\frac{PV}{TV}\right) \times 100. \tag{1}$$

2.5.3 | Preparation of LPMT sandwich culture

The LPMTs were sandwiched between two layers of GelMA hydrogel (Figure 8a). The prepolymer solution of GelMA was prepared in serum-free MEM containing 10% (w/v) GelMA and 1% (w/v) Irgacure-2959 (2-hydroxy-4'-(2-hydroxyethoxy)-2-methylpropiophenone; Merck-Sigma, Cat.#410896) as photoinitiator. The first layer of hydrogel was prepared by pouring GelMA solution (100 µl) into a cylindrical mold (5 mm diameter) and was crosslinked with ultraviolet (UV) light of 365 nm for 5–7 min. The hydrogel was placed inside a 12-well plate, and approximately 200 LPMTs ($n = 3$) were carefully transferred over the hydrogel. The plate was incubated inside a CO_2 incubator for 30 min for the LPMTs to settle on the hydrogel. The second layer of GelMA solution (25 µl) was poured on the LPMTs and crosslinked as mentioned above. The enhancement of tissue-specific functions of LPMTs by GelMA was studied by comparing GelMA sandwich-cultured LPMTs (GelMA sw-LPMTs) with Alginate sandwich-cultured LPMTs (Alginate sw-LPMTs). A 5% (w/v) GelMA hydrogel sandwich was made for comparison using the same procedure as described above. The sodium alginate powder (Merck-Sigma, Cat.#A2033) was first sterilized by exposing it to UV radiation for 30 min within a biosafety cabinet, followed by pasteurization at 60°C for 30 min. Alginate was dissolved in serum-free MEM to prepare a 5% (w/v) solution. The first layer of alginate hydrogel was prepared in a cylindrical mold by crosslinking using 20 mM calcium chloride solution for 10 min. About 200 LPMTs ($n = 3$) were carefully transferred over the hydrogel layer and the second layer of alginate solution was added on settled LPMTs. The second layer of alginate was crosslinked to form the hydrogel sandwich, and 1 ml culture medium was added to each well. The sandwich culture was incubated at 37°C inside the humidified incubator with 5% CO_2 for 15 days.

2.5.4 | Functional analysis of sandwich-LPMTs

Spent media from suspension and sandwich-LPMT cultures were collected from triplicate samples at 48 h intervals for 15 days and stored at −80°C. The albumin and the urea secreted were estimated using Human Albumin ELISA kit (Bethyl Laboratories Inc., Cat.#E88-129) and Urea assay kit (Biochain, Cat.#Z5030016), respectively, as per the manufacturer's protocol. The absorbance values were measured using a microplate spectrophotometer (BioTek Model#). The albumin and urea values estimated from the assay were normalized to the total protein content of LPMTs.

CYP3A4 enzyme activity in LPMTs was determined using P450-Glo CYP3A4 assay kit (Promega, Cat.#V9001) as per manufacturers protocol. Briefly, LPMTs from 210 droplets ($n = 3$) were seeded into each well of a white opaque 96-well microplate. The microtissues were then incubated in 150 µl of luciferin-Isopropyl Alcohol (IPA) substrate solution and incubated for 1 h at 37°C. The substrate solution was then replaced with 50 µl of luciferin detection reagent, and the plate was incubated at room temperature for 20 min. The luminescence intensity was measured using a multimode plate reader (Plate Chameleon V, Hidex Model#425-106). For sandwich-cultured LPMTs, to retrieve the microtissues, GelMA sw-LPMTs were treated with collagenase A enzyme (Cat.#10103586001, Merck-Sigma,) at a final concentration of 1 mg/ml for 20 min and Alginate sw-LPMTs were treated with alginate dissolution solution (0.03 M EDTA, 0.055 M sodium citrate and 0.15 M sodium chloride in water, pH 7) for 1 min. The microtissues were then separated by centrifugation at 11*g* for 30 s and were seeded into the microplate for assay.

2.5.5 | Statistical analysis

Statistical analysis was performed with one-way ANOVA using the GraphPad Prism (Version 8), and all data were expressed as mean ± standard deviation. Student's t tests analyzed differences between groups, and p value of <0.05 was considered as significant.

3 | RESULTS

3.1 | Design and fabrication of an HdCC

The chamber was compact in size, transparent, easy to assemble, and portable (Figure 1). A single chamber can accommodate eight substrates having the dimensions 70 mm × 65 mm × 0.1 mm (length × breadth × height). The design ensured a closed environment and maintained an aseptic condition within the chamber. The chamber was reused after proper washing and ETO sterilization.

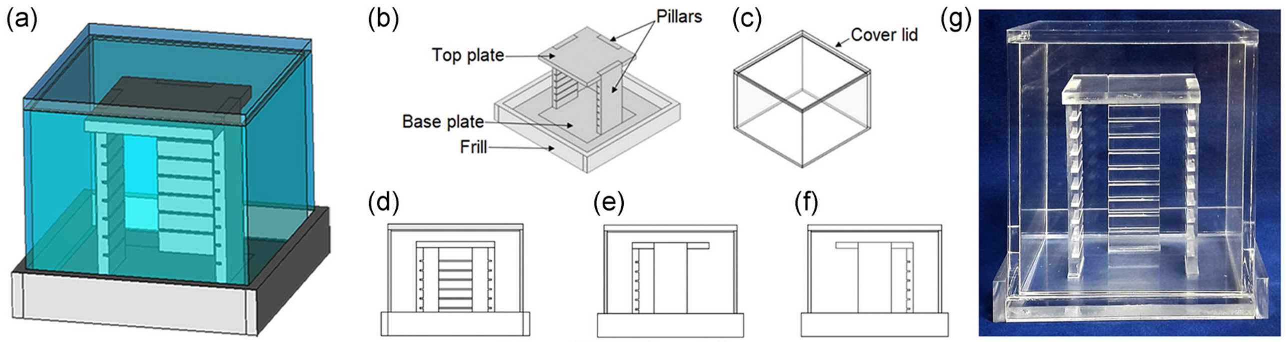

FIGURE 1 Design of the Hanging-drop Culture Chamber. (a) The computer-aided design (CAD) model of the HdCC. (b) Inner components, such as base plate, vertical pillars, and the top plate. (c) The lid covers the unit entirely for maintaining the aseptic environment around the inner components. Different views of the chamber: (d) front view, (e) left side view, and (f) right side view. (g) The image of HdCC used for the experiments. HdCC, Hanging-drop Culture Chamber

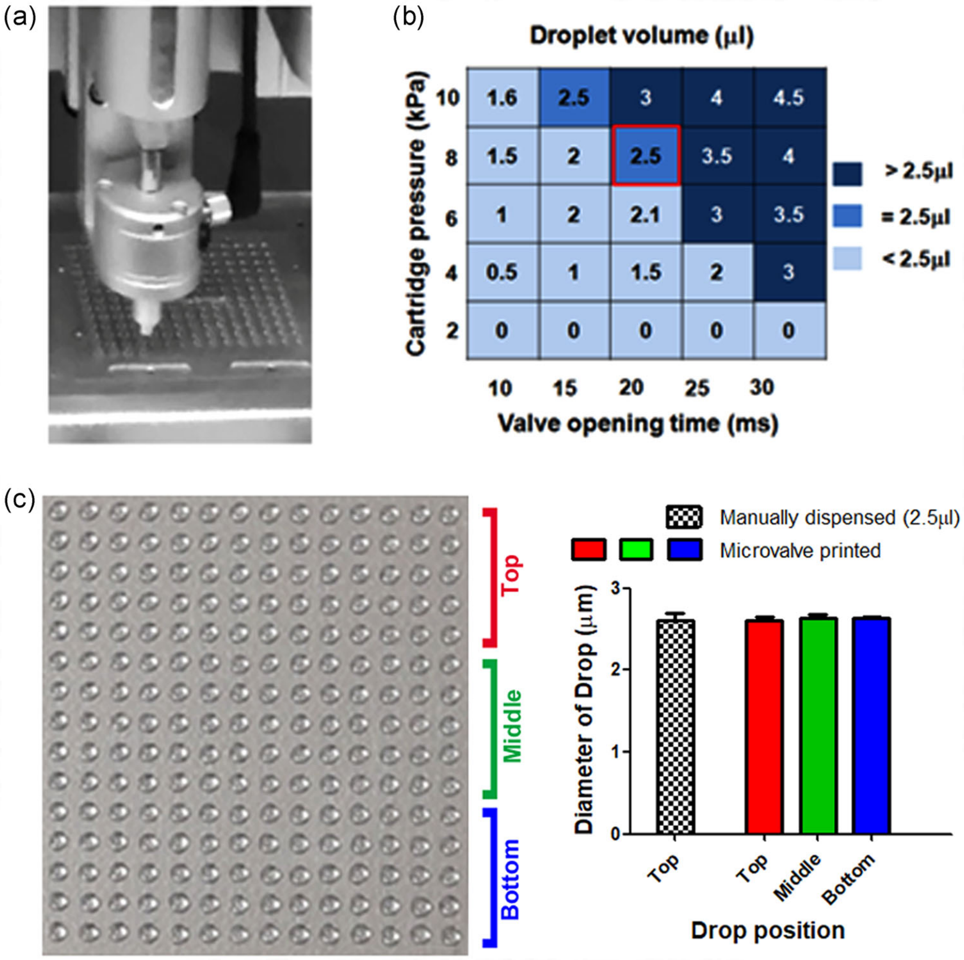

	10	15	20	25	30
10	1.6	2.5	3	4	4.5
8	1.5	2	2.5	3.5	4
6	1	2	2.1	3	3.5
4	0.5	1	1.5	2	3
2	0	0	0	0	0

FIGURE 2 Determining the optimum printhead parameters for microvalve-based printing: (a) A digital image of the cell-friendly printhead with the cartridge connected to the microvalve. (b) Phase diagram depicting the variation in droplet volume with varying cartridge pressure and valve opening time. Values of the parameters corresponding to the highlighted cell (red) were considered optimum for microvalve-based printing. (c) A digital image showing a uniform droplet array of water printed using the optimum value and the uniform droplet size across different locations of the array (top, middle, and bottom) compared with manual dispensing. Scale bar = 4 mm

3.2 | Optimization of microvalve-based printing

Liquid droplets having a volume ranging from nanoliters to microliters were printed at high precision and optimum speed using a microvalve nozzle (Figure 2a). A droplet volume of 2.5 µl yielded the desired diameter close to 2 mm. The results from 25 different combinations of printhead parameters with VOT and CPR as variables were plotted into a matrix format as shown in Figure 2b. It was observed that the required volume of 2.5 µl was obtained at two conditions. The settings with a lower CPR of 8 kPa and 20 ms of VOT were selected for cell printing. Figure 2c shows the array of 15 × 14 droplets printed on a PET substrate. The time taken to complete a single array was 45 s. The droplets were uniform in size and shape, with adequate space between one another. The variation in size of printed droplets was analyzed using ImageJ software. The diameter of the printed droplet analyzed randomly from 5 × 14 droplets from top, middle, and bottom regions of array, matched with the manually dispensed drops having a volume of 2.5 µl. There was no difference in droplet size across different locations (top, middle, and bottom) of the array (Figure 1S).

3.3 | Microvalve-based drop-on-demand bioprinting of hepatocytes

A uniform 15 × 14 droplet array containing ~500 cells/droplet was bioprinted on the PET substrate and cultured as a hanging drop inside the HdCC device (Figure 3a,b). Cells within the droplet formed an aggregate after 24 h of incubation at 37°C. The cell aggregate became more compact after 48 h and formed a spherical microtissue at the end of 72 h postprinting (Figure 3c). The efficiency of microtissue formation by microvalve-based bioprinting (97.4% ± 0.7%) was significantly higher compared with the manual dispensing method (62.8% ± 2%; Figure 3d). We observed that the size (diameter) of the microtissues generated on different PET substrates varied significantly during the initial stages of bioprinting. The nonuniformity among the microtissues was due to the difference in cell number, which occurred due to cell sedimentation during bioprinting. To overcome this limitation, we introduced a short agitation step before initiating each print command. Cell bioprinting following agitation yielded uniform microtissues. Figure 3e shows the variation in size of

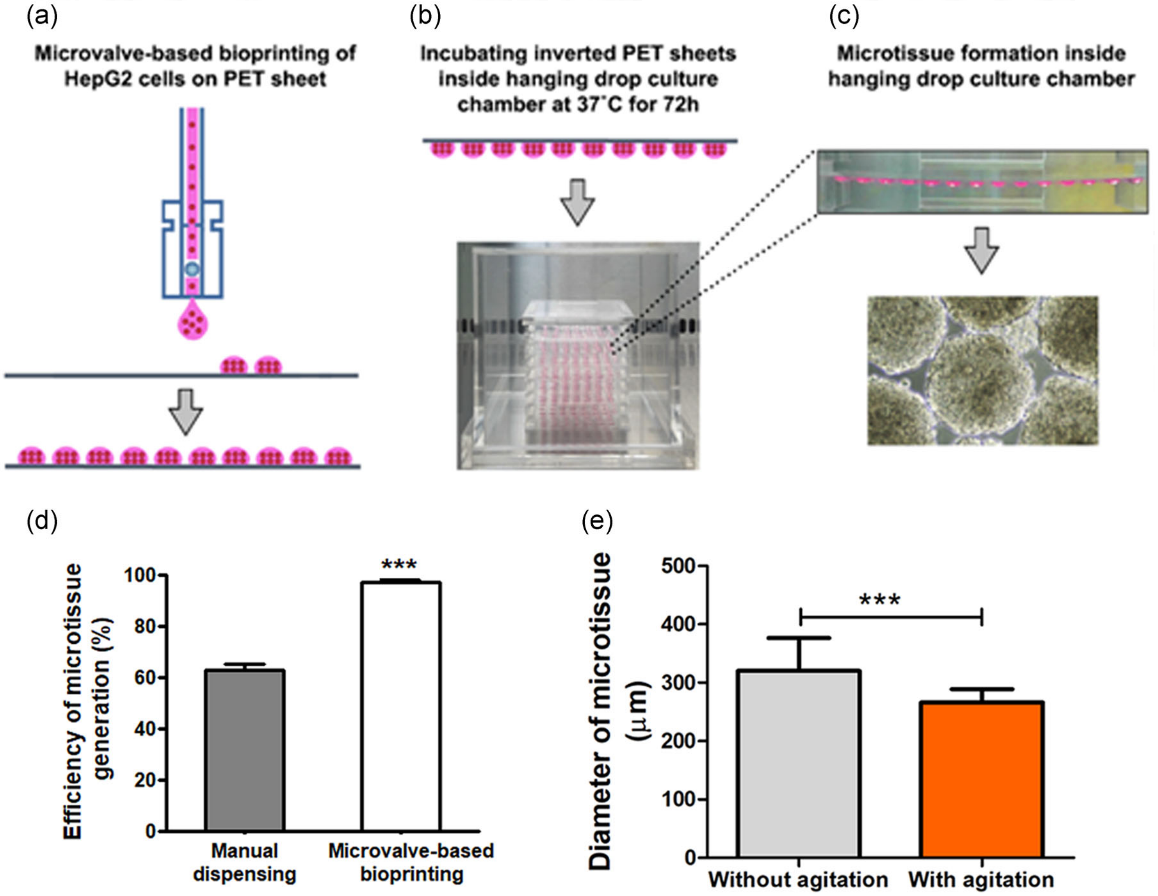

FIGURE 3 Steps in the generation of LPMTs in HdCC and efficacy of microvalve-based bioprinting. (a) Illustration showing microvalve-based bioprinting. (b) Culture of HepG2 cells in hanging drops inside HdCC. (c) Formation of microtissue inside HdCC. (d) Data showing the comparison between manual dispensing and microvalve-based bioprinting method for their efficiency in generating microtissues ($n = 630$, $***p < 0.001$). (e) Data showing variation in size of the microtissues formed post-bioprinting with and without agitation. HdCC, Hanging-drop Culture Chamber; LPMT, liver parenchymal microtissue; PET, polyethylene terephthalate

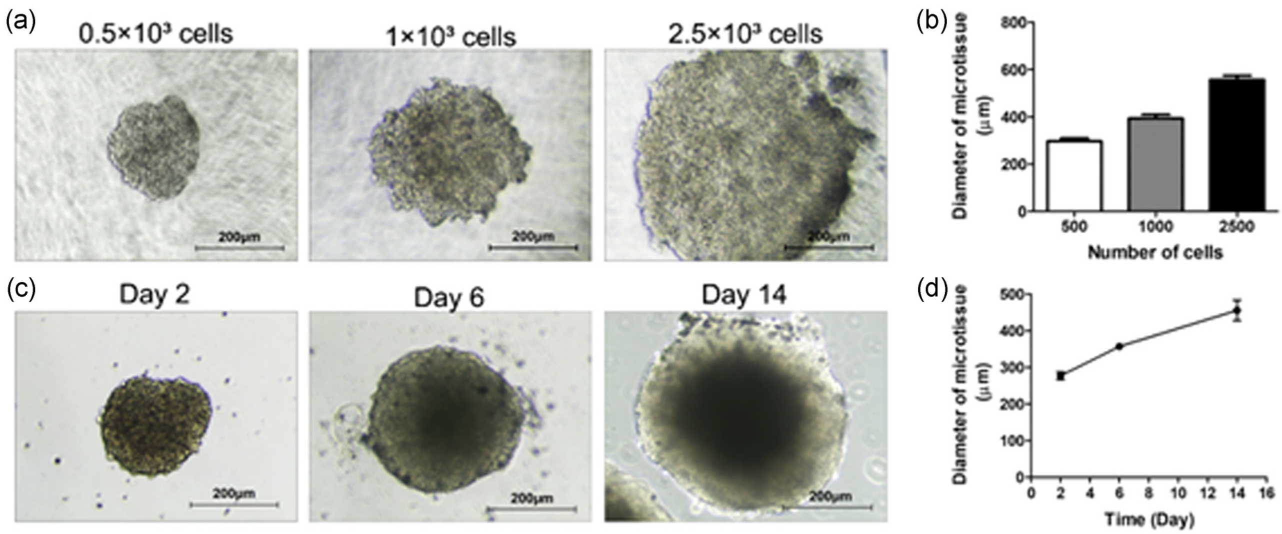

FIGURE 4 Assessing the size and stability of the LPMTs. (a) Phase-contrast images of representative microtissues generated from three different cell concentrations after 72 h. (b) Data representing the average diameter of the microtissues (*n* = 4) with different cell numbers after 72 h. (c) Phase-contrast images of the microtissue (500 cells) depicting the growth of the microtissue in culture. (d) The changes in the size of the microtissue (500 cells) over time in culture (*n* = 9). Scale bar = 200 μm. LPMT, liver parenchymal microtissue

the microtissues generated in the bioprinted droplets with and without agitation.

3.3.1 | Microtissue harvesting, culture, and size analysis

A single sheet of PET substrate generated around 200 microtissues, and about 1600 microtissues were obtained from an HdCC chamber. The efficiency in harvesting microtissue from PET sheet was 92.2% ± 3%. A positive correlation was observed between the number of cells dispensed per droplet and the size of the microtissue (Figure 4a). The average diameter versus cell number in the microtissue is shown in Figure 4b. The diameter of LPMT and the cell number per microtissue was 297.15 ± 11, 393.69 ± 16, and 557.71 ± 17 μm for 0.5×10^3, 1×10^3, and 2.5×10^3 cells, respectively. Microtissues with the smallest diameter were chosen for the later experiments, considering the efficient nutrient transfer possibilities. The microtissues were stable without any sign of disintegration up to 2 weeks in suspension culture (Figure 4c). The microtissue diameter increased over time with an increment of 28.8% and 35.6% on days 6 and 14 of culture to the second day (Figure 4d). The increase in diameter of the microtissue could be attributed to the cell proliferation at the peripheral zone.

3.3.2 | Assessment of cell viability

Microvalve-based bioprinting of HepG2 cells yielded viable LPMTs. The total ATP content in microtissues was quantified to determine the number of metabolically active cells. The microtissues exhibited a stable production of ATP up to 2 weeks in culture (Figure 5a). Percentage of cell metabolic activity at days 1, 7, and 15 was 100% ± 11%, 109% ± 20%, and 99.4% ± 2%, respectively. Further, we confirmed the cell viability of 7-day old LPMTs using live/dead staining and confocal microscopy imaging. The Z-stack projections (Figure 5b) of the stained LPMTs revealed that the cells were viable in the microtissue.

3.3.3 | Glucose uptake assay

Hepatic glucose uptake and release are dependent on the ability of microtissues to respond to insulin. The insulin sensitivity of LPMTs was assessed by quantifying the uptake of fluorescently labeled glucose by microtissues in the presence and absence of insulin (Figure 5c). The quantity of glucose uptake by microtissues in the presence of insulin was significantly higher (646.6 ± 22 ng/μg total protein) compared with the untreated group (505.8 ± 5 ng/μg total protein). The microtissues were intact, and labeled glucose uptake was visibly different between the two groups (Figure 5d).

3.3.4 | Histomorphology analysis and immunostaining

The structural characteristics of LPMTs were analyzed by staining paraffin-embedded sections. Hematoxylin and eosin (H&E) staining of cultured microtissue after 7 days (Figure 6a) showed dense tissue-like cellular distribution mimicking the hepatic plates

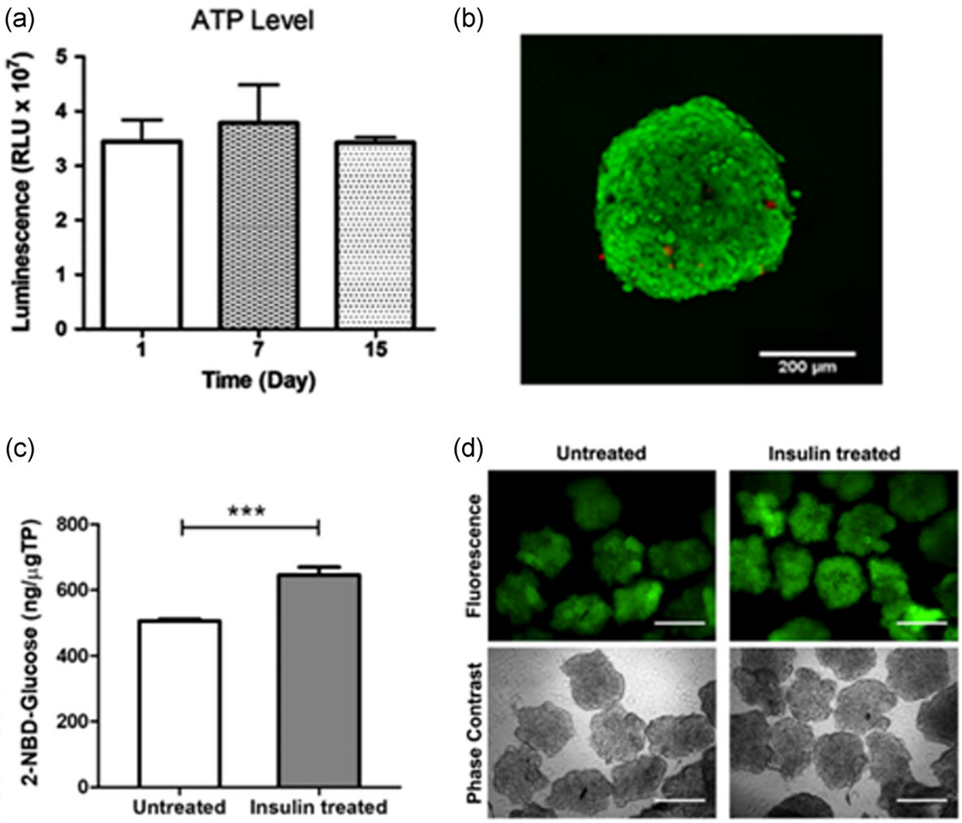

FIGURE 5 Cell viability and insulin-stimulated glucose uptake in LPMTs. (a) Results of cell viability assay calculated based on quantification of ATP in the tissue lysate. Relative Luminescence Unit (RLU) correlates with the ATP level and thus with the quantity of metabolically active (viable) cells (a pooled sample of 210 microtissues was analyzed in triplicates). (b) Confocal image showing live/dead staining of 7-day old LPMT with FDA (green, live cells) and PI (red, dead cells). (c) Data representing the quantity of 2-NBD glucose absorbed by microtissues in the absence and presence of insulin. (d) Fluorescent image showing uptake of 2-NBD glucose by microtissues and phase-contrast images showing the integrity of the microtissues. Scale bar = 200 μm. ***$p < 0.01$. ATP, Adenosine TriPhosphate; FDA, fluorescein diacetate; LPMT, liver parenchymal microtissue; PI, propidium iodide

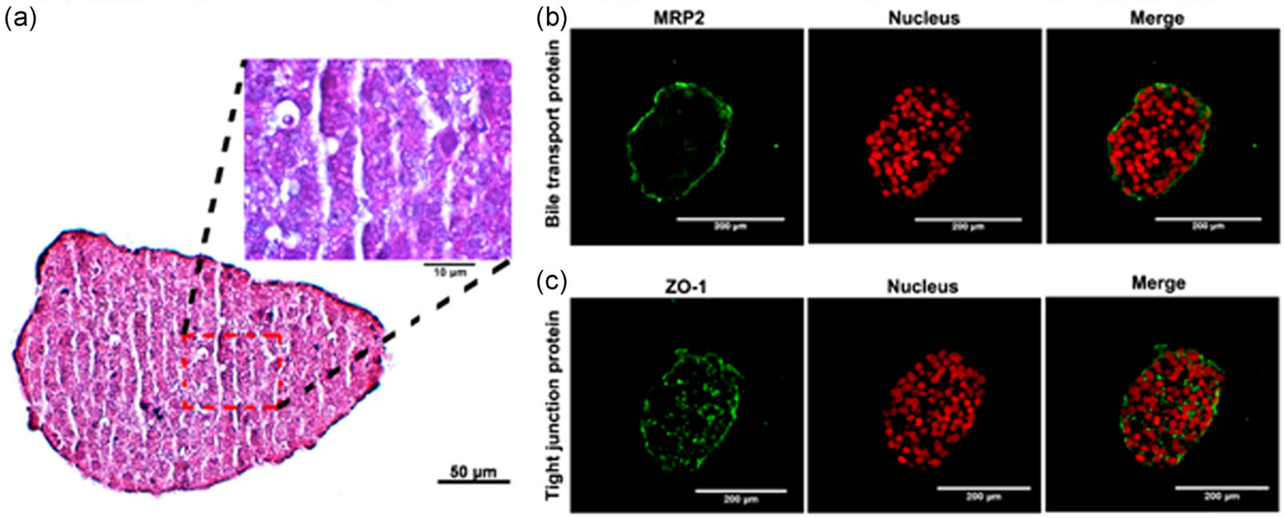

FIGURE 6 Histomorphological and immunohistochemical analysis of LPMTs. (a) Bright-field image of H&E stained microtissue showing hepatic plate-like cellular arrangement. Scale bar = 50 μm. (b, c) Confocal images showing the immunofluorescent stained LMPTs positive (green) for hepatocyte polarization markers MRP2 and ZO1. Cell nuclei were counterstained with PI (red). Scale bar = 200 μm. H&E, hematoxylin and eosin; LPMT, liver parenchymal microtissue; MRP2, Multidrug Resistance Protein 2; PI, propidium iodide; ZO1, Zonula Occludens 1

present in vivo. Immunofluorescence staining of LPMTs was performed to visualize the expression of hepatocyte polarization markers MRP2 (apical) and ZO1 (basolateral). Expression of MRP2 was primarily confined to the periphery of the microtissue with less abundance within (Figure 6b). However, positive staining for the protein ZO1 throughout the microtissue indicated the formation of tight intercellular junctions required for epithelialization (Figure 6c).

3.4 | LPMT sandwich culture

3.4.1 | Synthesis and characterization of GelMA

The overall percent yield of GelMA synthesis was 70% and an illustration of GelMA polymer is shown in Figure 2Sa. The ^{1}H NMR spectrum of the GelMA (Figure 2Sb) confirmed the functionalization of gelatin by the methacrylamide group. Resonance signals at 2, 5.5, and 5.7 ppm in GelMA correspond to methyl protons of methacrylamide grafts and acrylic protons of methacrylamide grafts on hydroxyl lysine and lysine, respectively. The signal at 3.09 ppm corresponding to methylene protons of unreacted lysine was lower in GelMA than gelatin.

The porosity of hydrogel is a detrimental factor that influences the diffusion of nutrients and metabolites, affecting cellular viability and functions. SEM images (Figure 2Sc) of the lyophilized GelMA showed a porous network of polymer with smooth walls separating the pores. Micro-CT analysis provided the cross-sectional images of lyophilized GelMA (Figure 2Sd) depicting porous internal structure. Quantitative morphometric analysis yielded a PV/TV ratio of 0.3867 and the percentage porosity was determined to be 61.33%. The pore diameter of the hydrogel ranged from 10 to 300 µm. The percentage pore volume occupied by pores having diameter 10–100, 100–200, and 200–300 µm was 67.2%, 29.5%, and 3.2%, respectively (Figure 2Se).

3.4.2 | LPMTs in GelMA and alginate sandwich culture

The suspension and sandwich culture of LPMTs is illustrated in Figures 7a,b. The LPMTs sandwiched in GelMA culture ensured immobilization of LPMTs, and the microtissues maintained an intact structure without any gross changes in size over 15 days (Figure 7c). The LPMTs in alginate showed irregular edges but with intact structure (Figure 7d). On the contrary, microtissues in suspension culture exhibited fusion and agglomeration (Figure 7e).

3.4.3 | Functional analysis of sandwich-LPMTs

Further, to understand the influence of extracellular matrix on the microtissue function, we compared the basic liver functionality of both groups. Liver-specific functions such as protein synthesis, ammonia detoxification, and phase I metabolism-related enzyme activity in the LPMTs in sandwich culture were analyzed for 15 days. Albumin secreted into the culture medium represented the protein synthesis function of the liver. Though the albumin synthesis in sandwich-LPMTs on day 1 was similar to LPMTs in suspension, the synthesis increased over time. It was significantly higher than LPMTs in suspension on days 7 and 15 (Figure 7f). The detoxification ability of microtissues was assessed by the estimation of urea secreted into the culture medium (Figure 7g). Similar to the albumin secretion, urea secreted by sandwich-LPMTs increased over time and was significantly higher on days 7 and 15. In contrast, LPMTs in suspension showed a significant decrease in urea secretion. Cytochrome P450 3A4 monooxygenases are the liver's major enzymes involved in the phase I metabolism of xenobiotics. The enzyme activity of CYP3A4 increased significantly over time in sandwich-LPMTs compared with LPMTs in suspension, where the activity was substantially less throughout the culture (Figure 7h).

The organ-specific functions of LPMTs sandwiched on GelMA hydrogel (5% wt/v) were compared with LPMTs sandwiched in the same concentration of sodium alginate hydrogel. The albumin synthesis significantly increased in both sandwich systems from day 1 to 7 and was stable till the 15th day. However, the total amount of albumin synthesized in GelMA sw-LPMTs was significantly higher than that in Alginate sw-LPMTs throughout the culture period (Figure 8a). The urea synthesis significant linear increase in both the groups from day 1 to 15 while the total amount of urea synthesized in GelMA sw-LPMTs was always significantly higher than that in Alginate sw-LPMTs (Figure 8b). The CYP3A4 enzyme activity was maintained in GelMA sw-LPMTs, whereas the enzyme activity in Alginate sw-LPMTs significantly decreased from day 1 to 15 of culture (Figure 8c) indicating enhanced organ-specific functions of LPMTs in GelMA sandwich.

4 | DISCUSSION

Three-dimensional microtissues can serve as functional building blocks for tissue engineering as they mimic the physiological features in vitro (Mironov et al., 2009; Okudaira et al., 2016). Recent advances in the 3D culture of liver cells have shown that microtissues can be used as microscale tissue analogs to study cell–cell interaction, disease mechanism, and tissue response to drugs (Hurrell et al., 2020). Hanging-drop culture is the most straightforward and reproducible method for fabricating homogeneous microtissues (Pampaloni et al., 2007). It is a scaffold-free method wherein the cells self-assemble mimicking events during organogenesis (Achilli et al., 2012; Moscona & Moscona, 1952). At present commercialized hanging-drop culture plates (e.g., GravityPLUS plate, InSphero and Perfecta3D plate, 3D Biomatrix) are available in the standard microplate format. These are expensive (~100 US$ per plate) culture wares, and the number of microtissues generated is limited. To scale up the production of microtissues, a cost-effective alternative has to be implemented that is precise and reproducible.

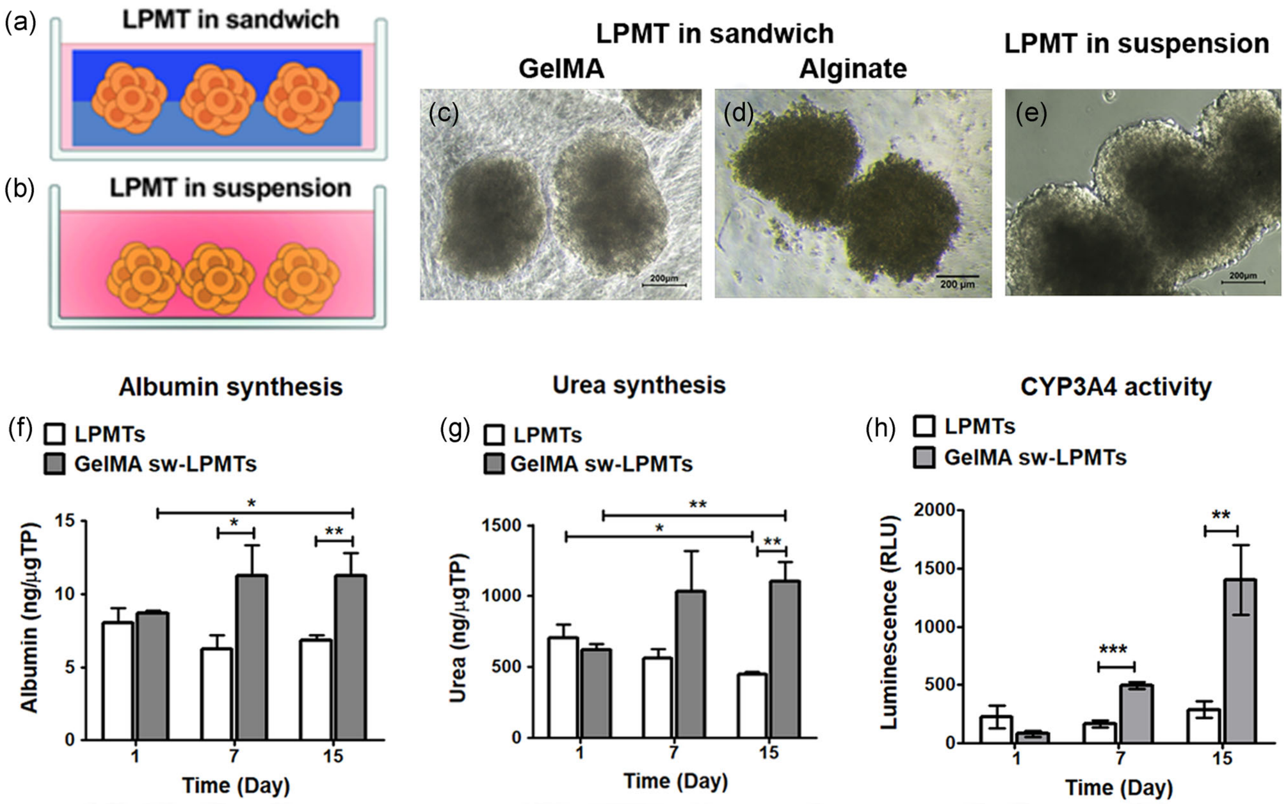

FIGURE 7 Comparison of the structural and functional integrity of LPMTs in the sandwich and suspension culture. (a, b) Schematic of the microtissue sandwich culture and suspension culture. Phase-contrast images of the microtissues sandwiched in (c) GelMA and (d) Alginate and (e) LPMTs in suspension. (f) Graph showing an increasing level of albumin secretion by sandwich-LPMTs compared with LPMTs. (g) Urea secreted by GelMA sandwich–LPMTs increased while that of LPMTs decreased. (h) CYP3A4 enzyme activity increased significantly sandwich-cultured LPMTs. Luminescence intensity correlates with the amount of luminescent product produced by the active enzyme (a pooled sample of 210 microtissues was analyzed in triplicates for all the assays, $^{*}p < 0.05$, $^{**}p < 0.01$, and $^{***}p < 0.001$). Scale bar = 200 µm. GelMA, gelatin methacrylamide; LPMT, liver parenchymal microtissue; sw-LPMT, sandwich-cultured LPMT

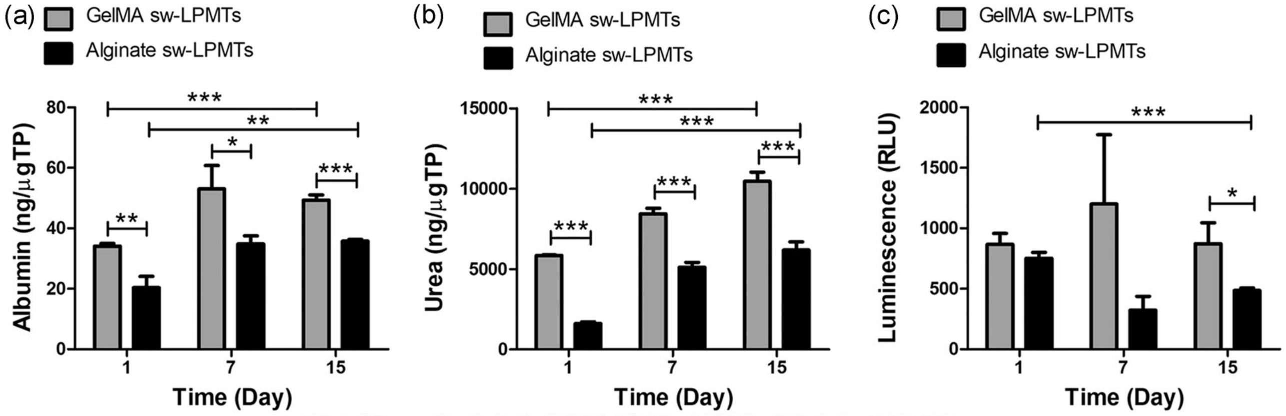

FIGURE 8 Comparison of the functional capabilities of LPMTs in the GelMA and Alginate sandwich culture. (a) Graph showing the enhanced level of albumin secretion by GelMA sandwich-cultured LPMTs compared with Alginate sandwich-cultured LPMTs. (b) Graph showing the enhanced level of urea secretion by GelMA sandwich-cultured LPMTs compared with Alginate sandwich-cultured LPMTs. (c) CYP3A4 enzyme activity is maintained in GelMA sandwich-cultured LPMTs while the activity decreases in Alginate sandwich-cultured LPMTs (a pooled sample of 210 microtissues was analyzed in triplicates for all the assays, $^{*}p < 0.05$, $^{**}p < 0.01$, and $^{***}p < 0.001$). GelMA, gelatin methacrylamide; LPMT, liver parenchymal microtissue; sw-LPMT, sandwich-cultured LPMT

In this study, three key aspects related to microtissue production and culture were addressed: (1) fabrication of a cost-effective and customizable hanging-drop culture platform, (2) microvalve-based bioprinting to generate cell-laden hanging drops in a high-throughput manner, and (3) preparation of a microtissue sandwich culture model for preserving structural–functional integrity of LPMTs in vitro.

The hanging-drop culture platform works in conjunction with the microvalve-based printing technology for the mass production of 3D microtissues. The substrate used for holding the drops was transparent thin PET sheets. It has been previously reported that PET sheets can serve as carriers for cell constructs (Joseph et al., 2011). The advantage of the PET sheet is its lightweight, optical clarity, and high strength-to-weight ratio. A custom-designed culture chamber that can accommodate PET carriers with hanging drops was designed. The laboratory level cost estimate for the fabrication of reusable HdCC was approximately 30 US$, whereas PET culture substrates required for one HdCC unit is only 100 center coins. Both the chamber and the PET sheets can be sterilized using alcohol wiping, ultraviolet irradiation or, most efficiently, by ETO sterilization. Taken together, the total cost of our culture system was many times lesser than commercially available hanging-drop culture plates.

The manual dispensing of cell suspension for microtissue production by hanging-drop method is labor-intensive and has to be replaced with an automated liquid dispensing technology. There are reports on automated liquid handling systems for dispensing cell suspension into a specially designed hanging-drop multiwell plate (Drewitz et al., 2011; Tung et al., 2011). Recently, a drop-on-demand printing technique has been used to generate cell-laden hanging-droplets for producing 3D microtissues. Faulkner-Jones et al. (2013) first demonstrated the application of a valve-based cell printer to produce human embryonic stem cell spheroid aggregates. In their study, a dual nanoliter dispensing system was used to generate the hanging-drop array.

Similarly, Gutzweiler et al. (2017) reported the large-scale production of human umbilical vein endothelial cells spheroids using a disposable, electromagnetic dispensing valve. In this study, we utilized the microvalve-based bioprinting technique for preparing an array of cell-laden hanging droplets on the PET substrate. Hepatocarcinoma cell line (HepG2) was used for the in vitro experiments due to its unlimited life span and widely used as an alternative to primary hepatocytes (Gómez-Lechón et al., 2014). Although the metabolic representation of cytochrome P450 by HepG2 cells in conventional monolayer culture is deficient, 3D microtissues exhibit enhanced enzyme activity (Ramaiahgari et al., 2014). A high-precision microvalve was mounted on the printhead of a 3D bioprinter to dispense the droplets, and the parameters for the bioprinting were optimized. Microvalve-based bioprinting was proved to be an efficient method for the high-throughput production of microtissues compared with the manual dispensing system. The efficiency of microtissue formation by bioprinting was greater than 95%, whereas it was only 60% in the manual method. However, due to the low viscosity of cell suspension, the cells tend to settle down during the printing, resulting in the variable number of cells per droplet (Faulkner-Jones et al., 2013). The cell sedimentation was prevented by short-time agitation of cell suspension using a cell-friendly agitator before each print job. The data presented in Figure 3e clearly show the uniformity in the size of the microtissues with agitation due to equally distributed cell number. Such improvisations in the process methodology increased the efficiency of our printing technique and yielded uniform microtissues. The efficiency of harvesting the microtissues from the substrate is also a detrimental factor in assessing the reliability of high-throughput methods. Gutzweiler et al. (2017) reported a high efficiency of spheroid formation (~96%) in hanging droplets, while the efficiency of harvesting the microtissues was significantly less (~54%). The hydrophilic nature of PET substrate allowed an easy collection of microtissues with a harvesting efficiency greater than 90%. Earlier reports have shown the advantages of an integrated approach consisting of automated cell dispensing with hanging-drop culture platforms. Popova et al. (2019) have developed a highly miniaturized single spheroid hanging-droplet microarray based on hydrophilic–superhydrophobic patterning to form tumor spheroids. However, it involves a series of complex fabrication steps for developing the droplet microarray device that can accommodate 588 spheroids in contrast to our HdCC that can yield 1600 spheroids at one go.

An inherent limitation of microtissues is the formation of hypoxic core with the increase in size, due to the limited diffusion of oxygen and nutrients (Asthana & Kisaalita, 2012). Since the size of the microtissue is directly proportional to the cell number dispensed per droplet, the size versus cell number was analyzed. As shown in Figure 4a, at the end of 3 days of initiating hanging-drop culture, the microtissue size showed a linear relationship to the cell number. When proliferating cell lines are used for microtissue culture, the cell multiplication increases cell number and thereby the size of LPMTs over the days. Hence lower cell number is preferred for seeding over high cell number to avoid necrotic core formation as showed by Gaskell et al. (2016). We opted for 500 cells per droplet as the optimum cell concentration because the radius of the spherical microtissue formed was close to 150 μm which was well within the range of diffusion limit. The viability staining ensured the absence of necrotic core and consistent levels of ATP production within the LPMTs over 2 weeks (Figure 5a,b).

One of the liver's primary functions is to assist in glucose homeostasis by regulating the interconversion of glucose and glycogen. Glucose uptake and glucose conversion to glucose-6-phosphate in hepatocyte are partly controlled by the hormone insulin (Iozzo et al., 2003). The sensitivity of LPMTs to insulin was analyzed by quantifying the uptake of labeled glucose after a short period of starvation. Insulin-treated LPMTs showed a significant increase in glucose uptake, indicating an active response towards hormonal stimuli.

Earlier studies have shown that the microtissues preserve the native cell morphology and better cell-to-cell interactions compared with conventional monolayer culture (Peshwa et al., 1996; van Zijl & Mikulits, 2010). To characterize the structural features of LPMTs, we examined the stained sections. To our knowledge, this is the first report that has shown a typical hepatic plate-like cellular arrangement within microtissues developed by hanging-drop culture. Another essential structural characteristic that we have analyzed was the expression of the hepatocyte polarization markers MRP2 and ZO1. It has been reported that HepG2 spheroids formed on a PDMS mold expressed MRP2 and ZO1 when encapsulated in GelMA and are useful for the liver on a chip platform (Bhise et al., 2016). Expression of MRP2 and ZO1 in LPMTs generated using novel HdCC confirms that the cells are structurally polarized with epithelial characteristics.

Lack of control over the size and shape of microtissues and the need for pooling of microtissues to yield sufficient analyte for detection, hampers their use for high-throughput screening assays. Immobilization of microtissues within a definite space using a suitable biomatrix can be a solution. Earlier studies on collagen sandwich culture of hepatocytes have proven the positive impact of extracellular matrix on hepatocyte survival and functions (Dunn et al., 1989). Pinkse et al. (2005) have shown that the interactions between arginylglycylaspartic acid (RGD) peptides and integrins confer survival benefits to hepatocytes via ILK-pAkt pathway activation. In our study, we have chosen GelMA, a functionalized gelatin derivate that is rich in RGD peptides. Hence, it is expected that the GelMA sandwich culture will provide in vivo-like extracellular cues to the microtissues. First, we studied the advantages of GelMA as a biomatrix for enhancement of LPMT function in 10% GelMA sandwich and compared with LPMTs in suspension. Further to investigate the specific role of GelMA as a better biomatrix for LPMTs, we compared the organ-specific functions of GelMA sw-LPMTs with Alginate sw-LPMTs. Alginate is a polysaccharide-based polymer capable of forming hydrogels by ionic crosslinking. It is considered as an important biomaterial used for a wide range of applications like tissue engineering and drug delivery (Lan et al., 2010). However, the native form of the polymer lacks bioactive molecules present in the native extracellular matrix and has limited long-term stability (K. Y. Lee & Mooney, 2012). Hence, alginate hydrogel was chosen as a control for evaluating our GelMA hydrogel. However, it was difficult to prepare sandwich culture with 10% (w/v) alginate solution. Hence, we used 5% (w/v) of GelMA and Alginate for this experiment. Higher levels of liver functions in GelMA sw-LPMTs substantiated the fact that GelMA was a better biomatrix for enhancing organ-specific functions of LPMTs. Another critical factor that influences the diffusion of nutrients and metabolites across the matrix is its porosity. The morphological characterization of GelMA hydrogel has proved that it is highly porous. The enhanced liver-specific functionalities of LPMTs in GelMA sandwich culture also support the fact that the mass transfer was not affected due to immobilization within the hydrogel.

Conclusively, a proof-of-concept of high-throughput production of LPMTs and their functional enrichment in vitro has been demonstrated successfully. However, a detailed investigation regarding the molecular changes that lead to the enhanced liver functions in sandwich culture has not been done. Our future research will focus on developing microtissues using primary hepatocytes and non-parenchymal cells to represent liver physiology better. An investigation at the molecular level will be carried out to establish the microtissue sandwich model further.

5 | CONCLUSIONS

A high-throughput method for LPMT production was developed using a microvalve-based bioprinting technique with a novel hanging-drop culture device. The microvalve-based bioprinting technique offered a high degree of miniaturization in cell number, droplet volume, and substrate area without compromising microtissue formation and viability. The simple design of the HdCC enabled the easy fabrication of the culture device at a significantly lower cost, and the use of PET substrate offered high tissue harvesting efficiency. This culture device can be quickly adopted in laboratories and industries with an automated liquid dispensing system. The microtissue sandwich culture preserved the structural integrity of LPMTs and enhanced the liver-specific functions without affecting the mass transfer of nutrients. The proposed methodology and the sandwich culture model will find potential application in liver tissue engineering and drug testing.

ACKNOWLEDGMENTS

Anil Kumar P. R. acknowledges the fund of Technical Research Center, SCTIMST (TRC/8141/PSN) received from the Department of Science and Technology, Government of India. Roopesh R. Pai thanks SCTIMST for the Ph.D. Fellowship. Senthilkumar Muthusamy is grateful to the Department of Biotechnology (DBT), Government of India for the research grant (BT/RLF/Re-entry/48/2016) with Ramalingaswami Fellowship. We thank Dr. Ganesh Kadasoor (Olympus) for the technical help in confocal imaging, Mr. Ramesh Babu (Precision Fabrication Facility, SCTIMST) for the fabrication of Hanging-drop Culture Chamber, Dr. D. R. Deepu for the Micro-CT analysis, and Central Laboratory and Instrumentation Facility, Kerala University for NMR spectroscopy.

CONFLICT OF INTERESTS

The authors declare that there are no conflict of interests.

DATA AVAILABILITY STATEMENT

Data are available on request from the authors.

ORCID

Ramesh Pai Roopesh https://orcid.org/0000-0003-0311-4399
Senthilkumar Muthusamy https://orcid.org/0000-0003-1603-9965
Shiny Velayudhan https://orcid.org/0000-0002-3906-5915
Arumugham Sabareeswaran https://orcid.org/0000-0002-9365-1106
Pallickaveedu RajanAsari Anil Kumar https://orcid.org/0000-0003-1610-7323

REFERENCES

Achilli, T.-M., Meyer, J., & Morgan, J. R. (2012). Advances in the formation, use and understanding of multi-cellular spheroids. *Expert Opinion on Biological Therapy*, *12*, 1347–1360. https://doi.org/10.1517/14712598.2012.707181

Asrani, S. K., Devarbhavi, H., Eaton, J., & Kamath, P. S. (2019). Burden of liver diseases in the world. *Journal of Hepatology*, *70*, 151–171. https://doi.org/10.1016/j.jhep.2018.09.014

Asthana, A., & Kisaalita, W. S. (2012). Microtissue size and hypoxia in HTS with 3D cultures. *Drug Discovery Today*, *17*, 810–817.

Berthiaume, F., Moghe, P. V., Toner, M., & Yarmush, M. L. (1996). Effect of extracellular matrix topology on cell structure, function, and physiological responsiveness: Hepatocytes cultured in a sandwich configuration. *FASEB Journal*, *10*, 1471–1484. https://doi.org/10.1096/fasebj.10.13.8940293

Bhise, N. S., Manoharan, V., Massa, S., Tamayol, A., Ghaderi, M., Miscuglio, M., Lang, Q., Shrike Zhang, Y., Shin, S. R., Calzone, G., Annabi, N., Shupe, T. D., Bishop, C. E., Atala, A., Dokmeci, M. R., & Khademhosseini, A. (2016). A liver-on-a-chip platform with bioprinted hepatic spheroids. *Biofabrication*, *8*, 14101. https://doi.org/10.1088/1758-5090/8/1/014101

Chang, T. T., & Hughes-Fulford, M. (2009). Monolayer and spheroid culture of human liver hepatocellular carcinoma cell line cells demonstrate distinct global gene expression patterns and functional phenotypes. *Tissue Engineering: Part A*, *15*, 559–567. https://doi.org/10.1089/ten.tea.2007.0434

Drewitz, M., Helbling, M., Fried, N., Bieri, M., Moritz, W., Lichtenberg, J., & Kelm, J. M. (2011). Towards automated production and drug sensitivity testing using scaffold-free spherical tumor microtissues. *Biotechnology Journal*, *6*, 1488–1496.

Du, Y., Han, R., Wen, F., Ng San, S. S., Xia, L., Wohland, T., Leo, H. L., & Yu, H. (2008). Synthetic sandwich culture of 3D hepatocyte monolayer. *Biomaterials*, *29*, 290–301. https://doi.org/10.1016/j.biomaterials.2007.09.016

Dunn, J. C. Y., Yarmush, M. L., Koebe, H. G., & Tompkins, R. G. (1989). Hepatocyte function and extracellular-matrix geometry—Long-term culture in a sandwich configuration. *FASEB Journal*, *3*, 174–177.

Faulkner-Jones, A., Greenhough, S., King, J. A., Gardner, J., Courtney, A., & Shu, W. (2013). Development of a valve-based cell printer for the formation of human embryonic stem cell spheroid aggregates. *Biofabrication*, *5*, 1758–5082.

Gaskell, H., Sharma, P., Colley, H., Murdoch, C., Williams, D., & Webb, S. (2016). Characterization of a functional C3A liver spheroid model. *Toxicology Research*, *5*, 1053–1065. https://doi.org/10.1039/c6tx00101g

Glicklis, R., Merchuk, J. C., & Cohen, S. (2004). Modeling mass transfer in hepatocyte spheroids via cell viability, spheroid size, and hepatocellular functions. *Biotechnology and Bioengineering*, *86*, 672–680. https://doi.org/10.1002/bit.20086

Gómez-Lechón, M. J., Tolosa, L., & Mt, D. (2014). Cell-based models to predict human hepatotoxicity of drugs. *Reviews in Toxicology*, *31*, 149–156. https://www.redalyc.org/articulo.oa?id=91932969007

Gutzweiler, L., Kartmann, S., Troendle, K., Benning, L., Finkenzeller, G., Zengerle, R., Koltay, P., Stark, G. B., & Zimmermann, S. (2017). Large scale production and controlled deposition of single HUVEC spheroids for bioprinting applications. *Biofabrication*, *9*, 1758–5090.

Haisler, W. L., Timm, D. M., Gage, J. A., Tseng, H., Killian, T. C., & Souza, G. R. (2013). Three-dimensional cell culturing by magnetic levitation. *Nature Protocols*, *8*, 1940–1949. https://doi.org/10.1038/nprot.2013.125nprot.2013.125 [pii.

Hiemstra, S., Ramaiahgari, S. C., Wink, S., Callegaro, G., Coonen, M., Meerman, J., Jennen, D., van den Nieuwendijk, K., Dankers, A., Snoeys, J., de Bont, H., Price, L., & van de Water, B. (2019). High-throughput confocal imaging of differentiated 3D liver-like spheroid cellular stress response reporters for identification of drug-induced liver injury liability. *Archives of Toxicology*, *93*, 2895–2911. https://doi.org/10.1007/s00204-019-02552-0

Hurrell, T., Kastrinou-Lampou, V., Fardellas, A., Hendriks, D. F. G., Nordling, Å., Johansson, I., Baze, A., Parmentier, C., Richert, L., & Ingelman-Sundberg, M. (2020). Human liver spheroids as a model to study aetiology and treatment of hepatic fibrosis. *Cells*, *9*, 964.

Iozzo, P., Geisler, F., Oikonen, V., Mäki, M., Takala, T., Solin, O., Ferrannini, E., Knuuti, J., & Nuutila, P. (2003). Insulin stimulates liver glucose uptake in humans: An 18F-FDG PET study. *Journal of Nuclear Medicine*, *44*, 682–689.

Jin, Y., Kim, J., Lee, J. S., Min, S., Kim, S., Ahn, D.-H., Kim, Y.-G., & Cho, S.-W. (2018). Vascularized liver organoids generated using induced hepatic tissue and dynamic liver-specific microenvironment as a drug testing platform. *Advanced Functional Materials*, *28*, 1801954. https://doi.org/10.1002/adfm.201801954

Lan, S. F., Safiejko-Mroczka, B., & Starly, B. (2010). Long-term cultivation of HepG2 liver cells encapsulated in alginate hydrogels: A study of cell viability, morphology and drug metabolism. *Toxicology in Vitro*. *24*, 1314–1323. https://doi.org/10.1016/J.TIV.2010.02.015

Lee, B. H., Kim, M. H., Lee, J. H., Seliktar, D., Cho, N.-J., & Tan, L. P. (2015). Modulation of Huh7.5 spheroid formation and functionality using modified PEG-based hydrogels of different stiffness. *PLOS One*, *10*, e0118123. https://doi.org/10.1371/journal.pone.0118123

Lee, B. H., Shirahama, H., Cho, N.-J., & Tan, L. P. (2015). Efficient and controllable synthesis of highly substituted gelatin methacrylamide for mechanically stiff hydrogels. *RSC Advances*, *5*(128), 106094–106097. https://doi.org/10.1039/c5ra22028a

Lee, K. Y., & Mooney, D. J. (2012). Alginate: Properties and biomedical applications. *Progress in Polymer Science*, *37*, 106–126. https://doi.org/10.1016/J.PROGPOLYMSCI.2011.06.003

Liao, W., Wang, J., Xu, J., You, F., Pan, M., Xu, X., Weng, J., Han, X., Li, S., Li, Y., Liang, K., Peng, Q., & Gao, Y. (2019). High-throughput three-dimensional spheroid tumor model using a novel stamp-like tool. *Journal of Tissue Engineering*, *10*, 204173141988918.

Manley, P., & Lelkes, P. I. (2006). A novel real-time system to monitor cell aggregation and trajectories in rotating wall vessel bioreactors. *Journal of Biotechnology*, *125*, 416–424. https://doi.org/10.1016/j.jbiotec.2006.03.030

Martignoni, M., Groothuis, G. M. M., & de Kanter, R. (2006). Species differences between mouse, rat, dog, monkey and human CYP-mediated drug metabolism, inhibition and induction. *Expert Opinion on Drug Metabolism & Toxicology*, *2*, 875–894. https://doi.org/10.1517/17425255.2.6.875

Mironov, V., Visconti, R. P., Kasyanov, V., Forgacs, G., Drake, C. J., & Markwald, R. R. (2009). Organ printing: Tissue spheroids as building blocks. *Biomaterials*, *30*, 2164–2174. https://doi.org/10.1016/j.biomaterials.2008.12.084

Moscona, A., & Moscona, H. (1952). The dissociation and aggregation of cells from organ rudiments of the early chick embryo. *Journal of Anatomy*, *86*, 287–301. https://pubmed.ncbi.nlm.nih.gov/12980879

Nguyen, D. G., Funk, J., Robbins, J. B., Crogan-Grundy, C., Presnell, S. C., Singer, T., & Roth, A. B. (2016). Bioprinted 3D primary liver tissues allow assessment of organ-level response to clinical drug induced toxicity in vitro. *PLOS One*, *11*, e0158674. https://doi.org/10.1371/journal.pone.0158674

Nithya, J., Anil Kumar, P. R., Tilak, P., Leena, J., Sreenivasan, K., Kumary, T. V. (2011). Intelligent thermoresponsive substrate from modified overhead projection sheet as a tool for construction and support of cell sheets In vitro. *Tissue Engineering Part C: Methods*, *17*(2), 181–191. http://doi.org/10.1089/ten.tec.2009.0783

Okudaira, T., Amimoto, N., Mizumoto, H., & Kajiwara, T. (2016). Formation of three-dimensional hepatic tissue by the bottom-up method using spheroids. *Journal of Bioscience and Bioengineering*, *122*, 213–218.

Okuyama, T., Yamazoe, H., Mochizuki, N., Khademhosseini, A., Suzuki, H., & Fukuda, J. (2010). Preparation of arrays of cell spheroids and spheroid-monolayer cocultures within a microfluidic device. *Journal of Bioscience and Bioengineering*, *110*, 572–576.

Pampaloni, F., Reynaud, E. G., & Stelzer, E. H. K. (2007). The third dimension bridges the gap between cell culture and live tissue. *Nature Reviews Molecular Cell Biology*, *8*, 839–845. https://doi.org/10.1038/nrm2236

Peshwa, M. V., Wu, F. J., Sharp, H. L., Cerra, F. B., & Hu, W.-S. (1996). Mechanistics of formation and ultrastructural evaluation of hepatocyte spheroids. *In Vitro Cellular & Developmental Biology—Animal*. *32*, 197. https://doi.org/10.1007/bf02722946

Pinkse, G. G., Jiawan-Lalai, R., Bruijn, J. A., & de Heer, E. (2005). RGD peptides confer survival to hepatocytes via the beta1-integrin-ILK-pAkt pathway. *Journal of Hepatology*, *42*, 87–93. S0168-8278(04)00432-5 [pii]. https://doi.org/10.1016/j.jhep.2004.09.010.

Polonio-Alcalá, E., Rabionet, M., Gallardo, X., Angelats, D., Ciurana, J., Ruiz-Martínez, S., Puig, T., & Electrospun, P. L. A. (2019). Scaffolds for three-dimensional triple-negative breast cancer cell culture. *Polymers (Basel)*, *11*(5), 916.

Popova, A. A., Tronser, T., Demir, K., Haitz, P., Kuodyte, K., Starkuviene, V., Wajda, P., Levkin, P. A., Popova, A. A., Tronser, T., Demir, K., Levkin, P. A., Kuodyte, K., Starkuviene, V., & Wajda, P. (2019). Facile one step formation and screening of tumor spheroids using droplet-microarray platform. *Small*, *15*, 1901299. https://doi.org/10.1002/SMLL.201901299

Ramaiahgari, S. C., den Braver, M. W., Herpers, B., Terpstra, V., Commandeur, J. N. M., van de Water, B., & Price, L. S. (2014). A 3D in vitro model of differentiated HepG2 cell spheroids with improved liver-like properties for repeated dose high-throughput toxicity studies. *Archives of Toxicology*, *88*, 1083–1095. https://doi.org/10.1007/s00204-014-1215-9

Shri, M., Agrawal, H., Rani, P., Singh, D., & Onteru, S. K. (2017). Hanging drop, a best three-dimensional (3D) culture method for primary buffalo and sheep hepatocytes. *Scientific Reports*, *7*, 17–1355.

Tung, Y.-C., Hsiao, A. Y., Allen, S. G., Torisawa, Y., Ho, M., & Takayama, S. (2011). High-throughput 3D spheroid culture and drug testing using a 384 hanging drop array. *Analyst*, *136*, 473–478. https://doi.org/10.1039/c0an00609b

Wang, D., Cheng, D., Guan, Y., & Zhang, Y. (2011). Thermoreversible hydrogel for in situ generation and release of HepG2 spheroids. *Biomacromolecules*, *12*, 578–584.

Watkins, P. B. (2011). Drug safety sciences and the bottleneck in drug development. *Clinical Pharmacology & Therapeutics*. *89*, 788–790. https://doi.org/10.1038/clpt.2011.63

Yang, H., Sun, L., Pang, Y., Hu, D., Xu, H., Mao, S., Peng, W., Wang, Y., Xu, Y., Zheng, Y. C., Du, S., Zhao, H., Chi, T., Lu, X., Sang, X., Zhong, S., Wang, X., Zhang, H., Huang, P., … Mao, Y. (2021). Three-dimensional bioprinted hepatorganoids prolong survival of mice with liver failure. *Gut*, *70*, 567–574. https://doi.org/10.1136/gutjnl-2019-319960gutjnl-2019-319960 [pii].

van Zijl, F., & Mikulits, W. (2010). Hepatospheres: Three dimensional cell cultures resemble physiological conditions of the liver. *World Journal of Hepatology*, *2*, 1–7. https://doi.org/10.4254/wjh.v2.i1.1

SUPPORTING INFORMATION

Additional supporting information may be found in the online version of the article at the publisher's website.

How to cite this article: Roopesh, P. R., Muthusamy, S., Velayudhan, S., Sabareeswaran, A. & Anil Kumar, P. R. (2022). High-throughput production of liver parenchymal microtissues and enrichment of organ-specific functions in gelatin methacrylamide microenvironment. *Biotechnology and Bioengineering*, 1–15. https://doi.org/10.1002/bit.28010

Bioprinting 27 (2022) e00214

Contents lists available at ScienceDirect

Bioprinting

journal homepage: www.sciencedirect.com/journal/bioprinting

Radical scavenging gelatin methacrylamide based bioink formulation for three dimensional bioprinting of parenchymal liver construct

Roopesh R. Pai [a,1], Shilpa Ajit [a,1], Anupama Sekar J [a], Sarath S. Nair [b], Anil Kumar P.R. [a,*], Shiny Velayudhan [c,**]

[a] *Division of Tissue Culture, India*
[b] *Division of Extra Corporeal Devices, India*
[c] *Division of Dental Products, India*

ARTICLE INFO

Keywords:
3D Bioprinting
Bioink
GelMA
HepG2
ROS

ABSTRACT

Methacrylated gelatin (GelMA) in the form of methacryloyl, methacrylate, and methacrylamide is an established and widely accepted photocrosslinkable bioink, for three dimensional bioprinting of various tissues. One of the limitations of photocrosslinkable bioinks is the inability to control the free radicals generated by photoinitiators and ultraviolet (UV) rays. The presence of excess free radicals compromises the viability and functionality of cells during crosslinking. In this study, ascorbic acid, a known free radical scavenger (FRS) molecule, was introduced into the GelMA bioink formulation to protect the cell viability, proliferation, and tissue functions of 3D bioprinted parenchymal liver constructs. The concentration of FRS in the bioink was optimized and used for 3D bioprinting of HepG2 cells. The results confirmed that the inclusion of 3.4 mM FRS in the GelMA bioink formulation nullified the excess ROS formed inside the cells. Furthermore, the optimized GelMA formulation containing FRS preserved and improved the cell activity, albumin, and urea synthesis in the 3D construct over 7 days in culture. In the future, this concept could be implemented in the biofabrication of large liver constructs that require multiple or longer durations of UV irradiation.

1. Introduction

Three-dimensional (3D) bio-printing has evolved as a promising tool in tissue engineering and regenerative medicine and is considered an advanced technology that helps in engineering structurally similar biological substitutes by precisely positioning the cells in predefined locations. This technology belongs to the family of additive manufacturing techniques that allow rapid prototyping of tissue constructs by layer-by-layer simultaneous deposition of multiple cell types, proteins, and bioactive substances [1,2]. Accurate spatiotemporal control based on a computer-generated design allows a 3D bioprinting strategy to fabricate biological substitutes with organized micro-architecture, interconnected pores, precise distribution of cells inside the structure, and biochemical demands of the tissues and organs. To accomplish this task of cell deposition in accordance with a particular design, a carrier medium or bioink, that not only supports the cells but also functions as the framework of the bioprinted construct.

A bioink is defined as 'a formulation of cells suitable for processing by an automated biofabrication technology that may also contain biologically active components and biomaterials' [3]. To facilitate enhanced cell function and survivability, bioinks should closely resemble the cell extracellular matrix (ECM) and possess suitable gelling characteristics for different bioprinting approaches are the ideal candidates. In this regard, hydrogels perfectly fit this bill as they are structurally closer to the ECM and can be cross-linked to obtain highly hydrated three-dimensional (3D) networks, are used as excellent scaffolds for tissue engineering scaffolds and are capable of providing mechanical stability to the biofabricated constructs/tissues [4]. Numerous hydrogel systems have been explored as bioinks. However, modified gelatin, known as gelatin methacryloyl, gelatin methacrylamide, and

---

* Corresponding author. Department of Applied Biology, Biomedical Technology Wing, Sree Chitra Tirunal Institute for Medical Sciences and Technology Thiruvananthapuram, Kerala, 695 012, India.

** Corresponding author. Department of Biomaterial Science and Technology, Biomedical Technology Wing, Sree Chitra Tirunal Institute for Medical Sciences and Technology Thiruvananthapuram, Kerala, 695 012, India.

E-mail addresses: anilkumarpr@sctimst.ac.in (P.R. Anil Kumar), shiny@sctimst.ac.in (S. Velayudhan).

[1] Equal contribution.

https://doi.org/10.1016/j.bprint.2022.e00214
Received 13 February 2022; Received in revised form 20 May 2022; Accepted 23 May 2022

gelatin methacrylate, all abbreviated as GelMA is one of the most widely studied hydrogel systems for the bio-fabrication of tissue constructs [5].

GelMA is a photo-crosslinkable polymer that can be readily cross-linked by irradiation at a specific wavelength range in the presence of a photoinitiator (PI), which initiates rapid crosslinking at physiological temperature, pH, and ionic environment and allows for the incorporation of living cells by *in situ* gelation [6]. During photo-crosslinking, PIs generate free radicals upon exposure to a specific wavelength of light and initiate polymerization by cross-linking, which leads to the formation of hydrogels. However, the concentration of PI, inactivated residues, or byproducts formed after cross-linking can elicit toxic effects on cells [7]. The popular photo-initiators used in bioinks are Irgacure (2-hydroxy-1-[4-(2-hydroxyethoxy) phenyl] – 2 -methyl-1-propanone) (Irgacure 2959), Eosin Y, Biokey and VA-086 [8–11]. Among these, Irgacure 2959 elicits minimal cytotoxicity over a wide range of cell types [12] and has been reported safer within a range of 0.2–1 wt percentage for cross-linking GelMA [13].

The free radicals formed during photo-initiated cell encapsulation interact within the cell membrane, proteins, and deoxyribonucleic acids, causing serious cellular damage by affecting many biochemical and physiological activities [14]. One of the adverse effects of free radicals is its influence on the serine/threonine-specific protein kinase known as AKT (v-Akt murine thymoma viral oncogene). Another study by Williams et al. compared UV-sensitive PI on cell types over a range of mammalian species and showed that Irgacure 2959 is well tolerated for photo-encapsulation [12]. However, different cell types displayed variable responses with respect to cell survival and proliferation towards identical concentrations of the same photo-initiator. This is due to the lack of control over excess free radicals generated during photo-polymerization. Moreover, UV irradiation generates reactive oxygen species (ROS) within cells that can damage macromolecules such as DNA, proteins, carbohydrates, and lipids. Thus, cells encapsulated in photo-crosslinkable hydrogels encounter exogenous and endogenous cytotoxic radical species. Many enzymatic and non-enzymatic antioxidants are known to eliminate pro-oxidants and scavenge free radicals in tissues [15]. Vital molecules such as tocopherols (vitamin E), ascorbic acid (vitamin C), and carotenoids (vitamin B) are well-known antioxidants in living systems that react with peroxyl free radicals and protect biological systems [16]. Hence, we hypothesized that the inclusion of free radical scavenging (FRS) molecules in the hydrogel system will improve cell viability and prevent free radical-induced cell damage.

In this study we report a novel photo-protective bioink formulation for bioprinting functional liver constructs. We have added the ascorbic acid (FRS) as a biologically active component in our bioink. L-ascorbic acid can function as the photo-protective molecule to the bioink formulation, and liver tissue constructs. Human hepatoma cell HepG2 is a commonly used liver cell line which proliferates easily and can secrete liver-specific molecules which are routinely analyzed during liver function test. Therefore, we have chosen HepG2 cells in our study to highlight the potential benefits of GelMA-FRS bioink on bioprinted liver constructs. The role of ascorbic acid as a free radical scavenger is well established, however there are no reports on its use as a biologically active component in any bioink formulations reported so far [17,18]. The bioprinted constructs were evaluated for their functional activity. In this study, we report the development of a photo-protective bioink formulation based on GelMA.

2. Materials and methods

2.1. Materials

Porcine skin gelatin (Type A, 175 bloom), methacrylic anhydride (MAA), dialysis tubing (12–14 kDa), fluorescein diacetate (FDA), Cell Counting Kit – 8 (CCK-8), collagenase-A, and glutaraldehyde were purchased from Sigma, India. Irgacure 2959 (photo-initiator, 2 – hydroxy - 4 - (2 – hydroxyl ethoxy) – 2 – methyl propiophenone) was purchased from Ciba Specialty Chemicals, Tarrytown, NJ. Propidium iodide (PI) was procured from HiMedia, India. Syringes and needles were purchased from BD Biosciences, USA; Minimum Essential Medium (MEM), Penicillin-Streptomycin (Pen Strep - 10,000 U/ml), fluorescein isothiocyanite-tagged phalloidin (FITC – phalloidin), Trypsin – Ethelene Diamine Tetra Acetic acid, and fetal bovine serum (FBS) were purchased from Invitrogen, USA. The mouse subcutaneous fibroblast cell line (L-929) was procured from American Type Culture Collections (ATCC, USA), and human liver carcinoma cells (HepG2) were obtained from the National Center for Cell Sciences, India. The human albumin ELISA kit was procured from Bethyl Laboratories, USA, and the urea assay kit was procured from BioChain, USA. All cell culture grade plastic ware such as Petri dishes, T25 flasks, and multi-well plates were purchased from Eppendorf India Limited. The consumables for 3D bioprinting were procured from regenHU, Switzerland.

2.2. Synthesis of gelatin methacrylamide

GelMA was synthesized using a modified buffer method [19]. Briefly, 10 g of gelatin was dissolved in 100 ml alkaline buffer (carbonate bicarbonate, CB, pH > 10) at 50 °C. 167 μL of MAA was sequentially added every 30 min to the gelatin solution at 50 °C for 3h. Following every addition of MAA, the pH of the reaction solution was monitored, and CB buffer was added to maintain a pH > 10. At the end of 3h, the pH of the reaction was adjusted to 7.3. The reaction mixture was then dialyzed against distilled water for 4 days at 40 °C and lyophilized. The lyophilized polymer (GelMA) was stored for-20 °C further use. For biological analysis, GelMA was sterilized by ethylene oxide gas 37 °C and stored at − 20 °C until further use.

2.3. 1H Nuclear magnetic resonance spectroscopy (1H NMR)

^{1}H NMR analysis was performed to confirm the functionalization of gelatin with MAA. Briefly, clear solutions of the sample were prepared by dissolving 10 mg each of gelatin and GelMA in 1 ml deuterium oxide (D_2O) at 40 °C. The NMR spectrum was obtained using a Bruker Avance 400 MHz FT-NMR spectrometer (Germany).

2.4. Degree of functionalization

The degree of functionalization (DoF) was determined using the ninhydrin method reported by Loessner *et al* [20]. Briefly, to 850 μl of ninhydrin solution (2.5 mg/ml ninhydrin in a mixture of 0.5 M sodium citrate monobasic: glycerol at 1: 2 ratio) and 150 μl GelMA solution (10% wt/V in deionized water) was incubated at 50 °C for 12 min. Linear dilutions of gelatin in deionized water were used as the standard solutions. The solution was cooled to room temperature and the absorbance was measured at 570 nm using a spectrophotometer (Biotek, USA). The absorbance obtained for a gelatin concentration of X% in the standard curve was extrapolated to obtain the concentration of unreacted groups in GelMA. The DoF was calculated as 100–X %, considering that the reduction in absorbance was due to methacrylamide functionalization.

$$Degree\ of\ functionalization\ (DoF) = 1 - \left(\frac{GelMA}{Gelatin}\right) \times 100$$

2.5. Preparation of gelatin methacrylamide hydrogel

Gelatin methacrylamide hydrogels were prepared by crosslinking methacrylamide groups by photoinitiated chain polymerization. GelMA (10% w/v) solution was prepared in phosphate-buffered saline (PBS) or serum-free MEM containing 1% Irgacure as a photoinitiator at 60 °C until fully dissolved. A requisite amount of this solution was exposed to 365 nm UV light at an intensity of 8–12 mW/cm^2 to initiate crosslinking. The exposure time was varied from to 2–7 min depending on the thickness of the prepared gels. Photo-protective GelMA was prepared by adding various concentrations of FRS(X) (X representing 1, 1.5, and 2.25 or 3.4 mM) to 10% GelMA in serum-free medium containing 1% Irgacure. The range of FRS concentration was selected based on IC50 analysis as described in sections 1.1 and 2.1 of supplementary data. The GelMA-FRS(X) mixture was crosslinked with UV, as described above. The time taken to form the photoprotective hydrogel was noted.

2.6. *Selection of free radical scavenger concentration*

The effective concentration of FRS, expressing photoprotectivity to HepG2 cells, was evaluated by analyzing cell viability within GelMA and GelMA-FRS in a sandwich culture model. Cells were cultured in MEM supplemented with 10% FBS and 1% penicillin-streptomycin antibiotics in a CO_2 incubator (New Bronswich, USA) set at 37° °C with 5% CO_2 and >90% relative humidity. Cells were harvested by trypsinization and cultured in a sandwich model, as illustrated in Fig. 1. The sandwich method is similar to cell encapsulation, with the additional advantage of placing cells on a single plane that makes the cell-based assays and imaging for analysis efficiency. GelMA-FRS(X) systems with various concentrations of FRS, where X = 0, 1, 1.5, 2.2, or 3.4 mM) were prepared and added to 48 well plate (100 μL/well) and cross-linked with UV light. Approximately 1×10^5 HepG2 cells were seeded over the cross-linked GelMA-FRS hydrogel and incubated for 2h for cell adhesion. A second layer of 100 μl GelMA-FRS system was overlaid on cells and cross-linking was repeated to entrap cells in a sandwich fashion. Sufficient cell culture medium was added and cells were incubated for 24 h. Cells sandwiched in GelMA (FRS = 0 mM) were considered as the control.

2.6.1. *Cell viability*

Cell viability was analyzed at the end of 24h by live/dead staining. Cells sandwiched within GelMA-FRS(3.4) were incubated for 5 min in serum-free medium containing 0.01% FDA and 0.005% PI and observed under a fluorescence microscope (Leica DMI 6000, Switzerland).

2.6.2. *Cell proliferation*

The proliferation of the cells in the sandwich was estimated from the cell activity expressed in a standard curve plotted with known concentrations of cells. HepG2 cells at different cell densities (0.5×10^6, 1×10^6, 2×10^6, 2.5×10^6 cells/well) were seeded in triplicate into a 24 multi-well plate, incubated for 24h and CCK-8 assay was carried out according to the manufacturer's instructions. Briefly, the culture medium was removed and the cells were incubated with 500 μl CCK-8 reagent (1:10 dilution in serum-free MEM) for 2h. The medium was then transferred to a clear 96 multi-well plate and the absorbance was measured at 450 nm using a multi-well plate reader (BioTek, USA). Approximately 1×10^5 HepG2 cells were sandwiched in the GelMA-FRS (X) system. The cell suspension used for plotting the standard curve was used to estimate the cell number in the sandwich culture within GelMA and GelMA-FRS(X). The cells were cultured for 7 days and proliferation was analyzed on every alternate day (1, 3, 5, and 7 days) using the CCK-8 assay as described above. The number of cells at various concentrations of GelMA-FRS was calculated from the standard curve. The GelMA-FRS(X) system, which supported maximum cell viability and proliferation, was considered for further experiments.

2.6.3. *Photoprotective effect of gelatin methacrylamide -Free radical scavenger system*

Based on the cell proliferation data, GelMA-FRS(3.4) was selected for further evaluation of the photoprotective properties. The reactive oxygen species (ROS) generated within cells suspended in GelMA FRS during UV crosslinking was estimated. The GelMA and GelMA FRS solutions were prepared using HepG2 cells at a concentration of 5×10^5 cells/mL and were dispersed in PBS. The solution (200 μL) was transferred to multi-well plates and irradiated with UV light at 365 nm for 3 min to form a hydrogel. Cell monolayers adhered to similar multi-well plates formed from the same cell number were used as controls. Cells exposed to UV were considered as a positive control and the cell monolayer without UV treatment was treated as a negative control. Cells in controls and hydrogels were harvested by incubating with 200 μL of 0.3% collagenase – A in calcium containing HEPES buffer (100 mM HEPES buffer with 20 mM calcium chloride) for 20 min at 37 °C. The cells were transferred to a centrifuge tube and centrifuged (Eppendorf 5430R, India) at 1500 rpm for 2 min to pellet the cells. The supernatant was discarded, and the ROS activities of the cells were determined per product sheet (Lot# AB113851, Abcam). The cell suspension was transferred to a black-bottom-clear 96 well plate and 2′, 7′ – dichlorofluorescein diacetate formed due to ROS activity inside the cells was quantified by measuring the fluorescence at excitation/emission of 485 nm/535 nm in a spectrofluorimeter (Synergy H1, Biotek, USA). The relative fluorescence unit (RFU) obtained for the cells from GelMA, GelMA-FRS(3.4), and the positive control was compared with that of the negative control using the following equation:

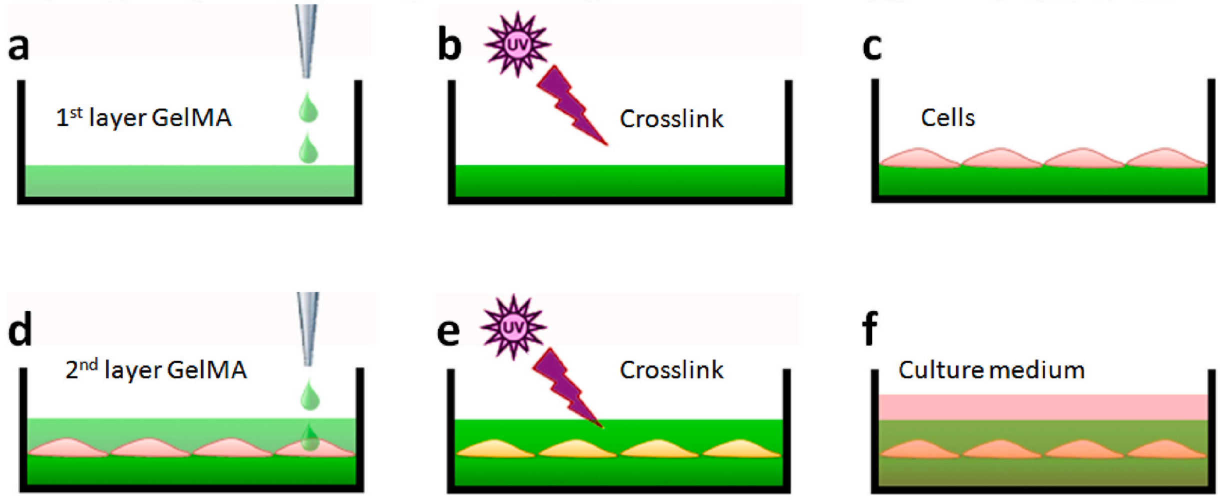

Fig. 1. Illustration showing the steps involved in sandwich culture model: (a) A thin layer of hydrogel was applied first on multiwell plate, (b) Crosslinking of first layer by UV irradiation, (c) Cells are evenly seeded on first layer of hydrogel and allowed to settle for 1 h, (d) A second layer of hydrogel was applied on the cells, (e) Crosslinking of the second layer with UV to entrap cells in sandwich form, (f) Add sufficient culture medium and maintain cells.

$$\text{ROS activity } (\%) = \frac{Test_{RFU}}{Negative_{RFU}} \times 100$$

2.6.4. Functional evaluation of HepG2 cells in sandwich culture

The effect of the photoprotective nature of GelMA-FRS(3.4) hydrogel in preserving liver-specific functions was determined by analyzing albumin and urea synthesis in HepG2 cells sandwiched within the hydrogel. The HepG2 cells were sandwiched in GelMA-FRS(X) systems and maintained for 7 days with medium changes on days 1, 3, 5, and 7. The spent medium was collected and stored at −80 °C until analysis.

Albumin synthesis by HepG2 cells was analyzed using an ELISA kit (Bethyl Laboratories, USA) according to the manufacturer's instructions. Serial dilutions of standards and the spent culture medium collected at various time points were added in duplicate to the first antibody (100 μL) coated 96 wells. After 1 h incubation at room temperature, wells were rinsed four times with wash buffer, and the second antibody (100 μl) was added. After 1 h incubation, the wells were rinsed again and sequentially treated with 100 μL of horse radish peroxidase solution and 3,3,5,5-tetramethylbenzidine (TMB) substrate for 30 min in the dark with a washing step in between. Color formation was observed, and the reaction was stopped by adding 100 μL 2 N H_2SO_4. Absorbance was measured at 450 nm using a multi-well plate spectrophotometer. The concentration of albumin synthesized by the cells was calculated from the standard curve and presented as the mean ± standard deviation.

The ammonia detoxification ability of HepG2 cells was analyzed by estimating urea in the spent medium using a urea assay kit (Biochain, USA). Fifty microliters of medium, urea standard, and control medium (blank) was added in triplicate to a 96 well plate. The working reagent (200 μL) was added to each well and incubated for 50 min. The color developed was quantified from the absorbance values at 450 nm, and the concentration of urea was calculated according to the manufacturer's instructions in product sheet.

2.7. Characterization of hydrogel

2.7.1. Scanning electron microscopy

Hydrogels were prepared from GelMA and GelMA-FRS(3.4) solutions and lyophilized to obtain discs with dimensions of Φ 8 mm × 2 mm. The discs were sputter-coated with gold and imaged using a scanning electron microscope (FEI Quanta 200, Hitachi) to observe the morphology.

2.7.2. Hydrogel porosity and pore size distribution

The porosity of hydrogel was determined using a micro-computed tomography (micro-CT) scanner (Scano Medical, Model# μCT 40, Switzerland). The GelMA and GelMA-FRS(3.4) hydrogel samples having dimensions (9 mm diameter and 10 mm height) was lyophilized and scanned using a cone-beam X-ray source having 5 μm spot size set at 70 kV and 160 μA. 3D reconstruction of the 2D images were done using the software μCT V6.1. Morphometric analysis was also carried out to determine pores size, percentage pore volume, polymer volume (PV) and total volume (TV). The pore size distribution was plotted using percentage pore volume against pore size. The percentage porosity of the hydrogel was calculated from the equation given below.

$$\text{Porosity } (\%) = \left(\frac{PV}{TV}\right) \times 100$$

2.7.3. Compressive modulus of hydrogel

The compressive modulus of hydrogel was determined by compression test using a universal testing machine (UTM) (Bioplus 3345, Instron, USA). Two different sets of cylindrical hydrogels (diameter = 9 mm, height = 10 mm) consisting of 10% GelMA and 10% GelMA-FRS (3.4) were cast in a cylindrical mold by UV-crosslinking. The compression test was performed at 25 °C using a 100 N load cell. The samples were compressed at a strain rate of 10 mm/min until a strain of 50% was achieved. The compressive modulus was calculated from the stress-strain curve.

2.8. Formulation of bioink and rheological analysis

The bioink formulation was established for 3D bioprinting of GelMA systems. An ideal polymer system used for 3D bioprinting should exhibit reversible physical gelling and shear-thinning properties. Bioink formulations were obtained using a mixture of GelMA, gelatin, glycerol, and Irgacure 2959 and FRS were obtained. The GelMA-FRS(3.4) formulation consisted of 10% GelMA, 3% gelatin, 10% glycerol, 1% Irgacure 2959 and 3.4 mM ascorbic acid and were subjected to rheological analysis on a Physica MCR 301 Rheometer (Anton Paar, Germany) using cone and plate geometry (1° cone plate, 0.4 mm measuring distance). Viscosity variation of the bioinks was measured with a variable shear rate (0.02–1000 per second) using a light source Omnicure 1000 (Lumen Dynamix LDGI) with a wavelength of 365 nm was routed through a 5 mm optical fiber to illuminate the sample through a quartz crystal stage. This formulation was compared with the basic GelMA-FRS (3.4) polymer solution (10% GelMA, 1% Irgacure 2959 and 3.4 mM ascorbic acid) under similar conditions.

2.9. Three-dimensional bioprinting of liver construct

Three-dimensional bioprinting was carried out on a 3D bioprinter (3D Discovery, RegenHU, Switzerland) using GelMA formulation (10% GelMA, 3% gelatin, 10% glycerol, and 1% Irgacure 2959) and GelMA-FRS(3.4) formulations. To prepare the bioinks, approximately 3×10^6 HepG2 cells were mixed with 1 mL of the respective GelMA systems, equilibrated at 20 °C, and loaded into the extrusion print head of the 3D bioprinter. A tapered plastic nozzle with a 410 μm orifice was also connected. A 3D model square grid pattern (final size of 10 × 10 × 5 mm) with straight lines and cross-overs was designed using BioCAD software (regenHU, Switzerland), and the construct was bioprinted at a printing speed of 10 mm/s at 20 °C into a non-cell-adherent culture plate. The bioprinted constructs were irradiated with 365 nm UV light for 90s. Sufficient culture medium was added to the bioprinted constructs and maintained in a CO_2 incubator at 37 °C for 7 days.

2.10. Functional evaluation of 3D bioprinted construct

The photoprotective nature of GelMA-FRS(3.4) formulation on liver-specific functions was determined by analyzing cell viability, albumin, and urea synthesis in comparison to the construct bioprinted using GelMA formulation.

2.10.1. Cell viability of 3D bioprinted liver construct

The proliferation of HepG2 cells in the 3D bioprinted constructs (fabricated using GelMA and GelMA-FRS (3.4) formulations) was compared. The bioprinted constructs were cultured for 24 h and cell proliferation was analyzed by CCK-8 assay on days 1, 3, 5, and 7. The culture medium was replaced with CCK-8 medium (1:10 dilution of CCK-8 reagent in serum-free MEM) and incubated for 2 h. The medium was then transferred to a 96 multi well plate and the absorbance was measured at 450 nm using a multi-well plate reader. The same constructs were further maintained to repeat the CCK-8 assay on the following days.

2.10.2. Functional evaluation of 3D bioprinted liver construct

The functional evaluation of the 3D bioprinted liver construct was confirmed from the amounts of albumin and urea secreted from the construct into the culture medium. Culture medium was collected at the end of 1, 3, 5, and 7 days and stored at −80 °C until used for estimation. The albumin and urea secreted from the 3D bioprinted construct were quantified using the Human Albumin ELISA Kit and Urea Assay Kit, respectively, as described previously.

2.11. Statistical analysis

All experiments were performed in triplicates (n = 3). The results are presented as mean ± standard deviation, and significance was calculated by Student's t-test. Statistical significance was set at 'p' ≤ 0.05.

3. Results and discussion

3.1. Synthesis and characterization of gelatin methacrylamide hydrogel

Gelatin methacrylamide is a biomaterial that is widely used in extrusion bioprinting. Owing to its excellent flow characteristics, biocompatibility, and tunable biodegradability, GelMA has been used for the fabrication of cardiac, skeletal, neuronal, bone, cartilage, and skin tissues [21–27]. We synthesized GelMA from Gelatin Type A based on the method reported by Lee et al., which exclusively converts gelatin to gelatin methacrylamide upon reaction in carbonate – bicarbonate buffer at pH 10.5 [19]. Type A gelatin was selected due to its higher storage modulus over other grades of Gelatin at similar concentration. The carbonate – bicarbonate buffer used in the synthesis ensured that the pH was above the isoelectric point of Type A gelatin aided in neutral free amino group of lysine. The neutrally charged amino groups effectively reacted with MAA, thereby providing a higher degree of functionalization. The presence of two peaks at 5.5 and 5.7 ppm in the ^{1}HNMR spectra confirmed the presence of methacrylamide moieties onto gelatin (Fig. 2). The formation of vinylic protons of the methacrylamide moiety confirmed that gelatin was successfully functionalized with gelatin methacrylamide [28]. These acrylamide bonds participate in the photopolymerization of GelMA for hydrogel formation.

The functionalization of gelatin was determined by estimating the unmodified free amino groups in GelMA using a previously reported protocol [20]. A standard curve of gelatin was generated, and the percentage of free amino groups was extrapolated from it (Fig. 3a). The degree of functionalization was calculated from three different batches of GelMA and was found to be approximately 90 ± 4% (Fig. 3b).

Morphological analysis of lyophilized GelMA and GelMA-FRS(3.4) was investigated by SEM. All the samples displayed porosity. The pore architecture, however, varied with the addition of FRS and post-crosslinking (Fig. 4). SEM images also indicated that the porosity of GelMA was uniform in size and shape compared to the crosslinked GelMA and GelMA-FRS(3.4) counterparts (Fig. 4a). Furthermore, scaffolds fabricated from GelMA hydrogels were circular in shape. Scaffolds from crosslinked GelMA and GelMA-FRS(3.4) on the other hand, were elliptical in shape. Nevertheless, the scaffolds were sufficiently porous to accommodate the cells and enable the proper transfer of nutrients and wastes across the scaffold.

The lyophilized GelMA and GelMA-FRS(3.4) hydrogels exhibited porosity of 74.1% and 74.8%, respectively. Fig. 5a shows lyophilized hydrogels used for μCT analysis. The maximum pore volume of the hydrogels was occupied by pores in the size range of 50–200 μm (Fig. 5b). A similar trend in pore size distribution was observed in both the hydrogel samples.

The compressive moduli of GelMA and GelMA-FRS(3.4) is shown in Fig. 6. The compressive modulus of GelMA and GelMA-FRS(3.4) was 1.37 ± 0.24 kPa and 0.29 ± 0.03 kPa. The addition of FRS lead to 78% reduction in the modulus values of the gel. Nevertheless, both the hydrogels were self-standing and exhibited sufficient handling stability. Hydrogels with lower modulus are known to support better cell viability, adhesion and proliferation [29].

3.2. Selection of free radical scavenger concentration

GelMA is a well-studied bioink material for 3D bioprinting with the capacity to form hydrogels when subjected to photo-initiated (mostly through UV irradiation) polymerization. When bioprinted GelMA constructs are irradiated with UV, a large number of free radicals are generated, initiating chain growth polymerization and subsequent cross-linking of GelMA. In the presence of a free-radical scavenger, the extra free radicals generated are scavenged, which might take a toll on the cross-linking of GelMA. Hence, it is imperative to strike a balance between cross-linking efficiency and free radical scavenger concentrations. Furthermore, most photocurable bioinks are based on crosslinking hydrogels with UVA (320–400 nm) and UVB (280–320 nm) radiation. Both A and B versions of UV radiation elicit a physiological effect through the formation of reactive oxygen species inside the cells [30]. In particular, UVA activates endogenous photosensitizers, resulting in the formation of ROS [31]. Moreover, UV exposure impairs the antioxidant

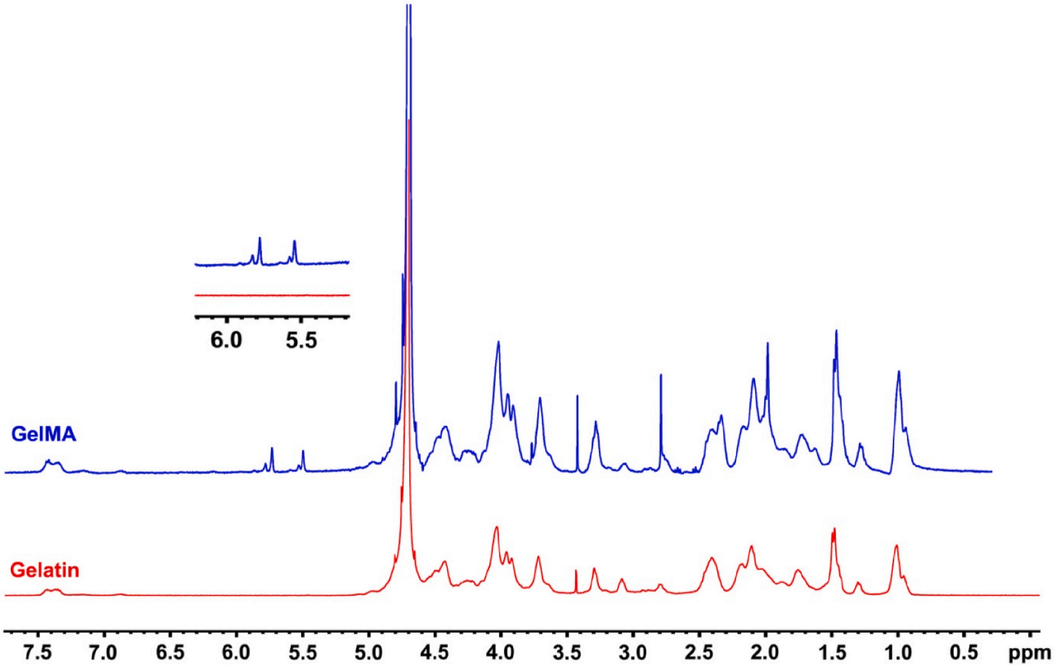

Fig. 2. ^{1}HNMR spectra of Gelatin and GelMA. The peaks (5.5 and 5.7 ppm) corresponding to grafted methacrylamide moieties have been zoomed in.

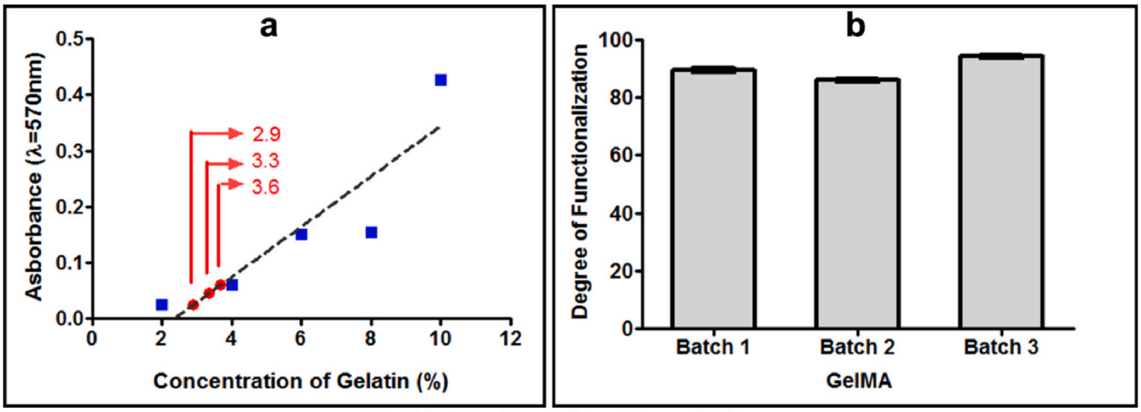

Fig. 3. Ninhydrin a) Free amino groups in GelMA extrapolated from free amino groups of gelatin; b) DoF calculated for three different batches of GelMA showing modification efficiency of 89 ± 0.6, 86 ± 0.5 and 94 ± 0.5%.

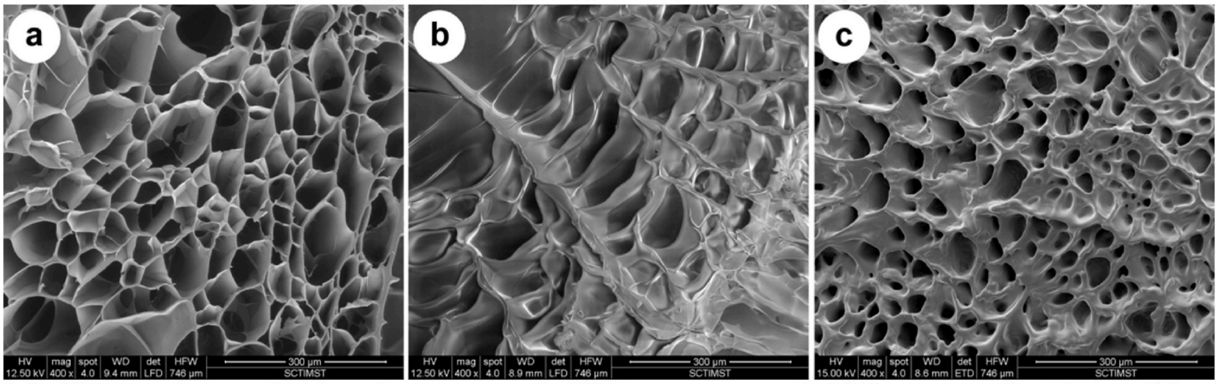

Fig. 4. SEM images showing porosity of GelMA. (a) GelMA before crosslinking, (b) GelMA-FRS(3.4) before crosslinking and (c) GelMA-FRS(3.4) after crosslinking.

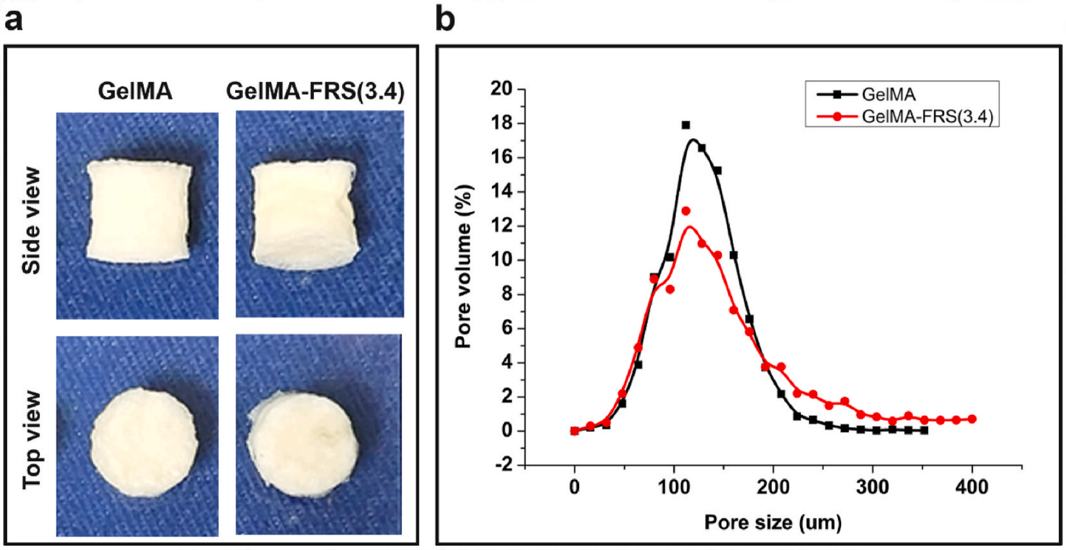

Fig. 5. Pore size analysis: (a) Images of the lyophilized GelMA and GelMA-FRS(3.4) hydrogels. (b) Pore size distribution graph plotted using µCT derived data.

defense mechanisms of the cells. To circumvent the harmful effects of UV, cells are treated with ascorbic acid when exposed to UVA to prevent ROS, GSH, and lipid peroxidation levels [32]. Hence, ascorbic acid was introduced into GelMA as a free radical scavenging system (FRS) to protect cells from free radicals formed during the UV cross-linking of GelMA. This concept of photoprotective effect was studied using a sandwich culture system, as illustrated in Fig. 1. The effect of ascorbic acid on FRS was monitored by evaluating cell viability, cell proliferation, cell activity, and ROS activity.

3.2.1. Cell viability

Fig. 7 shows the results of the viability assay carried out on HepG2 cells entrapped in GelMA-FRS by sandwich culture with various concentrations of FRS. It is clear from the figure that the number of viable

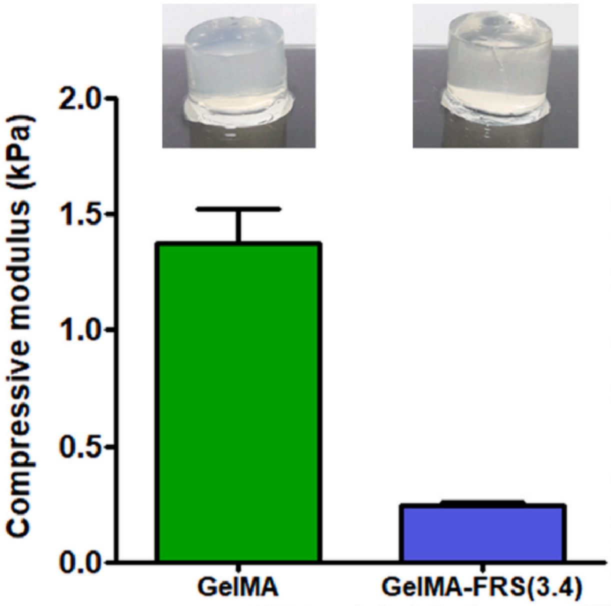

Fig. 6. Compressive modulus of GelMA and GelMA-FRS(3.4) system.

HepG2 cells in the GelMA-FRS sandwich increased with increasing FRS concentration (Fig. 7). The increase in viable cell numbers with increasing FRS concentration is encouraging, as it is a direct testimony of the photoprotective effect of FRS. The photo-protective effect of FRS observed in the cells, however, did not affect the physical cross-linking efficiency of GelMA. Furthermore, GelMA sandwich model the layers adhered to each other without any sign of delamination.

Cell viability assessed by live-dead staining showed an increase in viable cells with increasing concentration of FRS, displaying maximum viability at 3.4 mM. This observation is in line with the report of Tokuda et al., where ascorbic acid had an effect on UV-exposed retina [33]. They found a significant reduction in lactate dehydrogenase release in the presence of ascorbic acid between 1 mM and 3 mM, which confirmed the photoprotective effect.

3.2.2. *Cell proliferation*

The proliferation of HepG2 cells sandwiched between GelMA and GelMA-FRS(X) was quantified using the CCK-8 assay. Cells embedded in GelMA-FRS(1), GelMA-FRS(1.5), and GelMA-FRS(2.2) did not show any increase in proliferation over a period of 7 days (Fig. 8). However, the HepG2 cells sandwiched in GelMA-FRS(3.4), where 3.4 mM of FRS was employed, showed a linear increase in cell number with time. Thus, it was concluded that the minimum concentration of FRS required in the bioink for photoprotective effect is 3.4 mM, without compromising the crosslinking efficiency.

3.2.3. *Cell activity*

The effect of FRS on the functional ability of hepatocytes, such as albumin and urea synthesis, in the GelMA-FRS hydrogel was also evaluated over a period of 7 days. The variations in albumin and urea synthesis at various concentrations of FRS at different time points are shown in Fig. 9. The albumin secretion by cells embedded in GelMA was 60 ± 2 ng/ml (Day 1) and increased linearly to 86 ± 4 ng/ml at the end of 7 days (Fig. 9a). A similar increase in albumin secretion was observed in the cells sandwiched in GelMA with 1, 1.5 mM and 2.2 mM FRS concentrations up to day 5. The albumin secretion in cells sandwiched in GelMA with 2.2 mM FRS was 111 ± 7 ng/ml on day 7. The cells embedded in the gel with FRS 3.4 mM showed albumin synthesis of 94 ± 4, 100 ± 5, 131 ± 16, and 172 ± 11 ng/ml on days 1, 3, 5, and 7, respectively. This was very similar to albumin synthesis by the control cells on days 1, 3, and 5. However, the albumin synthesis of control cells on 7th day was 212 ± 18 ng/ml, which was significantly higher than that of the cells in GelMA/FRS 3.4 mM.

The detoxification ability of hepatocytes sandwiched within GelMA and GelMA-FRS hydrogels was analyzed by urea synthesis (Fig. 9b). The average urea synthesis of cells embedded in GelMA with 0, 1, 1.5 mM and 2.2 mM FRS was similar and did not show any significant variation. However, the cells embedded in GelMA with 3.4 mM FRS showed a significant increase in urea synthesis and had values comparable to those of the control cells. This clearly indicates that when GelMA was loaded with 3.4 mM FRS, the functional ability of hepatocytes was improved and was comparable to that of control cells even after entrapping in GelMA and UV crosslinking.

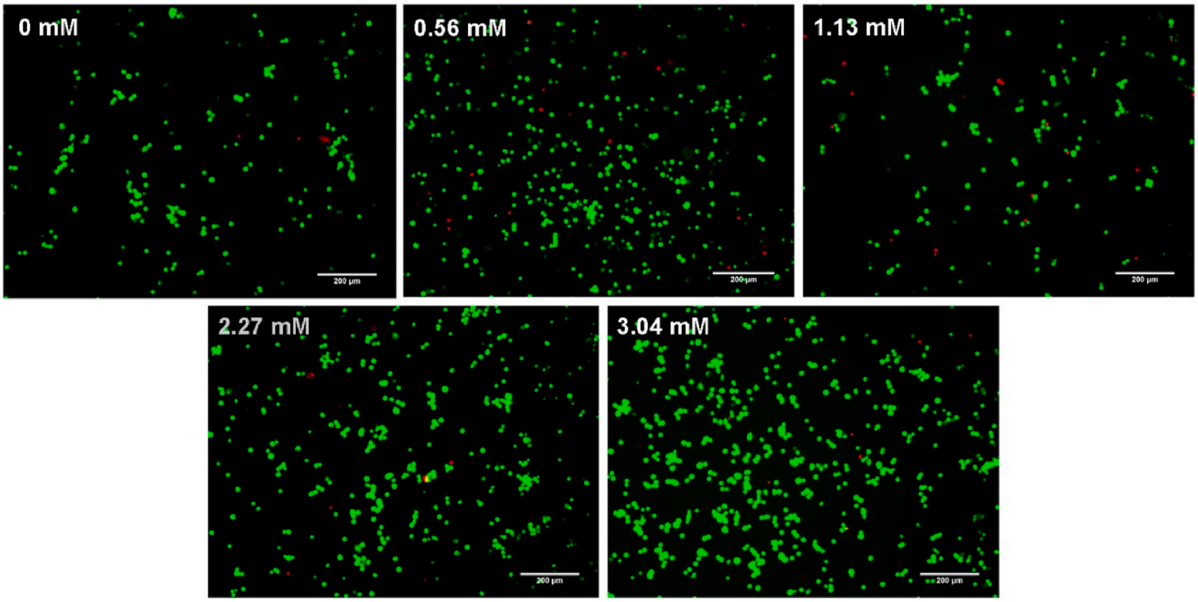

Fig. 7. Viability of HepG2 cells in GelMA with various concentrations of FRS, analyzed by sandwich culture method. Values shown in the figure shows the concentration of FRS present in the base 10% GelMA. The number of viable cells (green) increases with increase in concentration of FRS. (For interpretation of the references to color in this figure legend, the reader is referred to the Web version of this article.)

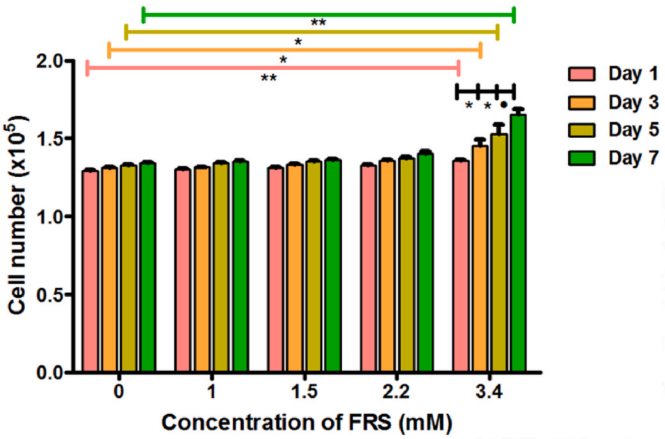

Fig. 8. Cell proliferation analyzed by CCK-8 assay. GelMA alone (0 mM) and FRS at concentrations 1 mM, 1.5 mM, 2.2 mM and 3.4 mM showed a steady increase in cell number. The values are normalized to cell number of cells in 2D monolayer of the respective days.
• = ($P > 0.05$), * = ($P \leq 0.05$), ** = ($P \leq 0.01$).

3.2.4. Radical oxygen species activity

The intracellular ROS activity of HepG2 cells embedded in the GelMA/FRS system (following UV irradiation) was compared with that of the bare GelMA hydrogel (following UV irradiation), cell monolayer exposed to UV (positive control), and cell monolayer unexposed to UV (negative control) (Fig. 10). It can be seen that while ROS activity of cells embedded in GelMA/FRS system was comparable to that of negative control, the ROS activity associated with cells embedded in GelMA was closer to positive control. The ROS values associated with the negative control (cells that were not exposed to UV) represent the normal amount of ROS produced inside the cells. It was encouraging to see that cells embedded in GelMA/FRS (77 ± 42%) showed values closer to this. On the other hand, the cells embedded in bare GelMA showed ROS activity of 212 ± 30%, which was closer to that of the positive control (200 ± 28%). It is hence clear from these values that the GelMA/FRS system induced protection against the radicals generated during photopolymerization. This is an interesting finding and is particularly relevant when clinically relevant/larger structures are bioprinted and stabilized using photocrosslinking.

The wavelength of light used for crosslinking was selected based on the polymeric system or the photoinitiator added to the formulation. Ultraviolet radiation is classified as UVA (320–400 nm), UVB (290–320 nm), and UVC (200–290 nm), of which UVB and UVC are fatal. One of the efficient ways to minimize UV-induced damage is by reducing the duration of UV exposure. The wavelengths widely proposed to be safe in 3D bioprinitng with respect to cell viability is 365 nm (Irgacure 2959) and 405 nm (LAP or Vis + Ru/SPS) [34,35]. In order to bioprint the clinically relevant size, the duration of crosslinking may be increased. Prolonged exposure of cells to UV causes lesions in genetic content indirectly through the generation of ROS or directly by damaging membrane lipids [36,37]. This limitation can be overcome by nullifying the UV radiation-induced damage using photo-protective methods. Photo-protection generally refers to a biochemical mechanism that helps living systems to prevent/control damage caused by light of harmful wavelengths. Cells neutralize the ROS formed during UV exposure, and any disturbance in ROS production and neutralization will create oxidative stress. Humans and other animals have also developed photoprotective mechanisms to prevent UV photo-damage to the skin, prevent DNA damage, and minimize the downstream effects of oxidative stress [38]. Irgacure 2959 has been shown to be the most suitable UV PI with different sensitivities to different cell types at the same concentration [12,39]. The concentration of PI must be accurately optimized to achieve low cytotoxicity and better crosslinking. It is known that an increase in the concentration of PI results in an increase in cell death due to the free radicals formed during UV irradiation. Irgacure 2959 dissociates into free radicals and initiates the polymerization of functionalized GelMA. The free radical effect of PIs on cells can be counteracted by antioxidants, such as ascorbic acid [40]. Their study used poly (N-isopropylacrylamide) nanoparticles and poly(ethylene glycol) diacrylate crosslinked in the presence of Irgacure 2959 and ascorbic acid,

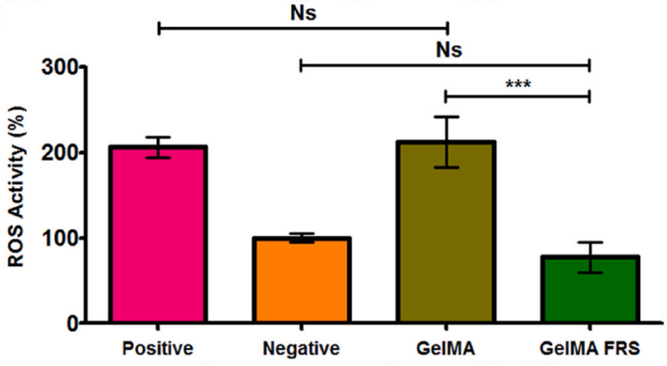

Fig. 10. The comparison of intracellular ROS activity of HepG2 cells due to phtocrosslinking of GelMA and GelMA-FRS bioink to normal cells (Negative) and UV exposed (Positive) cells. [Ns = Non significant, *** = $p \leq 0.0001$].

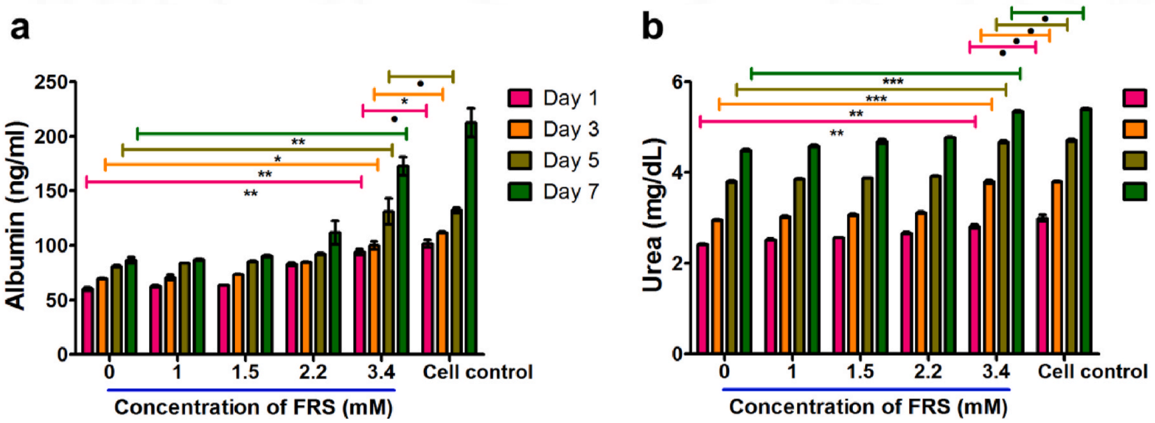

Fig. 9. Functionality assessment of HepG2 cells sandwiched in GelMA and GelMA FRS hydrogels. (a) Albumin secretion by cells sandwiched in GelMA and various concentration of FRS containing GelMA showing 3.4 mM FRS as a formulation that is similar to normal culture system. (b) Urea synthesis indicating the detoxification function did not show any dose related response. GelMA with and without FRS express same urea secretion. • = ($P > 0.05$), * = ($P \leq 0.05$), ** = ($P \leq 0.05$), *** = ($P \leq 0.005$).

which showed increased cell viability in the presence of antioxidants. The effect of ROS due to the photoinitiator can be best described by measuring intracellular ROS. To the best of our knowledge, this is the first report to explain the intracellular ROS activity of GelMA-based bioink. The aforementioned analysis aided in the effect of FRS concentration on cell viability and liver-specific functions of hepatocytes sandwiched in GelMA. GelMA-FRS(3.4) showed better viability and cell proliferation than GelMA and other GelMA/FRS formulations used in the present study. Hence GelMA/FRS with 3.4 mM FRS, hereafter referred to as GelMA/FRS (3.4), was used in the bioink formulation for all further studies. It has been reported that FRS at concentrations of 4 mM and 10 mM is not cytotoxic and exhibited hepatoprotective effect in cultured rat hepatocytes [41,42].

3.3. Formulation of bioink and rheological analysis

The base material in the bioink formulation was 10% GelMA in serum-free culture medium. To enhance printability, 3% gelatin and 10% glycerol were added as reported by Kang et al. [43]. While gelatin imparts thermosetting properties for the bioink, which enables one to carry out printing at temperatures ranging from 18 to 21 °C, glycerol functions as a plasticizer and helps to reduce the friction of the bioink at the nozzle and aids the bioink to drop on the printing platform with ease. Both gelatin and glycerol were gradually washed out during the post-printing culture [44].

Systematic analyses of the rheological properties were carried out to understand the gelation kinetics of the bioink solutions. The effects of time, temperature, shear stress, and shear rate on the gelation process of GelMA solutions were evaluated. The gelation temperature of the polymer solutions was assessed by cooling the GelMA solutions from 37 °C to 2 °C at a cooling rate of 5 °C/min (Fig. 11). It was noticed that as the temperature decreased, the viscosity increased gradually for both GelMA-FRS(3.4) and GelMA-FRS(3.4) formulations. At the gelation temperature (20–30 °C), there was a rapid increase in viscosity. The viscosity values showed nearly a 100 fold increase from 0.0156 Pa s (24 °C) to 9.991 Pa s (17 °C) for GelMA-FRS(3.4), and 0.00283 (24 °C) and 4.0155 (15 °C) for the GelMA-FRS(3.4) solution, after which the curve plateaued, demonstrating the stability of the gels formed. The precise gelling temperature of the GelMA solutions was determined from the derivative of the cooling curves. While GelMA-FRS(3.4) solutions gelled at 18.6 °C, the gelling temperature of GelMA-FRS(3.4) formulation was 20.5 °C. This is expected because of the presence of native gelatin in the GelMA-FRS(3.4) formulation that aids not only in increasing the viscosity but also in improving the thermo-responsive property of the bioink.

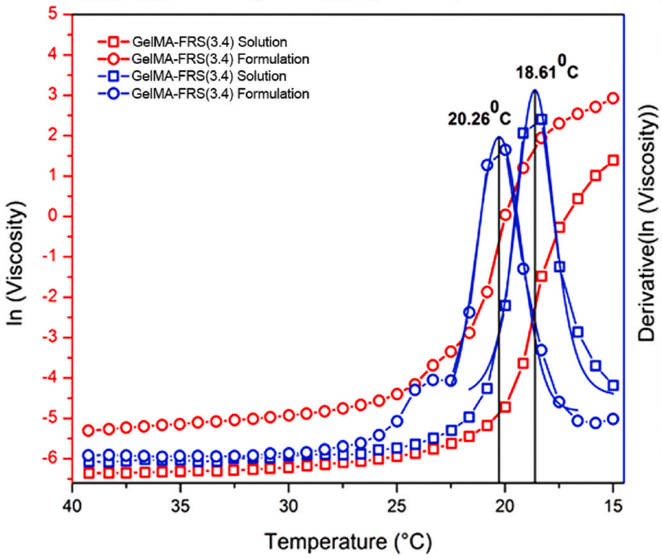

Fig. 11. Dependence of viscosity on temperature of GelMA-FRS(3.4) solution and GelMA-FRS(3.4) formulation.

In rheology, shear-thinning refers to the non-Newtonian behavior of fluids, where viscosity decreases under shear [45]. This property is particularly relevant to bioinks, as it determines continuous extrudability, high shape fidelity, and mechanical resilience [46]. Shear thinning of bioinks prevents clogging at nozzles during the printing process and aids in the reduction of shear stress that can lead to cell damage [47]. Furthermore, to attain constructs with a better resolution and higher aspect ratio, the printed scaffold should be mechanically sturdy and should not collapse on its own weight. Instant gelation after deposition or partially pre-gelled hydrogels is also preferred to ensure high structural integrity [48].

The shear thinning behavior of the polymer solutions is evident from the viscosity variations exhibited at different shear rates (Fig. 12). Both GelMA-FRS(3.4) and GelMA-FRS(3.4) formulations exhibited a decrease in viscosity with increasing shear rates, with GelMA-FRS(3.4) formulation showing a higher tendency of shear thinning. At a given shear rate, the GelMA-FRS(3.4) formulation displayed a higher viscosity than the GelMA-FRS(3.4) solution.

The gelation characteristics of the GelMA-FRS(3.4) bioink solution and formulation were also investigated in the presence of UV radiation. Fig. 13 shows the variation in the complex viscosity and storage modulus of the bioink with time during the crosslinking process. It is clear from the figure that both the viscosity and storage modulus increase with time. The increase was drastic at the beginning, indicating that the polymer solution underwent cross-linking. As the cross-linking moieties were consumed, the viscosity did not increase. A similar trend was shown by the storage modulus data, where the modulus increased and reached a plateau. With time, the elastic modulus finally dominates, and the solutions become more elastic than viscous. This also indicates that the gel retains sufficient elastic recoil, which is important for maintaining the shape of the gel after extrusion to avoid variations in product size.

3.4. Three-dimensional bioprinting of liver construct

Three-dimensional bioprinting of complex tissues, such as the liver, has been an interesting field since the time when this technology started popular. The main requirement for 3D bioprinting of the liver construct is the maintenance of hepatocyte-specific functions. Various bioinks have been proposed for bioprinting the liver, such as collagen-chitosan, alginate, and decellularized extracellular matrix [49–51]. Here, we report gelatin methacrylamide as the bulk polymer of the bioink with a photoprotective FRS additive to improve and maintain viability, proliferation, and liver-specific functions. The gelatin used for this study provided a better resolution and shape fidelity at room temperature and during 3D bioprinting. The gist of tissue engineering of the liver construct is the functional capability of metabolic activity. The design used for bioprinting is suitable for efficient mass transfer. The grid pattern enabled the diffusion of metabolites effectively, which could be measured in a static culture medium. The bioprinted construct did not show any swelling property, which is a unique characteristic expected in design-based biofabrication.

The bioink formulation was selected based on the outcome of the printed construct using the CAD design. The bioink was extruded with very smooth filaments with a width of 410 µm. The final printed construct was exactly the same size as the input design and was structurally stable before and after UV curing (Fig. 14).

3.5. Functional evaluation of 3D bioprinted construct

The metabolic activity of HepG2 cells in constructs 3D bioprinted with GelMA and GelMA-FRS(3.4) formulation was evaluated at two time points (day 1 and day 7) using the CCK-8 assay. The metabolic activity of

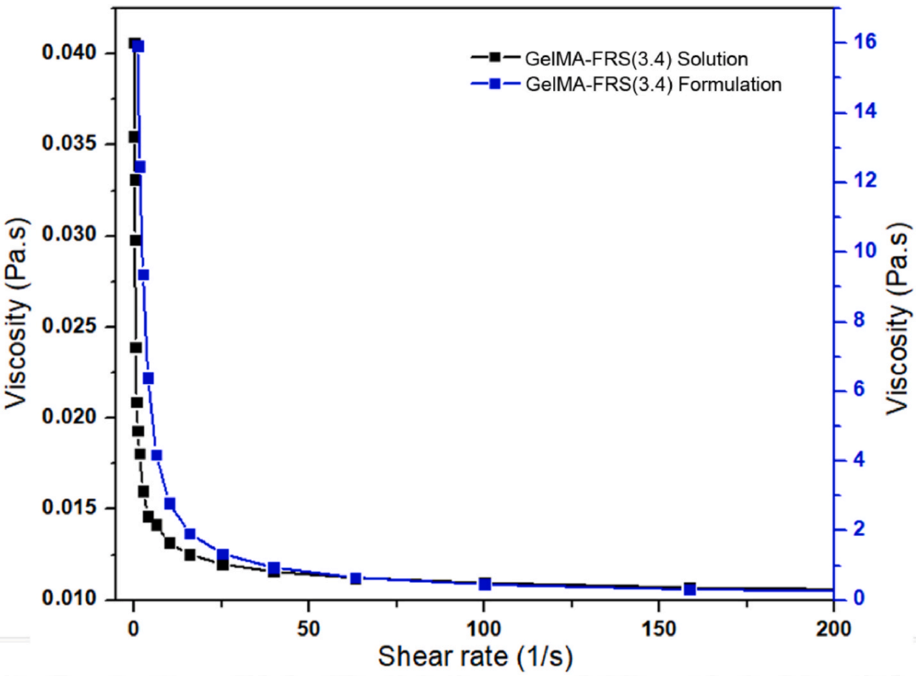

Fig. 12. Dependence of viscosity on shear rate of GelMA-FRS(3.4) solution and GelMA-FRS(3.4) formulation.

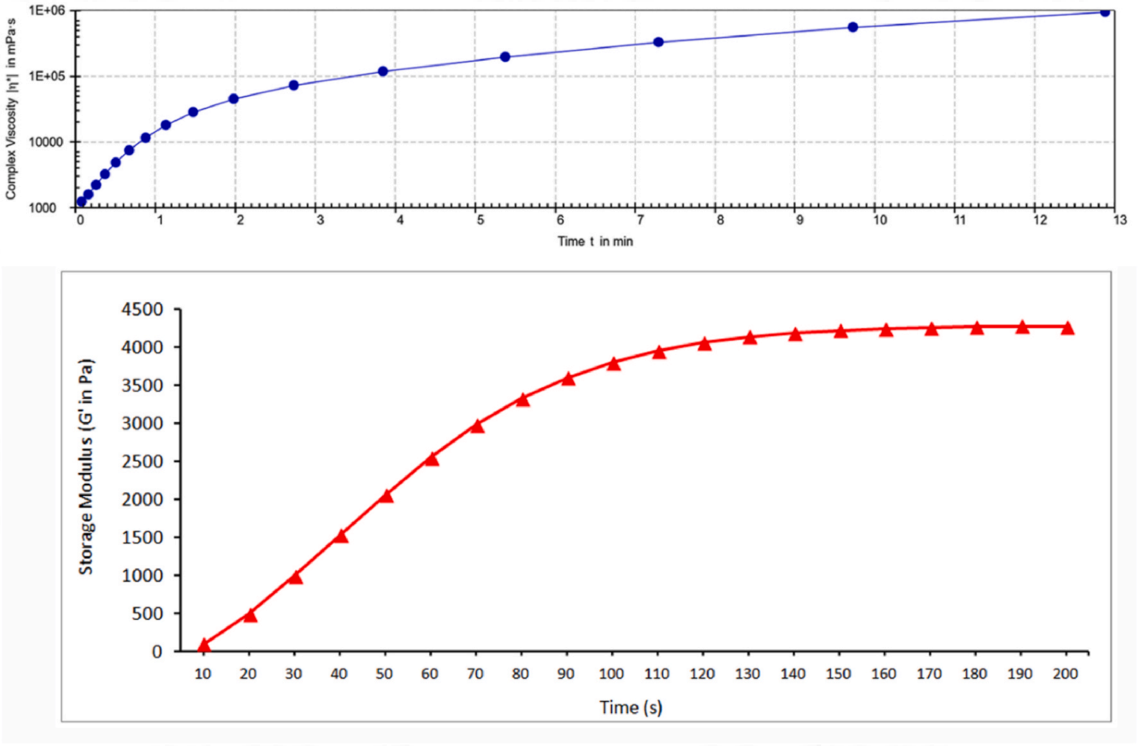

Fig. 13. Variation of complex viscosity and storage modulus of GelMA-FRS(3.4) formulation with time.

HepG2 cells in GelMA-FRS(3.4) bioink was considerably higher than that of HepG2 cells in GelMA (Fig. 15). At the end of 7 days, cell activity in the 3.4 mM FRS bioink formulation was significantly higher than that printed using GelMA alone. This clearly shows that the presence of FRS in the bioink maintained and improved the cell activity after cross-linking with UV.

The liver-specific functions expressed by the 3D bioprinted constructs showed that cells printed in FRS containing GelMA were more functionally capable than those printed using GelMA alone (Fig. 16). Albumin synthesis in the construct bioprinted with GelMA FRS was more than that in constructs printed in GelMA bioink alone (Fig. 16). The protein synthesis on day 1 in GelMA-FRS(3.4) was 50 ± 2 ng/ml and increased up to 128 ± 3 ng/ml on 7th day in a linear fashion. A similar trend of increase was observed in the construct printed using GelMA bioink, but a lower albumin synthesis of 32 ± 3 ng/ml and increased up to 91 ± 8 ng/ml on 7th day. The percentage increase in albumin

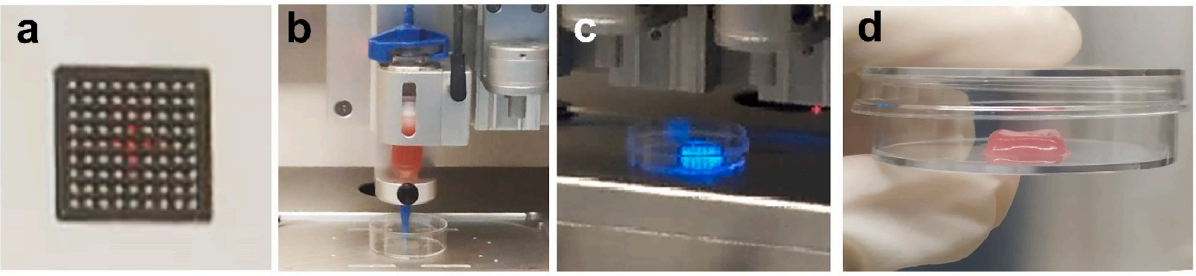

Fig. 14. 3D bioprinting of liver construct using GelMA-FRS(3.4) bioink. (a) The CAD design showing the dimensions of the construct. (b) Customized 3D Bioprinter for extrusion of hydrogels, (c) Image showing 3D bioprinting in action, (d) Bioprinted liver construct.

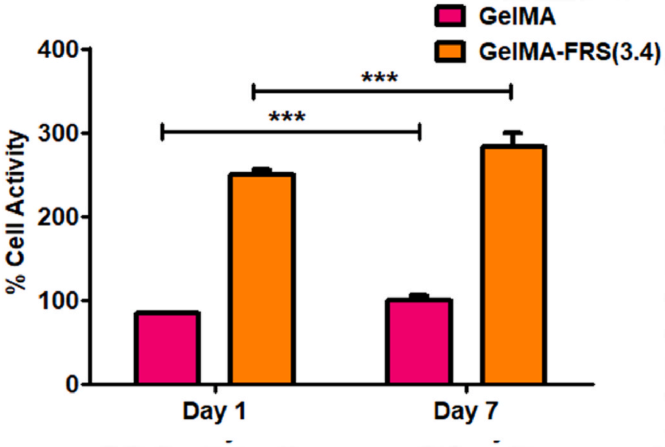

Fig. 15. Cell proliferation of HepG2 cells assessed by CCK-8 assay in 3D bioprinted in GelMA and GelMA-FRS(3.4) bioink formulations. The values are normalized to cell activity of construct in GelMA bioink. [*** = $p \leq 0.001$.].

synthesis relative to day 1 in the GelMA-FRS(3.4) construct was 27 ± 17%, 86 ± 18%, and 154 ± 5% on days 3, 5, and 7, respectively. On the other hand, the percentage increase in albumin synthesis by cells in GelMA on days 3, 5, and 7 was 22 ± 6%, 98 ± 5%, and 185 ± 24%, respectively. On the other hand, the urea showed 12 ± 2, 30 ± 5, 40 ± 0, and 33 ± 3% increase in GelMA-FRS(3.4) compared to GelMA bioink.

Cell proliferation in GelMA-FRS(3.4) bioink was significantly higher than that in GelMA. The functional capability of the construct as a biofabricated liver was evidenced by albumin and urea synthesis. The addition of FRS into GelMA clearly maintained or improved cell viability and functionality. The construct with functional hepatocytes is also a promising candidate for *in vitro* hepatotoxicity testing of drugs and small molecules. It is also useful to model disease-specific tissues for drug testing. Even though crosslinked with UV, the peculiar property of the bioink in maintaining intracellular activity increases its potential for use in cancer research and preclinical evaluation of drugs.

4. Conclusions

This study reports for the first time the use of a photoprotective GelMA-based bioink for 3D bioprinting of liver constructs. The results showed that radical scavenging during photocrosslinking improved the viability and functionality of the bioprinted constructs. The liver construct biofabricated using the photoprotective GelMA-FRS(3.4) bioink could be a simple and effective approach to enhance liver-specific functions in bioengineered liver tissues. The hepatocytes encapsulated within the novel formulation of bioink by UV irradiation clearly demonstrated the effective nullification of intracellular ROS and maintained liver-specific functions. The cells in the 3D bioprinted construct expressed more than 150 times the activity and improved cell functionality compared to normal GelMA. Our future studies are expected to address the physiological capabilities and structural organization of 3D liver tissues bioprinted with heterogeneous primary cells. We expect that this bioink formulation, when evaluated further based on regulatory standards, will be a realistic approach to develop transplantable liver constructs to overcome the problems of organ shortage in the future.

Conflict of interest

None.

CRediT authorship contribution statement

Roopesh R. Pai: Writing – original draft, Acquisition of data, Formal analysis, Writing – original draft, Critical revision for important intellectual content. **Shilpa Ajit:** Acquisition of data, Formal analysis, Writing – original draft. **Anupama Sekar J:** Acquisition of data, Formal analysis, Writing – original draft. **Sarath S. Nair:** Writing – original

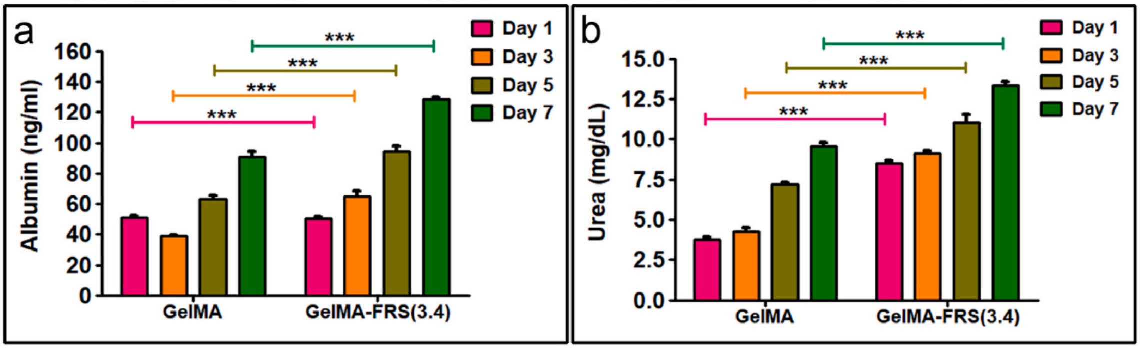

Fig. 16. Liver specific function exhibited by the Liver construct 3D bioprinted in GelMA-FRS (3.4 mM) compared with GelMA (0 mM). (a) Albumin synthesis and (b) Urea synthesis was more in GelMA-FRS(3.4) than hepatocyte printed in GelMA. [*** = $p \leq 0.001$.].

draft. **Anil Kumar P.R.:** Writing – original draft, Acquisition of data, Formal analysis, Writing – original draft, Critical revision for important intellectual content, Methodology, Final approval of the version to be published. **Shiny Velayudhan:** Writing – original draft, Acquisition of data, Formal analysis, Writing – original draft, Critical revision for important intellectual content, Resources, Final approval of the version to be published.

Declaration of competing interest

The authors declare that they have no known competing financial interests or personal relationships that could have appeared to influence the work reported in this paper.

Acknowledgments

Dr Anil Kumar PR acknowledges the financial assistance (Grant No: TRC/8141/PSN) from the Technical Research Center for Biomedical Devices, SCTIMST. Mr. Roopesh R. Pai is thankful to SCTIMST for the Institute PhD Fellowship. Authors acknowledge their Institute's support from Dr. Asha Kishore, Dr. TV Kumary, Dr. Harikrishna Varma PR, Mr. Muraleedharan CV, Dr. Roy Joseph and Dr. Kalliyana Krishnan V for carrying out this study. Dr. Anil Kumar PR is thankful to Dr. Anthony Atala, Dr. James J Yoo and Dr. Sang Jin Lee, Wake Forest Institute for Regenerative Medicine, USA for the basic training in 3D Bioprinting within the SCTIMST-WFIRM MoU. The technical help from Dr. Deepu DR and Ms. Priyanka is also thankfully acknowledged.

Appendix A. Supplementary data

Supplementary data to this article can be found online at https://doi.org/10.1016/j.bprint.2022.e00214.

References

[1] S.V. Murphy, A. Atala, 3D bioprinting of tissues and organs, Nat. Biotechnol. 32 (2014) 773–785, https://doi.org/10.1038/nbt.2958.

[2] C.M. O'Brien, B. Holmes, S. Faucett, L.G. Zhang, Three-dimensional printing of nanomaterial scaffolds for complex tissue regeneration, Tissue Eng. B Rev. 21 (2015) 103–114, https://doi.org/10.1089/ten.teb.2014.0168.

[3] J. Groll, J.A. Burdick, D.W. Cho, B. Derby, M. Gelinsky, S.C. Heilshorn, T. Jüngst, J. Malda, V.A. Mironov, K. Nakayama, et al., A definition of bioinks and their distinction from biomaterial inks, Biofabrication 11 (2018), 013001, https://doi.org/10.1088/1758-5090/aaec52.

[4] P.S. Gungor-Ozkerim, I. Inci, Y.S. Zhang, A. Khademhosseini, M.R. Dokmeci, Bioinks for 3D bioprinting: an overview, Biomater. Sci. 6 (2018) 915–946, https://doi.org/10.1039/c7bm00765e.

[5] B.J. Klotz, D. Gawlitta, A. Rosenberg, J. Malda, F.P.W. Melchels, Gelatin-methacryloyl hydrogels: towards biofabrication-based tissue repair, Trends Biotechnol. 34 (2016) 394–407, https://doi.org/10.1016/j.tibtech.2016.01.002.

[6] K.T. Nguyen, J.L. West, Photopolymerizable hydrogels for tissue engineering applications, Biomaterials 23 (2002) 4307–4314, https://doi.org/10.1016/S0142-9612(02)00175-8.

[7] J.P. Fisher, D. Dean, P.S. Engel, A.G. Mikos, Photoinitiated polymerization of biomaterials, Annu. Rev. Mater. Res. 31 (2001) 171–181, https://doi.org/10.1146/annurev.matsci.31.1.171.

[8] H. Aubin, J.W. Nichol, C.B. Hutson, H. Bae, A.L. Sieminski, D.M. Cropek, P. Akhyari, A. Khademhosseini, Directed 3D cell alignment and elongation in microengineered hydrogels, Biomaterials 31 (2010) 6941–6951, https://doi.org/10.1016/j.biomaterials.2010.05.056.

[9] T. Billiet, E. Gevaert, T. De Schryver, M. Cornelissen, P. Dubruel, The 3D printing of gelatin methacrylamide cell-laden tissue-engineered constructs with high cell viability, Biomaterials 35 (2014) 49–62, https://doi.org/10.1016/j.biomaterials.2013.09.078.

[10] B.D. Fairbanks, M.P. Schwartz, C.N. Bowman, K.S. Anseth, Photoinitiated polymerization of PEG-diacrylate with lithium phenyl-2,4,6-trimethylbenzoylphosphinate: polymerization rate and cytocompatibility, Biomaterials 30 (2009) 6702–6707, https://doi.org/10.1016/J.BIOMATERIALS.2009.08.055.

[11] Z. Wang, R. Abdulla, B. Parker, R. Samanipour, S. Ghosh, K. Kim, A simple and high-resolution stereolithography-based 3D bioprinting system using visible light crosslinkable bioinks, Biofabrication 7 (2015) 1758–5090.

[12] C.G. Williams, A.N. Malik, T.K. Kim, P.N. Manson, J.H. Elisseeff, Variable cytocompatibility of six cell lines with photoinitiators used for polymerizing hydrogels and cell encapsulation, Biomaterials 26 (2005) 1211–1218, https://doi.org/10.1016/j.biomaterials.2004.04.024.

[13] J. Jung, J. Oh, Influence of photo-initiator concentration on the viability of cells encapsulated in photo-crosslinked microgels fabricated by microfluidics, Digest J. Nanomater. Biostruct. 9 (2014) 503–509.

[14] L. Xu, N. Sheybani, W.A. Yeudall, H. Yang, The effect of photoinitiators on intracellular AKT signaling pathway in tissue engineering application, Biomater. Sci. 3 (2015) 250–255, https://doi.org/10.1039/C4BM00245H.

[15] P. Di Mascio, M.E. Murphy, H. Sies, Antioxidant defense systems: the role of carotenoids, tocopherols, and thiols, Am. J. Clin. Nutr. 53 (1991) 194S–200S, https://doi.org/10.1093/AJCN/53.1.194S.

[16] H. Sies, W. Stahl, Vitamins E and C, beta-carotene, and other carotenoids as antioxidants, Am. J. Clin. Nutr. 62 (1995), https://doi.org/10.1093/ajcn/62.6.1315S.

[17] R.E. Beyer, The role of ascorbate in antioxidant protection of biomembranes: interaction with vitamin E and coenzyme Q, J. Bioenerg. Biomembr. 26 (1994) 349–358, https://doi.org/10.1007/BF00762775.

[18] S. Oh, Y.J. Kim, E.K. Lee, S.W. Park, H.G. Yu, Antioxidative effects of ascorbic acid and astaxanthin on ARPE-19 cells in an oxidative stress model, Antioxidants 9 (2020) 833, https://doi.org/10.3390/antiox9090833.

[19] B.H. Lee, H. Shirahama, N.-J. Cho, L.P. Tan, Efficient and controllable synthesis of highly substituted gelatin methacrylamide for mechanically stiff hydrogels, RSC Adv. 5 (2015) 106094–106097, https://doi.org/10.1039/c5ra22028a.

[20] D. Loessner, C. Meinert, E. Kaemmerer, L.C. Martine, K. Yue, P.A. Levett, T.J. Klein, F.P.W. Melchels, A. Khademhosseini, D.W. Hutmacher, Functionalization, preparation and use of cell-laden gelatin methacryloyl–based hydrogels as modular tissue culture platforms, Nat. Protoc. 11 (2016) 727–746, https://doi.org/10.1038/nprot.2016.037.

[21] P. Koti, N. Muselimyan, E. Mirdamadi, H. Asfour, N.A. Sarvazyan, Use of GelMA for 3D printing of cardiac myocytes and fibroblasts, J 3D Print Med. 3 (2019) 11–22, https://doi.org/10.2217/3dp-2018-0017.

[22] R. Banan Sadeghian, M. Ebrahimi, S. Salehi, Electrical stimulation of microengineered skeletal muscle tissue: effect of stimulus parameters on myotube contractility and maturation, J. Tissue Eng. Regen. Med. 12 (2018) 912–922, https://doi.org/10.1002/term.2502.

[23] X. Zhou, H. Cui, M. Nowicki, S. Miao, S.J. Lee, F. Masood, B.T. Harris, L.G. Zhang, Three-dimensional-bioprinted dopamine-based matrix for promoting neural regeneration, ACS Appl. Mater. Interfaces 10 (2018) 8993–9001, https://doi.org/10.1021/acsami.7b18197.

[24] J. Cui, H. Wang, Q. Shi, T. Sun, Q. Huang, T. Fukuda, Multicellular Co-culture in three-dimensional gelatin methacryloyl hydrogels for liver tissue engineering, Molecules 24 (2019), https://doi.org/10.3390/molecules24091762.

[25] M.K. Aparnathi, J.S. Patel, Biodegradable gelatin methacrylate gel as a potential scaffold for bone tissue engineering of canine adipose-derived stem cells, J. Stem Cell. 11 (2016) 111–119, jsc.2016.11.3.111 [pii].

[26] X. Li, S. Chen, J. Li, X. Wang, J. Zhang, N. Kawazoe, G. Chen, 3D culture of chondrocytes in gelatin hydrogels with different stiffness, Polymers 8 (2016), https://doi.org/10.3390/polym8080269.

[27] X. Zhao, Q. Lang, L. Yildirimer, Z.Y. Lin, W. Cui, N. Annabi, K.W. Ng, M. R. Dokmeci, A.M. Ghaemmaghami, A. Khademhosseini, Photocrosslinkable gelatin hydrogel for epidermal tissue engineering, Adv. Healthc. Mater. 5 (2016) 108–118, https://doi.org/10.1002/adhm.201500005.

[28] K. Yue, G. Trujillo-de Santiago, M.M. Alvarez, A. Tamayol, N. Annabi, A. Khademhosseini, Synthesis, properties, and biomedical applications of gelatin methacryloyl (GelMA) hydrogels, Biomaterials 73 (2015) 254–271, https://doi.org/10.1016/j.biomaterials.2015.08.045.

[29] Y. Wu, Y. Xiang, J. Fang, X. Li, Z. Lin, G. Dai, J. Yin, P. Wei, D. Zhang, The influence of the stiffness of GelMA substrate on the outgrowth of PC12 cells, Biosci. Rep. 39 (2019), https://doi.org/10.1042/bsr20181748.

[30] M.A. Birch-Machin, H. Swalwell, How mitochondria record the effects of UV exposure and oxidative stress using human skin as a model tissue, Mutagenesis 25 (2010) 101–107, https://doi.org/10.1093/mutage/gep061.

[31] J. Cadet, M. Berger, T. Douki, B. Morin, S. Raoul, J.L. Ravanat, S. Spinelli, Effects of UV and visible radiation on DNA-final base damage, Biol. Chem. 378 (1997) 1275–1286.

[32] G. Petruk, A. Raiola, R. Del Giudice, A. Barone, L. Frusciante, M.M. Rigano, D. M. Monti, An ascorbic acid-enriched tomato genotype to fight UVA-induced oxidative stress in normal human keratinocytes, J. Photochem. Photobiol., B 163 (2016) 284–289, https://doi.org/10.1016/j.jphotobiol.2016.08.047.

[33] K. Tokuda, C.F. Zorumski, Y. Izumi, Effects of ascorbic acid on UV light-mediated photoreceptor damage in isolated rat retina, Exp. Eye Res. 84 (2007) 537–543, https://doi.org/10.1016/j.exer.2006.11.005.

[34] K.S. Lim, B.S. Schon, N.V. Mekhileri, G.C.J. Brown, C.M. Chia, S. Prabakar, G. J. Hooper, T.B.F. Woodfield, New visible-light photoinitiating system for improved print fidelity in gelatin-based bioinks, ACS Biomater. Sci. Eng. 2 (2016) 1752–1762, https://doi.org/10.1021/acsbiomaterials.6b00149.

[35] W. Hu, Z. Wang, Y. Xiao, S. Zhang, J. Wang, Advances in crosslinking strategies of biomedical hydrogels, Biomater. Sci. 7 (2019) 843–855, https://doi.org/10.1039/c8bm01246f.

[36] H. Sakurai, H. Yasui, Y. Yamada, H. Nishimura, M. Shigemoto, Detection of reactive oxygen species in the skin of live mice and rats exposed to UVA light: a research review on chemiluminescence and trials for UVA protection, Photochem. Photobiol. Sci. 4 (2005) 715–720, https://doi.org/10.1039/b417319h.

[37] M. Garmyn, D. Yarosh, The molecular and genetic effects of ultraviolet radiation exposure on skin cells, Photo Dermatol. (2007) 41–54, https://doi.org/10.1080/10408369891234192.

[38] A.T. Dinkova-Kostova, Phytochemicals as protectors against ultraviolet radiation: versatility of effects and mechanisms, Planta Med. 74 (2008) 1548–1559, https://doi.org/10.1055/s-2008-1081296.

[39] S.J. Bryant, C.R. Nuttelman, K.S. Anseth, Cytocompatibility of UV and visible light photoinitiating systems on cultured NIH/3T3 fibroblasts in vitro, J. Biomater. Sci. Polym. Ed. 11 (2000) 439–457, https://doi.org/10.1163/156856200743805.

[40] A. Sabnis, M. Rahimi, C. Chapman, K.T. Nguyen, Cytocompatibility studies of an in situ photopolymerized thermoresponsive hydrogel nanoparticle system using human aortic smooth muscle cells, J. Biomed. Mater. Res. 91 (2009) 52–59, https://doi.org/10.1002/jbm.a.32194.

[41] P.A. Glascott Jr., E. Gilfor, J.L. Farber, Relationship of the metabolism of vitamins C and E in cultured hepatocytes treated with tert-butyl hydroperoxide, Mol. Pharmacol. 48 (1995) 80–88.

[42] A.D. Halpner, G.J. Handelman, J.M. Harris, C.A. Belmont, J.B. Blumberg, Protection by vitamin C of loss of vitamin E in cultured rat hepatocytes, Arch. Biochem. Biophys. 359 (1998) 305–309, https://doi.org/10.1006/abbi.1998.0914.

[43] H.-W. Kang, S.J. Lee, I.K. Ko, C. Kengla, J.J. Yoo, A. Atala, A 3D bioprinting system to produce human-scale tissue constructs with structural integrity, Nat. Biotechnol. 34 (2016) 312–319, https://doi.org/10.1038/nbt.3413.

[44] M. Ali, P.R. Anil Kumar, J.J. Yoo, F. Zahran, A. Atala, S.J. Lee, A photo-crosslinkable kidney ECM-derived bioink accelerates renal tissue formation, Adv. Healthc. Mater. 8 (2019) 6, https://doi.org/10.1002/adhm.201800992.

[45] Z. Żołek-Tryznowska, Rheolgy of printing inks, in: J. Izdebska, S. Thomas (Eds.), Printing on Polymers, edn., William Andrew Publishing, 2016, pp. 87–99, https://doi.org/10.1016/B978-0-323-37468-2.00006-3.

[46] S.A. Wilson, L.M. Cross, C.W. Peak, A.K. Gaharwar, Shear-thinning and thermo-reversible nanoengineered inks for 3D bioprinting, ACS Appl. Mater. Interfaces 9 (2017) 43449–43458, https://doi.org/10.1021/acsami.7b13602.

[47] A.K. Miri, I. Mirzaee, S. Hassan, S. Mesbah Oskui, D. Nieto, A. Khademhosseini, Y. S. Zhang, Effective bioprinting resolution in tissue model fabrication, Lab Chip 19 (2019) 2019–2037, https://doi.org/10.1039/c8lc01037d.

[48] A. GhavamiNejad, N. Ashammakhi, X.Y. Wu, A. Khademhosseini, Crosslinking strategies for 3D bioprinting of polymeric hydrogels, Small 16 (2020) 2002931, https://doi.org/10.1002/smll.202002931.

[49] H. Jeon, K. Kang, S.A. Park, W.D. Kim, S.S. Paik, S.-H. Lee, J. Jeong, D. Choi, Generation of multilayered 3D structures of HepG2 cells using a bio-printing technique, Gut Liver 11 (2017) 121–128, https://doi.org/10.5009/gnl16010.

[50] Y. Wu, Z.Y. Lin, A.C. Wenger, K.C. Tam, X. Tang, 3D bioprinting of liver-mimetic construct with alginate/cellulose nanocrystal hybrid bioink, Bioprinting 9 (2018) 1–6, https://doi.org/10.1016/j.bprint.2017.12.001.

[51] C. Zhong, H.-Y. Xie, L. Zhou, X. Xu, S.-S. Zheng, Human hepatocytes loaded in 3D bioprinting generate mini-liver, Hepatobiliary Pancreat. Dis. Int. 15 (2016) 512–518, https://doi.org/10.1016/S1499-3872(16)60119-4.